論文 / 著書情報
Article / Book Information

題目(和文)	LHC-ATLAS実験における多数の粒子飛跡を伴い衝突点から離れた崩壊点を用いた長寿命超対称性粒子の探索
Title(English)	Search for long-lived supersymmetry particle by signature of a high track-multiplicity displaced vertex using the LHC-ATLAS Experiment
著者(和文)	PetterssonNora Emilia
Author(English)	Nora Petterson
出典(和文)	学位:博士（理学）, 学位授与機関:東京工業大学, 報告番号:甲第10023号, 授与年月日:2015年12月31日, 学位の種別:課程博士, 審査員:陣内 修,久世 正弘,柴田 利明,岡 眞,Todd Tilma
Citation(English)	Degree:, Conferring organization: Tokyo Institute of Technology, Report number:甲第10023号, Conferred date:2015/12/31, Degree Type:Course doctor, Examiner:,,,,
学位種別(和文)	博士論文
Type(English)	Doctoral Thesis

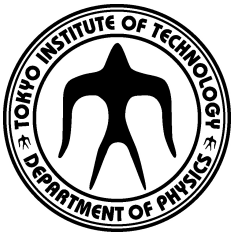

Ph.D Thesis
Search for long-lived supersymmetry particles by signature of a high track-multiplicity displaced vertex using the LHC-ATLAS Experiment

Nora Emilia Pettersson

Tokyo Institute of Technology, Department of Physics
November 16, 2015

This thesis has been submitted to the Ph.D School of the faculty of Physics at Tokyo Institute of Technology.

Abstract

Long-lived supersymmetry (SUSY) particles decaying within the tracking volume of the LHC-ATLAS Experiment can be reconstructed as a displaced vertex (DV). The search strategy involves attempting to reassemble the decay point of the long-lived particles (LLPs) by fitting vertices from the trajectories arising from the charged decay products. A search, looking for a signature of a massive high track-multiplicity DV has been conducted using data collected during 2012 by the LHC-ATLAS Experiment at $\sqrt{s} = 8$ TeV, equaling to an integrated luminosity of 20.3 fb^{-1}.

A signature of a massive displaced vertex is especially powerful due to the lack of any heavy long-lived standard model particles. Thereby, giving an analysis that is nearly background free. This dissertation describes the new, much more generic, "DV + jets" channel. In this channel events with high momentum jets and at least one displaced vertex are considered. Eliminating the requirement of an associated μ generated, to date of writing, the most powerful displaced vertex search. Several improvements have been made to the analysis. Extending the map over the tracking volume, used to veto nuclear interaction vertices, has made it feasible to increase the total fiducial volume from a previous 0.02 mm^3 to 0.07 mm^3 after applied veto. Moreover, a new technique to estimate combinatorial backgrounds of mis-reconstructed vertices has been developed, significantly reducing the total uncertainty on the estimate from 100% to 14.6%.

In the absence of any signal of new physics, limits on the production cross-sections are set. Interpreted in the context of R-Parity violating (RPV) SUSY, where the lightest SUSY particle decays to purely standard model particles through various RPV couplings. The excluded upper limits cross-section varies depending on lifetime of the long-lived particles and the targeted coupling, with a value of 0.3 fb in the best case scenario. A model-independent limit on the cross-section is set at 0.14 fb yielding an significant improvement from earlier result of 5.4 fb. These limits are the most stringent to date. Limits on RPV SUSY LLP are set over a range of proper decay length 1-1000 mm, focusing on $\tilde{g}(1000\,\text{GeV}) \rightarrow qq + \tilde{\chi}_1^0(108\,\text{GeV}) \rightarrow qq + l$, where the neutralino

is long-lived due to the smallness of the RPV coupling λ'. The upper limits on the cross-sections are set of neutralino decays to light flavour quarks and are ranging from 0.5 to 20 fb as a function of the proper decay lengths.

Declaration of Author's contribution

Part I: Consists of literature studies, aiming to explain the foundation necessary to follow the experimental analysis in Part II. The content in Part I should not be read as material created by the author but as a summary of material taken from the sources cited within the text.

Part II: Covers the Displaced Vertex Analysis. The work presented in this thesis is based on a team effort from several people dating back from the first article published in 2011. The majority of the content is made by the author but are based on years of optimisation of the analysis methods. The exceptions are; Chapter 6 - the data selection and Monte Carlo generations and simulations are not specifically developed for this thesis but is common for several searches at ATLAS for long-lived particles. Chapter 7 - contains the standard methods of reconstructing physics objects at the ATLAS experiment and are not work performed especially for this thesis but common ground for all analyses. Chapter 9 - Section 9.1-9.2 and Section 9.3.1-9.3.2 and Section 9.3.5 are conducted by the Displaced Vertex Analysis team and not by the author but are nevertheless required for a complete analysis.

All plots within the chapters are made for the purpose of the thesis if no other references are given to an other source, this is true both for Part I and Part II.

The limit setting procedures reviewed in Chapter 11 are common to the field of high energy physics and are not developed or modified just for this thesis. However, the results in the form of the upper limit on production cross-sections stated in Section 11.4 are of course produced by the author, but relying on familiar techniques.

The results presented in this thesis are entirely dependent on the smooth operation of the Large Hadron Collider and the ATLAS experiment. This thesis could not have been completed without the hard work of several thousands of people participating in the experiment. In order to justify the usage of the data recorded by the ATLAS experiment and to help out the collaboration, a service task has been performed. The task evolved into a complete analysis and the purpose, the motivations and the results are reviewed in Chapter 8.

Acknowledgements

I would like to extend my sincerest gratitude to Professor Osamu Jinnouchi for giving me the opportunity to do my Ph.D thesis at the Tokyo University of Technology under his guidance. He introduced me to the interesting field of long-lived particle searches, which later came to be the topic of my thesis and became a passion of mine. Without his ties to the exotic analyses at ATLAS I would not have been introduced to the interesting field of long-lived particles. Moreover, Professor Jinnouchi's door was always open and eager to engage in discussion about physics or life in general. When I first arrived in Japan, he helped me adjust to the life in a completely new country. Also I would like to thank the members of the group at Tokyo Institute of Technology, especially Minoru Hirose, Ryo Nagai, Kazuki Motohashi and Tobias Orthen for interesting chats about physics or about daily life. And of course, Kazuki (i)Todome for limitless supply of information. My thanks also goes out to ATLAS group at Tokyo Institutes of Technology and especially Professor Masahiro Kuze.

Professor Vivek Jain, whom I have worked together with for the ATLAS-service task, has offered me advise and guidance through out the years as a doctoral student. I would like to thank him for the countless discussions and chats about physics. Professor Jain has taught me how to think more like a physicist and an experimentalist rather than like a graduate student. Without any obligations he always had time for a chat, even if it was in the early mornings or in the late evenings due to the time difference between Japan and the United States of America.

Doctor Nick Barlow, who served as the leader of the ATLAS Displaced Vertex Analysis team, introduced me to the workings and methods of long-lived particle searches. He has been happily eager to teach and to offer suggestions or ideas from his non-surpassed expertise in the field. Even in the cases where posed questions might have been simple, his answers were sincere. I will always be grateful for his support.

Moreover, I would like to thank all the members of the ATLAS Displaced Vertex Analysis team for discussions and collaborations, with special men-

tion: Nick Barlow, Abner Soffer, Mike Flowerdew, Giovanna Cottin and Hidetoshi Otono. Without the collective work of all the team members my thesis would not have been possible.

Doctor Remi Lafaye, who was my supervisor during the time I wrote my Master thesis at the Royal Institute of Technology in Stockholm, inspired me to pursue a doctorate in particle physics. His knowledge of multiple subjects opened up my eyes to the prestige and vast knowledge necessary for a successful particle physicist. I would not have considered continuing in the research field without his encouragement and I will always be indebted to him.

During my time writing this thesis I received support through the 'Nanoscience and Quantum Physics' program at Tokyo Institute of Technology from the Center of Excellence Program funded by MEXT in Japan. I would like to thank Professor Susumu Saito and the secretariat for their support and assistance.

ATLAS Japan has also provided support for my long-term visit at CERN and the benefits of being at site would not have been possible without their help. I would also like to thank my office mate at CERN, Jia Jian Teoh, for many conversations and sometimes lowly gossips.

Lastly I want to extend my earnest and bona fide gratitude and thanks to my family and friends who have had to endure and share my frustrations, which are always involved in the research process. Foremost, to my brother Aron Pettersson and my dad Åke Hansson for all their never-ending support and provided motivational speeches when I needed it. Thanks to my long time friends Terho Siikanen and Mikko Ågren who suffered, but withstood, my complaints.

Och ett sort tack till alla glitterande får.

Contents

1. Introduction

Atoms compose the matter surrounding everyday life. Once thought to be the smallest, indivisible, constituents of matter. However, this hypothesis was proven wrong in 1897 by J.J Thomson who observed and identified the charged electrons in cathode rays [1]. In the early 20th century, physicist Ernest Rutherford et.al. discovered the presence of the atom-nucleus by scattering α particle onto gold atoms [2]. One after the other remarkable observations succeeded. Yielding significant advancements each decade. At first, the theoretical explanations often were formed to account for the phenomena in the empirical data. With the formation of the immensely successful theory "The Standard Model of Particle Physics", the table turned and theoretical prediction preceded discoveries.

Physicists have by no means given up on the idea to explain all the fundamental properties of the sub-atomic universe. The commissioning of the latest state of the art particle collider, the Large Hadron Collider (LHC) provides prospects to target energy regions never before probed. In 2012, as the last part to confirm Standard Model (SM), the Higgs boson was observed experimentally at the LHC by the A Toroidal LHC ApparatuS (ATLAS) Experiment [3] and the Compact Muon Solenoid (CMS) Experiment [4]. The domains at TeV scale, have already been frantically explored to search for new physics, beyond the reach of the SM. This thesis discloses one such search for new physics by looking for long lived particles; interpreted in the context of the Supersymmetric Theory. The data collected by the ATLAS experiment are scrutinised for signs of unknown phenomena. The strategy involves looking for displaced decays that form a high track multiplicity vertex in the tracking volume of the

detector. Preceding the completion of this thesis, the analysis has been made public by the ATLAS collaboration [5].

The thesis is structured as following. Part I will contain the necessary background information structured as: Chapter 2 aims to provide the essential theoretical and experimental background, giving focus to concepts Beyond Standard Model (BSM). Long lived particles and their properties are reviewed in Chapter 3. A brief introduction to the LHC and the ATLAS experiment will be given in Chapter 4. While Part II, Chapter 5 and onwards are dedicated to all elements involved in the Displaced Vertex Analysis. Containing a slight side track with Chapter 8 that covers a study of the material in the tracking detector conducted as a part of the minimum bias task force at the ATLAS experiment. Definitions and jargons often used in High Energy Physics (HEP) are collected in the Appendix. A.1, to keep a steady flow through the text.

Part I.

Theoretical Introduction and Experimental Equipment

2. Theoretical and Experimental Foundation

At the foundation of particle physics one finds the Standard Model (SM). The SM theory in particle physics describes the interaction of the fundamental particles through a set of force carriers. The theory has proven to be an immensely accurate description of the sub-atomic world. It explains a wide range of physical phenomena, not only present in particle physics but also in cosmology and astrophysics. The theoretically calculated values agree to great precision with the experimentally measured quantities. An assumption is made in that the average reader is familiar with the concepts of the SM theory. Nevertheless, the basic of particle physics is discussed briefly in this Chapter, while detailed explanations fall outside the range of this thesis. For a complete introduction to particle physics, the reader is referred the book *Particle Physics* by B. Martin and G. Shaw [6]. Likewise, preparatory contents regarding the experimental side of High Energy Physics (HEP) can be found in the books [7, 8]. The second part of this chapter is dedicated to the short-comings of the SM and explains why there is a need for an extended physics models reaching beyond the SM. The basic concepts and formalism of physics Beyond Standard Model (BSM) are discussed, focusing largely on the Supersymmetry (SUSY) theory; as the experimental search is interpreted on just this theory - this part is made as a compilation of the standard introductory literature to the subject and the reasoning mostly follows the pattern of Stephen P. Martin in his educational introduction *A Supersymmetry Primer* [9].

2.1. The Standard Model of Particle Physics

The SM is, in its own, a beautiful simple theory, providing explanations of physics occurring at a very small scale. In fact, the whole theory can be described with one equation, the SM Lagrangian $\mathscr{L}_{\mathrm{SM}}$:

$$\mathscr{L}_{\mathrm{SM}} = -\frac{1}{4}F_{\mu\nu}F^{\mu\nu} + i\bar{\psi}\not{D}\psi + \psi_i y_{ij}\psi_j\phi + \text{h.c.} + |D_\mu\phi|^2 - V(\phi), \qquad (2.1)$$

where each term represents the interactions of the fundamental particles through three forces (gravity, the fourth force is not explained by the SM). To be able to understand what the equation states, the particles and forces have to be introduced.

Nuclei are kept together by the strong force and this force is, as the name suggests, the strongest force. The second force in strength to that of 1/137 of the strong force, is the Electromagnetic (EM) force that affects charged particles such as the electrons. At a mere 10^{-6} of the strength of the strong force, acts the weak force. What drives β-decay is just interactions via the weak force. Gravity, known as the fourth force is exceedingly weaker than the three other forces, an operates at an order of 10^{-39} of the strong force.

The known and experimentally confirmed fundamental particles are summarised in Fig. 2.1. There are two classes of particles. Paul Dirac named the two classes after the famous physicists Enrico Fermi and Satyendra Nath Bose; Fermions (ψ in Eq. 2.1) and Bosons (F and D). These types of particles, fermions and bosons are treated differently by the Fermi-Dirac statistics and Boson-Einstein statistics respectively.

The fermions can either be charged and neutral but all of them have spin-1/2 and are therefore particles obeying the Pauli Principle [10]. In turn, the fermions come in two versions of particles, quarks and leptons. All fermions interacts via the weak force and all charged fermions participate in EM interactions. However, only the quarks can interact via the strong force as they contain colour charge. Fermions contain three generations with groups

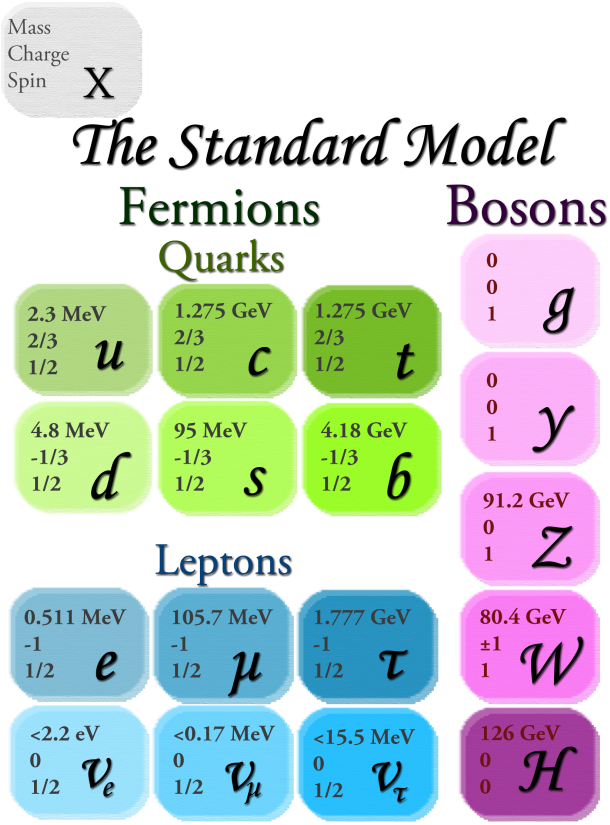

Figure 2.1.: The particle content of the standard model consists of two classes, fermions and bosons. The fermions are the constituents of matter in the form of quarks and leptons. The gauge bosons are the force carrying particles mediating the strong, the weak and the electromagnetic interactions. The Higgs scalar boson's interaction with the bosons and fermions gives these particles their mass. There are three generations of quarks and leptons with increasing mass going from the first, through the second to the third family. The lepton neutrinos are not yet confirmed to follow this pattern as their masses are yet not known.

of one lepton and one lepton neutrino. The lepton families have increasing

mass going from the first to the third, these are the electrons e, the muons μ and the tauons τ. Each of these leptons is grouped with a lepton neutrino ν_l, which is a neutral, weakly interacting and near-massless particle. The three fermion-lepton generations are;

$$\begin{pmatrix} e \\ \nu_e \end{pmatrix}, \qquad \begin{pmatrix} \mu \\ \nu_\mu \end{pmatrix}, \qquad \begin{pmatrix} \tau \\ \nu_\tau \end{pmatrix}. \tag{2.2}$$

There are in total twelve leptons with lepton and anti-lepton with charge $Q = -1$ and $Q = +1$, the lepton neutrinos are however, not charged. Neutrinos are always left-handed while antineutrino are right-handed with momentum direction relative to their spin direction $-1/2$ or $1/2$.

Likewise the quarks are ordered in three families, but without any neutrino counterpart. The first generation contains the up and down quarks (u and d), the charm and the strange quarks (c and s) are part of the second generation, and the third generation has the top and the bottom quarks (t and b);

$$\begin{pmatrix} u \\ d \end{pmatrix}, \qquad \begin{pmatrix} sc \\ s \end{pmatrix}, \qquad \begin{pmatrix} t \\ b \end{pmatrix}. \tag{2.3}$$

The up, charm and top quarks have charge $+2/3$, while the down, strange and bottom have $-1/3$. Bound states are formed from the quarks and held together with the strong force. Combination of two quarks, $q\bar{q}/\bar{q}q$ yields mesons and three-quark particles, $qqq/\bar{q}\bar{q}\bar{q}$ are called baryons (theoretically it is possible to form particles out of more than three quarks given that the combinations follow the set rules of e.g. integer number charge). Both mesons and baryons are considered to be hadrons. Hadrons includes all combinations of quarks but the combinations of the quarks must give an integer charge $Q = 0, \pm 1, +2$. Certain bound states of fermions demand that all the quarks would share the same quantum states, e.g. the baryon Δ^{++} consisting of 3 up quarks all with spin $+2/3$ Thereby, this particle seemingly violates the Pauli Principle. However, introducing a new quantum number solves this problem. In addition to spin and charge, quarks have colour charge with three degrees of freedom.

There are 36 quarks in the SM, 3 colour and 3 anti-colour degrees of freedom.

There are in total five bosons, four gauge bosons and one scalar boson. The gauge bosons propagate the fundamental forces and allow particles to interact via the exchange of a gauge boson;

- The strong interaction is mediated by the gluon g.
- The EM force is propagated via the photon γ.
- The W and the Z bosons mediate the weak force.

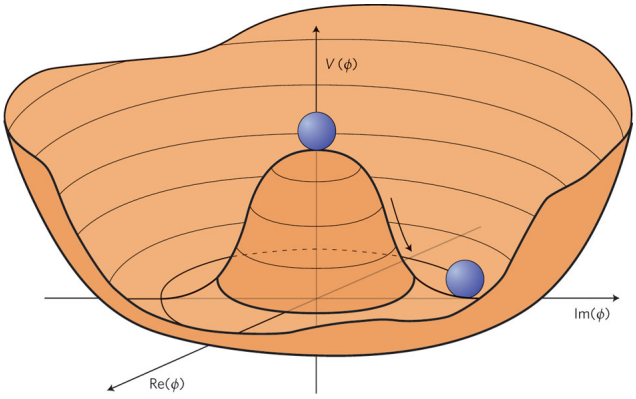

Figure 2.2.: A "Mexican Hat" illustrates the Higgs field, where the potential V is a function of ψ. Explained as "The vacuum — that is, the lowest-energy state — is described by a randomly chosen point around the bottom of the hat. In a global symmetry, movements around the bottom of the hat correspond to a massless, spin-zero, Nambu–Goldstone boson....The Higgs boson is a massive spin-zero particle." by the authors of the figure in reference [11].

Gauge invariance is a fundamental concept, inferring the conservation of a given unit under interactions. Interactions via the strong and EM force are gauge invariant, while interaction with the weak force are not. According to theory, if the W and Z bosons are invariant under gauge transformations, they would be massless particles. This is not true, as they have been observed

as massive particles. It was postulated that, if a universal non-typical field propagated through space, the local symmetry could be broken via interactions and yield a mass term to the particles. This is while maintaining global invariance in accordance with observed conservation laws. A characteristics of this field is that it is a non-zero ground state; with a Vacuum Expectation Value (*vev*) of magnitude larger than 0. This field is commonly illustrated by a "Mexican Hat" (Fig. 2.2), where the lowest value is not at the centre of the potential field. A feature of this field, later named after Peter Higgs, is that it is symmetrical at high energies, where the "blue" ball is at the centre. As the energy drops, the ball will fall down on either side. The process of going from one of the energy states to another involves, in fact, breaking of symmetry as the energy declines. This symmetry breaking is exactly what explains why the weak bosons are massive and the process, through which the masses are attained, is named after its three discovers - Robert Brout, François Englert and Peter Higgs - referred to as the Brout-Englert-Higgs (BEH) mechanism [12, 13]. At energies above 100 GeV, the electromagnetic and the weak force are unified. Above this energy-scale, there are three weak gauge bosons ($W_3 = W^{\pm}, W^0$) and one weak hypercharge boson (B^0). Equation 2.4 illustrates the correlation between the electroweak bosons.

$$\begin{pmatrix} \gamma \\ Z^0 \end{pmatrix} = \begin{pmatrix} \cos\theta_W & \sin\theta_W \\ -\sin\theta_W & \cos\theta_W \end{pmatrix} \begin{pmatrix} B^0 \\ W_3 \end{pmatrix} \tag{2.4}$$

Spontaneous symmetry breaking, through the BEH mechanism, splits the electroweak symmetry and creates the familiar massive weak bosons $W^{\pm}$, Z^0 and the massless EM-γ boson. The γ remains massless as its gauge group does not interact with the Higgs field and its symmetry remains unbroken. To explain this one needs to introduce the gauge groups of the interactions. The reader is again referred to introductory material on Particle Physics in reference [6] for details. The mass discrepancy between the charged and neutral weak bosons comes from the mixing of $M_Z = M_W / \cos\theta_W$ in Eq. 2.4. Yukawa interactions couples the fermions to the Higgs field and thereby also the quarks and leptons attain mass.

Strong interactions are mediated by the gluon bosons. Like the quarks, gluons

have colour charge. In total there are eight different gluons with contrasting setup of colour charge. Combined systems of quarks need to be colourless objects as such a confined object with colour charge has not been observed. The 8 gluons contain combinations of colour charges that cancel each other out in bound states. For example, a meson with a red and an anti-red quark needs to be bound with a gluon red-antired to cancel out the charge. The gluons themselves are massless as they do not interact with the Higgs field. Confinement is an important property of the strong interaction and refers to that the strength of the force is not reduced by distance. Because of this, free isolated quarks cannot exist. But rather, when quarks are forcefully separated, the gluon field will create a new quark pair from the vacuum.

Moving back to Eq. 2.1, the Feynman diagrams in Fig. 2.3 illustrates examples of each term in the form of the coupling processes. The first term in Eq. 2.1 portrays the boson-boson interactions e.g. of the type processes in Fig. 2.3, (f), (g), (h) and (i). The second term describes fermions interaction with the bosons giving the EM, weak and strong interactions with the leptons and quarks. A photon decaying to a fermion and an anti-fermion is an example of a process mediated by the EM force (Fig. 2.3 (b)). Inserting the electron lepton on the $f^{-C} f^{+C}$ position, is a typical case of photon annihilation; $\gamma \rightarrow e^- e^+$. The next term describes dynamics of the fermions field ψ and the Higgs field ϕ. Lastly, the remaining expressions are the interplay of the Higgs field and the Higgs potential. The simple expression quickly becomes more complicated when writing out each term explicitly. However, the exhaustive interworking of fundamental particle physics are concretely expressed by Eq. 2.1.

2.1.1. Experimental Results

Empirical data have to be consulted in order to establish the success of a given theory. One particular accomplishment of the SM theory, is the postulated existence of several particles before any experimental indications of such; the charm quark, the bottom quark, the top quark, the gluon, the W/Z boson and the Higgs Boson.

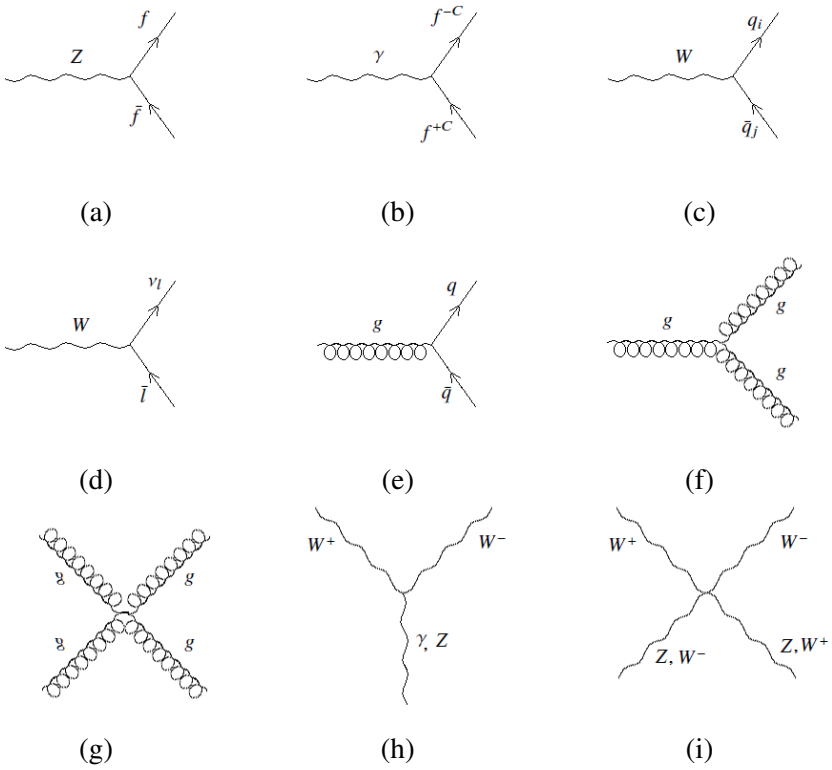

Figure 2.3.: The Standard Model Lagrangian described all possible interactions of the fermions and bosons. A few type examples are portrayed by the nine Feynman diagrams (a) to (i). (a) The weak interaction mediation through the neutral Z^0 to any fermion f. (b) is the electromagnetic interaction of a gauge boson, the photon decaying to two opposite charged fermions. (c) and (d) show the weak force carrying boson W decaying to a quark-antiquark pair or lepton-neutrino pair. (e) is an example of the gluon interaction to a quarks-antiquark pair. (f), (g), (h) and (i) are gauge boson interaction with themselves or other gauge bosons.

A further example would be that the masses of weak bosons are measured to extra precision. Experimental measured averages given by the Particle Data

Group in 2014 [14], are $M_W(M_Z)$ to 80.385 ± 0.015 (91.1876 ± 0.0021), while the theoretical predicted values are 80.390 ± 0.018 (91.1874 ± 0.0021).

A tremendous success is the theoretically predicted anomalous magnetic moment for the electron and with that the fine structure constant α. Classically, the magnetic moment is calculated at tree-level by the Dirac equation to $g = 2$. Experimental measured values vary from this prediction. The anomalous magnetic moment is a unity corresponding to the quantum corrections, defined as $a = (g - 2)/2$, to the magnetic moment. Including one-loop precision, the theory predicts, $a = \alpha/2\pi = 0.00115965218279(7.71)$ [15]. While the experimental measured number is 0.00115965218076(27) [16].

Precision measurements of cross-sections exhibit exceptional agreement with predictions. For example, the total production cross-sections of the SM, observed at the A Toroidal LHC ApparatuS (ATLAS) experiment in proton-proton (pp) collisions (during 2011 and 2012), agree to great precision with the theoretical values (Fig. 2.4).

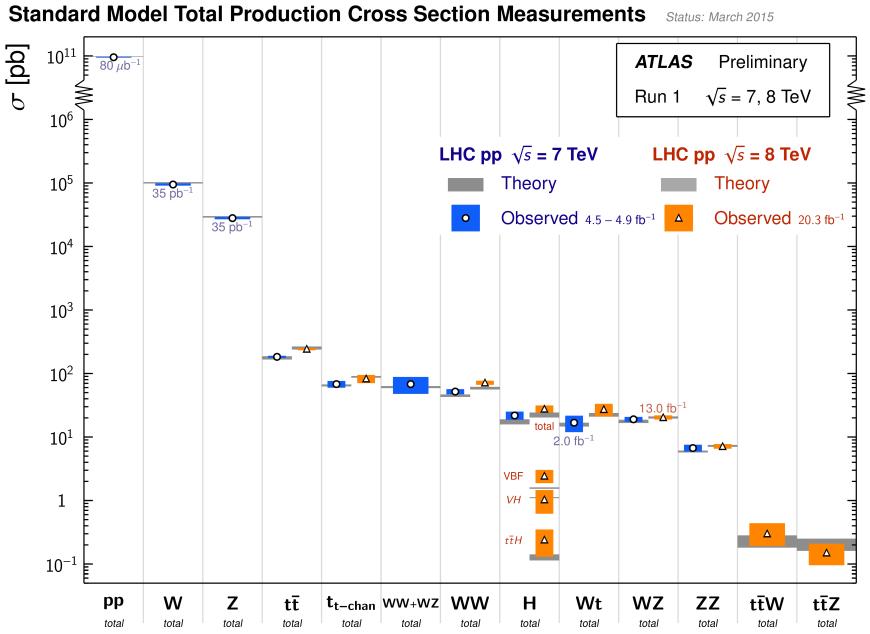

Figure 2.4.: Summary plot containing measurements by the ATLAS Experiment for the total production cross-sections from pp-collisions. The precision of the standard model is visualised by the great agreement between experimental data and the theoretically predicted values, calculated at NLO or Higher [17].

2.2. Beyond Standard Model Physics

Despite the success of the theory, there are still deficiencies as several physical phenomena cannot be accounted for. There is no doubt that "New Physics" is required to describe the world to and above the Planck scale mass (M_P). At these high energies the quantum gravity starts to have an effect and a theory including it is necessary. Another motivation for new physics is that there exists a certain amount of hierarchy problems, e.g. the huge gap between the strong, weak and EM forces and the gravitational force. Other types of hier-

archy problems are when the experimental measured values of parameters, e.g. couplings differ in magnitude. The mass of the Higgs boson m_H is considerably smaller than one would expect. The Higgs boson receives radiative corrections from particles interacting with the field, expressed as

$$\Delta m_H^2 = -\frac{|\lambda_f|^2}{8\pi^2}\Lambda_{UV}^2, \tag{2.5}$$

where Λ_{UV} is the maximum cut-off frequency often, assumed to be close to M_P^2, and where m_H is expected to become large. But this is not the case since m_H mass has been measured to around 126 GeV [3, 4]. This discrepancy of what is expected and what is observed indicate that there are missing parts in the theory. The magnitude between the observed mass of the Higgs boson and the Planck scale is considered to be the most important hierarchy problem.

A further indication is that the theoretical prediction of the μ anomalous magnetic moment α_μ^{SM}, does not agree with the experimentally measured values; with 0.00116591750 and 0.00116592091(54 (stat.))(33 (syst.)) [18] respectively. The two disagree outside 3σ. This measurement is sensitive to "New Physics" as the theoretical prediction includes all the parts of the standard model, $\alpha_\mu^{\mathrm{SM}} = \alpha_\mu^{\mathrm{QED}} + \alpha_\mu^{\mathrm{EW}} + \alpha_\mu^{\mathrm{Hadron}}$. Discrepancies observed between theoretically calculated value and the experimentally measure value could potentially give room to additional terms in the expression i.e. new physics.

One of the most commonly known issues is the cosmological observations of dark matter and dark energy, both lacking explanations in the SM. To incorporate these new entities requires an extension of the current theory.

Another cosmological observation is the antisymmetry in the distribution of baryon and anti-baryon matter in the universe. The baryon number conservation rules of the SM prohibit any explanation of the antisymmetry.

Concluding with stating that, the Standard Model is a beautiful working theory and explains the interaction between matters to an extreme precision. Nonetheless, it is not a perfect and complete theory and there is the need of new physics when moving closer to energy scales of the macroscopic universe.

2.3. The Supersymmetry (SUSY) Theories

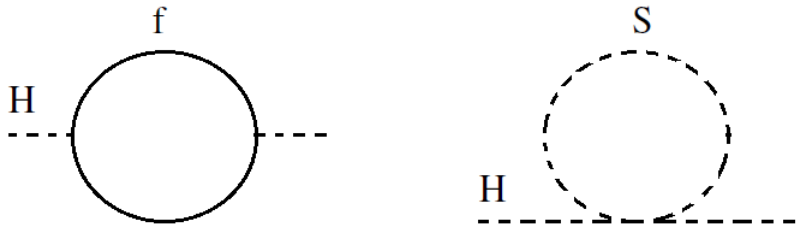

(a) (b)

Figure 2.5.: The interaction of a fermion with the Higgs field H, creates a large quantum correction to the Higgs boson mass (a). Adding a contribution of a boson S (b), which interacts with the H yields cancellations, after renormalisation, in the Higgs mass solving the Hierarchy problem.

SUSY is a principle which introduces an additional symmetry to the existing ones, namely a *fermion-boson* symmetry. There exist numerous SUSY theories which works on the concept of symmetries. The concept was first introduced in the 1970's with relation to string theory and quantum field theories to explain relations between particle species; that is between spin-1/2 and spin-1 particles, fermions and bosons [19, 20]. In fact, SUSY provides a number of solutions to the existing problems of the SM.

2.3.1. The SM Fine-Tuning Problem

Even though SUSY was created for different reasons, SUSY theories have recently been synonymous with solving the SM hierarchy and the fine-tuning problems [21]. Fermions interacting with the Higgs field H (Fig. 2.5) yield a correction term Δm_H^2 (Eq. 2.5) that is, at its maximum, proportional to the

square of the interaction scale Λ_{UV}[1]. Suppose there exists a corresponding boson interaction with the Higgs field (Fig. 2.5 (b)), the coupling of bosons contributes with a correction

$$\Delta m_H^2 = \frac{|\lambda_S|}{16\pi^2}\left[\Lambda_{UV}^2 - 2m_S^2 \ln(\Lambda_{UV}/m_S) + ...\right]. \tag{2.6}$$

If there is a set of scalars to the SM fermions, then the combined contributions to the corrections would cancel each other,

$$\Delta m_H^2 \sim (\lambda_S - \lambda_f^2)\Lambda_{UV}^2, \tag{2.7}$$

given that $\lambda_S = \lambda_f^2$[2]. The Introduction of a fermion-boson symmetry helped to provide a solution to the fine-tuning problem of the SM. Of course, perfect SUSY would require the masses of the superparticles to be the same as their SM partner. However, since no such super-partners have been observed at the SM mass scale, this is not the case and the symmetry has to be *broken* with regards to the masses. Therefore, it is important to point out that this cancellation of the quadratical behaviour occurs independent of whether the fermion m_f and boson m_S masses are equal as these do not enter into Eq. 2.7. However, after the cancellation the remaining contribution to m_H^2 is logarithmically dependent on Λ_{UV}. This is not an issue provided that the masses of the new super-partners are not too heavy. However, if the mass scale happens to be much above the weak scale, the logarithmic dependence becomes significant and would yield yet again large corrections to the Higgs mass. Essentially, to avoid fine-tuning, the supersymmetry particles (sparticles) should not be much heavier than a few TeV, which is exactly within the range of the Large Hadron Collider (LHC).

[1] Every fermion in the SM interacts with the Higgs field.
[2] In general field theory the signs of fermionic and bosonic interactions are opposite.

2.3.2. Few Words on the SUSY Formalism

A symmetry relating fermions to bosons implies that a SUSY quantum mechanical operator Q transforms fermionic quantum states ϕ_{fermion} into bosonic states ϕ_{boson} and bosonic ones into fermionic;

$$Q|\phi_{\text{boson}}\rangle = |\phi_{\text{fermion}}\rangle, \qquad Q|\phi_{\text{fermion}}\rangle = |\phi_{\text{boson}}\rangle. \tag{2.8}$$

These transformations turn one spin state into another, i.e. Q is a spinor. The relations in Eq. 2.8 suggest that Q is an anti-commuting spinor as the transformations are not uniform. Considering known rules and applying the limitation of reality on quantum field theory, the operators must satisfy the anti-commuting relations;

$$\{Q, Q\} = \{Q^\dagger, Q^\dagger\} = 0, \tag{2.9}$$

$$\{Q, Q^\dagger\} = P^\mu. \tag{2.10}$$

The first relation comes from the fact that Q is a hermitian operator and the definition of such operators is $Q = Q^\dagger$. The hermitian conjugate $Q^\dagger$ of Q is also a supersymmetry operator since they are spinors. The transformations, as they carry spin, require that the symmetry acts in space-time. Equation 2.10 includes on the left-hand side objects carrying $1/2$-spin, while P^μ is the four-momentum which transforms under Lorentz boost as a spin-1 object; the commutation relation then links spin-states differing by $1/2$-spin. From this follows that supersymmetry states commute with the mass-operator $-P^\mu$ i.e. they must share the same eigenvalues and have equal-sized masses (the mathematical solution to by-pass the mass is explored in the next section). Expanding the argument, the spin-operator $(-1)^{2s}$ is even for ϕ_{boson} ($s = 1$) and odd for ϕ_{fermion} ($s = |1/2|$). This operator must anti-commute with the

supersymmetry operators Q and $Q^\dagger$. Considering all possible quantum states for this operator gives,

$$\sum_i \langle i|(-1)^{2s} P^\mu |i\rangle = p^\mu Tr\left[(-1)^{2s}\right], \tag{2.11}$$

where p^μ denotes the eigenvalues of the momentum operator. The trace is then, given the behaviour of $(-1)^{2s}$, the sum of all bosonic states minus all the fermionic states. The left hand side can be shown to be $\sum_i \langle i|(-1)^{2s} P^\mu |i\rangle = 0$ replacing P^μ with $[Q, Q^\dagger]$ [9]. From these two expressions then follows

$$p^\mu Tr\left[(-1)^{2s}\right] = 0. \tag{2.12}$$

Then for $p^\mu \neq 0$, the number of bosonic states n_B then need to be equal to the number of fermionic states n_F

$$Tr\left[(-1)^{2s}\right] = \sum \phi_{\text{boson}} - \sum \phi_{\text{fermion}} = 0. \tag{2.13}$$

The conclusion from this is that the supersymmetry requires the same number of states for bosonic and fermionc degrees of freedom. The fermions of the SM are two compontent Weyl-spinors, $n_F = 2$. This needs a scalar counterpart with $n_B = 2$; the simplest solution would pair two scalars to the Weyl-spinors. For mathematical convenience, these two bosonic degrees of freedom are often expressed as a complex field. A complex field z includes by definition two degrees of freedom, a real $\Re(z)$ and an imaginary part $\Im(z)$. The supersymmetrical spin-0 particles are named by adding an "s" in front of their standard model names and indicated with a tilde. The quarks and leptons possess left and right-handed symmetries and transform differently under gauge interactions, e.g. u_R and $u_L^\dagger$, each is a Wely fermion. Therefore, there must exist a set of squarks and sleptons, which contains scalar spin-0 bosons to each of these fermions. However, as they are spin-0 particles, the helicity classifying these particles are a references to their SM counterpart, but must interact in the same way under gauge interactions[3].

[3] The left-handed quarks couples to the W while the right-handed particles do not.

Table 2.1.: The particle content of the MSSM. The Supemultiplets combining the supersymmetry partners to the SM particles. The SM fermions form chiral supermultiplets while the gauge bosons make up gauge supermultiplets. The Table is standard for MSSM but is directly obtained from [9]. The gauge groups are added in the most right column but are not referred to in the text to keep the arguments simple.

Chiral Supermultiplets				
Names		spin-0	spin-1/2	$SU(3)_C, SU(2)_L, U(1)_Y$
squarks, quarks	Q	$(\tilde{u}_L \tilde{d}_L)$	$(u_L d_L)$	$3, 2, 1/6$
(3 families)	$\bar{u}$	$\tilde{u}^*_R$	$u^\dagger_R$	$\bar{3}, 1, -2/3$
	$\bar{d}$	$\tilde{d}^*_R$	$d^\dagger_R$	$\bar{3}, 1, 1/3$
sleptons, leptons	L	$(\tilde{\nu}\tilde{e}_L)$	(νe_L)	$1, 2, -1/2$
(3 families)	$\bar{e}$	$\tilde{e}^*_R$	$e^\dagger_R$	$1, 1, 1$
Higgs, higgsino	H_u	$(H^+_u H^0_u)$	$(\tilde{H}^+_u \tilde{H}^0_u)$	$1, 2, +1/2$
	H_d	$(H^+_d H^0_d)$	$(\tilde{H}^+_d \tilde{H}^0_d)$	$1, 2, -1/2$
Gauge Supermultiplets				
Names		spin-1/2	spin-1	$SU(3)_C, SU(2)_L, U(1)_Y$
gluino, gluon		$\tilde{g}$	g	$8, 1, 0$
winos, W		$\tilde{W}^\pm \tilde{W}^0$	$W^\pm W^0$	$1, 3, 0$
binos, B		$\tilde{B}^0$	B^0	$1, 1, 0$

Furthermore, the bosons g, B^0 and W are spin-1 states with $n_B = 2$ as they have two helicity states. Follow the same logic as for the fermions, their supersymmetry partner must then be a spin-1/2 Weyl spinor. The counter-parts to the gauge bosons are named by adding an "ino" at the end e.g. gluino, wino and bino. Theoretically, these bosons need to be massless, if the symmetry is perfect. The treatment of the Higgs boson is not as straight forward, instead there is a need to introduce two supermultiplets with charge. These are required to couple to the different charged quarks (-1/3 and 2/3) and leptons. Table 2.1 reviews the minimal particle content of SUSY, when the number of supermultiplets is 1. This minimal version of SUSY is called Minimal Supersymmetry Standard Model (MSSM) [22]. This model has around 100 free parameters that included for instance flavour violating terms but the number

can effectively be reduced to around 20 with a few basic assumptions by setting terms contributing to flavour violation and charge and parity violation to zero, effectively reducing the number of free parameters to a more manageable number of around 20.

Mixed states with the neutral higgsinos and the Bino and the Wino, produce mass eigenstates named neutralinos $\tilde{\chi}_i^0$ and charginos $\tilde{\chi}_j^\pm$. There are four $\tilde{\chi}^0$ and two $\tilde{\chi}^\pm$.

2.3.3. Soft Supersymmetry Breaking

Since no SUSY particles have yet been found experimentally, it makes it near impossible to expect the masses of such particles at the same scale as the SM. Instead, the symmetry must be broken in one way or the other contributing to higher masses for all sparticles and gauginos.

The problem is solved by introducing soft-breaking terms in the Lagrangian on the form of $\mathscr{L} = \mathscr{L}_{\text{SUSY}} + \mathscr{L}_{\text{soft}}$ (Eq. 2.14) where the first term, on the right hand side, portrays the interactions of the fermions and bosons, while the last term introduces the mass-symmetry-breaking terms. The general effective soft-breaking terms include,

$$\begin{aligned}\mathscr{L}_{\text{soft}} = &-\frac{1}{2}(M_a \lambda^a \lambda^a + \text{h.c.}) - (m^2)^i_j \phi^{*j} \phi_i \\ &-(\frac{1}{2} b^{ij} \phi_i \phi_j + \frac{1}{6} a^{ijk} \phi_i \phi_j \phi_k + \text{h.c.}) \\ &-\frac{1}{2} c_i^{jk} \phi^{i*} \phi_j \phi_k + e^i \phi_i + \text{h.c.}\end{aligned} \tag{2.14}$$

Depending on the model under consideration, some of the terms in Eq. 2.14 might not be allowed. Each term in Eq. 2.14 represents an interaction or self-interaction of the boson and the fermions. Figure 2.6 illustrates these couplings by a few examples, where (a) represents the gaugino masses M_a for each gauge group and the squared masses (b) and (c) represent m^2 and b^{ij},

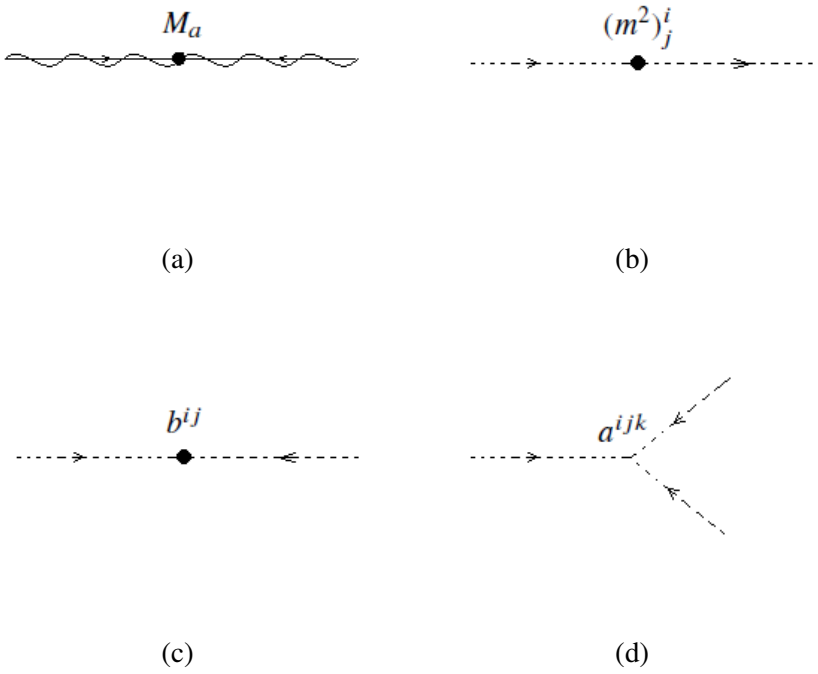

Figure 2.6.: Interactions and self-interactions of boson and fermions in the soft supersymmetry breaking Lagrangian are illustrated by Feynman diagrams. The gaugino mass and the squared mass terms from Eq. 2.14 are portrayed as their self-interaction in (a). The squared mass terms and the bilinear couplings are illustrated by (b) and (c) respectively. (d) shows the trilinear couplings and finally.

respectively, and (d) represents the trilinear couplings a^{ijk}. In the MSSM, the terms e^i and c_i^{jk} are not allowed. Under certain circumstances, these could yield large divergences and are generally neglected in MSSM to avoid any such effects.

It is possible to rewrite Eq. 2.14 more explicitly for the MSSM,

$$\begin{aligned}\mathscr{L}_{\text{soft}}^{\text{MSSM}} = &-\frac{1}{2}(M_3\tilde{g}\tilde{g} + M_2\tilde{W}\tilde{W} + M_1\tilde{B}\tilde{B} + c.c)\\ &-(\tilde{\bar{u}}\mathbf{a_u}\tilde{Q}H_u - \tilde{\bar{d}}\mathbf{a_d}\tilde{Q}H_d - \tilde{\bar{e}}\mathbf{a_e}\tilde{L}H_d + c.c)\\ &-\tilde{Q}^{\dagger}\mathbf{m_Q^2}\tilde{Q} - \tilde{L}^{\dagger}\mathbf{m_L^2}\tilde{L} - \tilde{\bar{u}}\mathbf{m_{\bar{u}}^2}\tilde{\bar{u}}^{\dagger} - \tilde{\bar{d}}\mathbf{m_{\bar{d}}^2}\tilde{\bar{d}}^{\dagger} - \tilde{\bar{e}}\mathbf{m_{\bar{e}}^2}\tilde{\bar{e}}^{\dagger}\\ &-m_{H_u}^2 H_u^* H_u - m_{H_d}^2 H_d^* H_d - (\mu H_u H_d + c.c).\end{aligned} \tag{2.15}$$

From this expression the masses of all the particles can be derived. The masses of the gauginos are given by M_1, M_2, and M_3 corresponding to the bino, the wino, and the gluino, respectively. The 3×3 matrices $\mathbf{a_u}$, $\mathbf{a_d}$ and $\mathbf{a_e}$ include the three families of squarks and sleptons. These are proportional to m_{soft} which is assumed to be of the order of TeV. The remaining terms in Eq. 2.15 all are $\sim m_{\text{soft}}^2$. This Lagrangian expression is gauge invariant and conserves matter parity, and includes 105 masses, couplings and mixing angles. The breaking of SUSY introduces a huge amount of unknown variables. It is possible with assumptions on the source of the breaking to limit these parameters. The SM third generation quarks (b and t) and lepton (τ) are significantly heavier than the first and second generations. Assuming that this is true in SUSY, the 3×3 matrices can be significantly simplified with only one non-zero element. One would keep only the heaviest generation in each of the three matrices; the element corresponding to the stop, sbottom and stau. The strength of the couplings can be modified by introducing radiative effects through different methods of supersymmetry breaking; however, these effects must be of finite size. The Yukawa couplings are often not the dominant production or the decay channels as they are often known to be small compared to the gauge interactions, proportional to M_1, M_2 and M_3. The method or physical phenomenon through which the symmetry is broken is vital to determine the mass or the decay channels. The Lightest Supersymmetry Particles (LSPs) are central to experimental searches as it would be within energy reach and the last step in decay chains. The identity of the sparticle often varies from theory to theory depending on the method for supersymmetry breaking.

A brief overview of how the sparticles attain mass and a mass differing from the particles and how the sparticles interact have been provided. However, a more detailed coverage of the complex workings of the SUSY theory falls outside of the scope of this thesis as it focuses on the experimental search for SUSY. Details regarding the theoretical calculations of the masses of sparticles are found in the excellent introductions to SUSY by S. Martin in *A Supersymmetry Primer* [9] and I. Aitchison *Supersymmetry in Particle Physics: An Elementary Introduction* [23].

2.3.4. R-Parity

In the SM the lepton number (L) and the baryon numbers (B) are conserved but the SUSY Lagrangian contains couplings that violates these numbers. Decays that violates these quantities are not allowed in the SM and no observations of lepton or baryon number violating processes have been made. To avoid causing contradictions to the SM, in SUSY one introduces instead a unit referred to as R-parity or matter parity which conserves the conjoint B and L;

$$P_R = (-1)^{3(B-L)+2s}, \tag{2.16}$$

where s is the spin. It follows from Eq. 2.16 that SM particles have $P_R = 1$ and sparticles $P_R = -1$. A simple example for a squark and a quark; a squark has $L = 0$, $B = 1/3$, $s = 0$ giving $P_R = (-1)^{3\cdot(1/3-0)+2\cdot 0} = (-1)^1 = -1$ while a quark on the other hand has $L = 0$, $B = 1/3$, $s = 1/2$ giving $P_R = (-1)^{3\cdot(1/3-0)+2\cdot 1/2} = (-1)^2 = 1$.

The R-parity violating terms in $\mathscr{L}_{\mathrm{SUSY}}$ are set to zero with the motivations that such interactions do not occur in the standard model. For instance, if the B-number is violated, the proton could potentially decay; dedicated searches exist for instance at the Super-Kamiokande experiment. To this date, no observations of proton decay exist, more details about this are given in Chapter 3.

On the one hand, conservation of R-parity has some interesting consequences; there should be no mixing between initial and final states, that is between -1

and 1 states. Sparticles can only be produced in pairs to conserve R-parity. The lightest sparticle can then not decay, as a decay of a $P_R = -1$ to $P_R = 1$ is forbidden. The lightest sparticle is therefore stable and the existence of a weakly interacting stable particle has huge impact on the typical experimental searches; this is the perfect candidate for dark matter.

On the other hand, many of the symmetries in the SM are not conserved. Parity operations, charge conjugations and time symmetries are all violated to a certain extent. Considering this, an assumption that R-parity needs to be conserved is non-intuitive.

2.4. Production of LLP SUSY Particles at the LHC

The specific channels target in the search for displaced vertices are covered in detail in Chapter 5. While this section aims to give a general overview of the production and decay process of sparticles at the LHC.

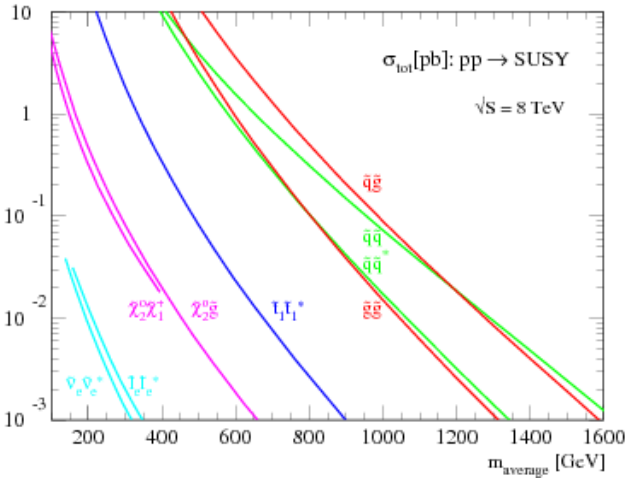

Figure 2.7.: The expected cross-sections for production of SUSY particles at the LHC for an average mass m_{average} at $\sqrt{s} = 8$ TeV. [24]

The production channels of SUSY particles at the LHC can either be via electroweak or the strong interaction. Since the protons are composed of quarks and gluons, it is easy to understand that the strong interaction production channel is favoured. Commonly, the $\tilde{g}$ is much heavier than the neutralinos and charginos, $M_3 > M_2 \& M_1$. Using the same logic, the lightest slepton is the $\tilde{\tau}$. The most straight forward process is the production of $\tilde{g}\tilde{g}$- or $\tilde{q}\tilde{q}$ pairs from gg and qq interactions,

$$gg \rightarrow \tilde{g}\tilde{g}, \qquad q\bar{q} \rightarrow \tilde{g}\tilde{g}, \tag{2.17}$$

$$gg \rightarrow \tilde{q}\tilde{q}^*, \qquad q\bar{q} \rightarrow \tilde{q}\tilde{q}^*, \tag{2.18}$$

$$qq \rightarrow \tilde{q}\tilde{q}, \tag{2.19}$$

$$gq \rightarrow \tilde{g}\tilde{q}. \tag{2.20}$$

The $\tilde{\chi}^0$ and $\tilde{\chi}^\pm$ are mixed states of $\tilde{B}$, $\tilde{W}^0$ or $\tilde{W}^\pm$ and the neutral and charged higgsino particles. These gauginos - as they are called - contain electroweak couplings and can be produced from $q\bar{q}$ pairs. Moreover, sleptons are created through electroweak interactions. A couple of examples in electroweak production that might occur in pp collisions,

$$q\bar{q} \rightarrow \tilde{l}\tilde{l}, \qquad q\bar{q} \rightarrow \tilde{\nu}\tilde{\nu}^*, \tag{2.21}$$

$$q\bar{q} \rightarrow \tilde{\chi}^0\tilde{g}, \qquad q\bar{q} \rightarrow \tilde{\chi}_2^0\tilde{\chi}_1^\pm. \tag{2.22}$$

The production cross-sections at the LHC at $\sqrt{s} = 8$ TeV are dominated by the strong production (Fig. 2.7). This is easy to understand as the LHC is a hadron-hadron collider and will be cluttered with quarks and gluons.

The decay chains of the sparticles after production are, of course, dependent on the specifics of the SUSY theory and on the supersymmetry-breaking mechanism. However, assuming that R-Parity is conserved and that the same decay channels hold even for the R-Parity violating scenarios, except for the non-decaying LSP, the predominant decays go as follows.

- **Gluino:** On-shell decays of the $\tilde{g} \rightarrow q\tilde{q}$ are only allowed, if the gluino is heavier than the squarks. The decays $\tilde{g} \rightarrow t\tilde{t}$ and $\tilde{g} \rightarrow b\tilde{b}$ are the most probable. This is due to that the two first generations of $\tilde{q}$ are mass degenerates, while there exist two mass eigenstates of the stop and sbottom. The squarks $\tilde{t}$ and $\tilde{b}$ are expected to be lighter than the other squarks due to the mixing effects. If the squarks are heavier than the gluinos, they might decay off-shell through three-body decay to neutralinos or charginos; $\tilde{g} \rightarrow qq\tilde{\chi}$.

- **Squark:** The dominant on-shell decay for squarks is $\tilde{q} \rightarrow q\tilde{g}$ due to Quantum Chromo Dynamics (QCD) interactions. If the squark cannot decay to a gluino, the gluino in the previous decay is replaced by a neutralino or a chargino; $\tilde{q} \rightarrow q\tilde{\chi}$. The chiral properties of the $\tilde{q}$ here play a significant role. Right handed $\tilde{q}_R$ possesses stronger couplings to $\tilde{B}$ and will then favour decays to $\tilde{\chi}^0$ ($\tilde{\chi}^0$ are bino-like in most cases). The squark $\tilde{q}_L$ on the other hand, has stronger squark-quark-wino couplings and favour decays to one of heavier charginos or neutralinos.

- **Neutralinos and Charginos (Gauginos):** The Gauginos have a large set of couplings and therefore a wide range of possible decays. For instance, they have gaugino-higgsino-Higgs couplings; neutralinos may decay into a higgsino and a lighter neutralino, $\tilde{\chi}^0 \rightarrow A^0\tilde{\chi}^0$, $H^0\tilde{\chi}^0$, $H^{\pm}\tilde{\chi}^{\pm}$ The same goes for chargino, $\tilde{\chi}^{\pm} \rightarrow A^0\tilde{\chi}^{\pm}, H^0\tilde{\chi}^{\pm}, H^{\pm}\tilde{\chi}^0$. Gauginos might also decay to pairs of quark-squarks. These decays are often suppressed as they contain heavy higgsinos. Rather, the decays, involving W, Z or h^0 and a lighter $\tilde{\chi}$, are more probable; $\tilde{\chi}^0 \rightarrow Z\tilde{\chi}^0$, $W\tilde{\chi}^{\pm}$, $h^0\tilde{\chi}^0$, $l\tilde{\nu}$, $\nu\tilde{l}$. If all these decays are forbidden, they might instead decay through three body off-shell decays into lighter gauginos and a pair of fermions; $\tilde{\chi} \rightarrow ff\tilde{\chi}$.

- **Slepton:** The preferred two-body decays of the sleptons are into combinations of leptons and gauginos. The chiral helicity of the $\tilde{l}$ plays yet again an important part. The $\tilde{l}_R$ prefers bino-like decays, while $\tilde{l}_L$ rather has stronger couplings to wino-like particles. The decays of the sleptons are on the form $\tilde{l} \rightarrow l\tilde{\chi}^0, \nu\tilde{\chi}^{\pm}$ or $\tilde{\nu} \rightarrow \nu\tilde{\chi}^0, l\tilde{\chi}^{\pm}$

In R-parity conserving theories, the decay chain continues until only the LSP remains. However, in R-Parity Violation (RPV) scenarios the decay, of course, continues and the lightest sparticle decays into SM particles.

2.5. Discussion

SUSY is a promising theory to solve the SM fine-tuning problem. R-Parity conserving theories provide a beautiful candidate to the cosmological indication of a need of dark matter. The SM cannot calculate the mass of the Higgs boson but it might be possible with the SUSY theory, provided that all the couplings are known etc. A number of SUSY extensions manage to unify the strong, electromagnetic and weak couplings at the unification scale, commonly referred to Grand Unification Theory (GUT). The GUT possibilities of SUSY have not been covered in this short summary, but a note can be made here stating that there is such a theory, which attempts to combine the forces into one at a larger mass scale. An important thing to point out is that the lightest sparticles must be within reach of the LHC, otherwise the mass scale becomes too high and the fine-tuning problem with the radiative effect to the Higgs mass once again becomes a problem.

2.6. Other BSM Models

Many, many more BSM theories exist, which - similar to the SUSY theory - try to provide solutions to the problem with the SM and to the phenomena observed in cosmology. All of these theories must extend upon the known physics as they need to take into account current observations. String theory is

perhaps the most familiar one. Point particles are considered to be one dimensional strings, the interaction of these strings attempts to explain the forces. The strings will appear as particles when moving away from the one dimensional "space". The Superstring theory endeavours to include the whole set of the fundamental particles and the forces. The forces are propagated through vibrations of the strings. Extra dimensions are compulsory in these theories as they are inconsistent in less than ten space dimensions. A further extension on the string theory is the so called, M-Theory. Though yet incomplete, this theory strives to include the gravitational force, moving into the eleventh dimension. Experimental searches for extra dimensions are conducted at the LHC, but at time of writing, no signs of such phenomena have been observed. More on this subject can be found in Michio Kaku's book *Introduction to Superstrings and M-Theory* [25].

Recently, another popular theory is the theory postulating the existence of a Hidden Valley. Here, the known universe is separated from a "Hidden" sector, which can not normally be reached. The Hidden Valley contains a set of particles that are weakly interacting with known matter. However, it is postulated that the high energies, in collisions at the LHC, open a window, through which the Hidden Valley is accessible [26]. This requires a mediator, which communicate with the Hidden Valley i.e. couples both to the hidden and the SM particles. Potentially, the mediator could decay into hidden particles and bring them into our universe. These rare particles could then be detected.

3. Long Lived Particles

The existence of Long Lived Particles (LLPs) is common in models treating topics of new physics. Additionally, the existence of LLPs in the Standard Model (SM) has been empirically confirmed numerous times. However, during recent years, focus of LLP searches has moved slightly away from the SM towards multiple dedicated searches for long lived exotic particles. These particles are frequently assumed to behave atypical and leave non-SM signature in the experiments. This thesis treats just one of these experimental searches for massive LLPs postulated in physics by Supersymmetry (SUSY). A short introduction to the concepts of longevity, the reasons, and the physics behind the notion of long-lived particles are given in this chapter, as well as their presence in the SM. The introduction is followed by a few words on the theoretical motivation and through which processes massive LLPs can be produced at the Large Hadron Collider (LHC).

3.1. Lifetime

Lifetime is a concept describing how long it takes for an entity to decay. It is a common concept in both nuclear and particle physics; where the entity is either a nucleus or a particle. The rate at which a quantity decreases is given by an exponential function,

$$N_t = N_0 e^{-\Gamma t}, \tag{3.1}$$

where N_0 specifies the initial amount of a unit, while N_t is the remaining size after time t. The decay constant or the decay width is given by Γ; the magnitude is dependent on the opportunities for decay, e.g. in the case of nuclear physics, if the decays are kinematically favoured. More than often, particles will have more than one possible decay channel. Additional decay constants are then added to Eq. 3.1 for each channel i; $\Gamma = \sum \Gamma_i$. The rate $\delta\Gamma$ at which a particle decays is derived from Fermi's Golden rule of Decays (for a complete description and derivation consult [27]);

$$\delta\Gamma = \frac{(2\pi)^4}{2M}|\mathscr{M}|^2 d\Omega_n(P; p_1, \ldots, p_n), \tag{3.2}$$

where M is the mass of the particles, n specifies the number of daughter particles, $\mathscr{M}$ represents matrix elements and $d\Omega_n$ is the phase space of the decay channels derived from the system's momentum, mass and energy. The probability that a particle decay at time t is;

$$P(t) = e^{-\Gamma t}. \tag{3.3}$$

The average or mean lifetime, τ is the expectation value of $P(t)$ for time t; related to the decay constant as $\Gamma = 1/\tau$[1]. The initial amount N_0, after τ, is reduced by a fraction $1/e$. The half life, on the other hand, is at which time, N_0 is reduced to half of the initial values; not commonly used in particle physics.

Relativistic speeds come into play both in particle physics experiment and in cosmology. Time dilatation or length contraction causes a particle to survive longer in the laboratory frame; the Lorentz factor $\gamma = 1/\sqrt{1 - v^2/c^2}$ is then multiplied with the mean lifetime τ, at rest. The Proper Decay Length ($c\tau$), is at which distance the particles decay in the laboratory system. Assuming relativistic speeds the distance needs to be corrected by the Lorentz factor; $L = \gamma\beta c\tau$.

[1] Keeping formalism in Natural Units.

3.2. Long Lived Particles

A perfect example of a particle with long lifetime is the proton. Perhaps, the classification "stable particle" suites it better. Protons are three quark systems bound together by the strong force. The Baryon and Lepton numbers, in the SM, are conserved unit due to gauge symmetries. Therefore, there are no permitted decay channels for the protons that do not violate these quantum number conservation laws. However, certain Grand Unification Theory (GUT) requires that protons have a finite lifetime of $\sim 10^{36}$ years. There are experiments dedicated to look for the proton decay. These typically look for the decay channels $p \rightarrow e^{+}\pi^{0}$ or $p \rightarrow \bar{\nu}K^{+}$. However, as of yet there have been no observations of decaying protons; exclusion for these decay modes are at $> 10^{34}$ years by the Super-Kamiokande [28].

Not stable, but long-lived, is the neutron with a mean lifetime of 881.5 s. The neutron decays $> 99\%$ of the time to $n \rightarrow p^{+} + e^{-} + \bar{\nu}_{e}$ which is β-decay. Neutrons' fairly long lifetime is explained by the rather small decay phase space (protons are comparable massive to the neutrons) and that their decay occur through the weak force.

To collider physics, even particles that decay within a micro- or nano-second are considered long-lived or meta-stable. An example of such is the second heaviest lepton, the muon μ. It possesses a mean lifetime of 2.197×10^{-6} s. At relativistic speeds, this type of particles can travel a substantial distance and deserves the classification long-lived. Muons from cosmic showers are possible to detect near the earth surface due to the relativistic effect of time dilatation (or length contraction).

The SM contains several of these meta-stable particles, with lifetimes around order of nano-seconds. Kaons K ($\tau \sim 10^{-11} - 10^{-8}$), are meson-states of a strange quark combined with an up or a down quark. Again, their decays are suppressed by their interaction via the weak force with decays to either combinations of pions or leptons. The same goes for the charged pion-mesons ($\sim 10^{-8}$), they are meta-stable and decay to leptons.

After reviewing the already confirmed examples of LLP let's not forget the potential ones on "the other side" of the SM. Previously mentioned, there are

several Beyond Standard Model (BSM) theories that predict particles with considerably long lifetimes. The lifetimes of these new particles are determined by the same physical principles as in the SM by, i.e. features of the models, the mass spectrum or minute couplings. This thesis is dedicated to SUSY and LLP in the scenario where R-Parity (Section 3.3) is not conserved. A few examples of these particles will be given for SUSY. However, their presences are not only restricted to SUSY models, but also to other exotic models e.g. Hidden Valley, but their hypothetical existence is outside the scope of this thesis.

SUSY-breaking in the Anomaly Mediated Supersymmetry Breaking (AMSB) model is realised only through the supergravity parts of the $\mathscr{L}_{\text{soft}}$. This means that the masses and internal hierarchy are solely decided by the supergravity interactions. Sparticles in one of the AMSB [29, 30] scenarios, the relation between the gaugino masses - M_1,M_2 and M_3 - generates mass degeneracy between the NLSP, $\tilde{\chi}_1^{\pm}$ and the LSP $\tilde{\chi}_1^0$. The small mass difference kinematically restricts the decay rate of $\tilde{\chi}_1^{\pm} \rightarrow \tilde{\chi}_1^0 X$; which is the only possible decay channel assuming R-Parity Conservation (RPC). The same holds for the Gauge Mediated Supersymmetry Breaking (GMSB) models [31], where the NLSP predominantly decays through the gravitational couplings.

In Split-SUSY [32, 33] the large mass splitting between the $\tilde{g}$ and the $\tilde{q}$ prohibits the decay of the $\tilde{g}$. The gluino, possessing colour charge, exclusively decays strongly to a $\tilde{q}q$. R-hadrons, are theorised as the long lived gluino ($\tau < 100$ s), could interact with free quarks and form hadrons.

A third potential scenario is when the couplings are minute, suppressing decays. A type example would be R-Parity Violation (RPV) model [34], as the RPV couplings need to be small not to contradict the SM (the proton decay). The small couplings would suppress the decay and cause the particle to become long lived.

The lifetime of an LLP in all of these examples is dependent on the mass spectra of the particle contents, like the gaugino masses. Nonetheless, considering the amount of unknown parameters in these new theories, the choices to dictate the properties and masses of the particle content might seem arbitrary. Generally, the decision is based on which the already experimentally excluded

regions are in order to target a sector of the parameter space previously not an object of a search (the same criteria apply to standard searches for promptly decaying particles).

3.3. SUSY and R-Parity Violating Scenarios

The proton-decay is certainly a good motivation to why R-Parity (Section 2.3.4) "should" be conserved. However, in SUSY, if B or L is violated individually, this would not lead directly to rapid proton-decays [34]. Consider the R-parity violating contributions to $\mathscr{L}_{\mathrm{SUSY}}$,

$$\mathscr{L}_{\Delta L=1} = \frac{1}{2}\lambda^{ijk} L_i L_j \bar{e}^k + \lambda'^{ijk} L_i Q_j \bar{d}_k + \mu'^i L_i H_u, \tag{3.4}$$

where the lepton violating couplings are λ, λ' and μ' and

$$\mathscr{L}_{\Delta B=1} = \frac{1}{2}\lambda''^{ijk} \bar{u}_i \bar{d}_j \bar{d}_k, \tag{3.5}$$

where the baryon violating coupling is λ''. Each of the four couplings in Eq. 3.4 and 3.5 represents possible decay types. Figure 3.1 shows examples of all these couplings.

- $\boldsymbol{\lambda}$ is one of three lepton flavour violating couplings ($\Delta L = 1$), where sleptons decay to leptons (Fig. 3.1 (a)).
- $\boldsymbol{\lambda'}$ involves quarks and leptons. For example, $\tilde{\chi}_1^0$ decays to leptons and quarks (Fig. 3.1 (b)).
- $\boldsymbol{\lambda''}$ is the baryon number violating coupling ($\Delta B = 1$) causing squarks to decay into quarks (Fig. 3.1 (c)).
- $\boldsymbol{\mu'}$ relates leptons to the higgs (Fig. 3.1 (d)).

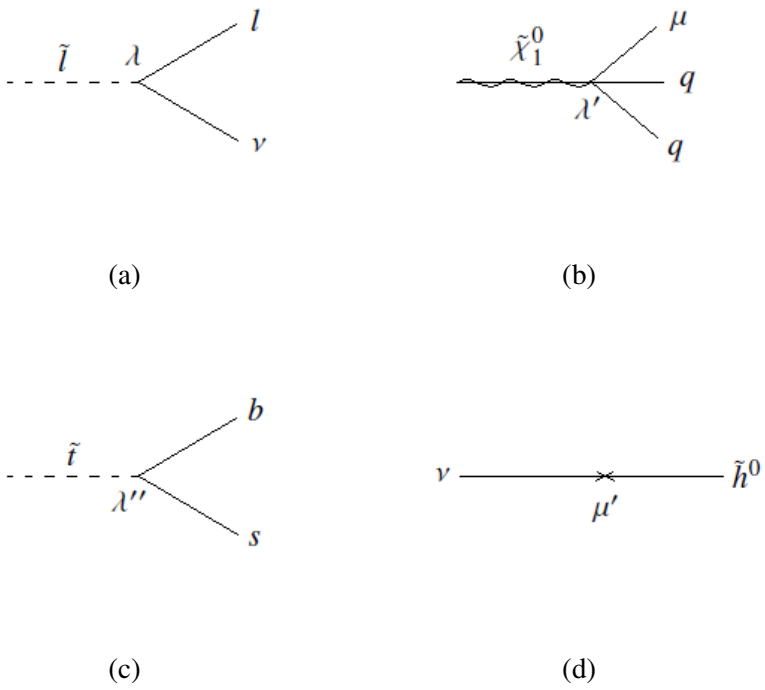

Figure 3.1.: The lepton and the baryon number violating coupling is illustrated. (a) shows an example of the lepton number violating coupling λ; a slepton decays to a lepton and a lepton neutrino. (b) shows the second lepton number violating coupling λ'; a neutrino decays into a final state with a lepton and quarks. The pure baryon number violating is the λ'' coupling (c); a stop decays directly to two quarks. Finally, (d) shows the μ' coupling relating lepton numbers to decays of higgs.

All of these have in common that a stable Lightest Supersymmetry Particle (LSP) no longer exists. Anyway, how small these couplings might be, the decays of sparticles to particle will always be kinematically allowed (the mass scale of the SM is lower than SUSY). Depending on the strength of the RPV couplings, the LSP might be relatively long-lived.

3.4. Experimental Searches

How to define particles to be stable or meta stable, differs from a theoretical and an experimental point of view. From the experimental viewpoint, the detector's ability to see the particle is the important matter. So, from the standpoint of the detector capability, there are typically three categories of lifetimes: the particles that instantly decay, and the particles that decay inside the range of the detector, and the particles that travel through the whole detector volume without decaying.

- The particles that instantly decays are, e.g. the top quark with a mean lifetime of $5 \cdot 10^{-25}$ s. If this type of particles is produced in a collision they cannot be directly observable and has to be identified and assembled by their daughter particles.
- The particles that decay inside the range of the detector, at some distance from the collision point, are referred to meta stable particles. The majority of particles produce in proton-proton (pp) collisions are pions and the charged pions are a prime example of meta stable particles[2]. They predominantly decay through the weak force, $\pi^{\pm} \rightarrow \mu^{\pm} + \nu_{\mu}$ ($2.6 \cdot 10^{-8}$ s). Another example that yields displaced vertices with a lifetime of $8.9 \cdot 10^{-11}$ s is the neutral Kaon, K-Short. Its decay is also delayed due to interactions via the weak force $K_S^0 \rightarrow \pi^+ + \pi^-/\pi^0 + \pi^0$.
- The particles that decay outside the detector, i.e. the collider stable particles travel through the whole detector volume without decaying. This does not per se, mean that the particles are stable in a relative sense, they could decay outside the detector volume. The muons are relatively massive compared to the electrons and possess longer interaction lengths than electrons. Muons decay through the weak force to electron and electron-neutrino pairs plus a muon neutrino ($\mu \rightarrow e + \nu_e + \nu_{\mu}$). The lifetime of particles are often stated in values of proper decay length of $c\tau$ instead of τ; to make it easier to interpret the properties on the detector system.

[2] The neutral pions decay significantly more rapidly through the electromagnetic force, $\pi^0 \rightarrow 2\gamma$. The average lifetime is $8.4 \cdot 10^{-17}$.

Experimental searches dedicated to find long lived massive particles have been conducted for several years. Fairbairn et.al. provide an excellent summary to pre-LHC searches for long lived particles in the article [35]. They summarise early results in both cosmological and accelerator experiments, serving as a foundation for LHC searches. Most of the preceding searches have targeted massive charged particles and neutral particles are next to untreated. Detectors at the Large Electron-Positron Collider (LEP), Apparatus for LEP PHysics (ALEPH) [36], Omni-Purpose Apparatus for LEP (OPAL) [37] and L3 experiments [38] all conducted $\delta E/\delta x$ measurements, searching for abnormally large deposits of energy. DEtector with Lepton, Photon and Hadron Identification (DELPHI) [39] conducted similar searches but combined Cherenkov imaging with ionisation loss measurements. See articles [40–43] for examples from each experiment, the references provide for each experiments are just one example out of many for long-lived charged particle searches at these four experiments. Likewise, LEP searched for monopoles or Q-balls, which are objects with non-standard values of magnetically or electrically charge. All these searches help set initial limit on LLP. In hadron collisions, the Tevatron looked for a wide range of phenomena of massive exotic particles. The interested reader, who wish to learn more, is referred to the previous mentioned article [35] which provides a comprehensive summary on these past experimental searches and the limits set.

The LHC has increased the mass range from the preceding searches with at least an order of magnitude. Extending the mass reach up to several TeV; once operating at full beam energy and luminosity. Accompanied side by side with the benefits the LHC brings, the LLP might become more difficult to detect. A major limitation is the rapid rate of bunch crossings as the detectors are designed to have a 25 ns interval between the collision of proton-proton bunches. This means, that the trigger system work on a too fast rate to associate the signal of slow moving particles with the right event. This could yield inefficiencies in the reconstruction of events with massive long lived particles. The particles are, at 25 ns bunch crossings, required to have a Lorentz boost $\beta > 0.5$ to fit in with the reconstruction algorithms. Other problems conducting exotic searches for non-prompt particles are that the detectors are generally optimised to reconstruct prompt particles. There are in fact, default cuts

that happen reduce the contribution of secondaries. Therefore, non-standard techniques are used and the analyses utilise methods for object reconstructions or background estimations that differ from the rest of the collaboration. These caveats and problems are discussed further in Chapter 5 in the concrete context of the Displaced Vertex Analysis for the A Toroidal LHC ApparatuS (ATLAS) experiment.

4. Experimental Apparatus

The Large Hadron Collider (LHC) is the world most powerful particle accelerator and is absolutely vital to this analysis. At the LHC, proton-proton (*pp*) are collided at higher energies and luminosities than anywhere else in the world. The accelerator ring has a circumference of 27 kilometres and is situated approximately 50 to 175 meter below the Jura Mountains, near the Franco-Swiss border. This chapter will go through a short introduction about the accelerator and then focus on the A Toroidal LHC ApparatuS (ATLAS) detector. Please refer to Section A.1 in the appendix for the definitions of the coordinate frames used thorough the chapter.

4.1. The Large Hadron Collider

The LHC is situated at Conseil Européen pour la Recherche Nucléaire (CERN) in Geneva, Switzerland. This machine is designed to operate at centre of mass energy of 14 TeV and at a luminosity of 10^{34} $\mathrm{cm}^{-2}\mathrm{s}^{-1}$. Two separate beams of protons are made to collide in the centre of four detectors (indicated by stars in Fig. 4.1). One beam travelling clock-wise through the synchrotron, while the other beam is going at an anti clock-wise direction, propelled by ingeniously designed magnets. The four detectors are, the ATLAS experiment [45], the Compact Muon Solenoid (CMS) experiment [46], the A Large Ion Collider Experiment (ALICE) [47] and the Large Hadron Collider beauty (LHCb) experiment [48]. The first two are multipurpose detectors, while ALICE is a heavy ion experiment and LHCb is a forward detector with the purpose to study the difference between matter and anti-matter.

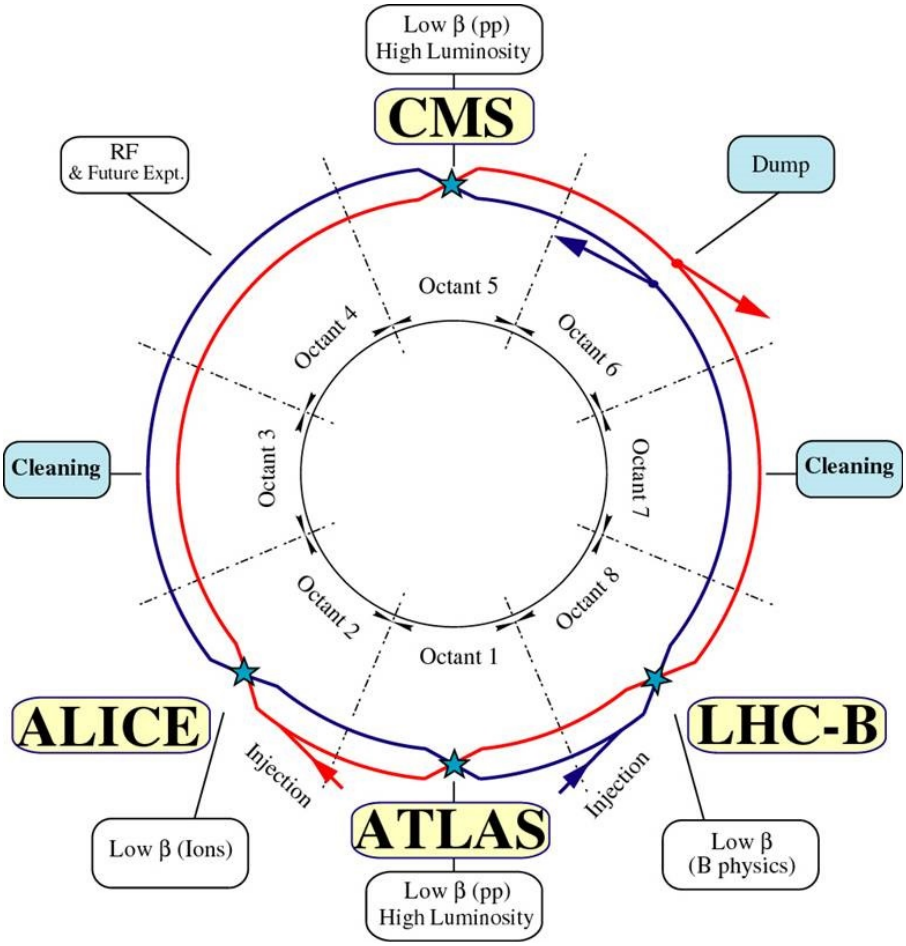

Figure 4.1.: Attached to the Large Hadron Collider ring is four major experiments. The ATLAS Experiment, The CMS Experiment, The ALICE Experiment and The LHC-B Experiment. These are all situated on points where the two parallel beams of protons are pushed together to collide, indicated by the stars [44].

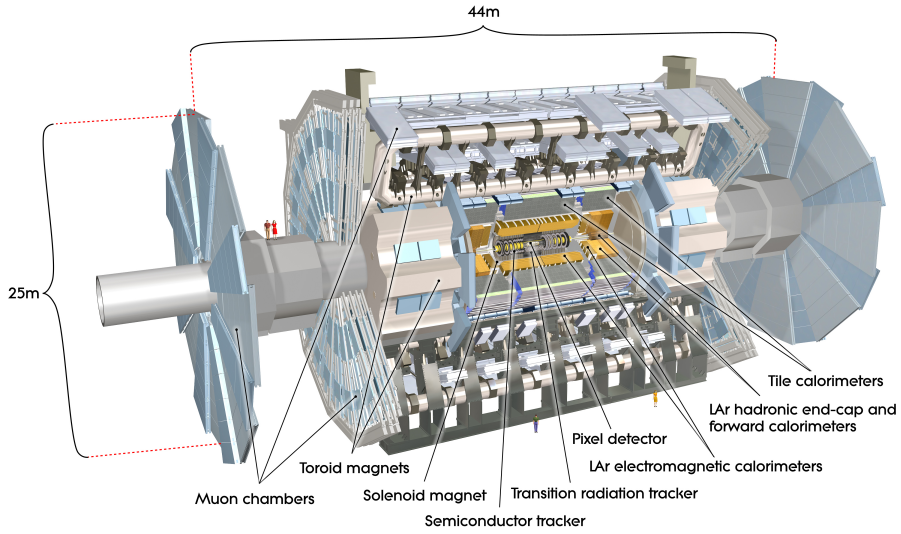

Figure 4.2.: Schematic illustration of the ATLAS Experiment. The interior of the detector is visible with the different sub-detectors marked out [45].

Superconducting magnets, creating a field up to $\sim$ 8 Tesla (for a beam energy of 7 TeV), accelerate the protons to the target energy. The magnets are required to be super-cooled to a temperature close to absolute zero, $-271.3°$ C, to operate at high enough efficiency. The protons are accelerated to relative speeds, near speeds of light. As the two beams are brought to collide, they are collimated by a set of magnets. This is done to increase the chance of collisions.

4.2. A Toroidal LHC ApparatuS

The ATLAS experiment is a universal particle detector, designed to be efficient in distinguishing and identifying a wide range of physical processes. Not only should it be able to make high precision measurements of known

Standard Model (SM) interactions, i.e. through Quantum Chromo Dynamics (QCD) or Quantum Electro Dynamics (QED) mechanics, but conjointly to possess the capability to observe new phenomenology related to Beyond Standard Model (BSM) physics. Nevertheless, at the time of drawing the technical layout of the detector, the search for the yet-to-be-discovered SM Higgs boson played a significant role alongside with benchmark Supersymmetry (SUSY) models. Few of the Higgs decay channels require lepton identification, b-tagging (this signifies the process of distinguishing slightly displaced jets originating from b-quarks) and measurements of $E_{\mathrm{T}}^{\mathrm{Miss}}$. The latter one is of huge significance to BSM theories assuming the existence of weakly interaction particles, which would escape the detector without leaving any energy deposits. All these criteria guided the design. The extreme high density of particle interactions at the LHC made further demands on the detectors ability to handle the high frequency of collisions, to withstand the radiation and to disentangle the numerous particles produced in pp collisions. ATLAS is a cylindrical structure with a diameter of 25 meters and a length of 46 meters. The whole machine is estimated to weigh 7000 tons. Over a hundred millions electric channels are connected to the detector modules and systems to read-out all information from collisions. The detector is built in cylindrical layer around the beam intersection point, with circular layers in the forward-backward regions (Fig. 4.2). All sub-detectors consist of a "barrel" region, which is the cylindrically layers parallel to the beam direction. At the forward-backward region, each detector layer have "end-caps", which are circular layers perpendicular to the beam line. The detector consists of four different sub-detectors. The most inner layer is the Inner Detector (ID), which provides momentum measurements, particle identification, interaction point reconstruction in the form of vertexing and tracking the path of charged particles. This detector is surrounded by electromagnetic coils producing a solenoidal field of 2 T envelop the whole ID. Further out, there are two calorimeters, supplying both position resolution and energy measurements, by absorption. The two types of calorimeters are an electromagnetic calorimeter and a hadron calorimeter. The most outer layer of ATLAS is the Muon Spectrometer (MS) providing μ identification and momentum measurements. Like the ID, the MS is surrounded by magnets, bending the path of the munos to provide momentum measurements. Further details for each of these subsystems are given in Sec-

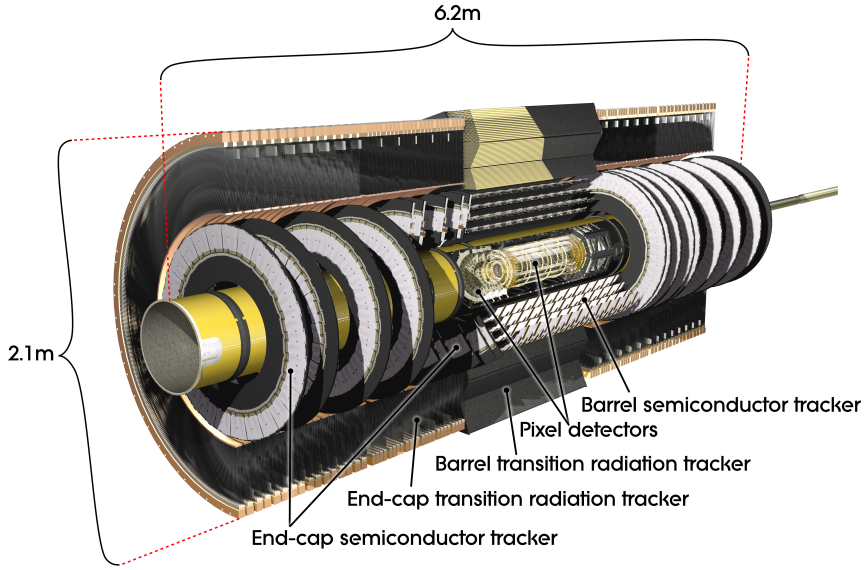

Figure 4.3.: Schematic view of the ATALS Inner Detector. The barrel is visible in the central part indicated by the cylindric layers around the beam axis. At each side is the end-cap region, with discs. The three sub-detectors are, going from the point closest to the interaction point: the Pixel Detector, the Semiconductor Tracker and the Transition Radiation Tracker [45].

tion 4.2.1, 4.2.2, and 4.2.3 along with some scarce coverage of the data management of the trigger system in Section 4.2.4.

4.2.1. The Inner Detector

Closest to the beam pipe is the ATLAS tracking detector. High granularities of semiconductor detectors provide pattern recognition of charged particles with good momentum and position resolutions. The momentum resolution of the ID is given in percentage of standard deviation over the momentum given with relative error; $\sigma_{p_T}/p_T = 0.05\% \oplus 1\%$. The spatial resolution ranges

from tens of μm to few hundred depending on the radial distances. Three sub-detectors make up the ID. Starting from the most inner radius the layers are, the Pixel Tracker (Pixel), the Silicon Tracker (SCT) and the Transition Radiation Tracker (TRT) (Fig. 4.3). The large expected doses of radiation sets requirements on the ID ability to withstand the expected dosages. The entire tracking volume is foreseen to be replaced after 15 years of operations due to radiation damage. The magnetic field surrounding the ID, bends the paths of the charged particles allowing for momentum measurements. Moreover, this detector is responsible of the crucial task to pin-point the initial interaction point, the Primary Vertex (PV). This information is vital to disentangle the rest of a collision event. The ATLAS tracker can also identify secondary decays such as meta-stable particles, e.g. b-mesons, by use of distinguishing secondary particles from primary particles. A common used term is b-tagging, which implies marking jets containing b-quarks. These quarks can potentially form hadrons - b-mesons and b-baryons - with lighter quarks and travel a distance in the detector before decaying. However, the expected lifetimes of these hadrons are relatively short and they will fall apart inside the tracker at average distances of a couple of millimeter. The decay of a b-hadron will yield a wide jet as the decay products of a b-quark are significantly less massive than a regular jet, and will instead have large transverse momentum. b-tagging then aims to identify these jets as they are highly important to physics at the LHC. The high production rates of $t\bar{t}$ in pp collisions yield a large rate of b-jets. Top quarks nearly always decay into a bottom quark and a W-boson. The W decays either to $l\nu_l$ or to completely hadronical final states, through first generation quarks.

The layout of the ID is made to keep the best performance and resolution while controlling that the material budget won't become too large. The monetary aspects played a significant role as well. The TRT is implemented to keep a large tracking volume, but to reduce costs of expensive semi-conducting silicon sensors. More extensive details of the three sub-detectors are explained in the following three paragraphs.

The Pixel Detector is designed to contribute with superb resolutions. This sub-detector consists of 80 million pixel channels to provide the sought after resolution, corresponding to 50% of the read-out channels in ATLAS. Track-

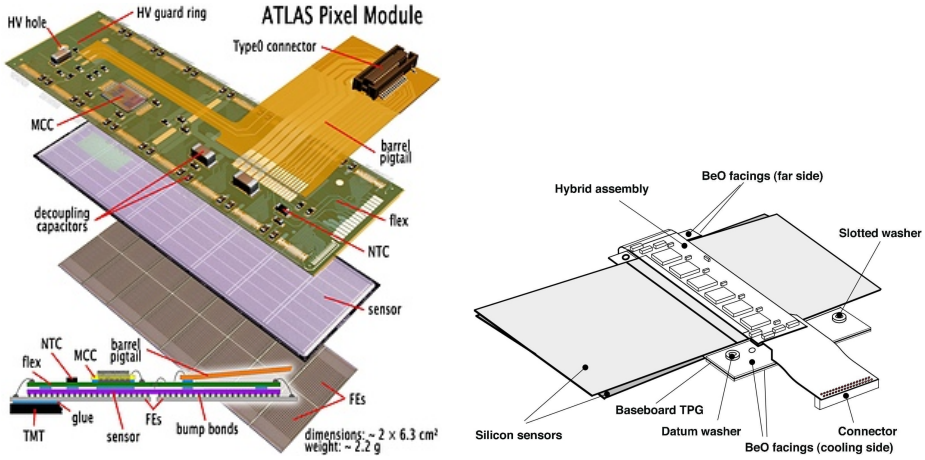

(a) (b)

Figure 4.4.: Barrel modules for the Pixel (a) and the SCT (b) are shown as schematics. The different components of the modules are marked out [45].

ing is often the moment in event reconstruction that requires the largest amount of CPU-power due to the large amount of signals to treat and interpret. The fine granularity of pixel sensors is designed to give the experiment high resolution and tracking of particles close to the Interaction Point (IP). The spatial resolution in the transverse plane ($r\phi$-plane) is 14 μm while slightly worse along the longitudinal axis of 115 μm (for the end-caps the resolution in $r\phi$ is 14 μm while only r is 115 μm). The Pixel on average provides three space-point measurements per particle trajectory. The barrel (end-caps) extends $r = 50 - 150$ mm and $|z| = 400$ mm ($r = 80$ to $r = 150$ mm and $|z| = 490$ to $|z| = 650$ mm) corresponding to a coverage of $|\eta| < 2.5$. There are three cylindrical barrel layers and six end-cap disks, three on either side of the barrel. The first pixel barrel layer is often referred to as the B-Layer, as this layer helps identifying b-jets. The barrel layers have around 67 million pixels while the end-caps consist of 13 million. The pixels are mounted on a set of modules, there are in total 1744 pixel modules. Figure 4.4 (a) schematically illustrates an exploded view of a barrel pixel module. The gray sensor layer

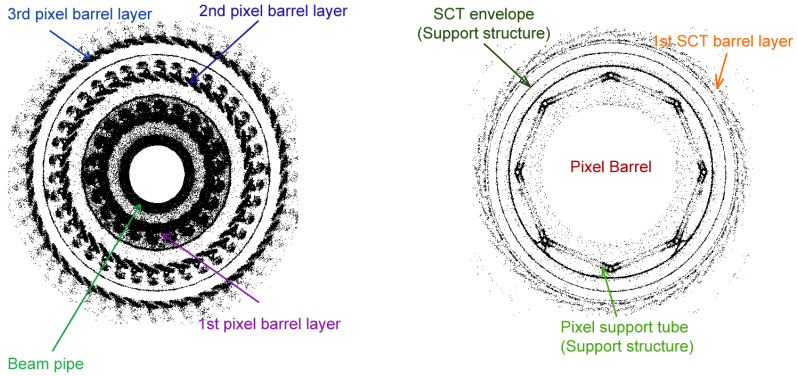

(a) (b)

Figure 4.5.: The ATLAS ID as radiology images formed by using the hadronic interaction vertices technique (described in detail in Chapter 8). (a) shows the pixel detector and the beam pipe which corresponds to the most inner part of the ID up to a radius of 150 mm. The interval outside $150 < r < 350$ mm is shown in (b) which include an octagonal structure that supports the pixel barrel, the envelope that indicates the start of the SCT followed by the first barrel layer of the SCT.

is sandwiched between the electronic and the read-out systems. The sensor layer of each module consists of circa 46000 pixels over an area 2×6 cm^2 and are planar n-on-n silicon sensors, 250 μm thick. The sub-detector is kept at a low temperature of around -5 to -10 ° C, in order to improve the detectors performance after irradiations and to suppress noise. Initially, the modules are operating under 150 V bias voltage, but this voltage is required to increase up to 600 V after a sufficient amount of irradiation dose. Signals are read out by 16 FE chips that are bump bounded to the sensor. They amplify and digitize the signals from the ionising particles crossing the sensor. The radiology of the pixel detector (and the beam pipe closest to the centre) is shown in the xy-plane in Fig 4.5 (a). The image is formed by the use of the hadronic interaction technique, which is covered in detail in Chapter 8 and includes many more similar images. The beautiful plots are made by finding nuclear interactions and plotting the points of interaction in the plane perpendicular to the beam line, here shown for the detector itself (this refers to that the image is

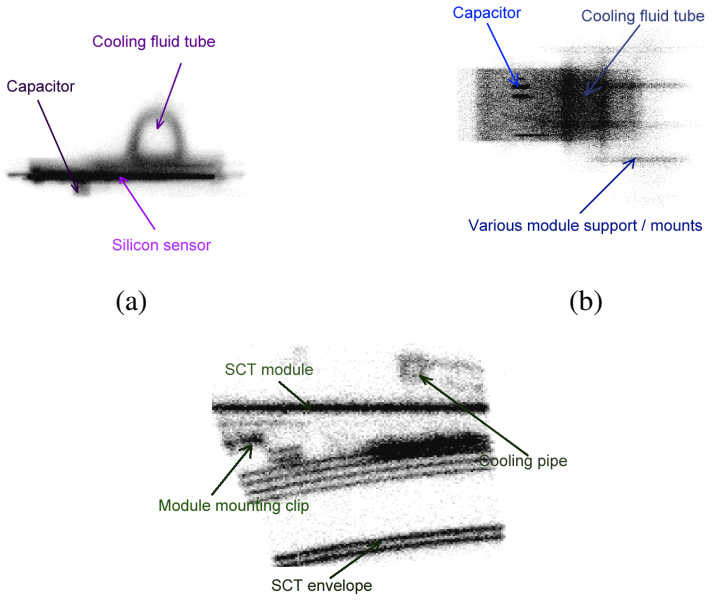

Figure 4.6.: Radiology imagery formed by using the hadronic interaction vertices technique (described in detail in Chapter 8). (a) and (b) show the pixel modules in the first barrel layer overlaid on top of each other from the side and above of the modules. The different structural components are indicated. (c) shows the sideview of overlain SCT module in the first barrel layer including the envelope also here the different parts are indicated.

not produced from simulations but is made by plotting the radiology from the actual detector). Circular structures in the same images are typically support frames to keep the sensor layers in place and are composed mainly by carbon fiber shells. The images in Fig 4.6 (a) and (b) provide clear view of the modules in the first layer. All the modules are overlain to form these two images, in (a) a side view (xy-plane) while (b) shows the module from the top (rz-plane). The cooling fluid tube on top of the module is made up by Aluminium and Kapton.

The SemiConductor Tracker is the second sub-detector and it is composed of strips rather than square pixels. This allows the tracker to extend larger volume than the Pixel while keeping moderate pricing. Each module contains 1536 strips spanning 80 μm by 12 cm. The binary read-out system only provides measured charge deposits in one dimension, as they cannot give any information on where along the strip the particle intersected the sensor. To provide read-out in two dimensions, two silicon sensors with 768 strip each, are mounted on the top of each other at a 40 mrad stereo angle (Fig. 4.4 (b)). The SCT has in total 4088 two-sided modules divided on four barrel layers and nine discs in each of the two end-caps; resulting in over 6 million readout channels. The SCT barrel (end-caps) stretches from $r = 275$ to $r = 520$ mm and $|z| = 750$ mm ($r = 275$ to $r = 560$ mm and $|z| > 749$ to $|z| > 2725$ mm). The resolution in the barrel (end-caps) $r\phi = 17$ μm and $z = 580$ μm ($r\phi = 17$ μm and $r = 580$ μm. On average a track crosses four of SCT layers emanating an equal amount of space-points. The SCT operates at a slightly higher temperature of -7 ° C. The SCT plays a vital role in track reconstruction as the detector spans a large distance. The radiology of the first SCT barrel layer is shown in Fig. 4.5 (b), also visible are the support structure that surrounds and keep the pixel barrel in place as well as the SCT support envelope. These supports are in majority made of Carbon Fibre Reinforced Plastic honeycomb shells. The cooling fluid tube here is made up by Aluminium and Kapton. Figure 4.6 (c) shows the radiology of the SCT modules in the first layer and different support structures surrounding this layer ($r \sim 300$ mm). Unfortunately the techniques relies on tracking and due to insufficient silicon layers it is difficult to use this technique further out than a radius of around 400 mm, therefore there will be no similar image of the TRT to look forward to.

The Transition Radiation Tracker is the last sub-detector of the ID. This detector is a straw tracker combined with a transition radiation detector. The latter provides the possibility for particle identification. Each straw tube has a diameter of 4 mm and is 144 cm (37 cm) long in the barrel (end-caps). The straw tubes are filled with a mixture of Xenon and Carbon-dioxide. Charged particles which cross the tubes, will ionize the gas, and the produced excess of ions is driven by a -1500 Voltage towards a fine wire at the centre of each

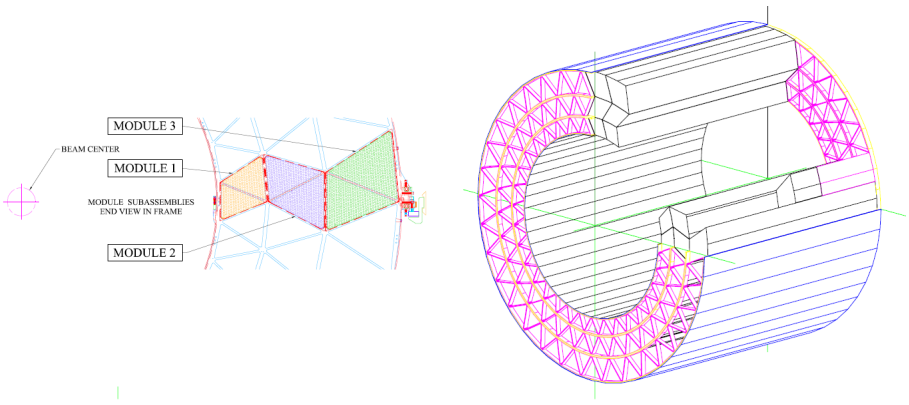

(a) (b)

Figure 4.7.: The layout of the barrel TRT is shown[49]. The straws are mounted parallel to the beam axis. The TRT is split into three modules with slightly varying shapes (a). (b) shows a three dimensional view of the layer.

tube. The charges are then read-out as signals from the specific module-wire. The TRT is only able to measure the hit position perpendicular to the straws and has a resolution of around 200 μm. In difference to the silicon based sub-detectors, the TRT contributes with continuous tracking with an average of 36 hits per particle trajectory. The drift tubes are packed in 73 (160) layers for the barrel (end-caps) covering a large volume of approximately 3.5 m^3. The volume between the straws is filled with material, which makes particles traveling at relativistic speeds produce transition radiation and will leave extra charges in the straws. The higher the speeds the more transition radiation the particle will produce. It is possible to identify the particles using threshold on the energy deposited. For example, a lighter particle such as an electron will travel at a higher relativistic speed and will therefore produce more transition radiation than say a pion which is heavier and thereby slower.

The TRT stretches from $r = 560$ to $r = 1070$ mm and $|z| = 650$ mm for the barrel, while the end-caps are slightly more narrow with $r = 640$ to $r = 1005$ mm and $|z| = 850$ to $|z| = 2710$ mm. The straw tubes are ar-

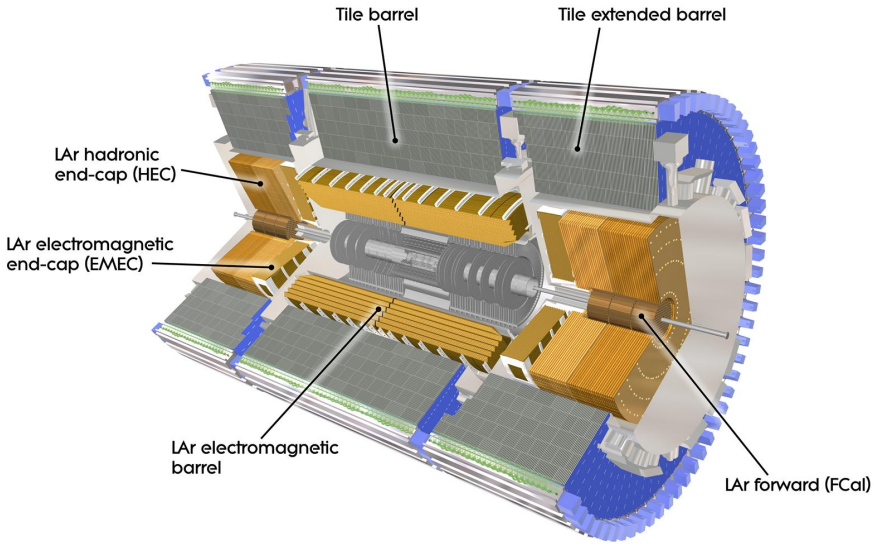

Figure 4.8.: Schematic view of the ATLAS detector, indicating the different components of the calorimeters[50].

ranged in three rings (Fig. 4.7 (a)) with 32 modules in each module layer (two intersecting triangular shapes in Fig. 4.7 (b) represent the support frame for one module).

4.2.2. Calorimeters

An electromagnetic calorimeter and a hadronic calorimeter are situated outside the tracking volume (Fig. 4.8). These cover a range of $|\eta| < 4.9$. Likewise the ID, the calorimeters are divided into barrel and end-cap components. Both the calorimeters provide energy measurements by absorbing particles and at periodic intervals sampling the deposited energies, but the targeted particles are different between the two calorimeter types. The electromagnetic calorimeters target particles interacting with the electromagnetic force and the

hadronic calorimeter absorbs particles interacting strongly. The principle of a sample calorimeter is that it typically consists of two different material to make the particles produce a shower[1] interacting with and to measure the deposited energy. The benefit of using this type of calorimeters is that a very dense material can be utilised to make the particles shower at a higher rate and thereby reducing the effective volume required, as the materials providing read-out signals are not always sufficiently dense. The calorimeters should be able to contain the showers and not have leakage which would continue travelling into the MS. This is important especially to ensure good quality measurements of $E_{\mathrm{T}}^{\mathrm{Miss}}$.

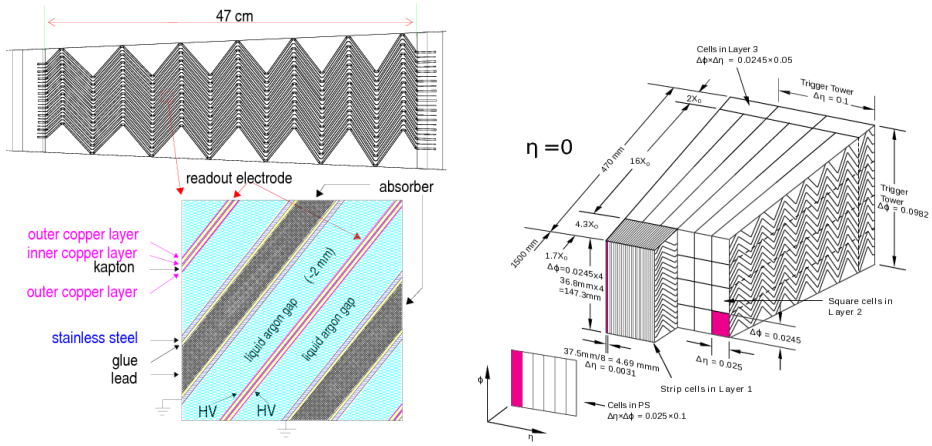

(a) (b)

Figure 4.9.: An electromagnetic-calorimeter section is shown, the composition and the accordion like structure is visible in (a). The shower material and the sampling material are indicated. (b) shows how the segment is built up in the three dimensional coordinate frame [50].

[1] Particles interacting with dense matter produce a cascade production/decay of particles. A typical example is a photon interaction with matter and become converted into two electrons. The electrons in turn produce new photons and electrons. As the particles keep converting a shower of particles gets created. The same principle works for hadronic showers except that instead of the electromagnetic force the hadronic showers are created by the strong force.

The Electromagnetic Calorimeter uses liquid argon (LAr) as the sampling material, while the lead is the shower-inducing materials (Fig 4.9 (a)). Not only does it provide excellent energy resolution of $\sigma_E/E = 10\%/\sqrt{E} \oplus 0.7\%$ but also precision in the spatial location of the energy deposit. The shower-inducing dense material, in each calorimeter cell, is in a wavy - accordion-like - pattern to maximise the amount of material on average the particles cross (Fig. 4.9 (b)). The barrel (end-caps) section covers $|\eta| < 1.475$ ($1.375 < |\eta| < 3.2$) and the whole calorimeter is surrounded by a cryostat system as it needs continuous cooling as the absorption process generates heat.

The Hadronic Calorimeter has two parts. One is a Tile calorimeter covering $|\eta| < 1.0$ in the barrel and two extra sections in two extended barrel regions for $0.8 < |\eta| < 1.7$. The other part, in the forward end-caps, is a LAr calorimeter. The forward calorimeter provides measurements of both electromagnetic and hadronic interactions. The dense material in the Tile calorimeter is steel with scintillating tiles as sample material. The energy and position precision are not good as that of the electromagnetic calorimeter. The energy resolution for the barrel and end-caps is $\sigma_E = 50\%/\sqrt{E} \oplus 3\%$ while the forward LAr at large η is $\sigma_E = 100\%/\sqrt{E} \oplus 100\%$.

4.2.3. Muon Spectrometer

The MS is a tracking detector dedicated to tracking the massive leptons, the muons. A set of toroidal magnets partly surrounding the MS produces the magnetic field required to bend the path of the muons. The description here is based on the TDR [45]. This sub-detector stretches from $r = 4.25$ to $r = 11$ m and consists of several types of muon chambers. The Monitored Drift Tubes (MDT's) provide tracking with high precision perpendicular to the magnetic field's propagation. The drift tubes work in a similar way as the TRT trackers straw tubes. At higher η but much closer to the interaction point, finer granularity chambers, called Cathode Strip Chambers (CSC's) are used. The higher precision in this region is required to suppress the background signals more effectively and not to be sensitive to them. The last part of the MS is the trigger system with Resistive Plate Chambers (RPC's) in the barrel and Thin Gap Chambers (TGC's) in the end-caps. The trigger system does not only

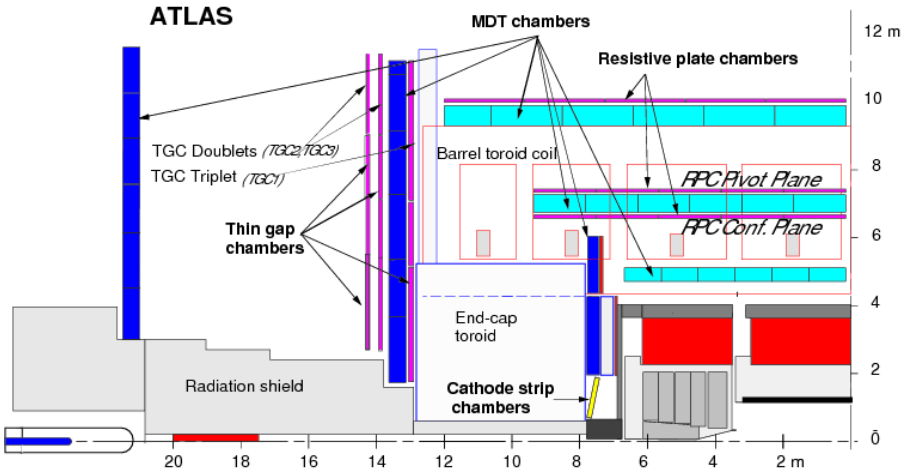

Figure 4.10.: The elements making up the Muon Spectrometer are shown [51].

provide the threshold momentum measurements to base event selection on, but also bunch-crossing identifications and spatial measurements in the plane perpendicular to that of the MDT's and CSC's.

4.2.4. Trigger System

The trigger system is designed to reduce the amount of data stored by selecting *good* events and discarding the ones that are less probable to have been interesting from a physics point-of-view. The LHC produces a staggering amount of data with around 1 petabyte of data per second. This corresponds to circa 40 million beam crossings per second. The ATLAS trigger system has three levels; two hardware triggers Level1 (L1) and Level2 (L2) and a software trigger Event Filter (EF).

The L1 trigger is a pure hardware trigger and works in real-time during data-taking. This level trigger has only access to a constrained amount of detector read-out signals to operate at high speed; the L1 trigger sorts out the events in $< 2.5\ \mu$s. The events are selected based on basic measurements such as high

transverse momentum object e.g. μ, e, $E_{\mathrm{T}}^{\mathrm{Miss}}$ or jets. The first level trigger reduces the rate from the initial amount of events to 75 kHz. Moreover, the trigger selects Regions-of-Interest (RoI's) that are pure coordinates in η and ϕ serving as seeds for the next level trigger.

The L2 trigger further reduces the rate to approximately 3.5 kHz. The L2 only considers the events selected by the L1 trigger. However, this step has access to the full detector responses within the seeded area. This trigger operates somewhat slower than L1 and requires on average 40 ms per event.

The Event Filter is software trigger applied after collisions based on information from the whole event. This stage reduces the final rate to 200 Hz with a process time of four seconds per event.

After the complete trigger chain, there remains an average of few hundred events per bunch crossing.

4.2.5. Luminosity Detectors

Some distance away (17 m), on each side, from the centre of ATLAS the forward detector is located, LUminosity measurement using Cerenkov Integrating Detector (LUCID); in the very forward region of $5.6 < |\eta| < 6$. The primary purpose of this detector is to monitor the luminosity during collisions, by detecting the inelastic collisions in the forward region. At $|\eta| = 4.2$ the Beam Condition Monitor (BCM) detector, provides information of the beam conditions as well. Parts of the calorimeter can be utilised as a bunch-blind luminosity measurement tool. Luminosity delivered by the LHC is at the foundation of all analysis. For example, to make background estimations, the simulated background process samples needs to be scaled to the amount of data collected. However, the complex process involved in the luminosity measurements are outside the focus on this thesis and the reader is referred to reference [52] which provides extensive information regarding the luminosity measurements and the systematic uncertainties therein.

Part II.

The Displaced Vertex Analysis at the LHC-ATLAS Experiment

5. Displaced Vertex Analysis

Particles with relative short $c\tau$ might decay inside the tracker volume of the particle detectors. The point of decay can be reconstructed using the particle trajectories from charged daughter particles. Provided that the particle is sufficiently massive, the vertex will have several tracks originating from it. Displacement, from the Interaction Point (IP), of the vertex is dependent on the mean lifetime of the particle.Long Lived Particle (LLP) decay, reconstructed as a secondary vertex is commonly referred to as a "Displaced Vertex" signature. This thesis presents the experimental search for massive high track multiplicity displaced vertices using the A Toroidal LHC ApparatuS (ATLAS) Experiment. Preceding experimental searches for similar lifetimes are reviewed in shortness before moving on to covering the details of this particular analysis. The structure and content of all chapters in Part II are listed at the end of this chapter.

A small note before moving on, providing definite results from LLP searches in form of excluded models or even masses prove to be a difficult task. The lifetime of a particle is often down to the tweaking of parameters of a given model; magnitude of couplings, mass differences, interaction strengths or many more options. Whenever an exclusion limit is set on a specific setup in a given model, any slight modification of one or several of the variables might results in that the model can escape exclusion. For similar reasons, giving direct comparisons with other experimental searches are big challenges. Most of the searches for LLP follow their own patterns - specific cuts, selection criteria, target lifetimes, and models - and are therefore near impossible to directly compare. The possible solution is to re-interpret the results from one or several searches on a particular model to see which analysis is the most

powerful for just that model. Performing a re-interpretation of several analyses is hard work and would amount up to an analysis of its own and will not fall inside the spectrum of this thesis. Instead, parts of the results presented in Chapter 11 are published in the article *Search for massive, long-lived particles using multitrack displaced vertices or displaced lepton pairs in pp collisions at* $\sqrt{s}$ = 8 TeV *with the ATLAS detector* [5] and this article is included in a re-interpretation made by theorists and their results are properly cited and added as a discussion in Section 11.5.

5.1. Past Searches for Displaced Vertices

In the pre-Large Hadron Collider (LHC) era, the D0 Collaboration searched for LLP X_{llp} decaying into muon pairs [53]. The massive particle is assumed to traverse a few centimeter before decaying into $\mu^+\mu^-$; matching the tracks in the tracker with the muon system and setting limits on the M_{llp} as a function of the branching ratio. D0 Collaboration also conducted a displaced vertex search where the $X_{\text{llp}} \rightarrow b\bar{b}$ interpreted on Hidden Valley models [54]. A search for two electrons in the final state, originating from a displaced Z-boson decay, was performed by the CDF Collaboration [55]; interpreted on a low-energy symmetry breaking model. More recent results are from the Compact Muon Solenoid (CMS) Collaboration having published results from three displaced vertex searches. Two of these have looked for dileptons arising from a displaced secondary vertex [56, 57]. However, even if the methodology deviates, the search that corresponds best to the one in this thesis is the third one of the CMS searches. This search looks for events containing two jets arising from a displaced vertex in the tracker [58]. Another displaced vertex search, where the LLP is assumed to decay into two hadronic jets, was conducted by the ATLAS Collaboration [59]; this analysis performed by the same collaboration, but differs significantly by, amongst many things, using another algorithm to reconstruct the vertex. The results from these more recent searches just stated will be compared to the ones achieved in this thesis and the latest publication of the same search.

The ATLAS Displace Vertex Analysis has previously published three earlier

iterations, in 2011 [60] and in 2012 [61, 62]. These iterations have been dedicated to the signature of a displaced vertex with high track multiplicity. A muon was required to be associated to the vertex; the $DV + \mu$ channel. This last criterion limited the application of the search to different models and the search was in these occasions only referred to R-Parity Violation (RPV) Supersymmetry (SUSY). Extending upon the old analysis, the last edition included additional three final states; $DV+e$, $DV+E_{\mathrm{T}}^{\mathrm{Miss}}$ and $DV+jets$, thereby increasing the search efficiency. Especially, the final state of $DV + jets$ is the most generic and often provides the strongest limits. This thesis will cover just this final state, and a discussion regarding the exact scenario will follow in the next Section. However, the work conducted producing this thesis has helped leading up to the publication of all final states in the latest Displace Vertex search at ATLAS [5][1].

5.2. Analysis Scenario and Structure

Important theoretical and experimental concepts necessary for this analysis have been discussed in the previous chapters. Now is the time, to proceed to the concrete scenarios, and review the analysis techniques utilised in this thesis and only debating and discussing topics directly involved in the experimental search for $DV + jets$. The chosen theoretical model is that of RPV SUSY, discussed in Section. 3.3, where one, and only one, of the R-Parity Breaking couplings, is assumed to be non-zero. Still, in order not to contradict observed limits on L-number violation, this coupling needs to be of minuscule order of magnitude.

The targeted decay is illustrated by the Feynman diagram in Fig. 5.1, where the production of sparticles and their sequential decays to particles are drawn. Squarks $\tilde{q}$ (red dotted line) are strongly produced in the proton-proton (pp) collisions followed by their decays to the Lightest Supersymmetry Particle (LSP) $\tilde{\chi}_1^0$ (red wavy line). The LSP decays through the RPV coupling λ'

[1] This paper covers also the final state of $DV + dilepton$, conducted side-by-side with the multi-track channel. However, this final state is not related to the work described in this documentation.

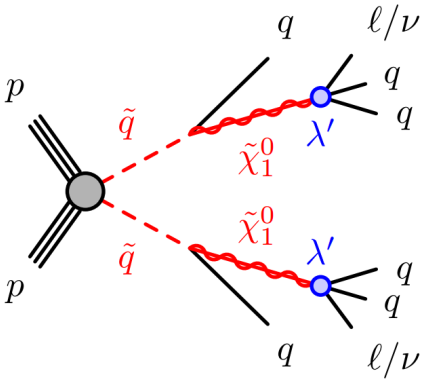

Figure 5.1.: Feynman diagram showing the production of a $\tilde{q}\tilde{q}$ pair from a pp-collision. Each squark then decays to the lightest supersymmetry particles $\tilde{\chi}_1^0$ and a quark. The neutralinos decay through the lepton flavour violating coupling λ' to a final state of two quarks and lepton or a neutrino.

(blue dot) to quarks and either to a lepton or a neutrino. The whole decay chain is;

$$pp \to \tilde{q}\tilde{q} \quad \text{where,} \quad \tilde{q} \to \tilde{\chi}_1^0 q \quad \text{and} \quad \tilde{\chi}_1^0 \to qql(\nu). \tag{5.1}$$

In this scenario, the sole RPV contribution to the $\mathscr{L}_{\text{SUSY}}$ (Eq. 2.15) is the L-number violating term;

$$\mathscr{L}_{\Delta L=1} = \lambda'^{ijk} L_i Q_j \bar{d}_k. \tag{5.2}$$

This term is referring to the latter part of Eq. 5.1, that is, the decay $\to qql(\nu)$. A variety of ijk is considered (Eq. 5.2). However due to logistical issues such as available disk space reduces the possibilities to use all of the possible couplings down to a selected few varieties of combinations. The samples are simulated by only setting one coupling to non-zero values. The rest are still set to zero. All other couplings of SUSY are considered to act as prompt decays and assume the decays happen instantaneously after creations. The index i

corresponds to the family of leptons participating; $i = 1$ means electrons while $i = 2$ is muons. Tauons are not included in this analysis so index $i = 3$ is not included. Likewise, the indices j and k correspond to the family of quarks, all three families are considered ($j, k = 1, 2, 3$). Nine couplings makes out the final selection, attempting to include as wide combination of decays as possible - electrons, neutrinos, light or heavy flavour jets.

$$\lambda'_{111} \quad \tilde{\chi}_1^0 \to e + jets \quad \text{(light flavour jets)} \tag{5.3}$$
$$\lambda'_{211} \quad \tilde{\chi}_1^0 \to \mu + jets \quad \text{(light flavour jets)} \tag{5.4}$$
$$\lambda'_{211} \quad \tilde{\chi}_1^0 \to \nu_\mu + jets \quad \text{(light flavour jets)} \tag{5.5}$$

$$\lambda'_{113} \quad \tilde{\chi}_1^0 \to e + jets \quad \text{(one light, one heavy flavour jet)} \tag{5.6}$$
$$\lambda'_{213} \quad \tilde{\chi}_1^0 \to \mu + jets \quad \text{(one light, one heavy flavour jet)} \tag{5.7}$$
$$\lambda'_{213} \quad \tilde{\chi}_1^0 \to \nu_\mu + jets \quad \text{(one light, one heavy flavour jet)} \tag{5.8}$$

$$\lambda'_{123} \quad \tilde{\chi}_1^0 \to e + jets \quad \text{(heavy flavour jets)} \tag{5.9}$$
$$\lambda'_{223} \quad \tilde{\chi}_1^0 \to \mu + jets \quad \text{(heavy flavour jets)} \tag{5.10}$$
$$\lambda'_{223} \quad \tilde{\chi}_1^0 \to \nu_\mu + jets \quad \text{(heavy flavour jets).} \tag{5.11}$$

Computer generated samples for each of these couplings are generated to study the signal efficiencies. The couplings are only considered one at a time, with a branching ratio of 100%. All the different versions are there to test the analysis efficiency to detect different types of decays. The strength of the couplings are $\lambda' \sim 10^{-4}$. The mass of the $\tilde{g}$ is 1000 GeV and the $\tilde{\chi}_1^0$ is set to 100 GeV. The LLP $c\tau$ is assumed to be 220 mm. These values are the same for all the nine samples. Applying a lifetime re-weighting strategy, the results can be displayed as a function of a variety of $c\tau$; this will be explained down the road in Section 6.7.

A LLP of around 100 GeV is assumed to decay into several daughter particles that can be associated with the displaced vertex. A classification is made that

a vertex needs to have at least 5 tracks and a mass larger than 10 GeV to be considered a candidate. If a vertex does not fulfil these requirements it is considered to be a background vertex. Moreover, the vertex is required to be reconstructed in the Inner Detector (ID) inside a cylinder with $r < 300$ mm and $|z| < 300$ mm.

The structure of Part II of this thesis goes as following; firstly, the data and the signal samples used are discussed further in Chapter 6. The "physics objects", the vertices and jets, have to be constructed from all the electronically read out signals from the detector. The process of forming trajectories after charged particles traversing the ID and how the vertices are fit from these are explained in Chapter 7. The non-standard tracking and vertexing algorithms used to look at these exotic types of decays are included. Moreover, the reconstruction of the jets objects will also be included. Moreover, reconstructions of jets are also reviewed. Other standard objects such as muons or electrons will not be discussed as they are not used in the analysis and do not play a vital part in this specific search.

Backgrounds to the channel have to be considered in detail. The major source of background vertices displaced is the nuclear interaction with the material in the detector. This source is removed by vetoing any vertices found in dense material regions. A detailed map over the material distribution in r, z and ϕ has been constructed by using a material-study technique developed at ATLAS [63]. The construction process is rather complex and the method utilised is discussed in Chapter 8. This chapter can be viewed as a stand-alone analysis but with the underlying purpose to conduct the material map. The hands-on application and effects of the map are discussed in Section 10.3. The signal efficiency and selection cuts, including all systematic uncertainties, are reviewed in detail in Chapter 9 together with a description of the lifetime re-weighting method. Chapter 10 covers all the background processes to the analysis channel. Followed by the results (Chapter 11) and the conclusions (Chapter 12).

6. Data and Event Simulations

From the initial set of collisions a small sub-set of interesting events is selected; referred to as data pre-selection. The main purpose of this is to reduce the size of the dataset and speed up the analysis process. Interesting events are selected by applying event characteristics out of significance to the analysis at hand. In the Displaced Vertex (DV) analysis this is done by selecting events with high p_{T} jets and a displaced vertex. More details on the specific criteria are reviewed in the first part of this chapter. The second part is dedicated to explaining the concept of event simulations and generated signal samples for the sought after Long Lived Particle (LLP) decay processes. These samples are used to optimise the analysis and to produce results interpreted on the corresponding model and cross-sections.

6.1. Data Selection

The dataset recorded by the A Toroidal LHC ApparatuS (ATLAS) detector during 2012 equal a total integrated luminosity of 20.3 fb^{-1}. All events are required to pass the Good Runs List (GRL) which specifies whether the data collected during just that run of the beam was good or if it failed quality requirements due to any reasons.

6.1.1. Event Pre-Selection

The total 20.3 fb^{-1} corresponds to approximately 10^{15} worth of proton-proton (pp)-collisions. Out of this huge number, 26.5 million events are pre-selected

to the initial dataset. The selection is divided into three categories; trigger requirements, offline object requirements, and stricter offline cut on the jets. An event is required to pass one of the following three triggers;

- EF_4j80_L2FS_a4tchad
- EF_5j55_L2FS_a4tchad
- EF_6j45_L2FS_a4tchad.

The EF stand for that this trigger is applied as an event filter and is an software-based trigger that have access to the information of the whole event - typically hardware triggers only have access to partial information as described in Section 4.2.4. The number convention, EF_XjYY, states that the trigger requires that the event has X number of jets with at least YY GeV transverse energy. The denotation a4tchad stands for that the number of X jets were reconstruct by a full set of information from the topological clusters in the hadron calorimeter using AntiKt4 reconstruction algorithm (more on the jet reconstructions in Chapter 7). All selected events are required have either; four jets with energy E_{T} 80 GeV *OR* five jets with slightly lower required energy of E_{T} 55 GeV *OR* six jets with E_{T} 45 GeV. These triggers are using the non-calibrated values on the energy, the stricter offline cuts are made on the calibrated variables to avoid extra systematic uncertainties due to using non calibrated jets. In the final event selection, these cuts are put at a higher value of E_{T} than these initial triggers in order to not fall below the threshold of the pre-selection trigger; as this could result in additional systematic uncertainties if the plateau on the turn-on curve in MC differs from the one seen in data, and would also reduce the trigger efficiency.

Additional cuts are made on the actual physics objects in the events, and they are required to correspond to the same values on jet multiplicity and E_{T}, using the Anti-Kt type of reconstructed jets (Section 7.3). These are required to pass the same combination of the triggers.

A final pre-selection requirement demands that each event should have a trackless jet. This means one jet with no associated primary tracks i.e. jet signature

expected by a LLP. The jet needs to have $E_{\mathrm{T}} > 50$ GeV and to have no or close to no tracks in the Inner Detector (ID). Requiring that the Σp_{T} of all tracks identified with a jet to be smaller than 5 GeV ensures a trackless jet.

6.2. Monte Carlo Method and Event Generators

Simulation of collision events is a very useful tool that is often turned to in the High Energy Physics (HEP) field. Collision of pp involves the strong interaction making the event topology extremely complex. The expected number of particles from an inelastic scattering event is of the order of 100 particles. It is impossible to make analytical calculations for a system involving creation of such a large quantity of particles. Especially since the underlying events are ill-defined and the low-energy strong interaction do not has an analytical solution. However, estimations of all types of background in the dense collisions environments are required to determine whether a target process has been observed. To give an example, $W + jets$, $Z + jets$, multijet events and so on give similar signatures as $t\bar{t}$ events. Failing assessing the quantity limits on the production cross-sections or exclusion limits cannot be set with statistical confidence. Therefore, generated samples of background processes are an invaluable tool to understand the physics in collision events.

Numerical methods are essential to do calculations to solve the complicated mathematical equations describing the involved physical processes and interactions. These systems of integrals are complex and multidimensional. Traditional numerical methods such as the Trapezoidal rule method or Newton's method converge of the order $1/N^{2/d}$ where d denotes the dimension of the operation required and N the number of steps. Dimensional dependent methods are not optimal for solving multidimensional problems; these conventional numerical techniques are therefore not suited for simulating particle physical processes.

A wide group of Monte Carlo (MC) algorithms are instead commonly implemented to solve physical multidimensional systems. The MC method is non-deterministic and often relies on random number generators. The principle

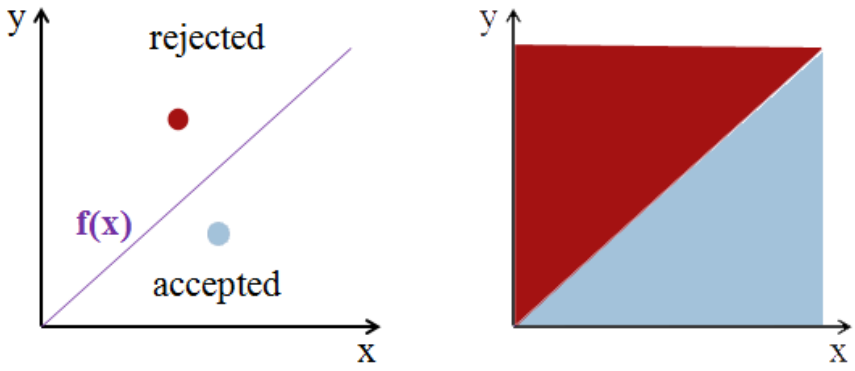

(a) (b)

Figure 6.1.: The principle of the Monte Carlo method is demonstrated to estimate the integral of $f(x)$. Random points are generated and (a) shows a red point which is rejected as the value y of the point at x is larger than $f(x)$, the blue point has an y value less than $f(x)$ and is accepted. The area after N random points have been generated is shown in (b), the ratio of the blue area to the red yields the integrated area.

of the method can be described by a simple example: assessing the integral $\int_0^1 f(x)\,dx$.

- First the parameter spaces need to be defined, take as an example the function $f(x) = x$, and the goal is to calculate the integral for $x \in [x_{\text{min}}, x_{\text{max}}] = [0, 1]$ and $f(x) \in [y_{\text{min}}, y_{\text{max}}] = [0, 1]$.
- Then, randomly generate coordinates in space x_i, y_i.
- If y_i is larger than $f(x_i)$, the point is rejected (as a part of the area needed to be integrated) (red point in Fig. 6.1 (a)).
- If y_i is smaller or equal to $f(x_i)$, the point is accepted (blue point in Fig. 6.1 (a)).
- Quantify the ratio of accepted to rejected points (Fig. 6.1 (b)).

- $\int_0^1 f(x)\,dx = (x_{\max} - x_{\min}) \times (y_{\max} - y_{\min}) \times \frac{\text{accepted points}}{\text{all points}}$.

The great benefits of MC algorithms are that they are only dependent on the number of generated points and always converge as $1/\sqrt{(N)}$ no matter what dimension of the numerical system needs to be calculated. Because of this, it is the perfect tool to solve the complex and multidimensional systems describing particle production in *pp* collisions. One note to be made is that these methods are affected by the performance of the random number generators. Having any form of repetition in the generated numbers affects the performance of the simulation. On the positive side, with the computing power available these days the periodicity is more of a historical problem but it is important to mention this to understand the method's weaknesses. The article *Introduction to Monte Carlo Methods* by S. Weinzierl [64] reviews a more in-depth exploration of the MC methods in particle physics.

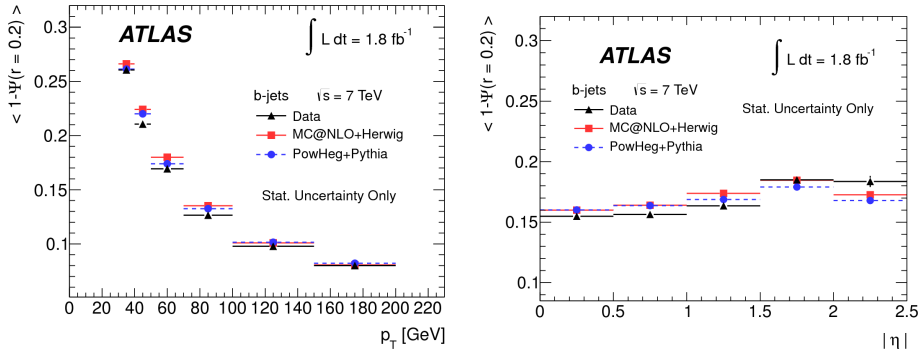

(a) (b)

Figure 6.2.: A comparison of how well Herwig and PowHeg+Pythia perform in simulating $t\bar{t}$ events, the two are compared to real data [65]. (a) shows the transverse momentum distribution for *b*-jets and (b) shows the $|\eta|$ spectrum. Both are quantified by the fraction of energy in the outer half of the jet cone (y-axis).

In HEP, the utilised MC programs are referred to as generators. These programs generate the events themselves; the particles created in a collision. There are a number of commonly used generators, which one to use for a

specific process is often depends on many different factors as the performance of the generators are not the same. Figure 6.2 illustrates this, with a study at ATLAS into the properties (p_{T} and η) of b-jets in $t\bar{t}$ events form data and events generated with two different programs [65]. To get a better overall representation of data, generators are often combined to complement each other. Example of generators are Pythia [66, 67], Herwig++ [68] and MadGraphs [69].

6.3. GEANT4 and Event Simulation

The event generators cannot on their own produce a correct representation of a collision event. Many physical processes occur when particles interact with matter. The ATLAS detector's full geometry is constructed using the GEANT4 toolkit [70].

After generating a number of events using MC generators, the events are fed through a GEANT4-package for the ATLAS experiment, to simulate the detector responses to all the particles in the event, such as hits in the ID layers for track reconstruction. Only after this procedure can one compare data with MC generated events. Moreover, this process involves accounting for scattering effects, energy losses due to radiations, etc. Immense precision on knowledge of the under-lying event and particles interaction with matter is required to construct simulations to the desired precision and is often tuned to what is observed in data as a guiding hand. The simulation of the ATLAS detector is constantly updating along with an improved understanding of the material or updated condition databases of particle interactions [71, 72]. Section 8.12.4 includes an analysis of how different variants of physics-lists interact with especially single element regions in ATLAS, in the beryllium layer in the beam pipe and in the ID modules of silicon.

In the DV analysis use MC samples for three different purposes, signal samples, backgrounds sample and samples used to estimate systematic uncertainties. All these three categories are explained in the following two sections.

Table 6.1.: Background MC samples for dijet events.These are used to estimate systematic uncertainties related to tracking and vertexing reconstruction efficiencies. The p_{T} range of the jets, the cross-sections σ and the number of events in each sample are listed.

ID	*jet* p_{T} [GeV]	cross-section σ [fb]	Number of Events (Million)
JZ0W	0-20	7.29×10^{13}	1
JZ1W	20-80	7.29×10^{13}	1
JZ2W	80-200	2.64×10^{10}	1
JZ3W	2000-500	5.44×10^{9}	1
JZ4W	500-1000	6.45×10^{6}	1
JZ5W	1000-1500	39.7×10^{3}	0.5
JZ6W	1500-2000	0.416×10^{3}	0.3

6.4. Background and Systematic Study Samples

Topologies of two jets are called dijet events and are produced at a high rate at the Large Hadron Collider (LHC). These types of events are common to the standard model and are well understood. MC samples of dijets are perfectly suited for validating signal efficiencies and cross-checks. Seven dijets samples, generated by Pythia8 [67], are used to help estimate systematic uncertainties and are used as well as a cross-check for the background estimation to see that the method works. The samples are generated using a set of different jet energies from $0 - 2000$ GeV (Table 6.1).

Radiative effects are not perfectly generated in Pythia (the signal MC samples are generated with Pythia6), therefore there might be certain systematic uncertainties on the signal efficiencies due to miss-modeling in the MC samples. A few Pythia8+Madgraph [69] samples are used to estimate systematic uncertainties on the signal efficiency related to radiative effects. Madgraph samples are chosen as it has been shown that it has produced better agreement with data in this area. These particular samples are simulated for the Supersym-

metry (SUSY) process,

$$pp \rightarrow \tilde{q}\tilde{q} \quad \text{where} \quad \tilde{q} \rightarrow \tilde{\chi}_1^{\pm} + qq \quad \text{and where} \quad \tilde{\chi}_1^{\pm} \rightarrow \tilde{\chi}_1^0 + W. \quad (6.1)$$

The target decay channels might not perfectly agree with the signal samples, but what is of interest is to estimate systematics related to radiative effects of the production process, where $\tilde{q}\tilde{q}$ is the only relevant fact. The cross-section for the subsequent decay is irrelevant and therefore any detail of this will not be given here. The only important fact is whether the mass of $\tilde{q}$ agrees with the one in the signal samples. Therefore, these samples were chosen with $\tilde{q}$ = 1100 GeV (the signal MC lies at 1000 GeV). This small mass difference is assumed to be negligible.

Table 6.2.: Signal MC samples are listed. The mass of the $\tilde{q}$ in all of these is at 1000 GeV and the mass of the $\tilde{\chi}_1^0$ is 108 GeV. The boost of each particle, $\beta\gamma$ is 5.5 and the cross-section is σ = 11.9 fb. The proper decay length is 220 mm for all the samples listed. These samples include three decays, to $\mu + jets$, to $e + jets$ and to $\nu + jets$ in the final states. For each type of final state there are samples with light and heavy flavour jets.

ID	LLP Decay	λ'_{ijk}
SIGMC1	$\tilde{\chi}_1^0 \rightarrow \mu + jets$	$\lambda'_{211} = 2 \times 10^{-4}$
SIGMC2	$\tilde{\chi}_1^0 \rightarrow e + jets$	$\lambda'_{111} = 2 \times 10^{-4}$
SIGMC3	$\tilde{\chi}_1^0 \rightarrow \nu + jets$	$\lambda'_{211} = 2 \times 10^{-4}$
SIGMC4	$\tilde{\chi}_1^0 \rightarrow \mu + jets$	$\lambda'_{213} = 3.55 \times 10^{-4}$
SIGMC5	$\tilde{\chi}_1^0 \rightarrow \mu + jets$	$\lambda'_{223} = 3.55 \times 10^{-4}$
SIGMC6	$\tilde{\chi}_1^0 \rightarrow e + jets$	$\lambda'_{213} = 3.55 \times 10^{-4}$
SIGMC7	$\tilde{\chi}_1^0 \rightarrow e + jets$	$\lambda'_{223} = 3.55 \times 10^{-4}$
SIGMC8	$\tilde{\chi}_1^0 \rightarrow \nu + jets$	$\lambda'_{213} = 3.55 \times 10^{-4}$
SIGMC9	$\tilde{\chi}_1^0 \rightarrow \nu + jets$	$\lambda'_{223} = 3.55 \times 10^{-4}$

6.5. Signal Monte Carlo Samples

The most important samples are the samples which are generated for the signal processes described in Eq. 5.1. The LLP decay through the R-Parity Violation (RPV) couplings λ'_{ijk} to either $\mu + jets$, $e + jets$ or $\nu + jets$ (Eq. 5.5-5.11). These processes are generated by setting the coupling to a non-zero value with a 100% branching ratio to the targeted decay channel. To target the λ' couplings a final state containing jets plus X is necessary, where X is a lepton or a lepton neutrino. Even though these lepton-objects exist in the final state the analysis does not directly use these lepton-objects in anyway and only look at the jets from the decay (the analysis looks for a displaced vertex from the LLP decay with four or more jets in the events, a requirement on leptons associated to the vertex will reduce signal efficiency and make the search strategy less generic). However, the targeted neutralino decay through the λ'_{ijk} couplings while always make a lepton or a lepton neutrino in the event but these are not used in anyway. The full set of signal MC is listed in Table. 6.2, generated with Pythia [66]. The production process of the LLP is either direct squark or direct gluino production[1]. An event filter is applied making sure that at least one of the produced LLP decays is within the fiducial volume ($r < 300$ mm and $|z| < 300$ mm).

Pile-up events are generated with Pythia8 [67] using low-energy $QuantumChromoDynamics(QCD)$ properties, over-laid upon the signal events. Moreover, the signal samples are reweighted to have the corresponding average collision per bunch crossing $< \mu >$ seen in data.

6.6. Corrections Applied to the Monte Carlo Samples

As mentioned several times, the processes are extremely complex and the simulations are not perfect, and often some properties are not calibrated to exactly

[1] The production type has no impact on displaced vertex reconstruction efficiency and the gluino-gluino production gives exactly the same efficiencies as the squark-squark production.

match data. The following two procedures are implemented to correct these discrepancies, and are standard procedures that follow ATLAS recommendations.

- The primary vertex distribution in the signal MC does not match the spectrum in data. Therefore a simple weight function is extracted by comparing the standard distribution in MC to data. The weight is applied on an event-to-event base. The (leading) primary vertex z-position is used to decide what weight to apply to the given event.

- The average number of interaction per bunch crossings, μ, are weighted in the simulated events to correspond to 2012 pile-up conditions.

6.7. Reweighting of Signal Sample τ

All signal MC samples, SIGMC0-SIGMC9 (Table 6.2) are generated with a fixed mean lifetime, τ_{MC}. This, in fact, limits the range of the analysis as the results are only given for a specific average lifetime. However, by adopting a re-weighting strategy of the τ_{MC}, this problem is avoided and the signal efficiency and cross-section exclusion can be provided as a function of $c\tau$.

The $c\tau$ of a particle directly dictates the lifetime t and probability whether the decay occurs inside the fiducial volume. Searching for $DV + jets$ includes physics objects dependent on all information from the complete event, i.e. the jets. In this case, either of the neutralinos can potentially create the jets triggered on. Therefore, both the $\tilde{\chi}_1^0$, in the decay must be considered (Fig. 5.1) when re-weighting the events. These weights are applied on the true decay time is known of the $\tilde{\chi}_1^0$. Given the true decay time t_1 of the first neutralino and t_2 for the second neutralino (Fig. 5.1), the weight w, is constructed by taking the ratio of the current exponential decay function (Eq. 3.1) by the one of the new targeted τ_{New} given the same t_1. This gives the weight that the neutralino in the event, with a different τ would have decayed at the

same t_1. The weight is computed as;

$$w(t_1, t_2) = \left(\frac{\tau_{\text{MC}}}{\tau_{\text{New}}}\right)^2 \frac{e^{t_1/\tau_{\text{MC}}}}{e^{t_1/\tau_{\text{New}}}} \frac{e^{t_2/\tau_{\text{MC}}}}{e^{t_2/\tau_{\text{New}}}}. \tag{6.2}$$

The weight is computed for each event in the signal MC. The probability that either of the two $\tilde{\chi}_1^0$, post weighting, would decay inside the fiducial volume and could be reconstructed is taken into account when re-weighting the efficiencies. The signal efficiencies as a function of $c\tau$ is given in Section 9.4.

7. Data Reconstruction

Converting detector readout and forming physics objects, e.g. an electron or a particle shower (jet), is called object reconstruction. The analyses are performed on the reconstructed objects. The displaced vertex analysis predominantly uses tracks and vertices, while triggering on a number of high p_T jets in the event. The relevant reconstruction techniques to this thesis are discussed in this chapter. Objects like electrons and muons et cetera are not used and will not be included here as they are not used directly.

7.1. Track Reconstruction

A crucial part in event reconstruction, in almost any given modern particle physics experiment, is tracking the paths, through the detector, of charged particles.[1] The three detector sectors in the Inner Detector (ID) work on the same basic principle, but with different underlying mechanics, which is to provide point-measurements along the passage of the particles.[2] These hits are used to extrapolate a particle's path through the detector volume. Track reconstruction, or tracking for short, is the process of combining the energy deposits in the form of coordinates, to a track of the particle's passage. This is illustrated in Fig. 7.1 with a collision event in *xy*- and *rz*-cross subsections of the ID. The gray points are recorded hits in the tracker volume and the

[1] Neutral particles leave no footprint in the typical silicon detectors, rather calorimeters prove records of the deposited energy of these neutral baryons or mesons (subsection 4.2.2).

[2] The same goes for the Muon Spectrometer (MS) but, as this is the designated $\mu^{\pm}$-tracker, it lies outside the main focus.

colourful lines are the trajectories of particles reconstructed using the gray points as input; each coloured line is traced through several hits.
Tracking is in no way a simplistic concept but rather a very complex task, and adding A Toroidal LHC ApparatuS (ATLAS)'s non-uniform magnetic field to this complexity will make the tracking exercise even more cumbersome.

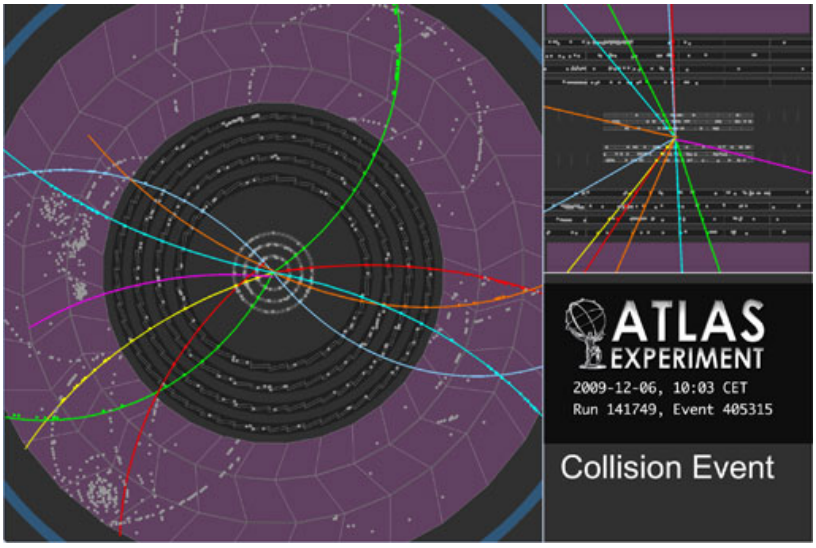

Figure 7.1.: An event-view from one collision event in the *xy*-(left figure) and *zr*-planes (top right); where the gray dots indicate hits in the detector layers, the coloured lines each correspond to a reconstructed track. The three most inner circular layers are the Pixel Tracker (Pixel), the four following layers are the Silicon Tracker (SCT) with the Transition Radiation Tracker (TRT) at the most outer region. [73]

7.1.1. Pattern Recognition aimed for Track Reconstruction

At the base of all track reconstructions is the assembly of the three dimensional coordinates in space gathered from the detector layers. After that there is a large collection of standard pattern finding algorithms, which are selected, depending on the topology of the detector structure or even sub-detector, used to recreate the trajectory of the particle. There are typically two sets of

algorithms. The first set of algorithms works in the global frame and observes the system as a whole and attempts to find all tracks in an event simultaneously using the combined information from the whole tracking volume e.g. Hough transformations [74][3] or Neural Network (NN) algorithms. The second set of algorithms, operating in the local frame, targets object by object, for example, evaluating the probability of a given hit to be compatible with the track, moving from hit to the next improving the track fit with each iteration, as is the case of the Kalman filter [75]. The Kalman approach, and other local methods, do not require exhaustive information about the whole collision event, which is to the benefit of situations, for example, where the underlying event structure is not clear. The interested reader can find an excellent summary, by R. Mankel, on the basis of pattern recognition techniques in reference [76].

7.1.2. Track Quality Requirements

The various tracking sequences have their own optimised tracking quality criteria, such as the number of hits required or the momentum of the track, summarised in Table 7.1. The most strict criteria are on the left, loosening as moving to back-tracking and the low p_{T} settings. Re-Tracking is a special tracking method developed by the displaced vertex analysis team at ATLAS, the details are covered in subsection 7.1.7.

7.1.3. Standard Tracking

ATLAS standard tracking utilises two types of pattern finding methods; global pattern search algorithms, which construct track seeds, and local pattern recognition which involves fitting of tracks using few variations of implemented techniques (such as the Kalman filter or a global χ^2 fitter). The track reconstruction process consists of two steps: the Inside-Out track reconstruction and the Outside-In track reconstruction. As the naming scheme suggests the two try to combine the outside-detector (the TRT) with the inside-detector

[3] Hough transformations are commonly used in ATLAS to find track seeds in the TRT volume as it only provide hits in two dimensional projection-slices.

Table 7.1.: Tracking Quality Cuts required by the three tracking sequences; Standard Tracking, Back Tracking and Low p_T. Standard Tracking is the default setting. Back Tracking is run after Standard Tracking, attempting to connect TRT track candidates with left-over silicon hits, it is run at a higher momentum threshold to ensure relative straight tracks can be directly connected. The Low p_T setting is typically run for specific analysis, such as Minimum Bias Studies where the underlying event is of interest.

Loose Requirements for $\pi^{\pm}$			
Quality Cuts	Standard Tracking	Back Tracking	Low p_T
p_T	> 400 MeV	1000 MeV	> 100 MeV
$\lvert d_0 \rvert$	< 10 mm	$< 100mm$	< 100 mm
$\lvert z_0 \rvert$	< 250 mm	-	< 250 mm
$\lvert \eta \rvert$	< 2.7	< 2.7	< 2.7
Number of Si Hits	≥ 7	≥ 4	≥ 5
Number of Pixel Hits	-	-	≤ 2
Number of TRT Hits	-	15	-
Number of Shared Hits	≤ 3	1	≤ 1
Number of Pixel Holes	≤ 2	1	≤ 2
Number of SCT Holes	≤ 1	1	≤ 1

(the Pixel and the SCT). The sequence in the track reconstruction chain can be seen in the simple schematics in Fig. 7.2 and Fig. 7.3; each step will be explained in more detail in the following subsections and is a summary of reference [77].

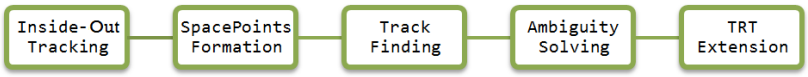

Figure 7.2.: The tracking reconstruction chain consists of two parts: first an Inside-Out tracking algorithm working to form tracklets from hits in the Pixel and the SCT.

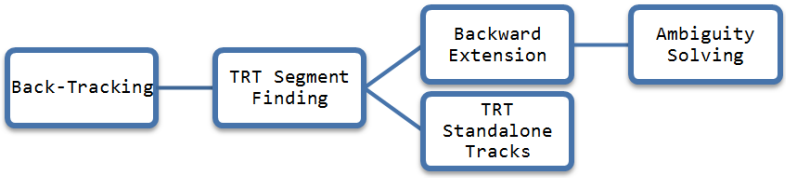

Figure 7.3.: The tracking reconstruction chain consists of two parts: the second chain looks for hits in the TRT and tries to extend the track backward to Si-tracklets.

7.1.4. Inside-Out Tracking

The concept when the measurements in the Pixel and the SCT are converted into track candidates and extended into tracks using hits in the TRT is called Inside-Out tracking. The reconstruction chain (Fig. 7.2) for the Inside-Out tracking consist of a few steps before the track candidate from the inside detector can be extended to the TRT. First, in the processes named **space-point formation**, recorded energy deposits are converted to coordinates in space - so-called space-points - in the global coordinate frame with respect to the beam line. Three-dimensional points are given by both the silicon detectors. Two-dimensional hits are given by the Pixel in the local coordinate frame, but as the layers are fixed in the third-coordinate frame, a three-dimensional coordinate is read-out in the global coordinate frame (after coordinate transformations). Typically, a strip detector can only read out the hit-position perpendicular to the strip, giving a two-dimensional point, but the composite structure of the SCT with two modules mounted on top of each other makes it feasible to construct a three-dimensional point using both measurements from top and bottom sides of the modules.

Track candidates (**track finding**) are fitted by seeds containing three silicon space-points; about ten percent of all the seeds in an event end-up as a track candidate. This step does not contain any checks on the quality of the tracks, such as if one space-point is used by more than one track. Therefore the resulting collection of track candidates is composed of a large quantity of low

quality, incomplete or fake tracks. The next step removes the majority of fake tracks.

The **ambiguity solver** is implemented to attempt to resolve the real tracks. At the beginning of the process, the tracks are refit by using a more exhaustive description of the material distribution in order to obtain high-quality track candidates. In order to reduce cpu-usage, this is done after the initial track candidates are found. After the refit, the track candidates are scored by their combined hits and holes. A hole is a lack of a hit along the trajectory e.g. a track missing a hit in the third pixel layer, but has successfully been fit through hits in the surrounding detector layers. The hits and holes are rated on a set of criteria. The hits are weighted by the precision of the sub-detector; where hits in the pixel are given a larger weight than hits in the SCT or the TRT. An additional scoring is set on the hits and holes; a missing hit in the B-Layer (Section 4.2.1) is considered severe, this criterion results in a prioritising of primary tracks over secondary tracks and such a track will receive a harsh penalty; while, in contrast, a hit in two overlapping modules - in the same detector layer - is given high scoring. Subsequently, if the tracks do not pass certain quality cuts, the shared hits are bestowed to the highest scoring track. At the end of the ambiguity solving process track candidates, which do not have high enough score, are removed. The final step in the Inside-Out tracking, is an attempt to extend the track candidates to tracks using hits in the TRT.

The **TRT-extension** process works on the track by track basis; each silicon seeded track is extrapolated to the TRT-volume, where the algorithm endeavours to connect the track to TRT-hits. Not all tracks pass the extension process and these shorter tracks are still kept as a final track; depending on the track quality cuts some of these tracks might be sorted out, if they e.g lack enough hits. However, if an extension is found, the track candidate is refit using these extra measurement points, including a second ambiguity solving step. A view of track candidates and TRT-extended tracks in a $t\bar{t}$-event show an example of the track extension (Fig. 7.4); the red paths of hits are reconstructed track, where some have been extended to the seeds found in the TRT. The beginning of the TRT-volume is indicated by the high density of hits at around 500 mm

in xy. Few track candidates lack extension and stop after the silicon detectors. While a few TRT-segments, the bold paths of hits, are connected to the silicon tracks in the back-tracking step, in Outside-In tracking.

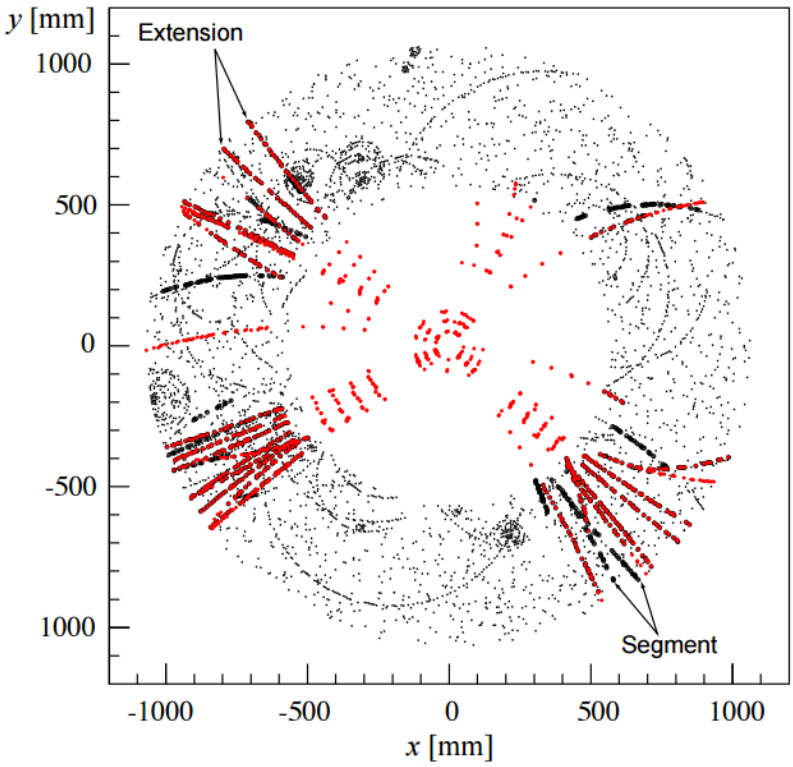

Figure 7.4.: Extending the silicon seeded track candidates using TRT segments (the bold black consequential dots) in a $t\bar{t}$-event, the red dots represent the final tracks after reconstruction; a couple of the track candidates are not connected with a TRT segment [77].

7.1.5. Back-Tracking

There is a probability that certain tracks are not found by the Inside-Out tracking. For instance, if the distance between two hits is minuscule, one of the hits can be sorted away by the ambiguity solving step; leading to that the track will not to be reconstructed. Moreover, tracks from secondaries such as hadronic interactions or K_S are not favoured by the Inside-Out tracking as they frequently fail the silicon hit requirements. Back-Tracking strive to find these types of tracks. Similar to the Inside-Out tracking, track candidates are formed from seeds. However, the seeds are made up by hits in the TRT. The TRT-seeds are called TRT-segments (the black thick lines in Fig. 7.4) and are constructed by coupling hits together using Hough transformations. Straight line propagation is performed to extend the segments backwards to the silicon detector on left-over hits not previously used by the Inside-Out tracking. High $p_T > 1000$ MeV requirement during back-tracking ensures that the particles' tracks are traveling on a straight trajectory. It is worth mentioning that the TRT can only provide measurement in a plane perpendicular to the straws; the segmentation is performed by two dimensional projections of the ID volume, often divided into η-subsections. Successfully extended tracks run through the same ambiguity solver checks as in Inside-Out tracking but with different criteria. The non-extended TRT-segments can be used as standalone tracks.

7.1.6. Low-p_T Tracking

Further steps are implemented to resolve the lowest momentum tracks from particles, e.g. from secondary decays, which have undergone scattering or suffered significant energy losses. These tracks fall under the category Low-p_T or even Very Low-p_T tracking, which have loosen track quality cuts, especially reducing the number of required silicon hit and lowered momenta requisitions; $100 < p_T < 400$ MeV and $p_T > 50$ MeV for Low-p_T and Very Low-p_T, respectively, where the standard tracking demands a transverse momentum larger than 400 MeV. Besides loosening the cuts, the reconstruction strategy is the same as for Inside-Out tracking. Only left-over silicon hits are used similar to the backward extension of TRT-segments.

7.1.7. Reconstruction of Tracks with Large Impact Parameters

The standard track reconstruction is mainly designed to reconstruct primary tracks that are assumed to have originated close to Primary Vertex (PV) and would have relatively small impact parameters with respect to the Interaction Point (IP). The regular selection criteria put strict limits on $|d_0|$ w.r.t. IP and $|z_0|$ w.r.t. IP. ATLAS tracking is optimised for the primary track reconstruction, the efficiency is therefore high with values above 90% for high p_{T} tracks (Fig. 7.5 (a)). However, these cuts on the impact parameters, inhibit reconstruction of tracks arising from long-lived decays; this is not only true for long-lived decays, but also for nuclear interactions with the detector material. The secondary track reconstruction efficiency is therefore significantly lower than for primary tracks (Fig. 7.5 (b)). It was shown in [60] that the signal efficiency to reconstruct displaced decay from long-lived particles is significantly constrained by the usual tracking criteria. The reconstruction cuts have been loosen (Table. 7.2) and the tracking is run a second time using only left-over hits from the standard tracking. The cuts have been optimised to keep the efficiency high, but also to keep the fake rate at an acceptable level. This method, named Re-Tracking, was developed by the ATLAS displaced vertex analysis team in order to improve the efficiency for Supersymmetry (SUSY) related searches. Both the tracks found during standard tracking and the Re-Tracking process are fed into the vertex algorithm (subsection 7.2). The result of the added Re-Tracking is a notable increase in the secondary vertex reconstruction efficiency (Fig. 7.6).

Table 7.2.: Changes made to the track selection process by implementing Re-Tracking. Increasing the lower thresholds on the impact parameters d_0 and z_0 relative to the primary vertex.

Normal Tracking	Re-Tracking
$\lvert d_0$ w.r.t. PV $\rvert < 10$ mm	$\lvert d_0$ w.r.t. PV $\rvert < 300$ mm
$\lvert z_0$ w.r.t. PV $\rvert < 250$ mm	$\lvert z_0$ w.r.t. PV $\rvert < 1500$ mm
Number of Not Shared Hits ≥ 6	Number of Not Shared Hits ≥ 5
Number of Shared Hits ≤ 1	Number of Shared Hits ≤ 2

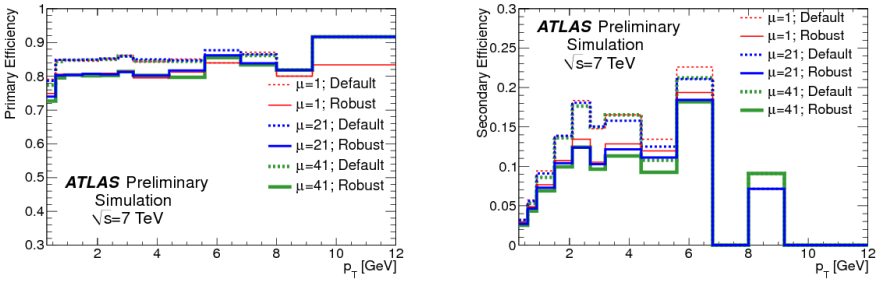

(a) (b)

Figure 7.5.: Primary (a) and secondary (b) track reconstruction efficiency in ATLAS as a function of transverse momentum for minimum bias MC samples at a few different average number of collisions (pile-up). Using the default and robust track selection criteria [78]. The primary reconstruction efficiency is significantly higher than for secondary tracks.

7.2. Vertex Reconstruction

The PV serves as a pinpoint of where the initial interaction took place. A large number of event related parameters is estimated using the PV location as a reference. High precision and efficiency in the determination of the PV therefore ensures strictness throughout the whole event. Secondary vertexing on the other hand, is significant in deriving information regarding meta-stable particles such as K_S or B-hadrons. Two separate approaches are used for PV and Displaced Vertex (DV) reconstruction as their position in the detector plays a huge role in how to optimise the process.

7.2.1. Primary Vertex Reconstruction

Similarly to the track reconstruction (subsection 7.1), the vertex reconstruction process is divided into two steps: the first step tries to reconstruct vertex candidates, and the second step executes algorithms attempting to fit the vertex's position [79]. Requirements on the quality of the tracks, which are used

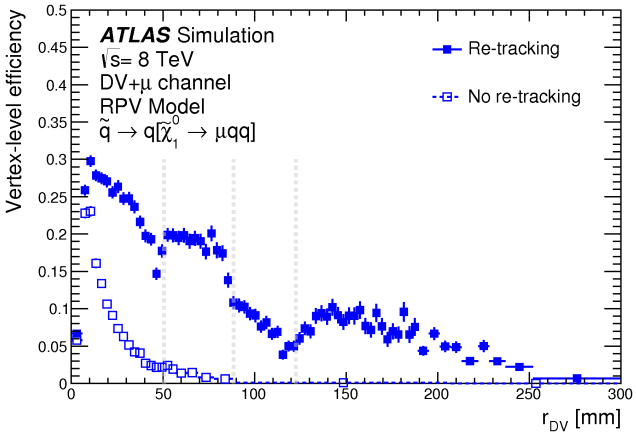

Figure 7.6.: The secondary vertex reconstruction efficiency as a function of r using only the standard ATLAS tracking sequence (hollow boxes) and the increase seen by adding the additional large impact parameter tracks reconstructed by Re-Tracking (filled boxes). The grey lines indicate the radial positions of the three pixel detector layers, the drop in efficiency right before each line is caused by requirements in the vertexing process demanding a certain number of maximum shared hits by tracks; tracks close-by an active detector layer are more likely to share hits.[5]

to fit primary vertices, are made in order to ensure high quality and precise measured position of the vertex. Only tracks which have, $p_{\mathrm{T}} > 400$ MeV, $|d_0| < 4$ mm and at least 4 SCT-hits and 6 or more combined silicon hits are input to the vertexing algorithm. There are also requirements on the quality on the impact parameters to ensure well measured tracks. These are enforced to be within $\sigma(d_0) < 5$ mm and $\sigma(z_0) < 10$ mm precision to reduce the fake rate. The standard vertex fitting procedure, described in [79], goes as follows.

Vertex candidates are constructed by seeds formed by tracks originating from the IP; passing all the cuts on the tracking parameters. The seeds are searched for with the help of the z-spectrum of the tracks, where tracks close to the global maximum of said function are selected to form seeds. A robust χ^2 algorithm, incompatibility graph [80], fits the vertex position, weighting the track by their distance to the seed-centre. Tracks deviating with more than 7σ

are discarded from the current vertex, but are kept to be used to make a new seed. The same general strategy is executed until no further vertex candidates can be established. Throughout the vertexing, the tracks identified as compatible with a vertex are refit to have said vertex as origin instead of the IP.
The quality of the vertex resolution depends heavily on the track multiplicity of the vertex as well as the transverse momentum of the tracks. The fewer tracks or low p_T tracks associated with the vertex, the worse will the spatial vertex resolution become; where the transverse resolution in low (high) track-multiplicity vertices are around > 100 μm ($30 - 60$ μm).

The primary vertex reconstruction is very efficient in ATLAS with an efficiency near 100%. Pile-up affects the efficiency and resolution of the PV, Fig. 7.7 indicates that even though the efficiency decreases with μ, the efficiency is very effective under the pile-up conditions in 2012 physics runs. The vertex with the highest amount of p_T associated to it via the primary tracks are selected as the most important interaction while the other vertices are often pile-up.

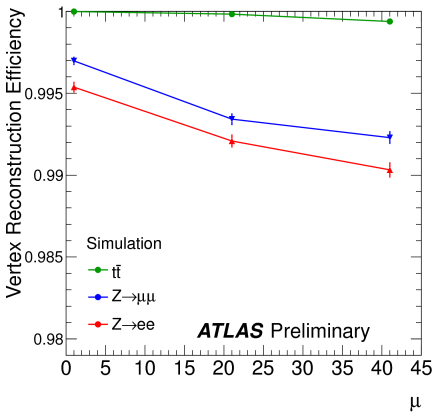

Figure 7.7.: The primary vertex reconstruction efficiency as a function of pile up [81]. Slight degradation in the efficiency is seen as a function of average bunch crossings μ. Different behaviours are observed depending on the physics process.

7.2.2. Inclusive Vertexing Algorithm

The approach for finding primary vertices does not apply directly for the secondary vertex reconstruction process. Neither the track selection criteria nor the seed finding scheme can be employed. However, the fitting process is based on the same incompatibility hypothesis. A global vertex finding algorithm finds the seeds to reconstruct secondary vertices, corresponding to displaced decays from long-lived particles. Likewise, this vertexing method is utilised to reconstruct material interactions by which the material-veto map (subsection 10.3) is constructed[4].
The first step, also in this vertexing finding, is the track selection process. An inversed cut on the transverse impact parameter, of $|d_0| \geq 2$ mm, makes it possible to select secondary tracks with high efficiency. The p_{T}-cut, in case of the displaced vertex analysis, is set at 1 GeV, to keep the fake rate low. The tracks originating from vertices further out in the fiducial volume will not always have tracks with many pixel hits, any demand on silicon hits in the Pixel would prevent vertices in certain regions to be assembled. However, at least two SCT hits are required to ensure that high quality tracks are used as input to the vertexing. Tracks having no hits in the TRT are required to have at least two pixel hits or they will be discarded; also this cut has been designed to remove further fake tracks, as a large quantity of fake tracks was found to consist of only SCT endcap hits.

From this selection of tracks, the universal vertex finding algorithm starts with finding all combinations of two tracks in each event. These vertices are required to have a vertex fit χ^2/number of degrees of freedom < 5, which removes the major part of random combinations of tracks. A fake removal enforces the deletion of non physical topologies such as back-to-back tracks; consisting of two types of demands. On the one hand, the vertex is discarded, if any one of the two tracks has a silicon hit at a radius smaller than the vertex position. On the other hand, the vertex is required to have tracks which have silicon hits in a detector layer at a larger radial position than the vertex. For

[4] These nuclear interactions with the material are also used to study the description of the material in simulations.

example, a vertex, found at very small $r < 25$ mm, needs to have the two tracks with a hit in the B-layer of the Pixel detector, and a vertex in between the first two Pixel layers, requires the two tracks to have no hits in the B-layer, although both tracks need to have hits in the second Pixel layer (Fig 7.8). The same logic is adapted for all vertices, changing the detector layers in question, depending on the position of the vertices.

After the first step of seed selection, the incompatibility graph method [80] attempts to combine close-lying two track seed vertices to construct vertices with track multiplicity larger than two. The vertices are merged or split based on a χ^2 fit. There is a probability that one track can have been used to form more than one seed. The vertices are merged or the worse fit vertex seed is broken depending on the track-vertex fit. The process is repeated until no track-duality is left in the sample and all close-lying vertices are merged. The final step merges all vertices within 1 mm of each other.

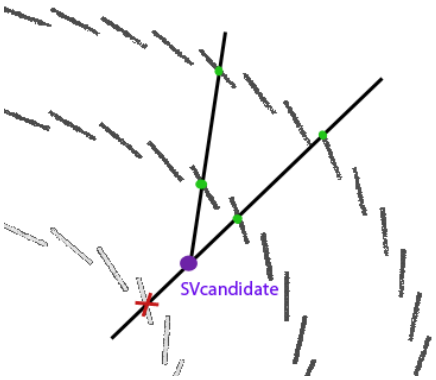

Figure 7.8.: Schematics over the fake removal process. Showing a circle sector of the detector in the $r\phi$-plane including the three Pixel layers with corresponding modules. The tracks in the secondary vertex candidate are checked so that neither of the tracks has a hit in a silicon layer at a radius smaller than the vertex itself. One of the track has a hit in the B-layer and the vertex will fail the fake removal.

7.2.3. Vertex Reconstruction Efficiency

The intrinsic efficiency of the secondary vertex algorithm is very high with an efficiency close to 100%. However, a lot more factors are involved, such as the tracking efficiency and various selection cuts. These reduce the effective vertex reconstruction efficiency to around 30% (Fig. 7.6). Moreover, the efficiency also depends on the mass of the decaying particle, the boost of the particle and the decay lengths.

7.2.4. Vertex Resolution

The secondary vertex resolution is dependent on several factors. Vertices further out in the detector will suffer a lower track reconstruction efficiency and will therefore have smaller fraction of total reconstructed tracks. The fewer tracks a vertex has the larger uncertainty in the DV position. The resolution is also heavily dependent on the quality of the tracks; tracks with fewer silicon hits will have worse measured track parameters. Particles decaying further out in the detector will then miss silicon hits, leading to that the vertex resolution will also worsen with radial position. Depending on the radial and z-coordinate, the vertex resolution is around tens of microns in r and two hundred microns in r. Figure 7.9 (a) and (b) show the average residual of $r\phi$[5] and z in mm respectively.

7.3. Jet Reconstruction

Jets are reconstructed in two steps; Calorimeter Clusterings and Jet Reconstruction. Initially, the clustering algorithms run on the output from the calorimeters. In ATLAS there are two different types of algorithms; "Sliding-Window" and Topological [82]. The Sliding-Window Algorithm summarises the output, i.e. the energy, from all calorimeter cells around a fixed "window".

[5] The residual is computed, looking at the simulated true information, giving the resolution from the vertex true radial position minus the reconstructed vertex position.

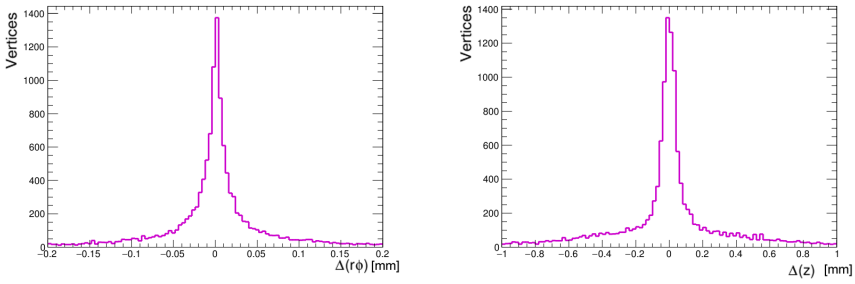

(a) (b)

Figure 7.9.: Vertex resolution for secondary vertices is shown for (a) $\Delta(r\phi)$ and (b) $\Delta(z)$. The resolutions vary depending on the distance of the DV from the interaction point. Loss of hits in the silicon layers of decays outside a numerous of layers directly translates into worsen vertex position resolutions.

The centre is chosen at a location where the energy included in the window is maximised. This algorithm is applied on electromagnetic showers and jets originating from taus; where the efficiency is high. For hadronic clustering a different, iterative, clustering process is more optimal. Cluster seeds are formed from all cells found containing energy higher than a given threshold, considering the noise to signal ratio. The cells neighbouring to the cluster seeds are added and merged if their energy are above another, slightly lower energy threshold. All neighbouring cells are looped over until a cluster is formed. This process is repeated until all seed candidates are processed. If necessary, and if the cluster passes criteria, the cluster is split; followed by a re-iterative process on all the neighbours.

Jet objects are produced by jet clustering algorithms. The jets treated in this thesis have been reconstructed using the Anti-kt jet algorithm [83]. This algorithm is described as follows. It consists of the computation of the distance d_{ij}, between the objects i and j; particles or pseudo-jets. Also the distance d_{iB} of the object relative to the beam line is computed. The algorithm attempts to find the smallest distance between two entries i and j;

$$d_{ij} = \min\left(k_{ti}^{2p}, k_{tj}^{2p}\right) \frac{\Delta_{ij}^2}{R^2}, \tag{7.1}$$

$$d_{iB} = k_{ti}^{2p}, \tag{7.2}$$

where Δ_{ij}^2 specifies the difference between the pseudorapidity and the azimuthal angle $((\phi_i - \phi_j)^2 + (\eta_i - \eta j)^2)$. The transverse momentum of the object is defined as k_{ti}^p. All objects within a cone R are inclusively considered by the algorithm. $R = 0.6$ is used in the analysis in the thesis. The two objects are merged if $d_{ij} < d_{iB}$ and their energy inform of the four-momenta is recalculated. However if d_{ij}=d_{iB} the iterative process is concluded and i is marked as a jet. After reconstructing the jets the cluster energy needs to be calibrated accounting for the responses in MC simulations described in [84]. In order to combine the energy output from the whole ATLAS detector, the energy measurements in all the different parts need to be scaled so they can be compared. This scaling process gives rise to uncertainties, something that have to be considered in order to have a precise measurement of the jets energy. This topic is treated in reference [85].

8. Hadronic Interactions - Detector Material

The Hadronic Interaction Analysis reviewed in this chapter should be read as an independent analysis from the displaced vertex analysis. This analysis covers the work conducted as the service task for the A Toroidal LHC ApparatuS (ATLAS) experiment and helps quantify the material budget in order to better understand the tracking efficiency of the Inner Detector (ID) tracker. The analysis relies and is based on developments done in the article "A study of the material in the ATLAS inner detector using secondary hadronic interactions [63]. The material covered in this chapter has previous been documented internally for the ATLAS experiment but by the author of this thesis. The improvements referred to throughout this chapter are in reference to the previous publication cited above.

Material studies at ATLAS or any experiments are of extreme importance. The material effects such as hadronic interaction and scatterings are the major source of inefficiencies in the process of track reconstruction; tracks are vital part in reassembling physics objects from all kinds of detector signatures. Currently, there are a few types of analyses that are dedicated to study the material in the ATLAS ID. They are using different kinds of approaches to estimate the amount of material in the tracker. Firstly, the traditionally adopted method for a wide range of particle physics experiments is the γ-conversions method. Photons interacting with the material can be converted into an electron-position pair. The rate of interactions is dependent on the material radiation lengths X^0 and by converting the measured rates of the amount of conversion to X^0, the material budget can be quantified and it corresponds

to the amount of material in the detector in terms of interaction or radiation lengths. Secondly, there is a method taking advantage of that the tracks are extended from seeds, or so called tracklets,[1] from one part of the ID to seeds in another part (Section 7.1). Between the Pixel Tracker (Pixel) and Silicon Tracker (SCT) there exists a significant amount of material in barrel support structures and cables from the electrons. This material is probed indirectly by the efficiency of extending tracklets from the Pixel to the SCT. The SCT extension efficiency analysis [86] studies this specific region. Thirdly, there is the technique of the Hadronic Interaction; which has proven most useful at providing detailed analysis of detector elements difficult or rather impossible by other kind of material studies, mostly, owning to the superb resolution of this technique.

Section 5.2 introduced briefly the "material map" which is applied to make sure no displaced vertex found is located in the dense material regions; as it is difficult to differentiate from a hadronic interaction vertex and a vertex from a Long Lived Particle (LLP) decay in just such regions. The third method, the hadronic interaction analysis, has been used to create this map. However, this chapter will discuss the details of the technique and how it provides quantitative measurements of the material in the ATLAS ID. And it should be viewed as a stand-alone analysis conducted during the process of producing this thesis. The results from the "Material Study" point of view, have been used to construct the material map and the details of this are reviewed in Section 10.3.

8.1. Hadronic Interactions

Primary particles that interact inelastically with the detector material produce secondary particles; the point of interaction is referred to as a hadronic interaction. The secondary particles often have low momentum and therefore have comparatively large opening angles giving just this material study approach an advantage of good spatial resolution. Hadronic interaction analysis

[1] Tracklets are short track which often contain few hits.

yields a resolution of the vertex position of $\sim$ 0.3 mm in z and r for $r < 100$ mm, an order of 10 better resolution compared to γ-conversion studies. This excellent resolution makes precise comparison of minute detector elements feasible. Moreover, it is possible to provide direct comparisons of the modelling in Monte Carlo simulations (Monte Carlo (MC)) and the detector by looking at collected data, without the need to convert the measurements depending on the materials interaction length. The study was first developed and published in 2011 [63]. This chapter covers the improved and broaden analysis, which has been extended by using Re-Tracking (Section 7.1.7) and improved vertex selection. The mentioned factors increased the targeted total volume from 0.09 m^3 to 0.3 m^3, which is an increase by a factor of about 3.

8.2. Minimum Bias Analysis

At ATLAS Minimum Bias (MB) analysis provides crucial measurements of charged particle distributions of soft-Quantum Chromo Dynamics (QCD) processes in pp-collisions. The charged particle distributions have been measured for different collision types at experiments and at a wide range of centre-of-mass energies. Information obtained from these studies often helps to tune the generators which simulate MC (Section 6.3) to enhance performance of strong interactions at the low energy scale. The low energy processes are fundamental pieces in order to understand the complete collision event and are referred to as the "underlying event". MB analyses are also a central part to physics at high energies, as they are sensitive to the underlying event and the effect of pileup. MB events, as the name suggest, are selected with a minimal bias to exclude any inclination or tendency due to dependencies of underlying structures that would introduce favouritism for one type of events. Material studies fall under the MB category as it helps improve the understanding of the physics observed.

8.3. Event Selection

Data collected in 2010 at a centre of mass energy of 7 TeV representing an integrated luminosity of 19 nb^{-1} are compared to a non-diffractive events MC sample. Non-, single- and double-diffractive define whether, after collision, the two protons diffractively scatters and to what degree. A non-diffractive sample is chosen since this reduces the uncertainty in simulation of diffractive events as this process is not naïve. The minbias trigger includes single-, double- and non-diffractive events, the contamination of single- and double-diffractive events is reduced by making requirements on the track multiplicity at the Primary Vertex (PV). Requiring a high track multiplicity at the PV, to put it simplistic, ensures that most of the energy went into the same interaction point and thereby eliminating diffractive events. MC-studies from the previous publication [63] show that a cut on the number degrees of freedom (ndof) at the PV of at least 22 removes 99% of the single- and double-diffractive events; this specific strategy only works for low pile-up conditions as the secondary collisions introduce predicaments. Generally this cut corresponds to a cut at 11 tracks or more as tracks in most cases have two degrees of freedom, however on occasions to bad fits the tracks can have fewer so it is hard to make direct comparisons. The 2010 dataset has been reprocessed with 2012 alignment with the purpose to improve the tracking and therefore, with the improved understanding of the detector and its efficiencies, one would profit by enhanced quality of the reconstructed objects. The MC is simulated using the latest version of the geometry descriptions used for the runs in 2012, containing drastic improvements from the 2010 geometry. For instance, the beam pipes position has been corrected and corrections of material in the end-region of the Pixel barrel have been implemented. These fixes have shown improvement in the modelling of the tracking efficiency.

8.4. Track Selection

A yield in efficiency and an increase in the amount of reconstructed vertices have been achieved by applying the strategy to re-run the tracking on left over

hits as described in Section 7.1.7. In general, secondary tracks in general have large impact parameters with respect to the PV. Tracks emerging from hadronic interaction are selected by making a cut on the transverse impact parameter $|d_0| \geq 5$ mm. This cut helps remove the majority of the primary tracks and many tracks from K_S- , Λ-decay and γ-conversion; these are the major sources of secondary vertices next to material interactions. No requirements are set on the number of Pixel hits as this would limit any vertices at larger r. At least one SCT hit per track is required to get a silicon hit. In order to improve the secondary vertex reconstruction purity, the cut on track's p_T during the track selection has been increased from the previous publication (which did not use re-tracking and had less fake tracks). However, an increased cut will yield a rapid decrease on the number of total reconstructed vertices. Wishing to keep the gain in purity from excluding additional low quality tracks, while still keeping a valid amount of statistics, the cut on $p_T > 0.4$ GeV was selected as optimal (previously this cut was at $p_T > 0.3$ GeV). Moreover, the track fit is required to pass χ^2/n.d.o.f. < 5.

8.5. Vertex Selection

The vertex algorithm discussed in Section 7.2.2 reconstructs the material interaction vertices. However, as the target process is different the cuts vary slightly. The cut $d_0 \geq 5$ mm made on the transverse impact parameter of the tracks allows one to reconstruct secondary vertices almost exclusively (from secondary tracks). The vertex fit is required to pass the same χ^2/n.d.o.f. < 4.5. MC studies [63] have shown that the cut removes 85% of random pairings, but keeps more than 83% of material interaction vertices. The last step of merging close-lying vertices is not applied for this case.

The low pile-up, present in 2010 data, facilitates the comparisons with MC. One primary vertex per event is required to remove any pile-up.

The mass spectrum of the secondary vertices has two clear peaks (Fig. 8.1 (a)). The peak at $\sim$ 300 MeV corresponds to γ-conversions, and the non-zero mass

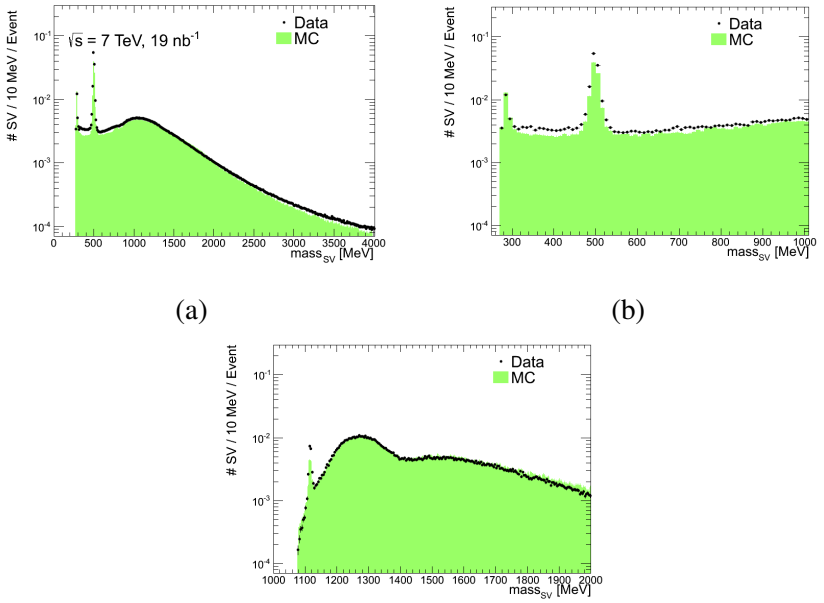

Figure 8.1.: Mass spectra of the secondary vertices in [MeV] (a). Peaks corresponding to γ-conversion, K_S-decay are visible and a zoomed version is shown in (b). While the Λ peak can be seen visible if the mass is recalculated considering proton and the pion mass for the tracks rather than only the pion mass (c). The green histogram is the secondary vertices found in MC while the black points are data.

is due to incorrect assignment of the $\pi^{\pm}$-mass to the $e^{\pm}$ tracks, which is the default in reconstruction if not specified otherwise. The second peak at around slightly higher mass of 500 MeV corresponds to K_S-decays, a zoomed in view of these two peaks are seen in (b). Vertices corresponding to these are not wanted sources of secondary vertices; accordingly vertices corresponding to these decays are vetoed by restrictions on the vertex mass. The sample contains a number of Λ baryons, the corresponding mass peak is only visible if one recalculate the vertex mass using the proton and pion mass for the two tracks rather than only the pion mass as is standard in the tracking in this case. Recalculated the invariant mass of two track secondary vertices using

proton-pion masses for the two tracks is shown in Fig. 8.1) (c) where a clear peak is visible at 1116 MeV. The vertex is vetoed, if the secondary vertex mass lies inside ±35 MeV of the K_S mass (494 MeV) or ±15 MeV of the Λ mass (1116 MeV after recalculated the vertex mass). Secondary vertices with masses below 310 MeV are removed to eliminate the vertices corresponding to γ-conversions.

8.6. Corrections and Normalisation

Track reconstruction of data is generally well simulated in MC, but there are some discrepancies in the number of primary tracks reconstructed [86]. The amount of primary tracks directly affects the number of secondary interactions. The more primary particles, the more hadronic interactions will occur. In turn, secondary particles created in hadronic interactions can also interact with the material and produce even further hadronic interactions. Since data have more primary tracks, MC has to be corrected by a correction factor to make up for this difference. The number of primary tracks intersecting a given material layer is counted by extrapolating the intersection points for all primary tracks with the material layers. Because tracks travelling at an angle will cover more material and have a higher probability to interact with the material than tracks travelling straight, the tracks are also weighted depending on their polar angle by $1/\sin\theta$; an r-dependent scale factor is applied to MC, derived from the difference in primary track multiplicity between data and MC (Figure 8.2 (a)). These scale factors ranging from corrections of $6.0 - 7.6\%$ for the barrel layers, while smaller corrections of $4.5 - 6.0\%$ are applied for the Pixel end-cap discs. Moreover, the PV z coordinate distribution varies from data to MC with a shift in the mean value for MC by -3.0 mm. A weight function is extracted by comparing the distributions in Figure 8.2 (b) giving a mean weight of ~ 0.57.

The results of the hadronic interactions in data are normalised to number of secondary vertices per event (in data) if not stated otherwise. Simulation are,

weighted for the primary vertex position, scaled for the track multiplicity and also normalised the number of vertices per events (in MC).

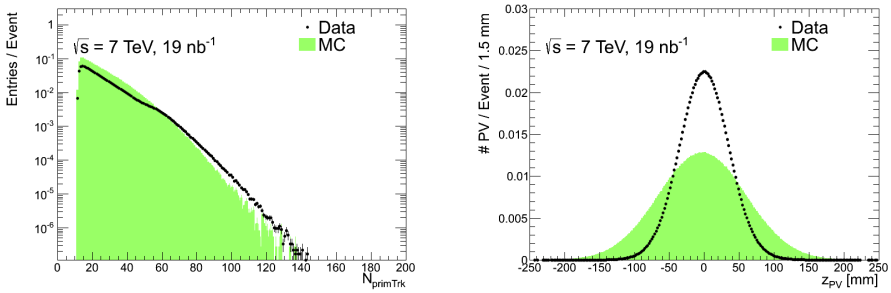

(a) (b)

Figure 8.2.: The number of tracks at the primary vertex for both data and MC (a). The z coordinate of the primary vertex for data and MC (b).

8.7. The Barrel Region - Qualitative Comparison

The excellent spatial resolution mentioned in the chapter introduction, is visualised by the fine details in Fig. 8.3, 8.4 and 8.5 (the xy-view was shown centred on the Pixel and SCT detectors in the detector introductory in Fig. 4.5). These figures show the reconstructed material interactions in data are plotted for different cross sections of the ID. All secondary vertex quality cuts, which will be discussed in Section 8.8 including the mass vetoes on the secondary vertices mentioned in Section 8.5, have been applied. All plots in this chapter, unless states otherwise, will show the secondary vertices remaining after all cuts are applied, since the cuts are designed to isolate the material interactions and eliminate the low quality vertices. For example, in Fig. 8.5 clear details of the composition of the beam pipe are visible, e.g. the increase in vertex density at $r \sim 29$ mm indicates the layer made out of Beryllium. Moreover, the fine structure of the modules in the three Pixel- and the two first SCT (though comparatively faint to the Pixels) barrel layers are visible. Vertices further out than the second SCT layer are expected to have worse resolutions and

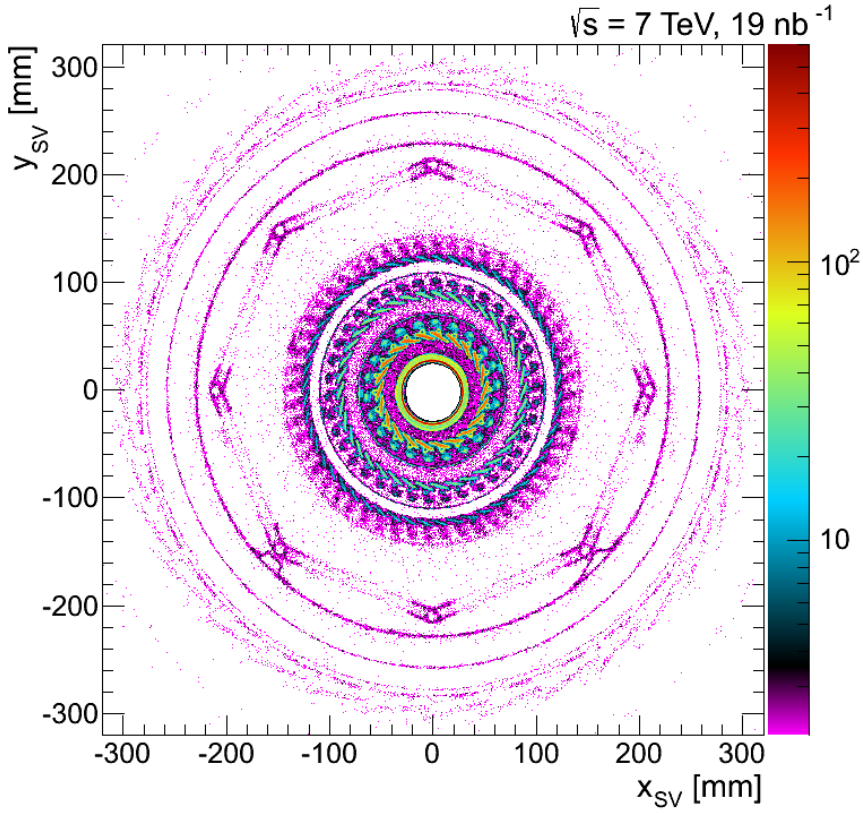

Figure 8.3.: The number of secondary vertices in data after all quality cuts and applied mass veto in the Inner Detector's x-y-plane perpendicular to the beam pipe including all vertices $|z| < 300$ mm. The circles indicated by higher density than their surroundings are going from the most inner to the outer; the beam pipe, the first-, the second-, the third Pixel layers, the Pixel support tube (the hexagon), the first SCT layer, and at the very edge with low statistics is the second SCT layer.

purities due to the lack of silicon hits, these layers are therefore disregarded. The drop in vertices between the Pixel barrel and the Pixel endcaps (Fig. 8.5 at $z\sim$ 400 mm) is due to the transition from applying the fake-removal cri-

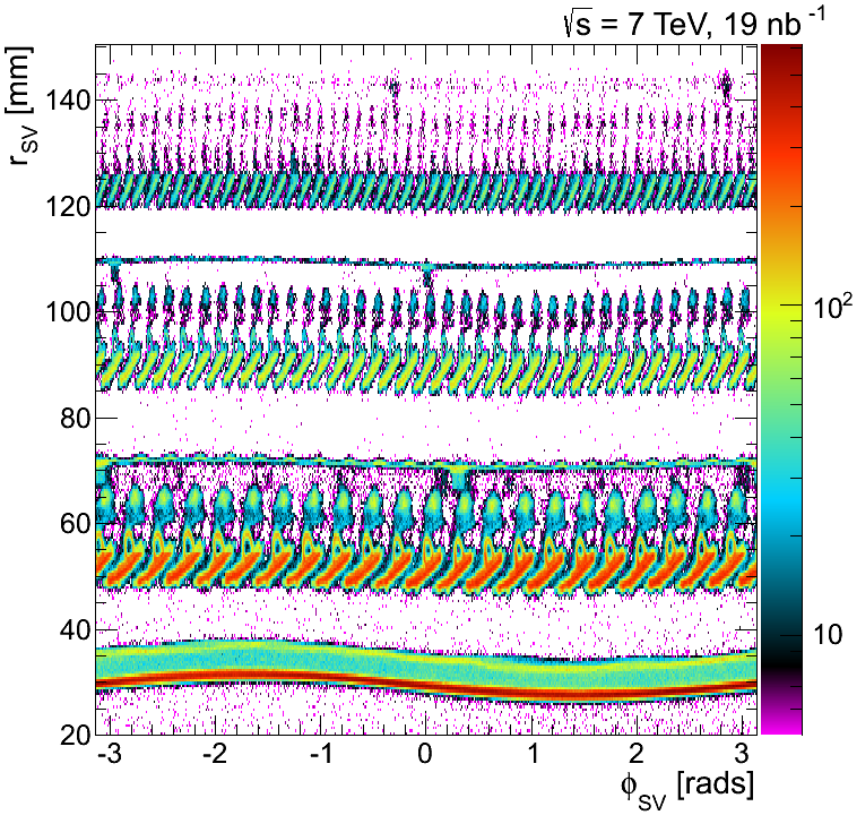

Figure 8.4.: The number of secondary vertices in data after all quality cuts and applied mass veto in the Inner Detector's r-ϕ-plane all vertices $|z| < 300$ mm. The wave-like behaviour of beam pipe and the three Pixel layers are due to the fact that the layers are not centred around [0,0]; the average displacements in x and y are listed in Table 8.3.

teria during vertexing (Section 7.2.2) in the barrel region to only requiring at least one SCT hit in the endcap region. The corresponding geometrical cross-sections of the detector but for the simulated geometry are presented in Fig. 8.6, 8.7 and 8.8.

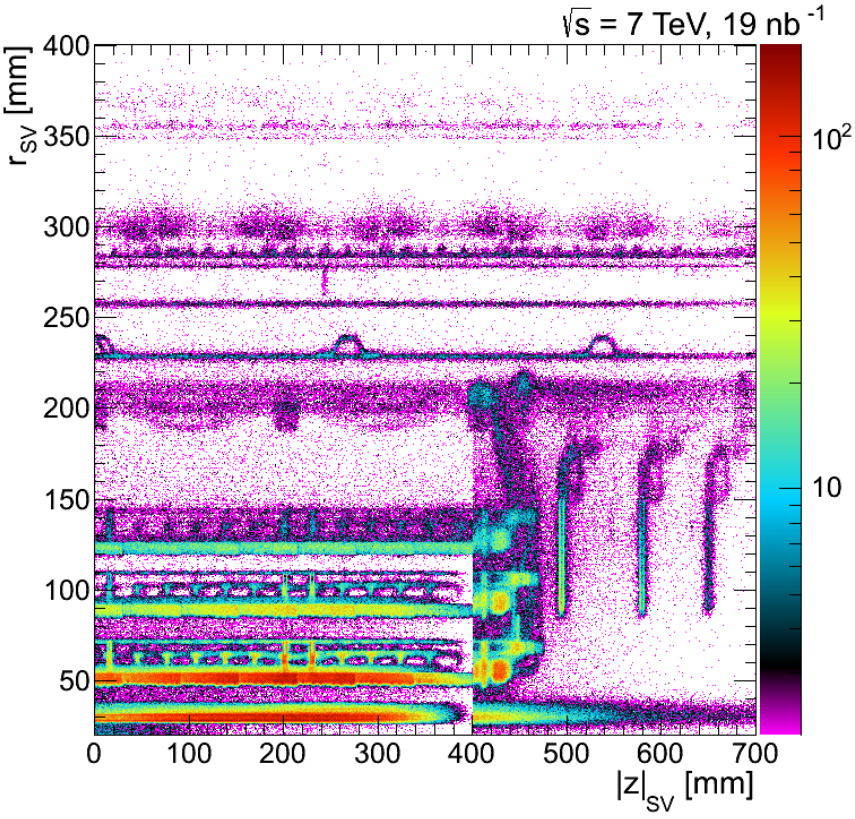

Figure 8.5.: The number of secondary vertices in data after all quality cuts and applied mass veto in the Inner Detector's r-z-plane. The discontinuity of the beam pipe (and the Pixel barrel material layers) going around $|z| \sim 400$ mm is due to change in the fake removal condition going from the region of the barrel to the endcap regions.

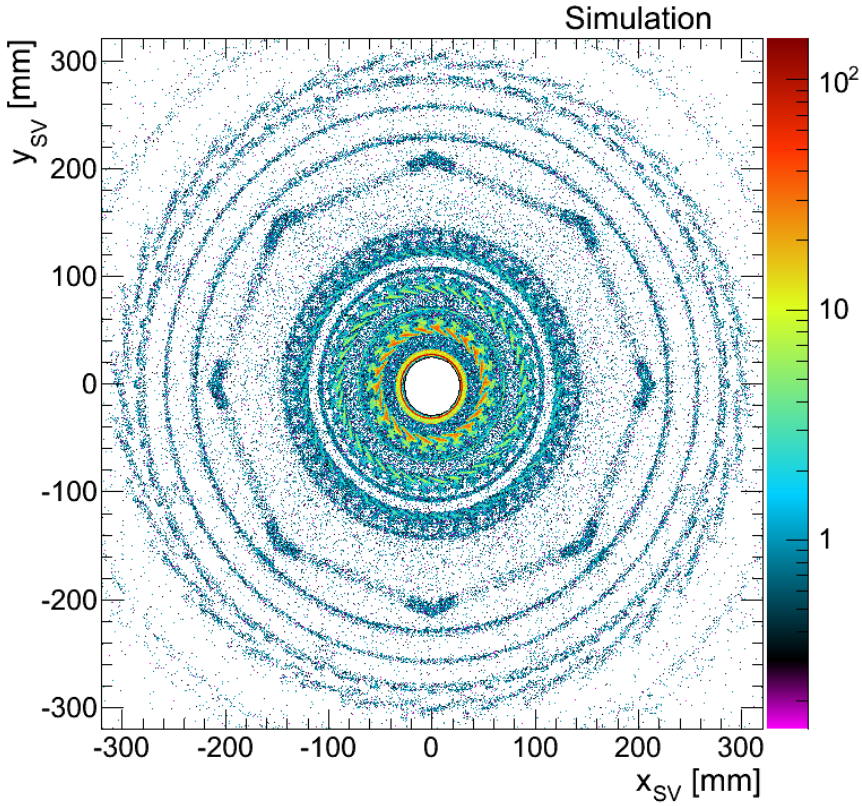

Figure 8.6.: The number of secondary vertices in MC after all quality cuts and applied mass veto in the Inner Detector's x-y-plane perpendicular to the beam pipe including all vertices $|z| < 300$ mm. The circles indicated by higher density than their surroundings are going from the most inner to the outer; the beam pipe, the first-, the second-, the third Pixel layers, the Pixel support tube (the hexagon), the first SCT layer, and at the very edge with low statistics is the second SCT layer.

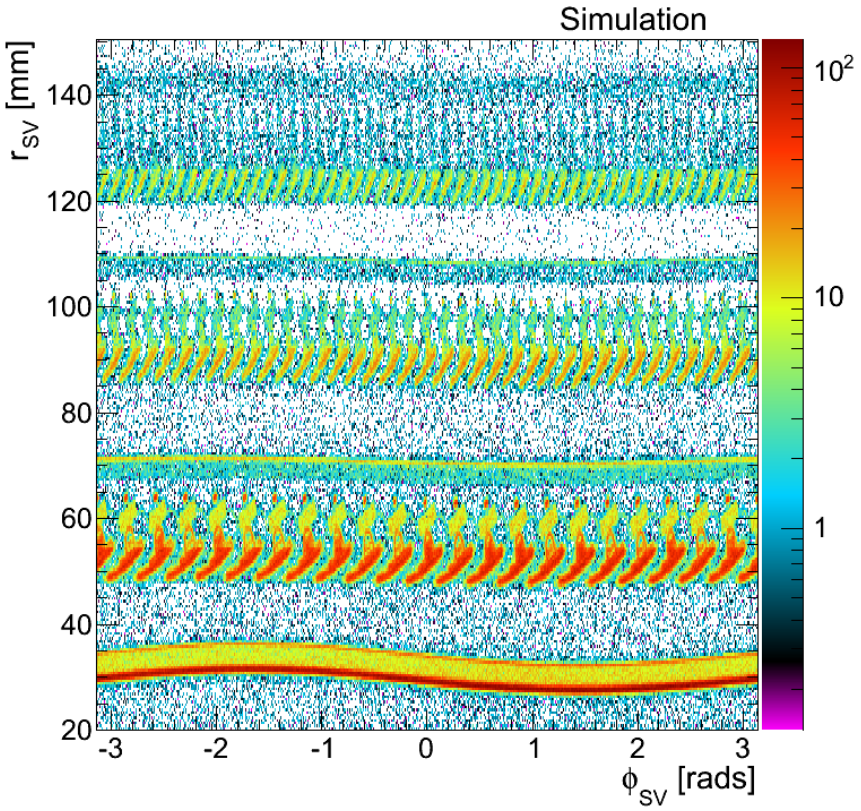

Figure 8.7.: The number of secondary vertices in MC after all quality cuts and applied mass veto in the Inner Detector's r-ϕ-plane all vertices $|z| < 300$ mm. The wave-like behaviour of beam pipe and the three Pixel layers are due to the fact that the layers are not centred around [0,0]; the average displacements in x and y are listed in Table 8.3.

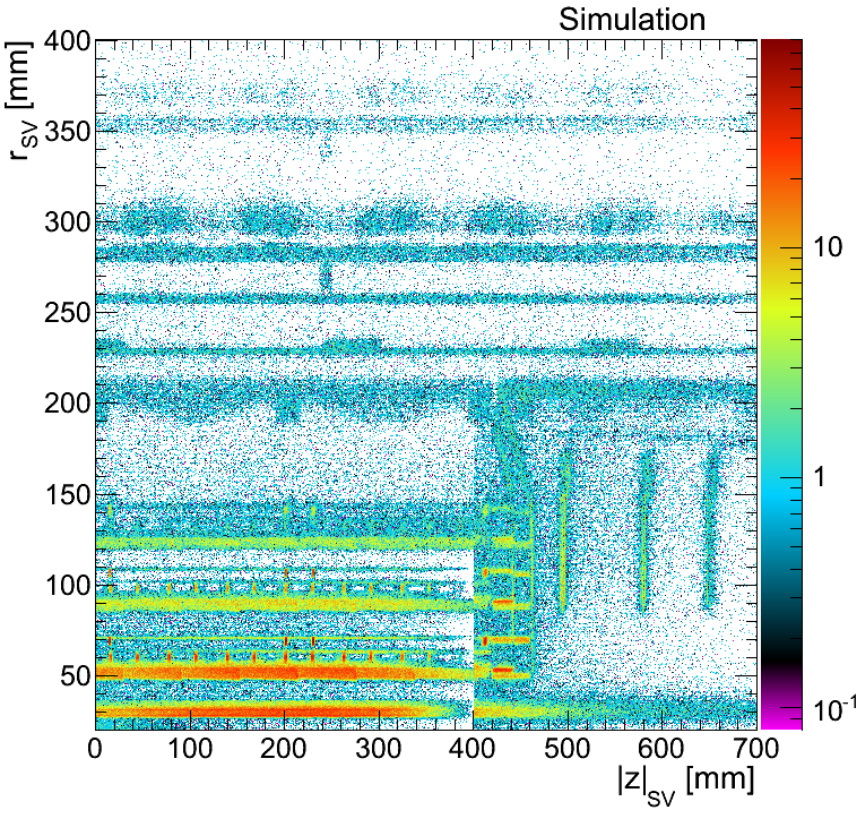

Figure 8.8.: The number of secondary vertices in M after all quality cuts and applied mass veto in the Inner Detector's r-z-plane. The discontinuity of the beam pipe (and the Pixel barrel material layers) going around $|z| \sim 400$ mm is due to change in the fake removal condition going from the region of the barrel to the endcap regions.

The spatial resolution of the position of the secondary vertex is dependent on the quality of the track reconstruction. Vertices at small r will have tracks with more silicon hits and can therefore be reconstructed with less uncertainty. The vertex resolutions are defined as the difference in the reconstructed position r_{reco}, z_{reco} and the real position, generated in the MC r_{truth}, z_{truth}: the resolutions are then $\Delta r = r_{\text{reco}} - r_{\text{truth}}$ and $\Delta z = z_{\text{reco}} - z_{\text{truth}}$. The spectra for each material region of interest are fit with a double Gaussian function for the signal and a polynomial for any background. The resolution is interpreted as the composite sigma ($\sigma = f_{\text{sig1}} \cdot \sigma_{\text{sig1}} + (1 - f_{\text{sig1}}\sigma_{\text{sig2}}$, where f_{sig} denotes the fraction of each Gaussian in the signal and σ_{sig} the σ of the individual Gaussian functions) of the two Gaussian functions. Figure 8.9 shows the fits for the secondary vertices $|z| < 700$ mm for both Δr and Δz for the radial region of the beam pipe. Resolution for $|z| < 700$ mm for all the material layers can be seen in Table 8.1.The vertex resolution for the two regions $|z| < 300$ mm and $|z| < 700$ mm agrees well. No significant drop in vertex resolution in r or z has been indicated as a result of increasing the targeted $|z|$ interval from 300 to 700 from previous analysis. The given resolutions are; Δr and Δz for $r < 300$ mm and $r > 300$ mm are ~ 0.2 mm and < 0.7 mm respectively.

Table 8.1.: The vertex resolution in all material layers for vertices up to $|z| < 700$ mm.

Vertex Radius	$\Delta r = r_{\text{reco}} - r_{\text{truth}}$	$\Delta z = z_{\text{reco}} - z_{\text{truth}}$
Beam pipe (R:28-36 mm)	0.23 mm	0.24 mm
Pixel 1 (R:45-75 mm)	0.22 mm	0.20 mm
Pixel 2 (R:83-110 mm)	0.22 mm	0.26 mm
Pixel 3 (R:118-145 mm)	0.22 mm	0.23 mm
1st SCT (R: 276-320 mm)	0.20 mm	0.23 mm
2nd SCT (R: 347-390 mm)	0.34 mm	0.69 mm

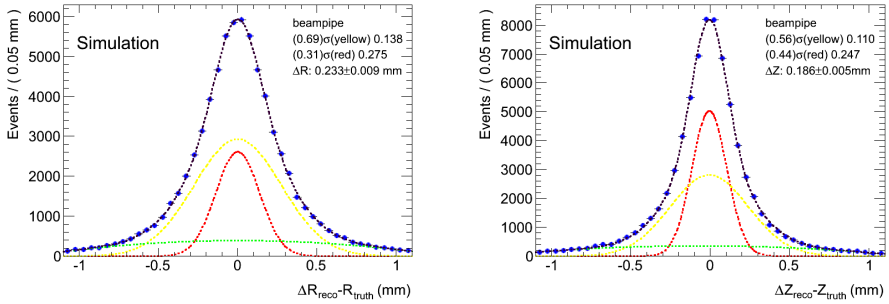

(a) (b)

Figure 8.9.: Double Gaussian fit to the residual of the reconstructed and truth secondary vertex coordinates r (a) and z (b) including all vertices in $|z| < 700$ mm.

8.8. Secondary Vertex Quality Cuts

Re-Tracking has improved the vertex reconstruction efficiency comprehensively for r and z. However, a side effect of Re-Tracking, is the decrease of the secondary vertex reconstruction purity; the material study differs from the Displaced Vertex (DV) analysis in a much lower track p_{T}-cut, which makes it extra sensitive to and prone to reconstruct low quality vertices. The most important purpose of the analysis is to provide precise comparison of data and MC, i.e. a good purity is of the highest priority. The aim is to get a purity for each targeted material layer above, at least 50%. If the purity is less one would then compare a majority of fake vertices which have no meaning. Of course one would want to gain 100% purity but this would require extremely strict cuts, losing all the efficiency for reconstructing secondary vertices. With lower efficiencies the analysis loses its capability to make any quantitative measures of the vertex yields without huge statistical fluctuations.

A few quality cuts on the secondary vertices' tracks have been introduced keep to improve the purity but at the same time keep the efficiency at reasonable values. The following quality cuts are applied:
$|d_0$ w.r.t SV$| < 1$ mm , $|z_0$ w.r.t SV$| < 2$ mm and $\Delta p_{\mathrm{T}}/p_{\mathrm{T}} < 0.05$. The cuts are made after track selection and vertex reconstruction since what is of interest

are the parameters relative to the reconstructed vertex. The entire vertex is discarded, if a track in a secondary vertex is found to exceed the set cut-limits. Secondary vertex track multiplicity is $\sim$ 90% two-track vertices and $\sim$ 10% vertices with higher multiplicity in both data and MC. Therefore, any loss in the efficiency by disregarding three-track vertices is considered minimal and no effort has been made to recover this small drop in efficiency; there is no attempt to re-fit the vertex, even if only one track fails the cuts. The purity p as a result of the quality cuts has improved and brought all material layers up from a minimum of 17% (pre-cuts) to 58% (post-cuts); corresponding to similar values for the layers at $r < 200$ mm as reported in [63], while clear improvements are noted for $r > 200$ mm with up to 30% for the first SCT barrel layer (the second SCT layer was omitted in the referred publication). The completely new region of the three Pixel end-cap discs is also included, where all the discs have purities above 60%. The efficiency ϵ_1 is defined as the vertex reconstruction efficiency incorporating the tracking efficiency (including the vertex quality cuts), whereas ϵ_2 shows the fraction of vertices with two charged tracks and $p_{\mathrm{T}} > 400$ MeV that has been reconstructed (Table 8.2).

Table 8.2.: The secondary vertex purity p, the secondary vertex reconstruction efficiency ϵ_1 and the fraction of reconstructed reconstruct-able vertices ϵ_2 for vertices inside $|z| < 700$ mm.

Layer	Purity p	Efficiency ϵ_1	Efficiency ϵ_2
Beam pipe	84%	8.7 ± 0.02%	78.0 ± 0.1%
Pixel 1	76%	6.0 ± 0.01%	67.0 ± 0.1%
Pixel 2	81%	3.7 ± 0.01%	59.0 ± 0.1%
Pixel 3	68%	2.6 ± 0.01%	50.9 ± 0.2%
PST	73%	2.1 ± 0.01%	42.8 ± 0.2%
SCT 1	77%	1.4 ± 0.01%	36.0 ± 0.2%
SCT 2	58%	0.3 ± 0.01%	7.3 ± 0.1%
Pixel 1 Disk	62%	2.6 ± 0.04%	42.6 ± 0.1%
Pixel 2 Disk	69%	1.7 ± 0.03%	26.8 ± 0.3%
Pixel 3 Disk	66%	0.8 ± 0.02%	14.8 ± 0.3%

The purity and efficiencies are shown for the region $|z| < 700$ mm, although similar values of purity are found for the smaller interval $|z| < 300$ mm, but with slightly higher values due to better z-resolution. The quality cuts reduce the reconstruction efficiency, but due to the increase in the number of vertices from Re-Tracking a surplus of vertices still remains after applied cuts.

The purity and efficiencies are strictly derived from MC and calculated by the following expressions:

$$p = \frac{sv_{\text{Match}}}{sv_{\text{Reco}}}, \quad \epsilon_1 = \frac{sv_{\text{Match}}}{sv_{\text{Truth}}}, \quad \epsilon_2 = \frac{sv_{\text{Match}}}{sv_{\text{Truth2}}} \tag{8.1}$$

where sv_{Reco} is the number of reconstructed secondary vertices after all cuts, sv_{Match} is the number of secondary truth vertices matched to a reconstructed vertex within $\Delta r < r_{\text{min}}$ and $\Delta z < z_{\text{min}}$, where r_{min} and z_{min} varies from 1 mm to 6 mm with r as the vertex resolution changes. At least two truth tracks are required to be matched to the reconstructed tracks with a matching probability greater than 80%. The matching probabilities are assigned based on the number of matched hits on a track. The denominator sv_{Truth} has the value of all truth vertices, that is all simulated vertices identified as an hadronic interaction. While sv_{Truth2} is similarly defined but requires that the truth vertex should also has at least two charged high $p_{\text{T}} > 400$ MeV tracks.

8.9. Qualitative Comparison Data to MC

8.9.1. Barrel

To make a simplistic comparison the vertex yield is plotted versus the r-axis (Fig. 8.10), each material layer is clearly visible as indicated by the increase in vertex density at specific values of r. The MC simulation follows the spectrum of data to great precision, especially for the detector layers; there are slight disagreements corresponding to the simplifications in the model indicated by sharp peaks as well as in the air gaps in between detector layers.

The distribution of secondary vertices for the full z-spectrum shows similarly levels of agreements (Fig. 8.11). Comparison of the beam pipe and five first detector layers over z, further indicates good understanding of the material budget (Fig. 8.12). Disagreements between data and MC are mostly due to the fact that MC simplify geometry structure into a smaller area but with higher density; this yields spikes in MC.

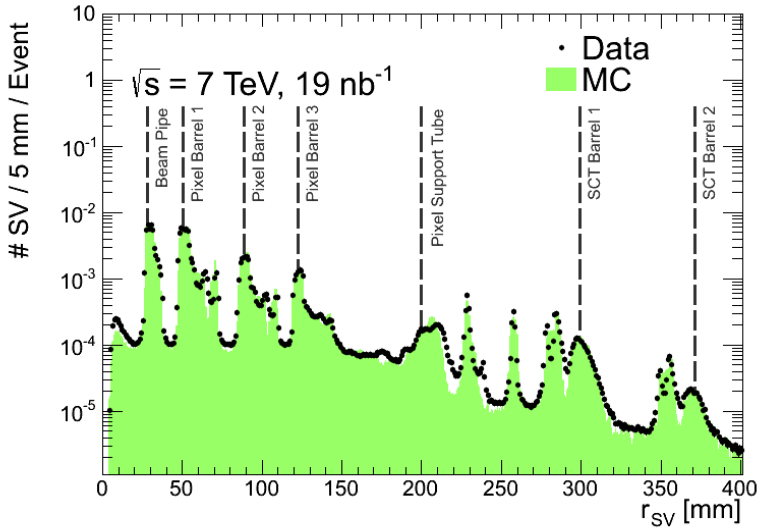

Figure 8.10.: Number of secondary vertices per event versus the r-axis in a region $|z| < 700$ mm after all quality cuts on the vertices. The green histogram is the secondary vertices found in MC while the black points are data. Each peak represents a region with high density of material, as indicated by the text.

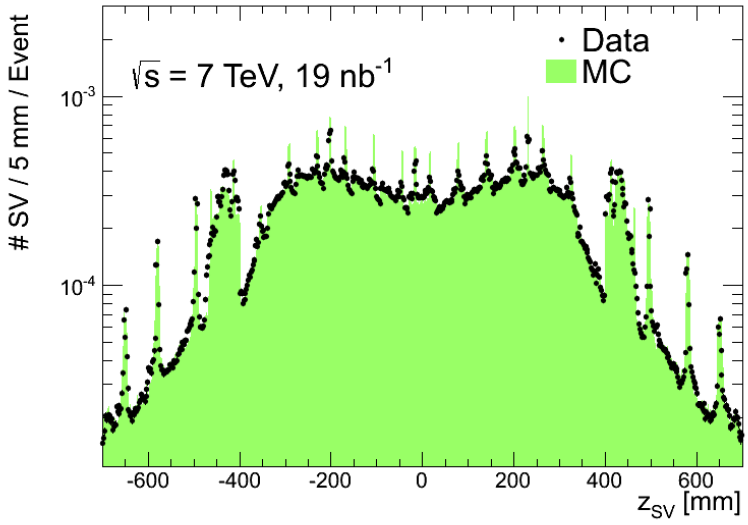

Figure 8.11.: Number of secondary vertices per event versus the z-axis in a region $|z| < 700$ mm after all quality cuts on the vertices. The green histogram is the secondary vertices found in MC while the black points are data. The peaks seen in MC for $|z| < 300$ mm are due to simplification of the support structures. The sudden drop at $|z| > 300$ mm until around 400 mm is the effect of going from one region with applied fake removal to the high η region where only one SCT hit is required. The end of the Pixel barrel and the three Pixel end-cap discs correspond to the four spikes at $z > 400$ mm

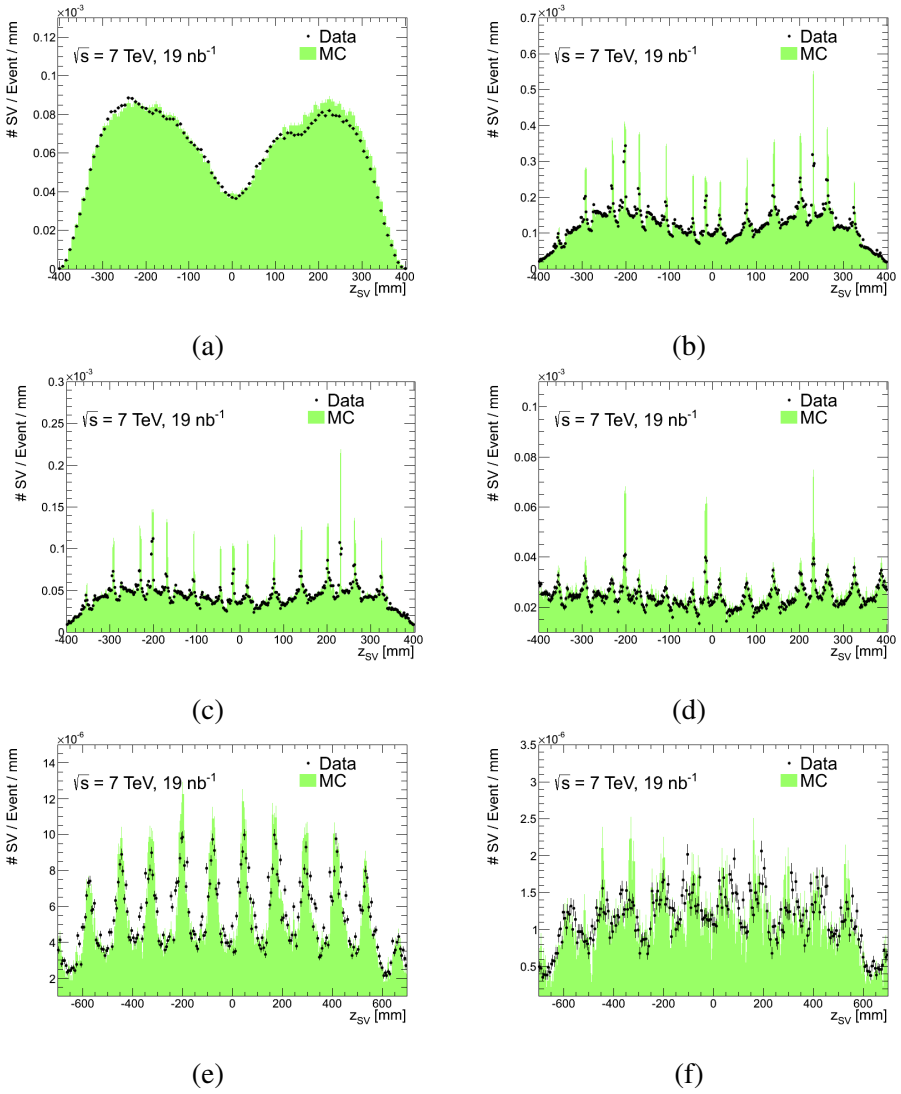

Figure 8.12.: Comparison of the secondary vertices in Data and MC for the six first material layers, the beam pipe (a), the first barrel layer (b), the second Pixel barrel layer (c), the third Pixel barrel layer (d), the first SCT barrel layer (e) and the second SCT barrel layer. MC contains spikes which correspond to simplifications of the material distribution.

8.9.2. Pixel End-Caps

Since the purity in all three Pixel end-cap discs is above 60% (Table 8.2), the material description of the Pixel end-cap discs corresponds well to what is observed in data (Fig. 8.13). To make the comparisons for this exact section of the detector volume, the vertex yield excludes vertices at $r < 50$ mm and $r > 155$ mm; to eliminate including detector parts such as the beam pipe. Discrepancies are observed in the dense cluster of vertices at $z < 470$ mm s(Fig. 8.13) corresponds to the end of the Pixel barrel. Again simplifications in MC give the sharp spikes. The discs in the z-ϕ-plane can be seen in Fig. 8.14 for (a) Data and (b) MC. The Pixel modules on the discs are mounted in periodicity of ϕ with a shift from the front and back side of each disc. The secondary vertex yield for vertices inside $r\sim 80-155$ and for z corresponding to a 15 mm interval around 495 mm are compared (the first end-cap disk). The disc at positive (negative) z is divided up into front and back side Fig. 8.14 (c)-(d) ((e)-(f)). The notable periodical peaks representing higher vertex intensity is located where the active material are present on the discs. That is the sensor modules with the silicon elements. Overall there are good agreements, but the low statistics in the MC sample give large statistical fluctuations at certain peaks. Generally, the back sides of the disc (at larger $|z|$) have more vertices as they have a larger amount of Pixel hits.

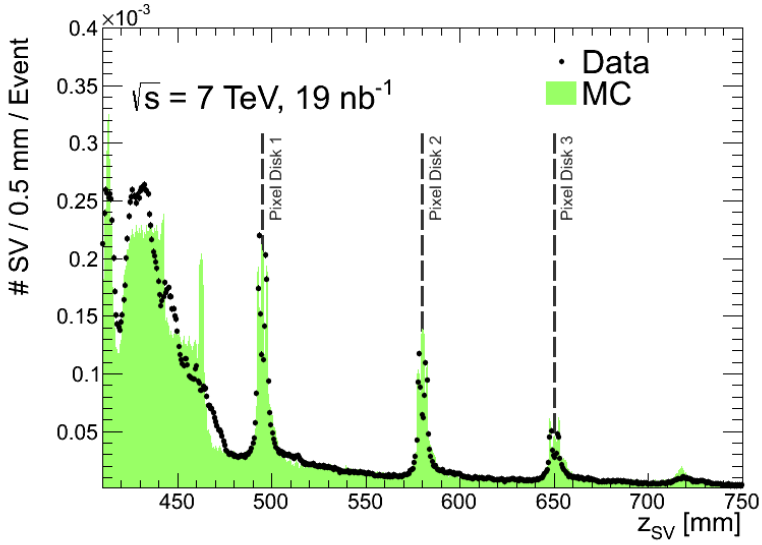

Figure 8.13.: Number of secondary vertices per event versus the z after all quality cuts on the vertices excluding vertices found at $r < 50$ mm and $r > 155$ mm to select the three end-cap discs at $z = 495$, 580 and 650 mm. The vertices at $r < 480$ mm are the structure of the end of the Pixel barrel. The green histogram is the secondary vertices found in MC while the black points are data.

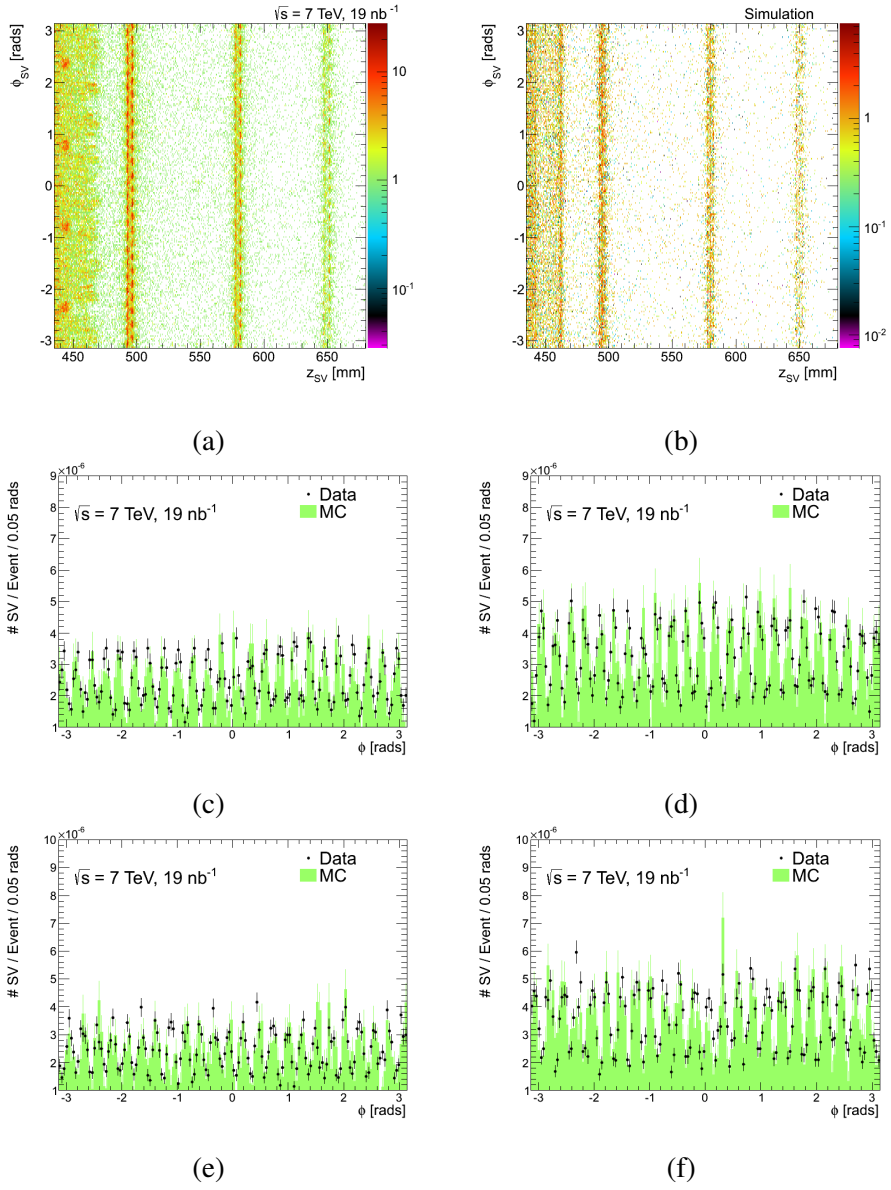

Figure 8.14.: The secondary vertices in Data (a) and (b) are plot in the z-ϕ-plane. The periodical structure of the discs is clear in (a) while low statistics and simplified geometry make (b) less sharp. (c) and (d) are the front and back side respectively of the first Pixel disc at $z\sim$ 495 mm. The same goes for (e) and (f) for the disc at the negative z.

8.9.3. SCT End-caps

Before the quality cuts, the purity in the first and second SCT discs was 7.2 ± 0.2% and 17.6 ± 0.3% respectively. After the quality cuts, the purities have increased for the first SCT disk to 68.6 ± 2.7% and 51.5 ± 3.3% for the second SCT disk. The very low amount of statistics in this region makes it is very difficult to perform any measurements in more detailed studies, especially due to the lack of MC statistics. Figure 8.15 shows the comparison versus the z-axis for Data and MC; any further comparisons are not possible without increasing the vertex reconstruction efficiency at this large z-region.

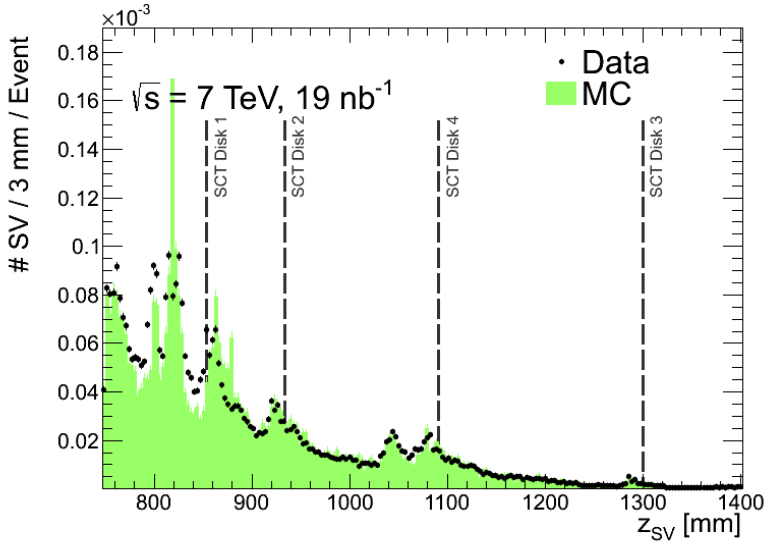

Figure 8.15.: The secondary vertices for Data and MC for the z region larger than 800 mm showing the SCT end-caps.

8.10. Shift of Detector Layers

8.10.1. Pixel Detector

The position of the beam pipe and the three Pixel layers are not perfectly centred around [$x = 0$, $y = 0$] in the detector, but displaced as can be seen by the sinusoidal behaviour of the layers in Fig. 8.4. The projection of the vertices on ϕ for different radial intervals corresponding to the different material layers visualises the periodicity. The complex structure of the detector layers including modules makes it difficult to perform a fit; instead the layers' support structures serve as an average measurement of the displacements. The radial intervals in Fig. 8.16 (a), (b), (c), and (d) are [20, 40], [70, 74], [108, 111], and [140, 147] mm. Sine functions are fit to each interval to estimate the displacement in x and y. Negative shifts of all layers are observed (Table 8.3). The shift in MC agrees within reason to data and has been introduced by shifting the Pixel detector layers position by a layer dependent constant.

Table 8.3.: The various material layers' displacement X and Y in mm from origin, for the four first material layers. Including the mean value for r for each layer. Data are compared with the displacements seen in MC. The values are computed using the fit functions in Figure 8.16.

	Data		
Layer	Mean [mm]	disp x [mm]	disp y [mm]
Beam pipe	30.51	-0.21	-1.90
Pixel 1	71.42	-0.32	-0.50
Pixel 2	109.22	-0.34	-0.46
Pixel 3	143.2	-0.15	-0.16
	MC		
Layer	Mean [mm]	disp x [mm]	disp y [mm]
Beam pipe	30.49	-0.21	-1.93
Pixel 1	70.90	-0.23	-0.32
Pixel 2	108.78	-0.25	-0.35
Pixel 3	142.78	-0.31	-0.18

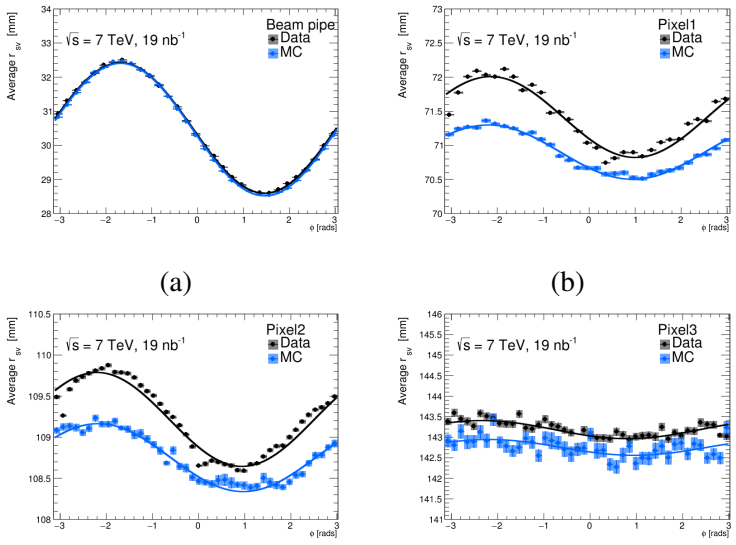

Figure 8.16.: Profile over ϕ for the radial region of the beam pipe (a), first- (b), second- (c) and third (d) Pixel barrel layers Due to the complex structures of the detector layers support structures for each layer are used as an average number for the displacements.

8.10.2. SCT Detector

A zoomed in view over the region of the SCT envelope and the first SCT layer in the R-ϕ-plane indicates that possible deformations exist on the structures (Fig. 8.17) next to a shift. The clearest example is the bumps at various ϕ (ϕ equal to $-1.8, -0.2$ and 1.0) on the envelope surrounding the SCT ($r \sim 258$ mm). The projection of the ϕ-dependency of the SCT envelope, the first and second SCT barrel layer deviate from a pure sinusoidal function (Fig. 8.18 (a), (b) and (c)) and thus confirming that the support structures are

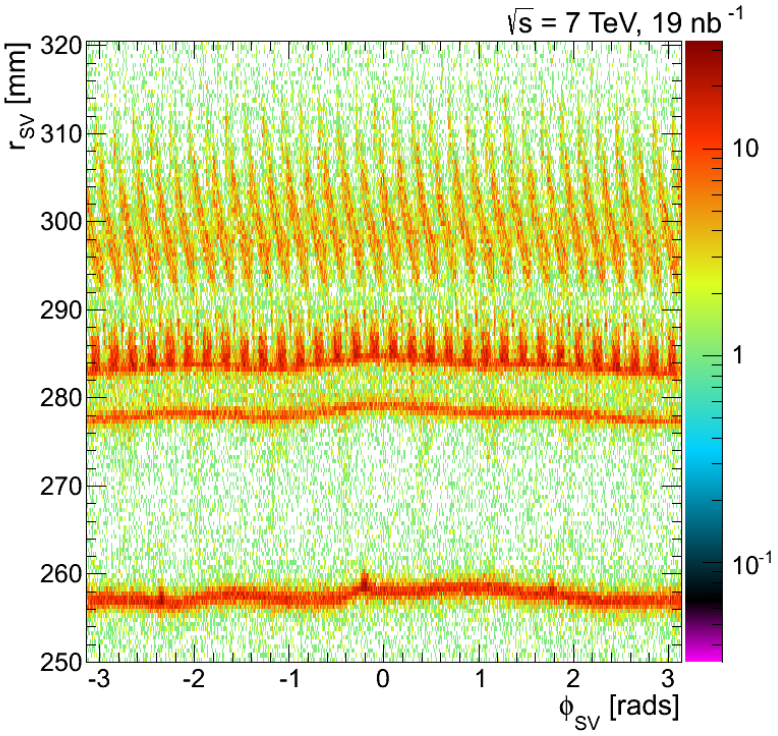

Figure 8.17.: Secondary vertices in data in the r-ϕ-plane for the radial range over the first SCT barrel layer. Clear deformations are visible on the SCT envelope at $r\sim$ 257 mm and of the SCT layer itself at $r\sim$ 280 mm.

somewhat deformed; these projections are for the radial intervals [253, 261], [282, 288] and [346, 351] mm. A maximum radial displacement of approximately 1 mm, 0.8 mm and 1 mm for the SCT envelope, the first SCT layer and the second SCT layer can be noted respectively, with possible deformations of a magnitude of $\sim$ 0.5 mm. MC is slightly shifted, but as the statistics are quite low so unfortunately it is hard to draw any real conclusions.

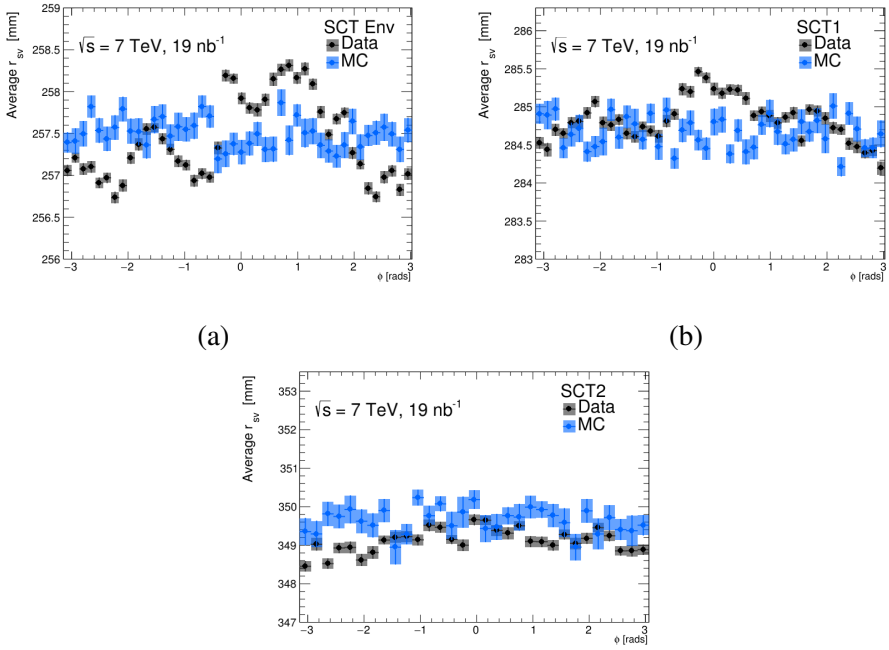

Figure 8.18.: Profile over ϕ for the radial region of the SCT envelope (a), the first- (b) and second SCT layers (c). Due to the complex structures of the detector layers with various overlain modules, support structures for each layer are used instead as an average number for the displacements.

8.11. Pixel and SCT Detector Modules in their Local Coordinate Frames

The detector modules in the barrel are overlapping in r, ϕ and z to give complete coverage of the whole detector volume (Fig. 8.19). However, due to this, the complex structures and low statistics studies of the individual modules proved difficult. Transforming the secondary vertices' global coordinates

x, y and z (and then stack the modules for all ϕ) to the module-specific local coordinate frame provides a powerful tool with which one can study the individual modules in more details. The mentioned transformations have been performed for the vertices in the first five detector layers of the inner detector barrel. The modules from the Pixel- and SCT layers (Fig. 8.20-8.25) will be covered in the following two sections.

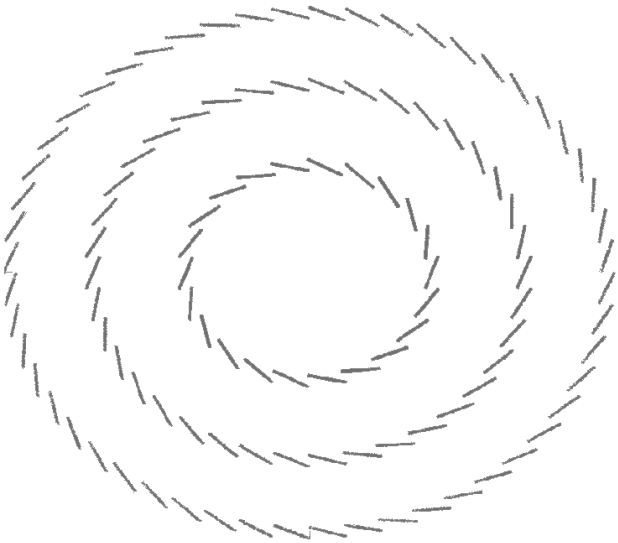

Figure 8.19.: The schematics over the Pixel modules positions in $r\phi$-plane.

8.11.1. Pixel Modules

The benefit of the excellent spatial vertex resolution presents itself again, as minute parts of the detector modules are visible for all the three Pixel layers for both data (a) and MC (b) (Fig. 8.20-8.22). Structural components such as the active Si-element (the highest density of vertices at the bottom of the module), the cooling fluid pipe (indicated as the half-circle on top of the module), and the circular shape a few mm above the main modules are support structures that hold the modules in place in the cylindrical barrel layers (the

position of these structures is a bit shifted in MC compared to data); these features are present in both data (a) and MC (b) in Fig. 8.20-8.22. However, due to the decrease in statistics with increasing r the details of the Pixel modules get degraded and some components fade away going from the first, through the second and to the last layer. The Pixel cooling pipe is made of Aluminium and Kapton, the fluid is Fluorocarbon C_3F_8 chilled to $-25°$

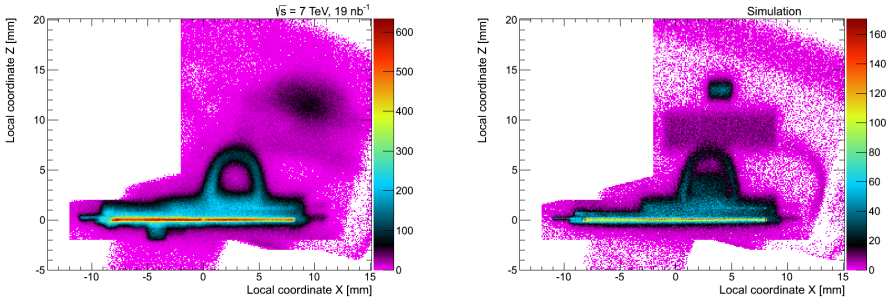

(a) (b)

Figure 8.20.: The local coordinate transformation for Data (a) and MC (b) of the secondary vertices in the first Pixel layer. The high intensity object at the lower part of the module is the active Si-element, the half-circle object at the top side of the modules is the cooling fluid pipe and in the bulk of module certain structures are visible.

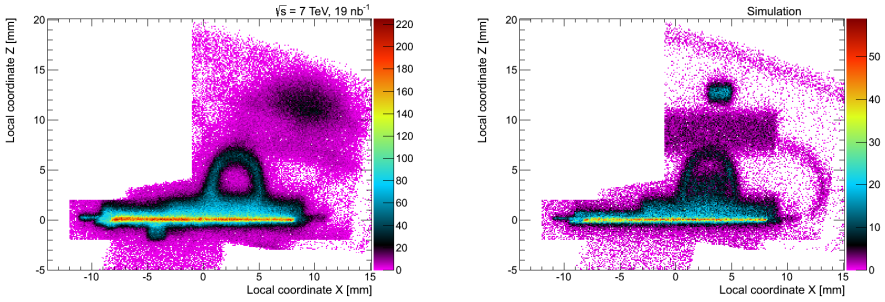

(a) (b)

Figure 8.21.: The local coordinate transformation for Data (a) and MC (b) of the secondary vertices in the second Pixel layer. The high intensity object at the lower part of the module is the active Si-element, the half-circle object at the top side of the modules is the cooling fluid pipe and in the bulk of module certain structures are visible.

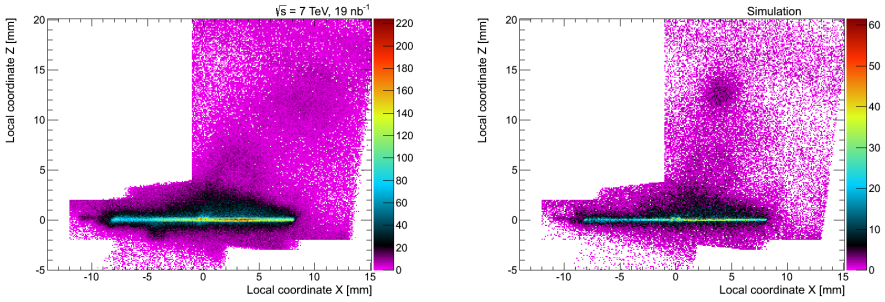

(a) (b)

Figure 8.22.: The local coordinate transformation for Data (a) and MC (b) of the secondary vertices in the third Pixel layer. The high intensity object at the lower part of the module is the active Si-element, the half-circle object at the top side of the modules is the cooling fluid pipe and in the bulk of module certain structures are visible.

Comparing the density of vertices inside the cooling fluid tube for the first Pixel layer for data and MC provides indications that the description of the fluid as the solution flow through the pipe in the geometry was not consistent with data. The flow of the Pixel cooling fluid, as it travels down the cooling stave, in the first Pixel barrel layer, is discontinues in the description in MC. The cooling fluid has input on the negative side of the z-axis, the C side of the detector (0-80 cm) , travels through the cooling stave along the z-axis to the positive side of, the A side, and back to the C side (80-160 cm) in a full 160 cm (Fig 8.23 (a)). There is a sudden drop in the vertex density as the fluid travels back from A to C. Figure 8.23 (b) visualises this by dividing the z-axis into 12 intervals for z $[-300, 300]$ mm and counting the vertex yield in a box inside the Pixel fluid cooling pipe. The yield is normalised to the number of vertices in the bulk of the modules as well as to the yield in the first bin (this bin is therefore one by definition). There is a notable drop in the density as the fluid turns, at $\sim$ 80 cm.

Moreover, the total amount of the fluid is three times higher in MC than data with 0.003 respectively 0.001 number of vertices found inside the tube per event. Except the observed differences in the cooling fluid good agreement is seen in the active Si-element for the Pixel (and the SCT) modules with a ratio data to MC close to one.

8.11.2. SCT Modules

A precise study of the SCT modules was not feasible in the preceding analysis due to the low vertex reconstruction efficiency at large r. After the improvements to the vertex reconstruction purity and efficiency, similar detailed comparisons, as for the Pixel modules, are possible for both the SCT barrel layers. However, the second layer is somewhat limited by statistics (Fig. 8.24-8.25); data (a) is more clear as there are more vertices in total than in MC (b). The horizontal section around $Z \sim 0$ mm spanning X $[-30,\ 30]$ mm is the SCT module. The SCT envelope and support rings ($Z \sim -38$ mm and $Z \sim 15$ mm) are thicker in data than in MC (made by Carbon Fiber Reinforced Plastic honeycombs). The reason for this is the deformations, present in data but not in MC, of the structures (Fig. 8.17) making the radial coordinate non-constant

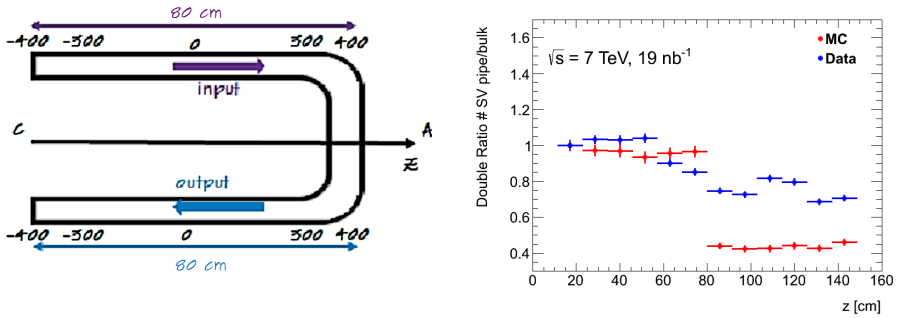

(a) (b)

Figure 8.23.: The flow of the cooling fluid has input on the C side of the detector (0-80) cm, travels through the cooling stave to the A side and back to the C side (80-160) in a full 160 cm (a). The ratio of secondary vertices in the cooling fluid tubes divided in intervals of z and is shown for the whole length of the bistave in (b) however due to the limitation of the analysis only the z interval up to $|z| < 300$ mm is considered so the total interval is not 180 cm but 120 cm.

for all ϕ. Parts connecting the module to the support frames are seen to the right between the module and the support frame. Finally, the most upper part indicates the cooling tube. Similarly for the Pixel modules, comparison of the vertex yield per event for the SCT modules shows good agreement for the first layer with a ratio data to MC (Section 8.13). The cooling fluid in the SCT is, like in the Pixel detector, Fluorocarbon C_3F_8

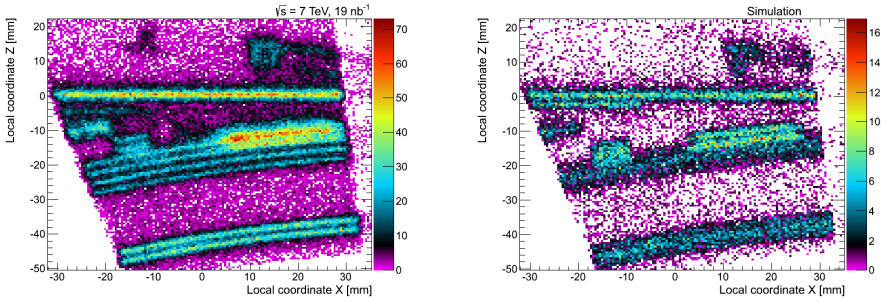

(a) (b)

Figure 8.24.: The local coordinate transformation for Data (a) and MC (b) of the secondary vertices in the first SCT layer. The flat element in the upper part is the module itself, the structure right above the module is the cooling fluid pipe and the circular sectors at the lower parts are support structures.

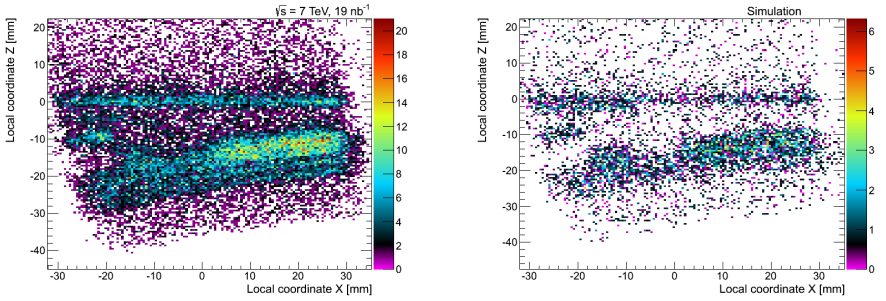

(a) (b)

Figure 8.25.: The local coordinate transformation for Data (a) and MC (b) of the secondary vertices in the second SCT layer. The flat element in the upper part is the module itself, the structure right above the module is the cooling fluid pipe and the circular sectors at the lower parts are support structures.

8.12. Systematic Uncertainties

A weakness of this analysis is that one has to rely on how well the hadronic interactions are understood and simulated in GEANT4. The analysis is also more or less dependent on that the knowledge of the primary particle composition is generated well in Pythia. A major part of uncertainty comes from that the secondary vertices are reconstructed using the charged particle tracks, where the largest uncertainty in track reconstruction comes from just material uncertainties. This somewhat circular problem is by-passed by taking a conservative estimate on the systematic uncertainty related to the tracking reconstruction as it is hard to assess the tracking uncertainty **without** including material uncertainties. There are several other sources of uncertainties as well related to e.g. cut criteria and all of them will be brought up in the following sections.

8.12.1. Tracking Efficiency

The major part of the systematic uncertainty to the analysis comes from the tracking reconstruction efficiency that is directly dependent on the material description. An increase in material leads to an increase in the number of hadronic interactions, i.e. a reduction in the track reconstruction efficiency. An estimate of the systematic uncertainty from the tracking efficiency is therefore not straight forward.
In general the tracking reconstruction is simulated well in MC, but this analysis is affected by the secondary track reconstruction which is less understood. The K_S method has been devised to explore the systematics from the secondary track reconstruction efficiency. The $\pi^{\pm}$ created in K_S-decays probes the material in similar ways as particles created in hadronic interactions. Decays of K_S provides a source of tracks that are independent on the hadronic interaction rate.

Two-track vertices within a window around the nominal mass of the K_S are considered. A double Gaussian function, for the signal, and a one degree polynomial, for the background, are fitted to the K_S yield. The number of

reconstructed K_S in data and in MC are counted. Since the production rate of K_S is not known, the yields are normalised to the yield inside the beam pipe at small r. A difference seen in the amount of reconstructed K_S in data and MC is assumed to come from the systematic uncertainty in the tracking efficiency. The double ratio (8.2) are computed for various decay lengths.

$$\frac{\text{Number of } K_S\text{(data)}/\text{Number of } K_S \text{ inside the beam pipe(data)}}{\text{Number of } K_S\text{(MC)}/\text{Number of } K_S \text{ inside the beam pipe(MC)}} \tag{8.2}$$

The total momentum distribution of the K_S in data and MC agrees well, otherwise the comparison would not be feasible without applying reweighting of various spectra. Figure 8.26 shows the double ratio of K_S in data to MC for different proper decay lengths. The maximum deviation from one is taken as the systematic uncertainty due to the tracking efficiency for a two-track vertex (a ratio of one would correspond to a perfect match of the track reconstruction). The inefficiency to reconstruct K_S, $(1 - \epsilon_{K_S})$ as a function of the track reconstruction inefficiency $(1 - \epsilon_{\text{trk}})$ can be calculated as in Eq. 8.3. Taking the estimate to the first order yields that the tracking inefficiency is half of the inefficiency in reconstruction K_S.

$$(1 - \epsilon_{K_S}) = 2 \times (1 - \epsilon_{\text{trk}}) - (1 - \epsilon_{\text{trk}})^2 + \ldots \tag{8.3}$$

Therefore, the maximum deviation at 3.6% translates to a systematic uncertainty of $\sim 1.8\%$ per track. The same method used in 2010 yielded a systematic uncertainty of $\sim 2.85\%$ per track; the values are compatible. Randomly removing tracks of a factor of 1.8% during the vertex reconstruction gives a reduction in the number of secondary vertices by 4.7%; this value is taken as the systematic uncertainty from the tracking efficiency for the hadronic interaction vertex yields.

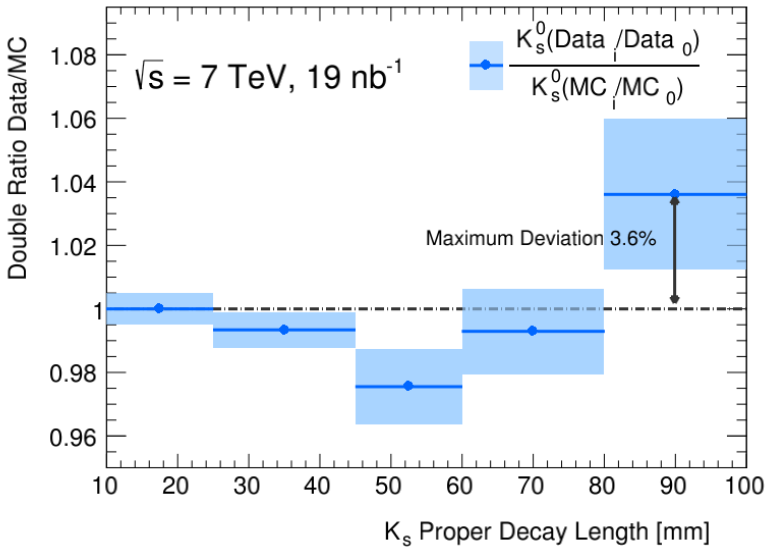

Figure 8.26.: The double ratio (Equation (8.3)) of K_S found in between material layers at different distances of proper decay lengths in mm.

8.12.2. Selection Critiera during Vertex Reconstruction

The systematics arising during the process of vertex selection come from the following sources: the χ^2 cut on the vertex fit, the merging of close lying vertices and the requirement that a track can only be used to form one vertex. The systematics from these sources are found to be less than 1% [63]. With the updated setup of the current analysis the systematics are estimated to be of the same magnitude. The vertex selection algorithm has not changed since 2010, which is reflected in the same level of systematic uncertainties.

8.12.3. Other Sources

A cut on the track multiplicity at the primary vertex is made in order to select non-diffractive events in data. The cut eliminates the major part of the

diffractive event contaminations, but $<\sim$ 1% of the events still remain. Increasing the cut should have no other effect on the non-diffractive MC sample than a reduction of statistics, while the reduction of vertices in data is due to the contamination as well as the statistical reduction. The difference in the change is taken to be the systematics and a factor of $\sim$ 0.3% is assigned to this source.

A systematic uncertainty of 1% is assigned to the process involving the correction of MC for the number of primary tracks for excluding to account for hadron interactions caused by secondary tracks. The corrections method does not include the contribution of neutral hadrons such as neutrons and K_S either. However, since the production rate of neutral hadrons is less than the rate for protons and $K^{\pm}$ and corrections are being made for these charged hadrons; the contribution from neutral particles is believed to be small. An effect could also arise from the fractions of particle species being incorrectly simulated in PYTHIA, but this is expected to be small.

8.12.4. GEANT4 Modelling

The modelling of hadronic interactions in GEANT4 could potentially yield uncertainties on the data to MC comparisons. The secondary tracks created when particles interact with matter provide a direct channel to probe the modelling in MC which can easily be compared with what is observed in data. To simulate hadronic interactions correctly, it is necessary to understand how particles interact with matter. However, these effects are not trivial but rather dependent on several factors such as the interaction length λ_0 of the material. Selecting structures composed, to the majority, of a single material facilitate comparisons and makes the comparisons easier to interpret. Comparing simulated properties of the secondary tracks emerged from hadronic interactions to the ones reconstructed in data, makes it possible to directly scrutinize the modelling in GEANT4. Moreover, studying specific attributes of the hadronic interaction vertices such as the total momentum, the opening angle between the tracks and fraction of momentum of the leading track makes it possible to disentangle effects and angular dependencies. To get a thorough understanding of the effect, in addition to the nominal MC sample a second MC sample with

a different physics list is compared to data. The nominal sample is simulated using FTFP_BERT while the additional sample uses QGSP_BERT. These two physics models possess the same descriptions of pions at low energies up to $\sim$ 5 GeV but varies at higher energies. The summation of momentum of the tracks in the hadronic interactions exhibits superior agreement with data for the FTFP_BERT physics list, while QGSP_BERT diverges at $p_{\mathrm{T}} > 5$ GeV (Fig. 8.27).

Table 8.4.: The Scalar summation of momentum for the secondaries $\Sigma|\bar{p}|$, the fraction of momentum of the leading tracks $|p_{\mathrm{leadtrk}}|/\Sigma|\bar{p}|$ and the opening angle between the two leading tracks θ_{Op} are compared data to two MC samples, using FTFP_BERT and QGSP_BERT physics lists. The weighted average for the ratio Data/MC is listed for secondaries from interactions both in beryllium and silicon. For FTFP_BERT the largest deviation from one is seen at silicon for the θ_{Op}.

Secondaries Properties	Element	Data/QGSP_BERT	Data/FTFP_BERT
$\Sigma\|\bar{p}\|$	Be	0.952 ± 0.003 (stat.)	0.997 ± 0.002 (stat.)
$\|p_{\mathrm{leadtrk}}\|/\Sigma\|\bar{p}\|$	Be	0.973 ± 0.003 (stat.)	0.987 ± 0.002 (stat.)
θ_{Op}	Be	0.977 ± 0.003 (stat.)	0.976 ± 0.002 (stat.)
$\Sigma\|\bar{p}\|$	Si	0.988 ± 0.004 (stat.)	0.993 ± 0.003 (stat.)
$\|p_{\mathrm{leadtrk}}\|/\Sigma\|\bar{p}\|$	Si	0.981 ± 0.004 (stat.)	0.981 ± 0.003 (stat.)
θ_{Op}	Si	0.963 ± 0.004 (stat.)	**0.971 ± 0.003** (stat.)

Furthermore, in addition to the momentum, the fraction of momentum carried by the leading track and the opening angle between the two leading momentum tracks are compared for the two elements (Table 8.4). The maximum observed deviation from data is taken as the systematic uncertainty due to the modelling in GEANT4. The nominal sample (FTFP_BERT) shows a deviation of 3% on the weighted average for the opening angle in silicon.

8.12.5. Total Systematic Uncertainty

Factoring in all sources of systematic uncertainties, the total value is found to be 5.0% to the vertex yield ratio.

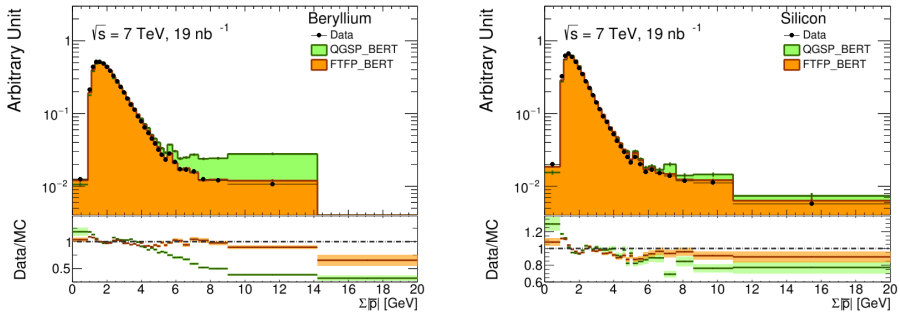

(a) (b)

Figure 8.27.: The scalar sum of the momentum for the secondary particles from hadronic interactions found in the beryllium part of the beam pipe (a) and in the silicon element in the Pixel modules (b). Two physics lists are compared to data, with superior agreement for FTFP_BERT.

8.13. Results

Comparing the vertex yield of reconstructed secondary vertices in data and MC is a straight forward way to get a quantitative measurement on how well the material is simulated in MC (Table 8.5). The amount of reconstructed secondary vertices in the beam pipe, the three Pixel layers, the Pixel support tube, the two first SCT layers, and the three Pixel end-cap discs are counted. All secondary vertex quality cuts have been applied before the vertex yields are calculated. A correction factor is multiplied to the vertex yield in MC to match the data primary track multiplicity. The vertex yield in MC is also reweighted to account for differences seen in the z-coordinate of the primary vertex spectrum (summarised in Section 8.5). The ratio of the vertex yield data to MC can be seen in Table 8.6 for two intervals of maximum $|z|$. As one increases the z-region one gets more secondary vertices in data than MC. This can be explained by differences seen in the material map at regions close to the Pixel endcaps, where the geometry used in simulations portrays simplifications of the material. The simple structure of the beam pipe and the beryllium part of the beam pipe seem to be well understood and the secondary vertex yield

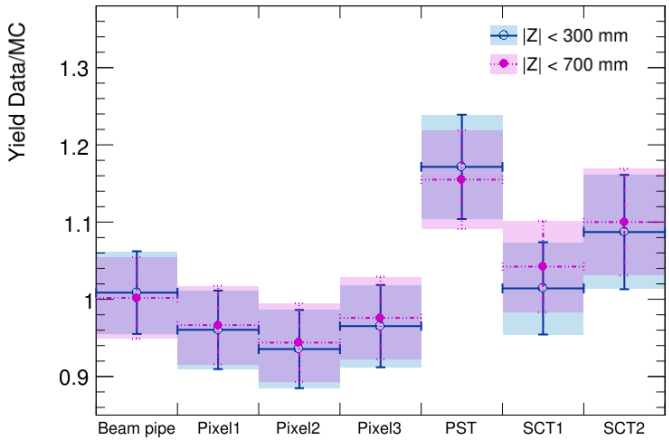

Figure 8.28.: Ratio of the secondary vertex yield, data over MC. The blue points include all vertices inside $|z| < 300$ mm and the purple point the larger region $|z| < 700$ mm. All quality cuts on the secondary vertices have been applied. The errors include both the statistical- and systematic uncertainties on the vertex yields and are dominated by the latter.

ratio in these two radial regions are 1.009 ± 0.002 (stat.) $\pm$ 0.051 (syst.) and 1.03 ± 0.003 (stat.) $\pm$ 0.052 (syst.) respectively ($|z| < 300$ mm).
Comparing an old geometry from 2010 with a much newer tag shows that the changes in MC have yielded a decrease in vertices as r increases (Fig. 8.29). However, the discrepancies observed, may not only come from pure differences in the geometry, but from the fact that the complex process of simulating the hadronic interactions might not be perfectly understood and might cause the amount of reconstructed secondary vertices to differ.

The yields at the different material layers for the barrel layers can be seen in Figure 8.28. The major part of the errors seen is the systematic uncertainties discussed in Section 8.12. The statistical errors are small due to Re-Tracking and the increased number of vertices. Table 8.7 lists the yield in the silicon element of the detector modules in the first five barrel layers using the local

Table 8.5.: Raw secondary vertex yield for the material layers in the barrel region from 28 mm to 390 mm, listed for both $|z| < 300$ mm and $|z| < 700$ mm without any normalisation to account for the difference number of events in data and MC.

Vertex Radius	Vertex Yield Data		Vertex Yield MC	
	$\|z\| < 300$ mm	$\|z\| < 700$ mm	$\|z\| < 300$ mm	$\|z\| < 700$ mm
Beam pipe (R:28-36 mm)	117613	1336770	380669	435552
Pixel 1 (R:45-75 mm)	1451600	1702620	471861	548695
Pixel 2 (R:83-110 mm)	475998	578227	158883	190863
Pixel 3 (R:118-145 mm)	245078	332184	79203	106272
PST (R:225-250 mm)	103542	250228	28846	70716
SCT 1 (R: 276-320 mm)	64246	135185	20425	41885
SCT 2 (R: 347-390 mm)	13984	28760	4122	8403
Pixel 1 Disc		48276		201647
Pixel 2 Disc		27219		14929
Pixel 3 Disc		11765		8847
Total	**3530578**	**4363974**	**551189**	**676790**

coordinate transformations in Section 8.11; these yields agree with the total yield for the entire layers.

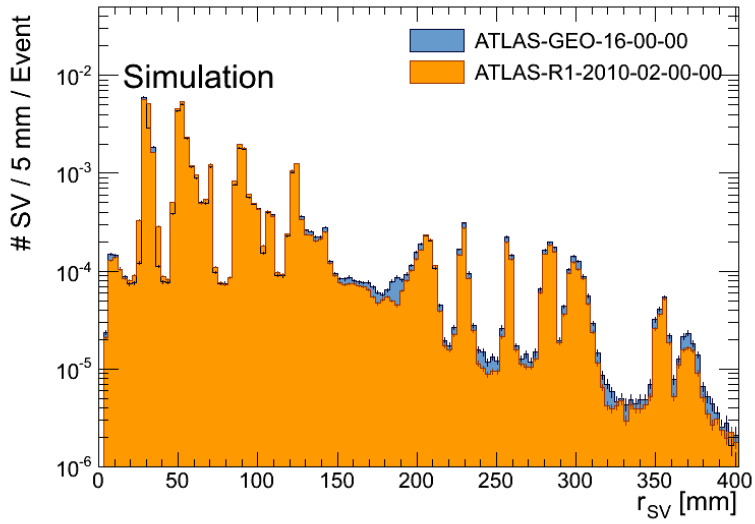

Figure 8.29.: The radial distribution for two different geometry tags, the blue histogram is the older ATLAS-GEO-16-00-00 which was used in the previous study. The orange histogram is the MC used in this note with the newer geometry tag ATLAS-R1-2010-02-00-00.

Table 8.6.: Ratio of secondary vertex yield Data to MC for the material layers in the barrel region from 28 mm to 390 mm for both of the z-regions.

Vertex Radius	Vertex Yield Data/MC	
	$\|z\| < 300\ mm$	$\|z\| < 700\ mm$
Beam pipe (R:28-36 mm)	1.009 ± 0.002 (stat.) ± 0.046 (syst.)	1.002 ± 0.002 (stat.) ± 0.046 (syst.)
Pixel 1 (R:45-75 mm)	0.960 ± 0.002 (stat.) ± 0.044 (syst.)	0.967 ± 0.002 (stat.) ± 0.044 (syst.)
Pixel 2 (R:83-110 mm)	0.936 ± 0.003 (stat.) ± 0.045 (syst.)	0.944 ± 0.003 (stat.) ± 0.043 (syst.)
Pixel 3 (R:118-145 mm)	0.965 ± 0.004 (stat.) ± 0.047 (syst.)	0.976 ± 0.003 (stat.) ± 0.045 (syst.)
PST (R:225-250 mm)	1.172 ± 0.007 (stat.) ± 0.054 (syst.)	1.155 ± 0.005 (stat.) ± 0.053 (syst.)
SCT 1 (R: 276-320 mm)	1.014 ± 0.008 (stat.) ± 0.047 (syst.)	1.042 ± 0.006 (stat.) ± 0.048 (syst.)
SCT 2 (R: 347-390 mm)	1.087 ± 0.018 (stat.) ± 0.051 (syst.)	1.100 ± 0.013 (stat.) ± 0.051 (syst.)
Pixel 1 Disc		1.060 ± 0.010 (stat.) ± 0.049 (syst.)
Pixel 2 Disc		1.011 ± 0.012 (stat.) ± 0.047 (syst.)
Pixel 3 Disc		0.984 ± 0.018 (stat.) ± 0.046 (syst.)
Average	**0.097 ± 0.002 (stat.) ± 0.043 (syst.)**	**0.985 ± 0.002 (stat.) ± 0.045 (syst.)**

Table 8.7.: The vertex yield Data/MC for the silicon element of the Pixel and SCT modules counted by the use of the local coordinate transformations.

Module Layer	Local coordinate transformations Vertex Yield Data/MC
Pixel 1	0.999 ± 0.003 (stat.) ± 0.046 (syst.)
Pixel 2	0.945 ± 0.004 (stat.) ± 0.044 (syst.)
Pixel 3	0.957 ± 0.006 (stat.) ± 0.044 (syst.)
SCT 1	1.029 ± 0.011 (stat.) ± 0.047 (syst.)
SCT 2	1.035 ± 0.030 (stat.) ± 0.048 (syst.)

9. Event and Vertex Selection

A small caveat to consider before reading this chapter. The event selection process for the displaced vertex analysis has been continuously developed and follows similar patterns as for the previous publications for the DV + μ channel [60–62]. Already mentioned previously, the latest paper [5] includes the DV+jets channel reviewed in this thesis. While the selection requirements have been thoroughly documented internally in A Toroidal LHC ApparatuS (ATLAS) through the years, the papers do not cover the selection criteria in great details for obvious reasons. This chapter goes through the selection criteria (Section 9.1) of the DV + jets channel and the related systematic uncertainties for each cut (Section 9.3), most of which have been documented in these internal notes. The methods therefore, will not be uniquely developed and optimised for this thesis. It rather, should be read as the collected results of a group effort, ongoing during the years the displace vertex analysis has been active at the ATLAS Experiment. The numbers and figures are produced for this thesis, if not stated otherwise through references.

Searching for a specific type of physics process means scanning millions of collision events. In this specific case it's all the data recorded during 2012 by the ATLAS detector. The data are scanned for event topologies which could correspond to the interaction of interest. Event cuts and various object selection criteria are designed to find the events, which have a potential to be the type of events that are the target of the searches. Typically, the signal significance is the main focus; the amount of signal to background events. For example, a very high cut on the missing energy of an event sorts out a large fraction of any type of Standard Model (SM) background events. However, it is not as simple as that, often the searches are limited not only by the signal

selection process, but by technical issues such as available cpu power or even constrained amounts of disk space. The event selection process is divided up in two steps, the first is the pre-selection that aims to reduce the rate of events and thereby the technical issues as cpu-power demands and disk space constraints. Section 6.1.1 contains the explanation of the pre-selection triggers and cuts. The second step focus more on the signal significance by e.g. applying physics object cuts, this step is reviewed in Section 9.1. Both steps have to be integrated and all factors have to be optimised at the beginning when the analysis methods are decided upon. This whole chapter is structured to take the reader through the selection process, including in the latter more specific event and vertex selection criteria. They are reviewed in the order they are applied, giving motivation at each step; event selection, primary vertex selection, and displaced vertex selection. The selection criteria are followed by a summary of the systematics uncertainties associated with the course of the selection criteria and object reconstructions. The signal efficiencies and the cross-section limits will be given as a function of $c\tau$ made possible through the τ-reweighting (Section 6.7).

9.1. Event Selection

Standard ATLAS data quality guidelines sort out low quality events; this can happen for instance if there are high levels of noise in one of the subdetectors or if the recorded signals from just that event have been corrupted. Events marked to have a noise burst in the Liquid Argon calorimeter (see Section 4.2.2); a noise burst can be identified when a large number of channels in the calorimeter gives off a signal but with a bad measured shape (Section 7.3). These are signals down to technical effects by the detector mechanics, but only occur during collisions. Events are also vetoed, if they have suffered from data corruption or if one of the calorimeter tiles, the hardware, has been marked to be corrupted.

Furthermore, events are removed if they are found to have a jet object classified as a bad jet. These cuts are designed to identify bad jets reconstructed

from noise in the calorimeter end-cap, noise in the electromagnetic calorimeter or jets from non-collision backgrounds. Events are also vetoed, if a jet position is too close to a region of the calorimeter marked as inefficiency or not working. Details of these cuts won't be reviewed in detail in this thesis as they are technical and won't provide the reader with any useful information. However, they are mentioned to show that the proper actions are taken to ensure good data quality (these cuts remove less than 1% of the total number of events).

Finally, there are event selection criteria to make similar cuts on the calibrated reconstructed jets matching the corresponding but slightly higher energy requirements than the triggers in the pre-selection. These events are required to pass one of three requirements on the jets;

- at least 4 jets with $p_{\mathrm{T}} > 90$ GeV and $|\eta| < 2.8$
- at least 5 jets with $p_{\mathrm{T}} > 65$ GeV and $|\eta| < 2.8$
- at least 6 jets with $p_{\mathrm{T}} > 55$ GeV and $|\eta| < 2.8$.

9.1.1. Primary Vertex Selection

An event, where the proton-proton (pp) collide head-on, the majority of the momentum is available for any physics process but this is not the case when one of the protons or both protons collide and are scattered diffractively where part of the energy are wasted. This type of events, often referred to as single- (when one of the protons breaks and scatters) or double-diffractive (both protons breaks and scatters) events, is less prioritised for physics analysis. Demanding at least one good primary vertex per event with five or more tracks makes sure that a direct pp-collision occurred. In the case of high pile-up events there exist several interaction points. The primary vertex with the highest momentum (sum of all tracks in the vertex) is taken as the primary interaction point. The Primary Vertex (PV) is also required to be within the fiducial volume of the analysis; the PV is required to be within $|z| < 200$ mm.

9.1.2. Displaced Vertex Selection

A sort of pre-selection of secondary vertices takes place during the vertexing itself (Section 7.2) by setting limits on the quality of the vertex and track fits, and the requirements of certain patterns of hits on tracks in detector layers depending on the r of the Displaced Vertex (DV). Another step of the vertex selection takes place after the initial event selection process; these involve the following steps. Vertex from here on will indicate a displaced vertex, if not stated otherwise.

The fiducial volume, in the detector global coordinate frame with the centre at $[0, 0, 0]$, stretches from $r \in [0,\ 300]$ mm and $z \in [-300,\ 300]$ mm. Any reconstructed vertex, found outside these limits on rz, is disregarded.

If a vertex is found within 4 mm of any PV in the event, the vertex does not pass the selection. The reason for this requirement is to remove any contribution of possible mis-reconstructed primary vertices as a displaced vertex. This cut serves as a kind of minimal r value that the vertices are allowed to be found at.

Material interaction can be reconstructed as displaced vertices. It is hard to distinguish this type of vertices from an actual decay of a Long Lived Particle (LLP) without making considerably higher demands on the track multiplicities or vertex mass. The vertices are vetoed if they are found in dense material regions of the detector. This material veto is applied by the use of a material map, marking dense material region as either "isMaterial" or "isnotMaterial". As this is a background to the analysis the details regarding the map will be covered in the Chapter 10 and more specific in Section 10.3. However, this is crucial to the DV analysis and suppresses the majority of the background vertices. The final criteria applied, are the signal region requirements. These requirements define the region where the signal is expected to be observed. The cuts are designed to reduce background from meta-stable particles and possibly mis-reconstructed vertices giving fake-signal signatures. The signal region is defined as the two following criteria on the vertices, the DV is required to have a large track multiplicity and an invariant mass greater than

10 GeV; there cuts are also written as $DV_{\mathrm{nTrk}} \geq 5$ and $DV_{\mathrm{mass}} > 10$ GeV.

9.2. Vertex Selection Efficiencies

The percentage of events remaining after the selection at 11% (Table 9.1) for the SIGMC1 sample. A large fraction of events is sorted out by various criteria. Especially powerful, are the material veto and the requirement of a large track multiplicity at the DV. In searches for new physics it is not uncommon to have signal efficiencies of only a few percent. The object reconstruction and triggering efficiencies are never perfect; therefore one will reduce the signal efficiency for every selection step. Moreover, strict cuts are often enforced to make sure the background sources are kept as low as possible even if this cuts out parts of the signal events. One tries to design the analysis cuts so that one can distinguished the signal+background from only background results. In the case of the displaced vertex analysis the seemingly low efficiency comes from the rather low track reconstruction efficiency of secondary tracks of up to maximum of 25 – 30%, this will always be a limitation.

All signal samples are included in Table 9.2. Figure 9.1 shows the vertex reconstruction efficiency, for two MC signal samples, after all selection cuts as a function of r. Here it is possible to see that the efficiency is slightly different when looking at a light flavour sample (SIGMC1) and a heavy flavour sample (SIGMC7). This is understood as being a function of where heavy flavour quarks form hardons and decay at a distance from the DV, the DV will then effectively be reconstructed with fewer tracks than a light flavour decay has - making more vertices fail the selection criteria.

9.3. Systematic Uncertainties on the Signal Efficiency

The methodical strategy developed to select events with the highest probability to contain event-signatures arising from a LLP decay involves many sources of uncertainties. Every cut and method for reconstruction must be considered and any systematic uncertainties involved must be assessed to give

Table 9.1.: The Event Selection includes all the requirements for the signal MC sample SIGMC1. The triggers, pre-selection, primary vertex and displaced vertex cuts are listed with the corresponding Relative and Overall efficiencies of that specific selection cut. The DV_{nTrk} is the strictest and removes 65% of the remaining events. The number in bold indicates the signal efficiency for this sample after all applied selection criteria.

Event Selection			
	Number of Events	Relative Efficiency (%)	Overall Efficiency (%)
All Events	40500	100	100
Trigger	33551	83	83
Pre-Selection	25827	77	64
PV Selection	25497	99	63
Jet Cleaning	24970	98	62
Displaced Vertex Selection			
DV Selection	20641	83	51
Material Veto	15076	73	37
$DV_{\text{nTrk}} \geq 5$	5332	35	13
$DV_{\text{mass}} > 10$	4529	85	**11**

confidence in the analysis methods. Any discrepancies between simulations and the actual parameters in data translate directly into errors of the estimated signal efficiencies; and therefore any limits will not be correctly set. The result could also change depending on the selection criteria. The following section will explain and quantify the uncertainties related to all sources involved in the DV analysis looking at the *jets* channel.

The systematic uncertainties are estimated as a function of $c\tau$, it is therefore not always easy to give a precise magnitude of a given source. Section 9.3.6 reviews the collected result from all sources over the full range of lifetimes while Section 9.4 contains the signal efficiency for the various Monte Carlo (MC) samples including all systematic uncertainties.

Table 9.2.: The Event Selection includes all the requirements for all signal MC samples in question. The triggers, pre-selection, primary vertex and displaced vertex cuts are listed in the Table. The strictest cut for all samples is the demand of many tracks at the vertex; $DV_{\text{nTrk}} \geq 5$. Once again, enforcing the point made on several previous occasions; the heavy flavour samples (SIGMC4-SIGMC9) show large relative cut efficiency than the light flavour samples due to the loss of tracks. The bold numbers in the last row indicates the signal efficiency for the samples after all applied selection criteria.

Event Selection									
	SIGMC1	SIGMC2	SIGMC3	SIGMC4	SIGMC5	SIGMC6	SIGMC7	SIGMC8	SIGMC9
All Events	40500	59200	59197	50000	50000	49998	49997	49500	37998
Trigger	33551	54397	48737	41004	41037	40798	40726	43048	32953
Pre-Selection	25827	44935	36564	31358	31268	30623	30541	33844	25850
PV Selection	25497	43052	35015	30027	30007	29356	29260	32448	24869
Jet Selection	24970	42245	34560	29449	29451	28973	28886	31975	24486
Displaced Vertex Selection									
DV Selection	20641	34763	27128	24333	24223	23859	23811	26266	20071
Material Veto	15076	25344	19557	18273	18250	17870	17894	19669	14953
$DV_{\text{nTrk}} \geq 5$	5332	8789	6155	4480	4194	4373	4082	4710	3324
$DV_{\text{mass}} > 10$	4529	7102	3426	2752	2520	2699	2479	2822	1915
Signal Efficiency	**11%**	**12%**	**6%**	**6%**	**5%**	**5%**	**5%**	**6%**	**5%**

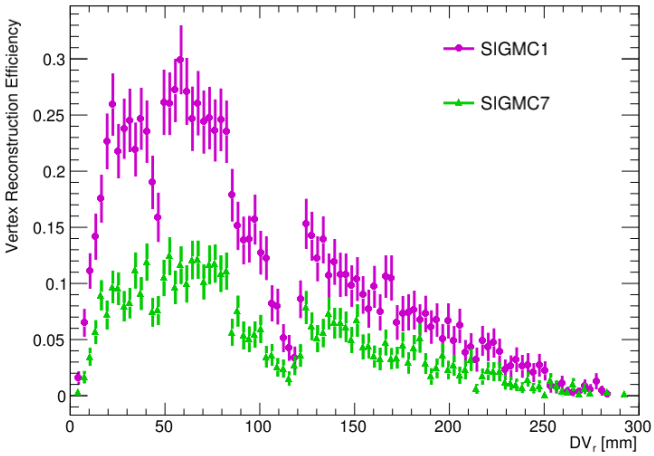

Figure 9.1.: The vertex reconstruction efficiency as a function of the radius of the displaced vertex is given for two of the signal MC samples. The magenta points are for SIGMC1 where the $\tilde{\chi}_1^0$ decays to light quarks, while the green points correspond to SIGMC4 where the $\tilde{\chi}_1^0$ decays to heavy quarks instead. Notable difference is since due to the differing tracking environments. The heavy quarks produce a displaced decay away from the displaced vertex, reducing the total amount of tracks associated with the vertex. For the lightest generation of quarks this is not the case and such a vertex will have more associated tracks.

9.3.1. Statistics

Many of the estimations are performed on MC samples, where one compares the signal efficiency before and after a variation of e.g. a cut value. These estimations are then limited to the amount of events available in the samples. The statistical uncertainties, especially at small $c\tau$, to the signal efficiencies are large.

9.3.2. Trigger Efficiency

The cuts on the jet objects are placed at a higher p_{T} than the value triggers on, this procedure eliminates any systematics from the triggers, as the cuts are made in order to be at the flat plateau of the turn-on curve. A minute change in the cut value (up and down) would yield exactly the same trigger efficiency. To be clear, an incorrect descriptions of the trigger efficiency in MC would yield an incorrect signal efficiency. However, selecting the cut as stated ensures that any such differences have no impact on the signal efficiencies.

9.3.3. Displaced Vertex Reconstruction Efficiency

The systematic uncertainties related to the displaced vertex reconstruction efficiency originate from two sources. One is from the vertexing itself and the other one is down to the track reconstruction efficiency. Any systematic uncertainties of the vertexing cuts in the vertexing process are small as shown in references [63], where they use the same vertexing technique. The tracking reconstruction efficiency on the other hand is assumed not to be negligible and needs to be estimated. Generally, the tracking efficiency is well understood and the description in simulation should correspond well to what is seen in data. The number of neutral Kaons (K_{S}) reconstructed in data and MC are compared to estimate the inefficiency in reconstruction of K_{S} (Eq. 8.2 and Eq. 8.3); this is the same methodology as described for the Hadronic Interaction analysis in Section 8.12.1. However, the minimum bias samples for the material mapping study are not suited to estimate the systematics for the DV analysis as it uses 2012 data with, amongst many different conditions, significantly higher pile-up. The resulting systematic uncertainties uses the same principle but with a few modifications will be reviewed in this section.

The yield of K_{S} in dijet MC-samples (Table. 6.1) is compared to the yield found in data-events that pass the pre-selection (Section 6.1.1). The five dijet samples have varying jet momenta, denoted as $JZXW$ where X goes from 0 to 6. The samples $JZ0W$, $JZ1W$ and $JZ2W$ have on average lower momentum jets than the data-event passing the pre-selection and are not included in the estimations. The exact pre-selection process is difficult to reproduce

on simulated samples. The cuts in the selection process are designed to assimilate them, however, as the total number of K_S in the samples is limited, additional cuts would reduce the statistic sample with a large fraction. These three samples are therefore not suited to be included in the study and are not used; large tendency of degradation of the K_S double ratio has been noted, with inclinations towards much fewer counted K_S in the data sample. This behaviour is due to biases, where the pre-selection sorts out events with low-p_T jets. The events in the dijet MC samples are required to pass at least the trigger requirements from the pre-selection to reduce biases.

A fundamental principle of the K_S study to work, is that the objects in the samples are comparable (MC to data). The properties, such as the momentum distributions of the K_S, should agree within reason. If the momentum distributions are different, the meta-stable particles would generally decay further out in the detector - creating inconsistencies in the double ratio. The spectra agrees very well in is the case for the minimum bias analysis (Section 8), but unfortunately this is no longer true for the samples used for the DV estimate. The transverse momentum distribution (Fig. 9.2 (a)) and the pseudorapidity spectrum (Fig. 9.2 (b)) of the reconstructed K_S display significant discrepancies. The primary vertex z-position (Fig. 9.2 (c)) is more narrow in data while also the spectrum in MC shifted slightly to the negative side of zero. The fact that the primary vertex longitudinal position is not perfectly simulated is well known, and analyses commonly needs to re-weight the events in simulations to account for this difference. A PV event weight is by default applied in the DV analysis. Individual event weights are produced for each dijet sample, by comparing the sample to data. A correlation is found between p_T and η, therefore a combined weight-function is applied depending on both these properties. The weight for primary vertex position is simply multiplied with the $p_T\eta$-weight as there are no correlations.

Lastly, the double ratio (Eq. 8.2) is computed for the proper decay lengths of the intervals; $[5-10]$, $[10-15]$, $[15-25]$, $[25-40]$ mm. The double ratio is plotted for two intervals of $|\eta| < 1$ (Fig. 9.3 (a)) and $|\eta| \geq 1$ (Fig. 9.3 (b)); as the tracking efficiency decreases with larger pseudorapidity, where tracks have hits in the end-caps. Following the same logic as in Section 6.1.1, the largest

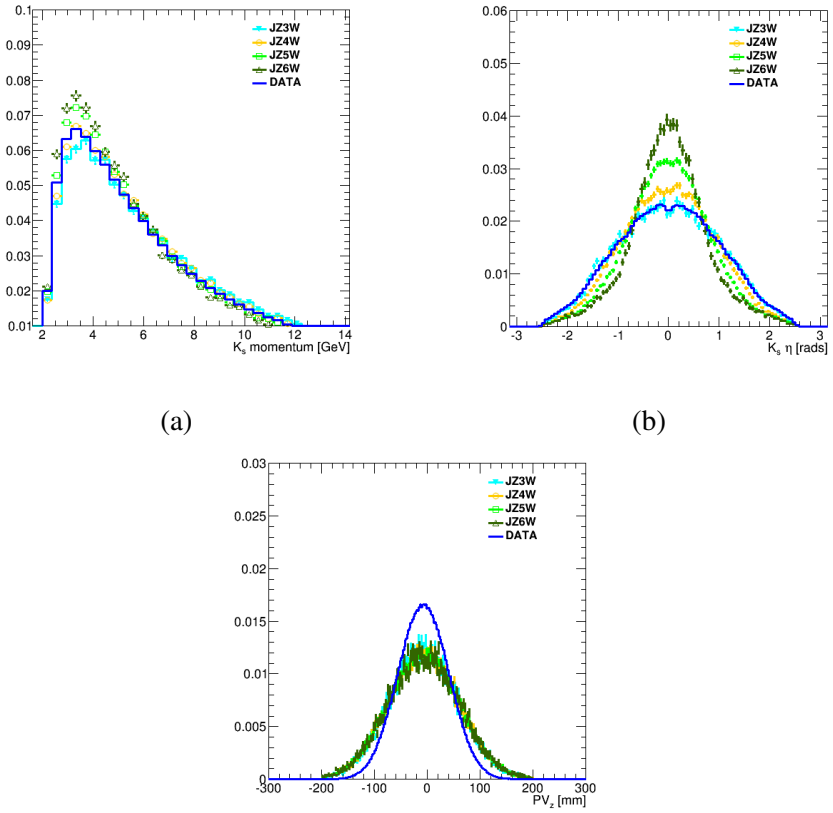

(a) (b)

(c)

Figure 9.2.: The transverse momentum distribution (a) and the η-distribution (b) of the K_S candidates, for the six dijet samples and data. The primary vertex z-position for the same samples is seen in (c). The discrepancies in the fundamental parameters are large and the MC samples are required to be re-weighted for all three different properties before a MC to data comparison can be made.

deviation of the ratio from one is taken as the inefficiency in reconstruction of K_S. The largest deviation is, for $|\eta| < 1$ ($|\eta| \geq 1$), 3% (20%) respectively.

The inefficiency in the tracking is assumed to be the halved amount, as K_S are two track vertices ($K_S \rightarrow \pi^+ \pi^-$). A random factor of 1.5% (10%) of tracks is removed for $|\eta| \leq 1$ ($|\eta| > 1$) respectively during the vertexing process; the factor used corresponds to which interval of pseudorapidity the vertex is located in. The vertex reconstruction efficiency before and after the removal of the extra fraction of tracks is shown in Fig. 9.4 for the two samples SIGMC1 and SIGMC2; these samples are the same as in Fig. 10.10. It is plain to see that the effect is seemingly minimal.

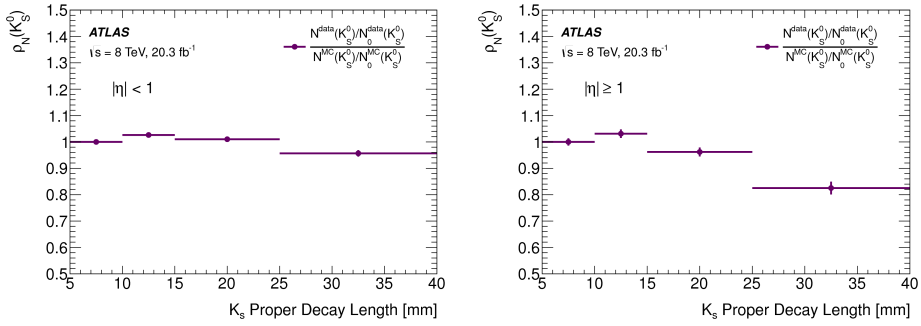

(a) (b)

Figure 9.3.: The double ratio of the number of K_S found in data and MC. The ratio is individually normalised to the amount found at the smallest interval, 5 − 10 mm. The maximum deviation of the ratio is taken as the systematic uncertainty from the tracking efficiency [5].

9.3.4. ISR and FSR

Initial State Radiation (ISR) and Final State Radiation (FSR) denote radiative effects of either a Quantum Electro Dynamics (QED) or a Quantum Chromo Dynamics (QCD) process in the initial state or final state of a production. A QED process could be the emission of e.g. a γ while QCD radiation occurs via a strongly interacting particle e.g. q or g. ISR and FSR have direct effects on the signal efficiency; if either produces q/g, the event will have extra jets. Figure 9.5 attempts to visualise a decay that has an extra jet due to ISR

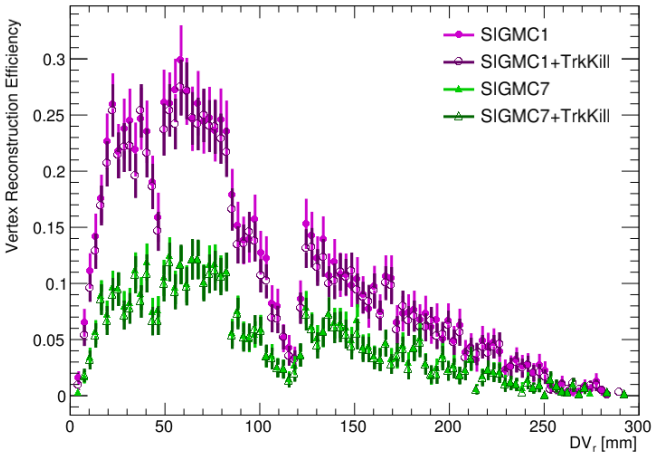

Figure 9.4.: The vertex reconstruction efficiency as a function of the radius of the displaced vertex is given for two of the signal MC samples. The magenta points are for SIGMC1 where the $\tilde{\chi}_1^0$ decays to light quarks, while the green points correspond to SIGMC4 where the $\tilde{\chi}_1^0$ decays to heavy quarks instead. The darker shaded points are corresponding to the signal samples where during the reconstruction a fraction of tracks was randomly removed equal to 1.5% (10%) for vertices in the regions $|\eta| < 1$ ($|\eta| \geq 1$). The total effect on the vertex reconstruction efficiency is minute as the two graphs, with and without removing extra tracks, nearly overlap.

(purple) and FSR (green). These jets are not always identified as radiative effect as they can be mistaken for jets coming from signal mechanisms and might cause the "fake" event to pass the selection process. The uncertainty on the signal efficiency expected from ISR[1], is evaluated using a method to re-weight the momentum of the production process in simulation, that is the momentum of the squark-squark system. Modifying the energy available for the production system for strong production, is similar to adding or removing radiative effects in the initial state.

[1] The uncertainty related to FSR is considered small in the considered process.

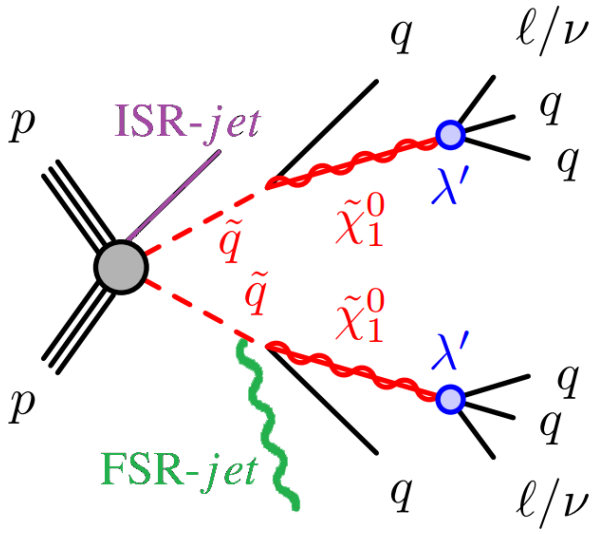

Figure 9.5.: Feynman diagram illustrating the concept of radidative effects. ISR occurs in the initial state, at the same time as the production process, in this case it is the $\tilde{q}$-pair. Here drawn as the purple emission of a photon. Meanwhile, FSR happens at certain point during, the final state of the $\tilde{q}$ decay, indicated by the green emitted gluon.

The signal MC is simulated using Pythia8, unfortunately, a known problem with this generator is that it does not contain the most accurate description of radiative effects. MadGraph [69] has been shown to contain a more optimal modelling of ISR and FSR [87] and can therefore be used to estimate the systematic uncertainties related to the descriptions of jets in the DV signal samples. The MadGraph samples for this purpose are discussed in Section 6.4. These samples are dedicated *R*-Hadron samples where the production process is $\tilde{q}\tilde{q}$. A weight extracted from a sample even though the final decay processes are not the same but as long as the masses of the production particles are comparable for both samples. The vector summation of the p_{T} of the production system (Fig. 9.6 (a)) indicates large differences between the two

generators, where Pythia is more prone to underestimate the radiative contributions. An event weight-function is extracted by taking the ratio between these two spectra (Fig. 9.6 (b)). The weight for each event, is chosen from the weight-function, depending on the momentum of the $\tilde{q}\tilde{q}$-system of just that event. After applying this weighting scheme, the change in the signal efficiency varies from 2% to 10% depending on $c\tau$ as well as on the target sample.

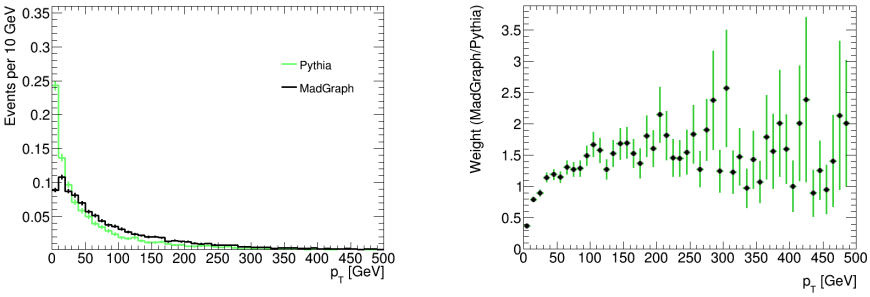

(a) (b)

Figure 9.6.: The vector summation of the transverse momentum of the gluino-gluino system for a Pythia and a MadGraph MC sample indicates that Pythia tends to underestimate the radiative contributions (a). The event weight used to estimate the ISR systematic uncertainties, extracted from (a), is shown in (b).

9.3.5. Jet Selection

Three expected sources of systematic uncertainties related to the jet selections and reconstructions are assessed. The measured p_{T} of the jets in ATLAS, is once again, calibrated for primary jets, or jets pointing towards the PV. However, the jets in the DV analysis stem from a displaced decay point and will not have exactly the same properties as primary jets. The deviation of jets, originating from displaced decays, relative to normal-jets increases with the decay length of the LLP; the rz position of the displaced vertex. The uncertainty in the reconstructed p_{T} is estimated by studying the correlation of

how much the reconstructed value diverges with r and z of the vertex. The p_{T} of the primary and the displaced jets diverge linearly in both r and z, with the same amount. The systematic uncertainty on the signal efficiency is then given as a function of decay distance of the DV in r scaled with the inclination (divided by the amplitude) of the linear dependency.

There are uncertainties in the measurements of the jet energy scales (the scales are briefly mentioned in Section 7.3). Applying standard methods of slightly varying the vital parameters a certain amount provide an estimate how this impacts the signal efficiency.

During the pre-selection of events, one requirement is demand one trackless jet in the event (Section 6.1.1). If the modelling of these jets in the MC simulations does not perfectly agree with the data, there could arise systematic uncertainties on the selection efficiency in the signal samples. To estimate this, the p_{T} cut is increased and differences in data and MC are taken as the systematic uncertainty from this source.

9.3.6. Total Systematic Uncertainties

The total systematic uncertainties are given as a function of $c\tau$ and are shown for SIGMC1 (Table. 6.2) in Fig. 9.7; where (a) shows the relative uncertainties and (b) shows the absolute values. Which systematic uncertainty dominates is dependent on $c\tau$, at low values of proper decay length the largest effect on the SIGMC1 sample is the uncertainty in the modelling of radiative effects in Pythia. However, for $c\tau$ larger than 10 mm, the dominating factor is the uncertainty in the tracking efficiency. Reweighting the signal MC to small lifetimes ($c\tau < 1$ mm) and large lifetimes ($c\tau > 500$ mm) yields on certain occasions large statistical uncertainties. This is down to the fact that there are smaller efficiencies to reconstruct vertices at short and relative large distances in the detector volume. The heavy flavour decays through λ_{i13} and λ_{i23}, have worse overall vertex reconstruction efficiencies, where fewer tracks can be associated with the DV as the heavy flavour quarks decay a distance away from the original DV. Appendix A.2 contains similar plots for the samples SIGMC2 to SIGMC9.

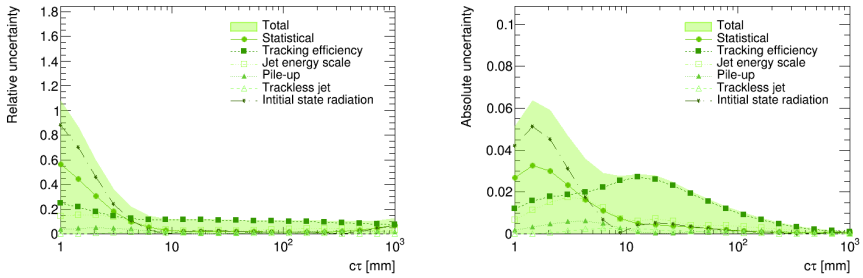

(a) (b)

Figure 9.7.: The filled curve is the total systematic uncertainties for SIGMC1 as a function of proper decay length. The different markers show the individual contribution for a single specific source. The relative uncertainty to the signal efficiency is shown in (a) while (b) shows the absolute uncertainty. At short decay length, the dominating systematic uncertainties are the statistical and the ISR related ones. While the tracking efficiency uncertainties are the major source at $c\tau > 5$ mm.

9.4. Signal Efficiency as a Function of $c\tau$

Combining all the points reviewed in this chapter, the signal efficiency as a function of $c\tau$ can be produced, including all the systematic uncertainty discussed. The final signal efficiencies for all the signal samples are collected in Fig. 9.8; (a) includes the efficiencies for the three couplings including a μ in the final state (SIGMC1, SIGMC4, and SIGMC5), (b) is the final states with an electron (SIGMC2, SIGMC6, and SIGMC7), lastly (c) shows the final states with a neutrino ν (SIGMC3, SIGMC8, and SIGMC9). The large uncertainties make themselves known with the thick error bands. For instance, the curve corresponding to the λ_{211} in Fig. 9.8 (a) exhibits very large uncertainties at $c\tau <\sim 5$ mm. Increasing error bands are seen in the same figure for the coupling λ_{213}. The reason for this is the lack of statistics at large decay distances when applying the τ reweighting.

The significant difference between the light and the heavy flavour samples for the vertex reconstruction efficiency seen in Fig 9.1 also provides the ex-

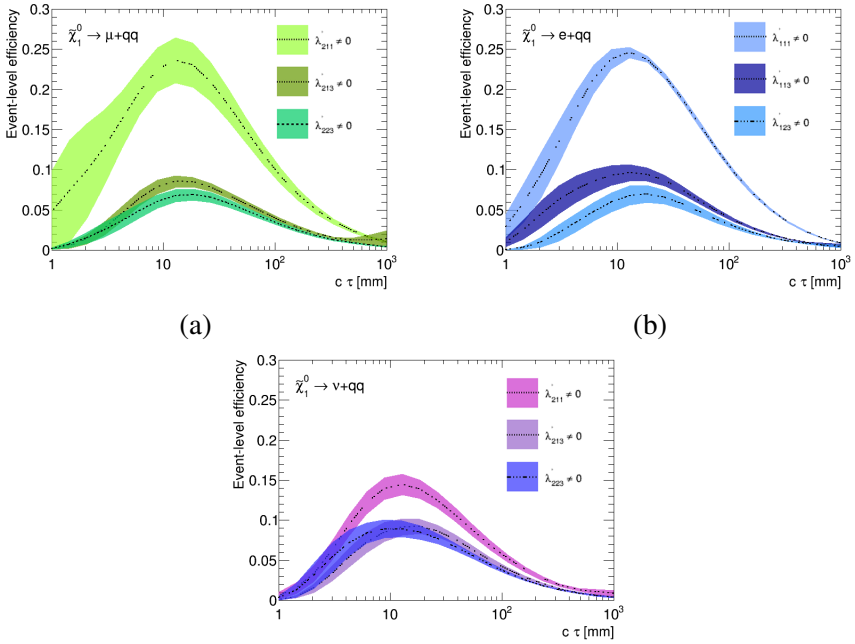

Figure 9.8.: The Signal Efficiency given as a function of $c\tau$ ranging from 1 mm to 1000 mm for all the signal mc samples. The error bands include the total systematic uncertainties, sorted by the decay modes. The decays $\mu + qq$ through the different couplings λ_{2jk}, for light and heavy flavour quarks are shown in (a), while the final states of $e + qq$ for λ_{1jk} are included in (b), and finally (c) shows the decay including a neutrino. The error bands are larger at low values of $c\tau$ due to statistical limitations. The widening bands at $c\tau > 500$ mm for few of the samples, are again caused by the lack of statistics in the τ-reweighting process.

planation to the large gap between the λ_{i11} samples in Fig 9.8 and the rest. Furthermore, the peak of the signal efficiencies at 10 mm is down to the lay-out of the Inner Detector (ID). Vertices around these distances will have the benefits of being within all the silicon detector layers; yielding more hits on tracks and higher tracking efficiency.

10. Background Estimation

The strong point of a search for a signature of a displaced vertex is that this signature is scarce in the Standard Model (SM) and is nearly a zero-background channel; nevertheless any imaginable origin of background vertices must be considered and evaluated. The potential SM sources of decays that mimic glssusy Long Lived Particles (LLPs), are meta-stable particles such as K, B-mesons and Λ-baryons to name a few. The majority of these mesons and baryons is removed by either the track cut on $|d_0| < 4$ mm (during vertexing described in Section 7.2) or by the signal region requirements of $DV_{\text{nTrk}} \geq 5$ and $DV_{\text{mass}} > 10$ GeV (Section 9.1.2). The expected background from meta-stable particles is therefore zero. However, there are three sources of background vertices originating from what could be named mis-reconstructions, these sources are hadronic interactions, random combination of tracks and merged vertices and vertices crossed by random tracks. Each of these sources hypothetically can give a contribution in the signal region, and it is necessary to evaluate their potential contributions. In making these estimations, what is important is the signal region requirements of track multiplicity and the mass of the vertices; the estimation techniques are based on replicating the invariant mass distribution for different track multiplicities Displaced Vertex (DV)s.

A few words regarding the authors contributions to the DV anayis follows. The technique to estimate one of the background sources where a random track cross a vertex and get mis-reconstructed as a complete vertex has been significantly improved and the work done on this method is a large part of this thesis. The systematic uncertainty on the previous method was at 100% *while after redesigned and introducing more advanced consideration, the systematic uncertainties has been reduced to* 14%. *The material map used to*

veto material interactions is not a new concept and has been using through previous iteration of the A Toroidal LHC ApparatuS (ATLAS) DV analysis. However, the map has been extended in r as well changed from 2D to 3D to effectively reduce the volume vetoed. The creation of the material map is a group effort but especially validation of the 3D map has been performed in relation to this thesis.

10.1. The Three Background Sources

The zero SM expected background is a huge benefit and the strong-point of the analysis. However, typical background estimations are of no use as the expected background is quite case-specific and down to mis-reconstructed vertices. For example, standardised recommendations or methods simply do not exist. Especially, since the expected background vertices are down to the precision of the tracking and vertexing for data, looking at these effects in Monte Carlo (MC) will not therefore be much of assistance. The descriptions in simulations are not perfect and if one is to estimate these background sources from MC one would have to account for a wide variety of systematic uncertainty such as tracking or vertexing efficiency being modelled wrong. Instead, fully data-driven techniques are used, exclusively developed for the DV analysis. Data-driven implies that the estimations are performed using data collected by the detector and not any form of simulated MC samples. Before going into details of the techniques used, the three sources of backgrounds mentioned in the chapter introduction are reviewed in more details.

Hadronic Interactions: Displaced vertices are not only formed from decays of particles, but are additionally created when particles interact hadronically with matter.

It is imaginable that a DV from a hadronic interaction could pass the signal region requirements. It is often troublesome or even impossible to distinguish a material interaction vertex from a LLP decay while at the same time to not introduce a surplus of cuts that would reduce the signal efficiency significantly. This is especially the case, if the said vertex is reconstructed in a very

dense material regions, e.g. inside the material of a detector layer. Material interaction vertices are background to the analysis and are removed by using a map over the dense material regions (Section 10.3).

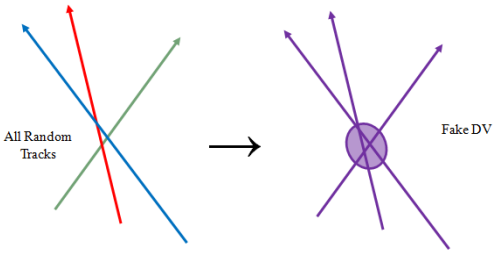

Figure 10.1.: Schematic view of a potential background source. Vertices might be fit (Section 7.2 explain the criteria needed to be passed) from random combinations of tracks at low r , the red, blue and green colours of the tracks indicate that the origin of the tracks are different. The vertexing algorithm creates high track multiplicity DV (in purple) out of these tracks.

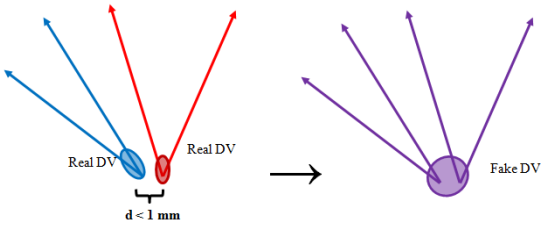

Figure 10.2.: Schematic view of a potential background source. At small r close-by real DV (blue and red), within a distance 1 mm might be merged by the vertexing and create a fake with high track multiplicity (purple).

Random Combination of Tracks and Merged Vertices: At small radii, close to the interaction point, the track density is high. A complete set of independent tracks could potentially cross and get reconstructed as a vertex. Figure 10.1 illustrates this source through a simple schematic, where random tracks, red, blue and green are reconstructed as a fake DV. Moreover, it is likely that there could exist DV close-by each other. If the distances between these vertices are within 1 mm, they are merged and produce a fake DV with many tracks (Fig 10.2).

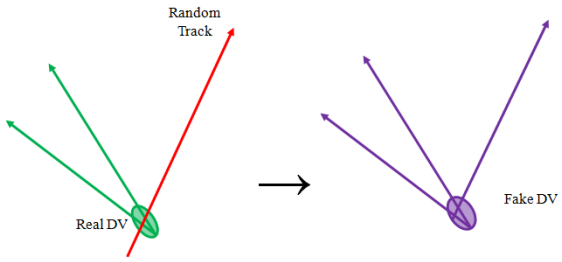

Figure 10.3.: Schematic view of a potential background source. Outside the beam pipe, $r > 32$ mm, the major source of the creation of background vertices is when a real DV (green) is crossed at a high relative angle by a random track (red). The vertexing could then reconstruct a potential high track multiplicity DV. The only real source of displaced vertices at large radius is often hadronic interactions with the gas molecules in between the detector layers.

Vertices Crossed by Random Tracks: After vetoing material interactions there still remain hadronic interactions of particles with the gas molecules in between the material layers. Potentially, any of these vertices could be crossed by a random track (Fig. 10.3) and be assigned to the vertex during reconstruction. In that case, the vertex would get an increase in the number of tracks as well a higher invariant mass (if the random track crosses at a large angle the vertex mass will increase by a large fraction).

10.2. Data Samples and Region of Interests

The background estimations are made on a selected set of vertices in the data sample (Section 6.1) that passes the primary vertex event cuts as expressed in Section 9.1.1 and the initial DV cuts as described in Section 9.1.2, with the exception of the cuts on the vertex track multiplicity and mass. Since a high statistic sample of vertices is sought neither trigger requirements nor any of the other object cuts are applied to the vertex-set. The initial set of triggers applied during the pre-selection of data, described in Section 6.1.1, are enforced since these are the basic dataset used in this analysis. In doing a data-driven estimate, it is important to divide the data sample into a couple of orthogonal regions in order not to bias the estimations. The DV analysis is divided into three regions by the track-multiplicity of the vertices. Three regions are defined:

- **The Control Region** includes all vertices with $DV_{\text{nTrk}} = 3$ and $DV_{\text{mass}} > 10$ GeV. This set of vertices, and all information extracted from them, are used to develop the background estimation model. The constructed model can be compared with data in this region without introducing biases directly using the signal region vertices. The information of interest is the $DV_{r,z}$ and the properties of the tracks assigned to the vertex.
- **The Validation Region**, on the other hand, corresponds to the set of vertices with $DV_{\text{nTrk}} = 4$ and $DV_{\text{mass}} > 10$ GeV. The method developed in the control region is verified here to see whether the technique works.
- **The Signal Region** has been mentioned a couple of times previously and still corresponds to all selected vertices that have $DV_{\text{nTrk}} \geq 5$ and $DV_{\text{mass}} > 10$ GeV.

These three regions are illustrated in the mass vs track-multiplicity plane of the displaced vertices in Fig. 10.4.

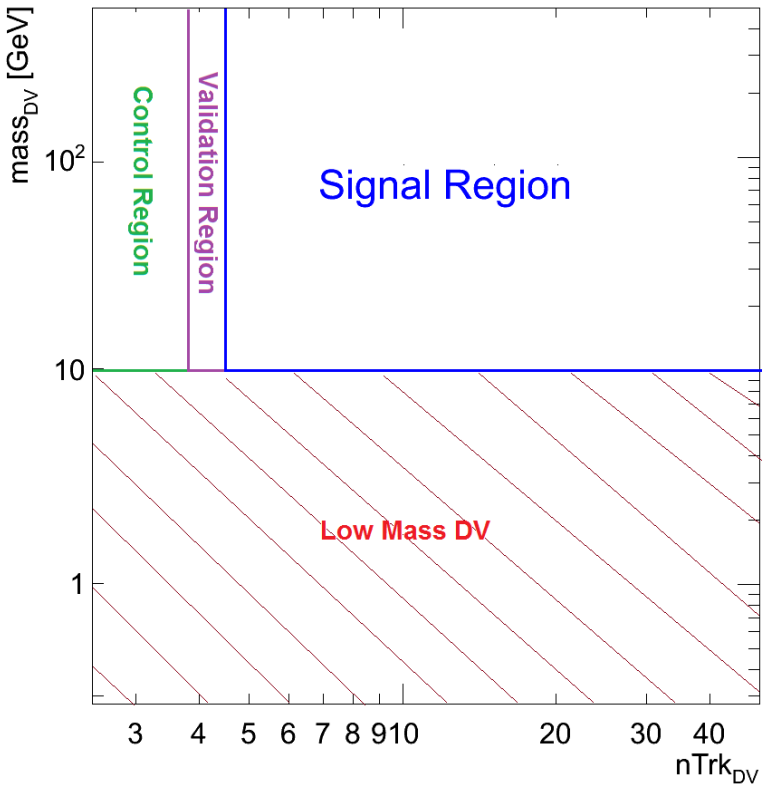

Figure 10.4.: The mass (mass$_{DV}$) and the track multiplicity of the displaced vertices (nTrk$_{DV}$) are properties used to define the different regions. Only the high mass DVs are of interest with mass larger than 10 GeV, the rest are labelled as Low Mass DV. The Control Region (green) use vertices with three tracks and high mass to help construct the background estimation. The Validation Region (purple) corresponds to vertices with four tracks and high mass, this region is defined to validate the background estimate on a source of vertices not in the signal region. While the Signal Region (blue) is where the signal would be expected and the region in which the expected background needs to be estimated.

10.3. Material Veto

Nuclear interactions with the material in the inner detector are the largest source of background vertices with high track multiplicities; distinguishing this background type of vertices from displaced decays of long-lived particles is not feasible. Any vertex found in the volume of the detector occupied by dense material therefore needs to be vetoed. A scheme to perform the veto is to construct a simplified map of these detector regions. In previous iteration [61, 62] of the DV-analysis, the map was a two dimensional map in the rz-plane; constructed with the aid of the hadronic interaction material study [63]. This time around a new improved three dimensional map is constructed and used as the material veto map; as the detector is not uniform and certain structures do not cover the full rz, a $3D$-mapping of the material will effectively veto less of the total fiducial volume, thereby increasing the signal efficiency. The map covers the whole fiducial volume of $r < 300$ mm, $|z| < 300$ mm and in the full 2π in ϕ. This is an extension of the radial region as the old $2D$-map only covered $r < 180$ mm.

10.3.1. Construction of the 3 Dimensional Material Map

There are two methods used in the construction of the different parts of the map. The more complex structures of e.g. the pixel modules are extracted from data using the hadronic interaction study, whilst geometrical approximations are made for the more uniform shapes such as support rings.

The hadronic interaction study, described in great detail in Chapter 8, applying the same selection criteria (except the vertex quality cuts as Re-Tracking is not used), maps the complex region of the three pixel detector layers. The total region is divided into a finite amount of bins in $r,\ z,\ \phi$, where bins with high hadronic interaction vertex density are marked as material and their coordinates are registered in a $3D$-map. The location and size of the simple structures such as the beam pipe or the circular support structures are extracted from the geometry in the simulation. Pure geometrical structures are constructed by a

"hard-coding" approach, e.g. a circle for a support ring, a rectangle for another kind of support structure. These hard-coded parts are afterwards added to the map over the pixel detector layers.

To clarify in additional details how the map is constructed, consider the following items;

1. The total fiducial volume of $r < 300$ mm and $|z| < 300$ mm is divided into numerous bins in $rz\phi$ equal up to around 30 million bins in total.
2. Each bin is looped over continuously checking whether it should be marked as material or not, i.e. either 1 or 0 respectively.
3. Two checks are performed.
    a) A check to see if the current bin is marked as material using the material map over the pixel regions extract from the hadronic interaction vertex density.
    b) A check to see if the current bin is within any of the hard-coded structures, e.g. if $r \sim 140$ mm, periodically in $|z|$ and for all ϕ the vertex is marked as material. The same is done for all the hard-coded geometrical shapes.

This resulting $3D$-map spans the complete fiducial volume and is visualised by three projections for the geometrical cross-sections xy (Fig. 10.7 (a)), $r\phi$ (Fig. 10.7 (b)) and rz (Fig. 10.7 (c)); it is clear that certain structures are built up by geometrical simplified structures while other elements have much more details. The position of any reconstructed displaced vertex is checked against this map to see whether it is within a region in $rz\phi$ that is marked as material. The intensity of the vertices in these projections represents the amount of material or bins marked as material, the three dimensional coverage makes the veto not completely uniform in all directions.

Cross-sections of the detector from the constructed map are compared to the ones seen in data thus to validate the map. The data is represented by plots extracted directly from the low pile-up data used in the hadronic interaction study (Chapter 8). The plots are compared by eye to see if any material structure is missing in the map or if the geometrically simplified structures do not

completely cover the real structures, e.g. if the width of one circular layer is too small.

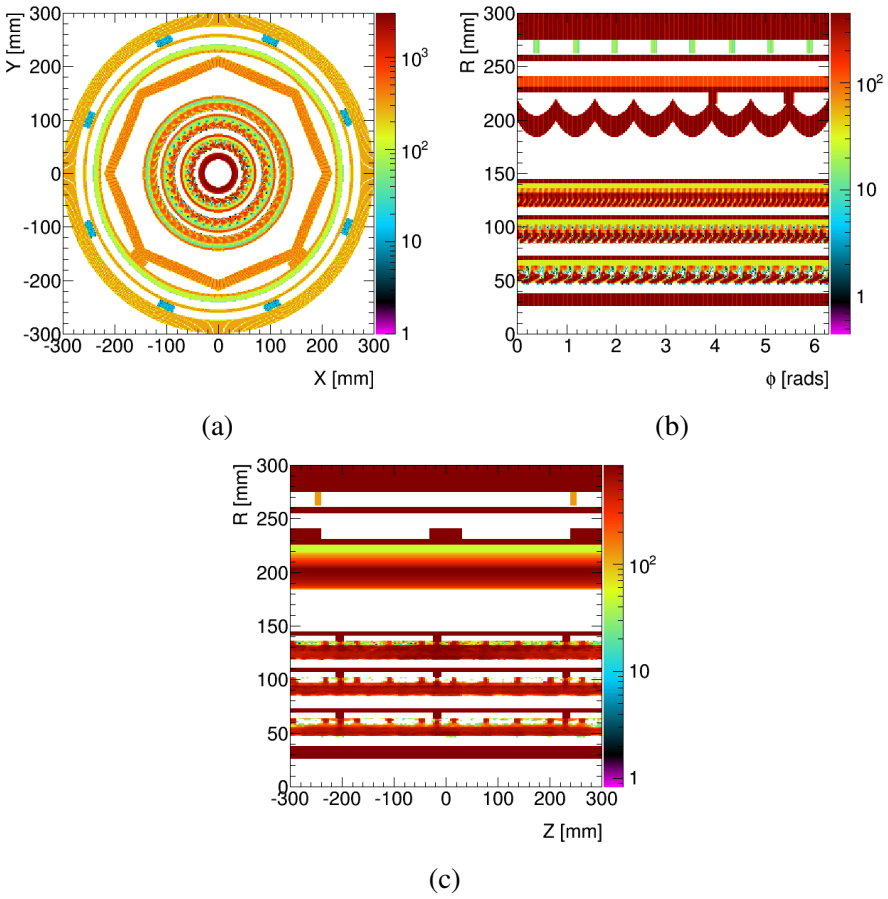

Figure 10.5.: Projection on the xy-plane (a), $r\phi$-plane (b) and rz-plane (c) from the material map. The third axis represent the amount of material vetoed. The map takes into account the three dimensional structures and doesn't veto the material uniform in all directions.

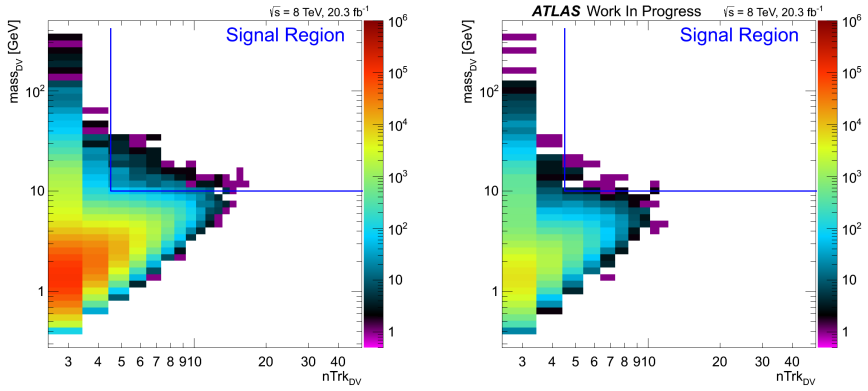

(a) (b)

Figure 10.6.: The number of reconstructed displaced vertices plotted by their track multiplicity $nTrk_{DV}$ versus the mass of the DV, $mass_{DV}$. (a) is showing the vertices before any of the selection criteria have been applied while (b) shows the vertices remaining after the material map has been applied. The majority of high mass vertices with five or more tracks are removed by the material map, indicating that these vertices are background to the signal region (marked by the blue box).

10.3.2. Hadronic Interaction Suppression Efficiency

Applying the material map significantly reduces the number of vertices in the signal region; this is portrayed by the reduction of the number of vertices in the signal region before (Fig. 10.6 (a)) and after (Fig. 10.6 (b)) applying the material veto, as about 80% of the displaced vertices with three or more tracks are removed. Going from a $2D$- to a $3D$-map, comparing the same total volume (i.e. of the total targeted volume of the ATLAS Inner Detector (ID)), the vetoed volume is reduced from 32.6% to 26.3%. A direct effect of a new larger material map is that the total fiducial volume could be increased from 0.02 m^3 to 0.07 m^3 (this is the region left after applied material veto).

The detector volume in the xy-plane for the total amount reconstructed DV is illustrated by Fig. 10.7, while Fig. 10.8 shows the region remaining after

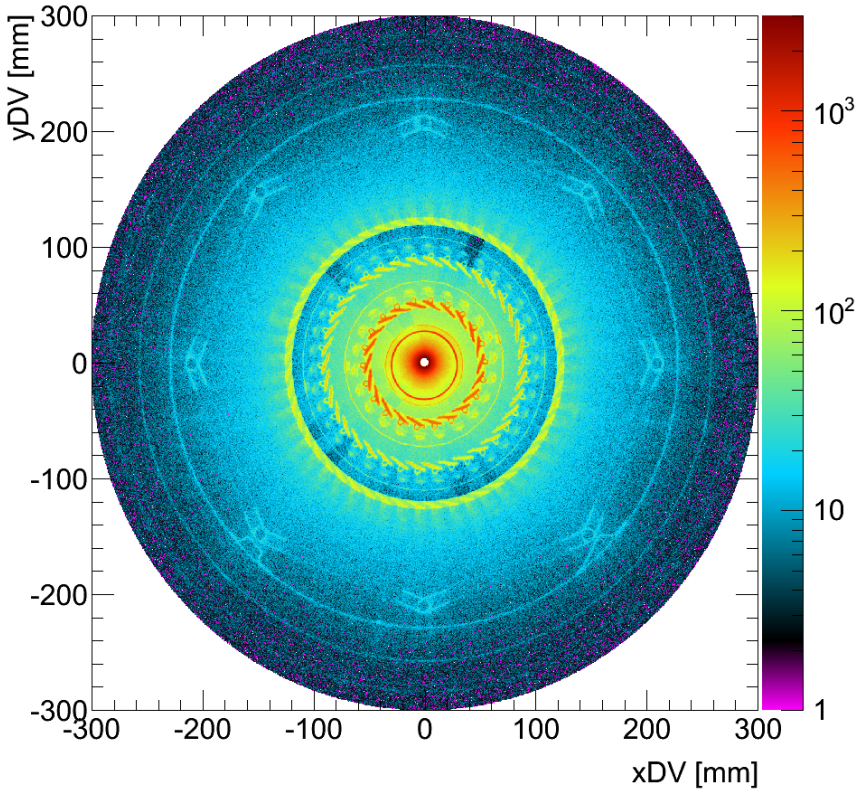

Figure 10.7.: The number of secondary vertices in data before material veto in the Inner Detector's *xy*-plane perpendicular to the beam pipe including all vertices $|z| < 300$ mm. The circles indicated by higher density than their surroundings are going from the most inner to the outer; the beam pipe, the first-, the second-, the third pixel layers, the pixel support tube (the hexagon), the first SCT layer and at the very edge.

applied veto, that is the fiducial volume.

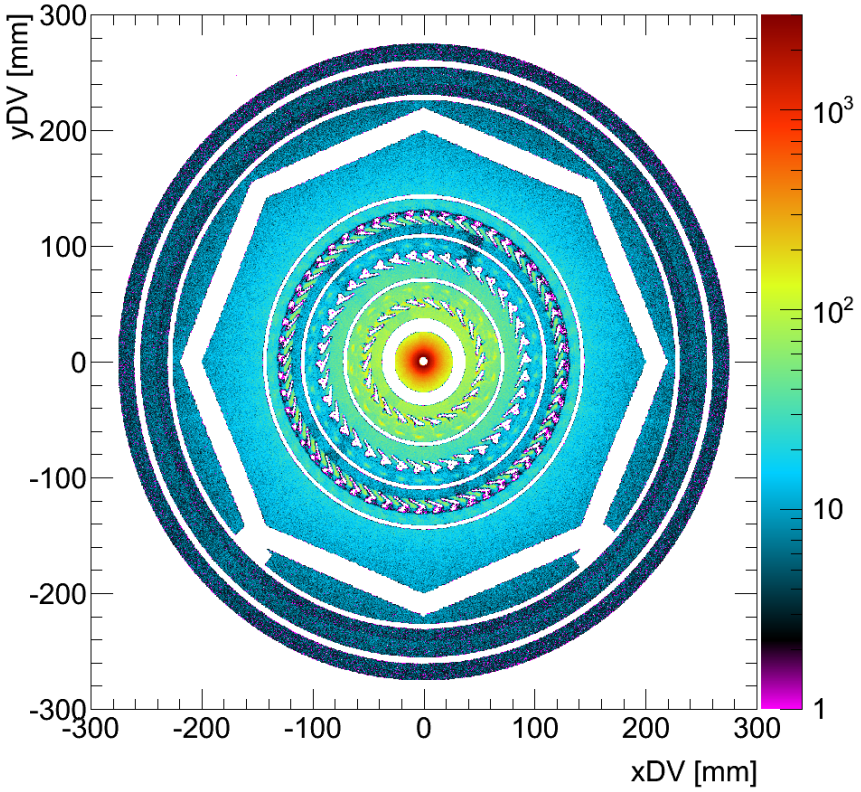

Figure 10.8.: The number of secondary vertices in data after material veto in the Inner Detector's *xy*-plane. The white regions indicate the vetoed material regions.

10.4. Random Combination of Tracks and Merged Vertices

The contribution of large track multiplicity vertices with a mass above 10 GeV from random combinations of tracks and merged vertices is estimated by the "vertex-distance" method. This involves assessing the number of falsely

merged pairs of low track multiplicity vertices, $DV_{i+j} = DV_i + DV_j$. For example, a two track DV_2 plus a three track DV_3 would yield a five track DV_5. The merged vertex could potentially have a high mass and would give a contribution to the signal region. The same logic goes for higher track multiplicities $DV_3 + DV_3$ etc. The target region is for r inside the beam pipe, so $r < 25$ mm. The method described in this section is the same as for previous publication of the analysis, see references [61, 62]. No major changes have been developed in this iteration.

A control sample with merged vertices is necessary to estimate the number of merged vertices. Fortunately, the last step in the vertexing algorithm is to merge close-lying vertices. Vertices that lies within 1 mm of each other are merged into one. Therefore it is possible to view random vertices within 1 mm of each other as "randomly merged vertices" (as they will be merged in the vertexing independent if they are a real vertex or two independent vertices!). However, since the merging takes place during vertexing, there are no close-by vertices in the dataset. Instead, a sample is created by comparing vertices in different events, all vertices in all events are used to check how many of them happen to be within 1 mm of each other. Any pair of vertices, in this sample, with a distance between them of $d_{2DV} = \sqrt{\Delta r^2 + \Delta z^2} < 1$ mm is then be to considered as one vertex created by a random combination of a pair of vertices.

The distributions at d_{2DV} for the 3D distance for vertices from all events are compared with the distribution of vertices in the same events. The two spectra are not in perfect agreement between as can be seen in Fig. 10.9, where the green histogram corresponds to the vertices found in the same event and the black line is the "model" created by vertices in all events. Here one can also see the significant lack of statistics looking at vertices found in the same event. There is also a clear discrepancy between the two distributions in Fig. 10.9 in the mean value. The modelled distribution is re-weighted to fit the one of the "data" in one coordinate as the largest discrepancies are seen in the z-direction. The whole spectrum is weighted by a simple Landau function and no bin-by-bin consideration is done. Higher track multiplicities, e.g. 3+2

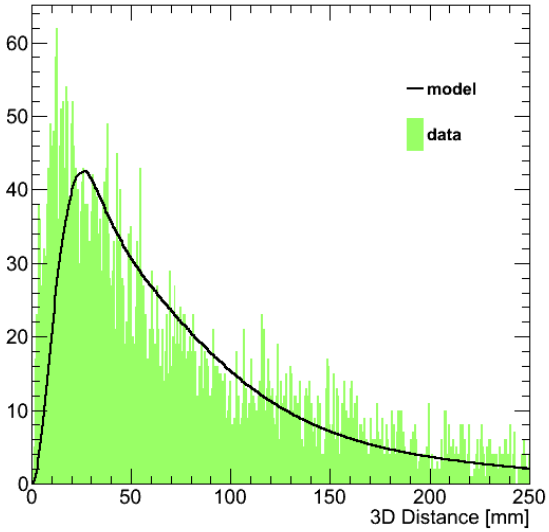

Figure 10.9.: The 3D Distance between pair of two track DV. The black line represents the distance using the sample of vertices collected from all events while the green histogram corresponds to the distance between the few vertex pair found in same events. The distribution does not agree perfectly so a weight is extracted from these two distributions to be applied on the model. The statistical fluctuation between in the data distribution introduces uncertainties in the method but are taken into account by the total uncertainty of 100% assigned to the estimate in the end.

track DV combinations are also re-weighted with the same weight function extracted from the 2+2 DV distributions. The difference observed between the two distributions comes from that vertices created in the same events are often correlated, and thereby introducing some kind of dependencies that are lacking when looking at the total random combinations of vertex pairs found in different events. Any uncertainties depending on the statistical fluctuation in the distance distribution for vertices found in the same events are covered by the total uncertainties of 100% assigned in the end on the estimated number of vertices.

After applying the weight, the distribution between data and the model agrees within reason. The final model for four track vertices and five track vertices can be seen in Fig. 10.10 (a) and (b) respectively. The small fluctuations (in Fig. 10.10) are accounted for by adding a 100% systematic uncertainty to the estimated numbers. The final step is to simply count the number of vertices seen in the model at $d_{2DV} < 1$ mm that have a combined mass $DV_{\text{mass}} > 10$ GeV. The number for DV_4 is 3.50 ± 3.50 and for DV_5 is 0.03 ± 0.03. The contribution for DV_6 or any higher track multiplicities is small and conservatively taken to be equal to the number estimated for DV_5. The total estimated background in the signal region from this source is then 0.06 ± 0.06. The total contribution from this source is about less than 1% of the background from random crossings i.e. very small.

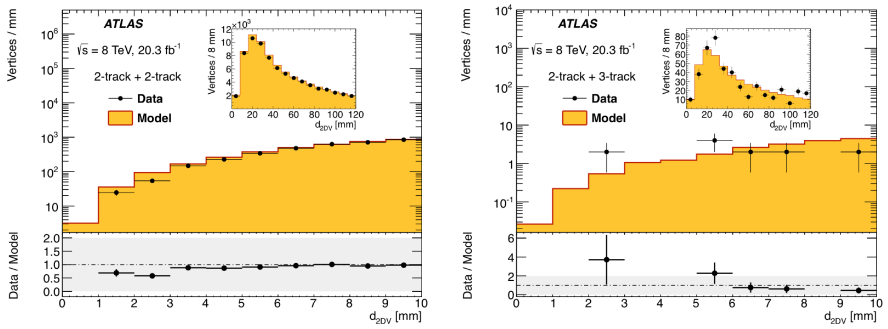

(a) (b)

Figure 10.10.: The distance d_{2DV} between two vertices looking at the same events (data points) and for vertices created using the model (yellow histogram). The model is shown after reweighting the distribution. The lower part of the figure shows the ratio how the data fluctuate from the model, the gray band represents the 100% uncertainty. The distance between two track vertices is shown in (a) while (b) is for two and three track vertices. The zoomed interval of 0 to 10 mm is shown in the main plot, while the small inlet plot includes a larger interval of up to 120 mm [5].

10.5. Vertices Crossed by Random Tracks

Hadronic interactions with gas molecules in the air-gaps between material layers produce a source of displaced vertices, typically with low mass (Fig. 10.11 (a)). However, if a random track happens to cross close-by the vertex, there is a chance that this random track will be reconstructed as a part of the vertex, yielding a high-track-multiplicity and high-mass displaced vertex producing a spectrum similar to the one shown in Fig. 10.11 (b). This type of vertices will be referred to as "random crossings". The complete invariant mass spectrum for the displaced vertices is represented by a combination of these two parts. The idea is to use the part of the template in Fig. 10.11 (b) to estimate the number of vertices with a $DV_{\text{mass}} > 10$ GeV. Without looking directly at data of the vertices with five tracks or larger but instead creating an independent model of the same process i.e. random crossed vertices.

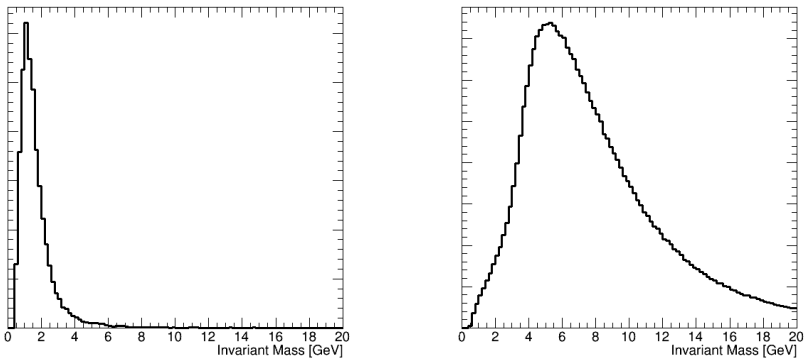

(a) (b)

Figure 10.11.: The mass spectrum of three track DV which has collimated tracks, with an average angle less than 0.5, makes up low mass vertices (a). Vertices crossed by a random track have large invariant masses as shown in (b).

Again, one of the most essential things in evaluating the background from random crossings is to fashion a signal-region-independent *control sample of*

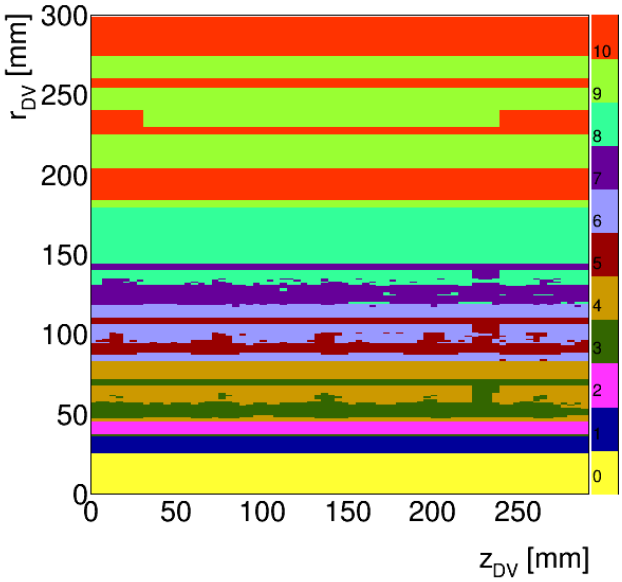

Figure 10.12.: The regions of the inner detector divided by r_{DV} and whether the region contains material or not.

random crossing vertices. A technique to create a source of vertices crossed by a random track has been developed and consists of three steps:

- Construct templates for the mass distributions of possible combinations of track multiplicity vertice; DV_{i-1} plus a random track (e.g. 2+1, 3+1, 4+1 and 5+1).
- Estimate the number of such random crossings expected and scale the random crossing template.
- Scale the total number of estimated vertices since these estimations are constructed using all events. Therefore the number of vertices needs to be scaled by the fraction of events expected after the event selection to make the estimations proportionally to what one expect to see in data.

The fiducial volume has been divided up into 10 radial regions, as can be seen in Fig. 10.12, where the different colours indicate the different regions. The regions marked with 1, 3, 5 and 7 are the vetoed dense material regions. The previously-mentioned mass templates are not only constructed for different track multiplicities, but also individually for the remaining six radial regions - regions 0, 2, 4, 6, 8 and 9 - to include dependencies on DV_r (any dependencies on DV_z have not be observed after tests). There will be six regional-templates for each track multiplicity of the DV.

10.5.1. The Invariant Mass Distributions

The invariant mass m_{DV} of a displaced vertex is obtained by adding all the four vectors v_4 of all tracks in the DV and then followed by a scalar sum preformed with the summation matrix $(+, -, -, -)$;

$$m_{DV} = \left\| \left(\sum_{n=1}^{i} v_4(\text{track}_n) \right) \right\|. \tag{10.1}$$

Construction of a model $model_i$, representing both the high and low mass spectra of vertices can be written as a function of m_{DV}, and for i-tracks,

$$model_i = P_i^{coll}(m_{DV}) + f h_i(m_{DV}), \tag{10.2}$$

where P_i^{coll} contains Low Mass Vertex (LMV) (Fig. 10.11 (a)) as a function of m_{DV} and h_i is the High Mass Vertex (HMV) (Fig. 10.11 (b)). The probability to have random crossings is f and is used to scale the HMV distribution. The model is constructed for track multiplicities $i = 3,\ 4,\ 5$ and 6 and for each of the 6 different radial regions in the detector i.e. regions 0, 2, 4, 6, 8 and 9 in Fig 10.12. In total there are 24 mass distributions. The 6 distributions for $i = 3$ have been used to develop the method, the distributions for $i = 4$ are there to validated the method and confirm acceptable agreement with data. The rest of

the templates are used to estimate the number of background vertices in the signal region.

All three parts of the $model_i$ will be explained in the following three paragraphs.

The low mass distribution: Typically the low mass vertices are real vertices e.g. hadronic interactions with gas molecules and meta-stable particles such as K^0_S. These real vertices often have relatively collimated tracks and this fact is taken into account by an angular cut applied when constructing the LMV part of the $model_i$. All the reconstructed DV with i-tracks that passes the data preselection criteria (as described in Section. 6.1.1) and have an average angle between all tracks < 0.5. These vertices are plotted to make up $P_i^{coll}(m_{DV})$. The average angle criterion is defined as an average of the angle between all track combinations in the vertex;

$$\frac{1}{i}\sum_{n=1}^{i-1}\sum_{m=2}^{i} cos^{-1}\left(\frac{v_4(\text{track}_n)\cdot v_4(\text{track}_m)}{||v_4(\text{track}_n)||\;||v_4(\text{track}_m)}\right) < 0.5. \tag{10.3}$$

The high mass distribution: The high mass vertices are made up of a real vertex crossed by a random track. The track must be in the same event but originates from a different source such as a reconstructed primary track which happened to be associated with the vertex. To replicate this feature or rather weakness of the vertexing, a seed vertex with one track less than the targeted track multiplicity is selected. A random track $\text{track}_{\text{rnd}}$ is then added to the seed vertex and the mass for the random crossed vertex m^{rc}_{DV} is recalculated as,

$$m^{rc}_{DV} = \left\|\left(\sum_{n=1}^{i} v_4(\text{track}_n)\right) + \; v_4(\text{track}_{\text{rnd}})\right\|. \tag{10.4}$$

The four different track multiplicities of h_i are created like;

$$\begin{aligned} h_3 &: DV_2 + \text{track}_{\text{rnd}}, \\ h_4 &: DV_3 + \text{track}_{\text{rnd}}, \\ h_5 &: DV_4 + \text{track}_{\text{rnd}}, \\ h_6 &: DV_5 + \text{track}_{\text{rnd}}. \end{aligned} \tag{10.5}$$

Once again, all reconstructed vertices passing the data pre-selection criterion are considered as seeds vertices. Finding a source of random tracks to add to the seeds is proven to be more difficult. The mass of the m^{rc}_{DV} is strictly dependent on the parameters of the random track. See the invariant mass for a two particle system in a collider experiment where $E >> m$ as an example;

$$M^2 = 2p_{\text{T}1}p_{\text{T}2}(\cosh(\eta_1 - \eta_2) - \cos(\phi_1 - \phi_2)), \tag{10.6}$$

where p_{T}, η and ϕ are the transverse momentum, pseudorapidity and azimutal angles of the two particles with indices 1 and 2. It is plain to see that all of these three track properties have impact on the magnitude of the invariant mass. Therefore one has to take great care when picking the random track to add to each vertex (Eq. 10.4). Say that the angular distributions of the random tracks do not correspond to what is seen in data, the created invariant mass distributions would not agree either.

Plotting the p_{T}, η and ϕ parameters for all tracks associated with reconstructed displaced vertices in data divided into the 6 radial regions depending on in which region the vertex is located. Doing this shows that these parameters are strongly dependent on where in the detector they are reconstructed. Figure 10.13 shows this fact for p_{T} and η of the track parameters, while ϕ is found to be more or less uniform for the 6 regions. The conclusion is that when picking a random track to add to the seed vertex, the track should also has been reconstructed in the same radial region. If failing to take this crucial fact into considerations will yield discrepancies in the HMV spectra in the model and in data.

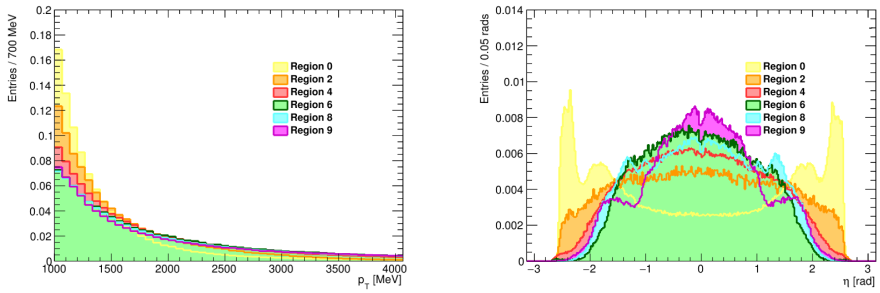

(a) (b)

Figure 10.13.: The track parameters for each of the radial regions are plotted for the tracks p_{T} in (a) and for η in (b). The parameters vary significantly depending on the regions. Each region is represented by a different color with yellow, orange, red, green, blue and purple for regions 0, 2, 4, 6, 8, and 9 respectively. Especially, region 0 shows large values of $|\eta|$.

Technically, to include the track dependencies on the radial regions in the HMV spectra, regional track templates are constructed. The track templates are three dimensional histogram with each axis divided up in a set number of bins. Picking a random bin in three dimensions from this template will give three values; p_{T}, $\Delta\eta$ and $\Delta\phi$, which corresponds to a real reconstructed track. The track templates are constructed by the following three steps are performed on all reconstructed vertices passing the data pre-selection criteria;

1. Select a vertex.
2. Check which radial region the vertex is reconstructed in and select one out of six track templates which corresponds to the same radial region.
3. Fill the selected template with p_{T} and the relative angles (between the vertex direction and the track direction), $\Delta\eta$ and $\Delta\phi$ of all the tracks in the vertex.

The motivation for using the relative angles in step 3 is that it is possible when a random track is taken from the template, its angles added to the seed vertex

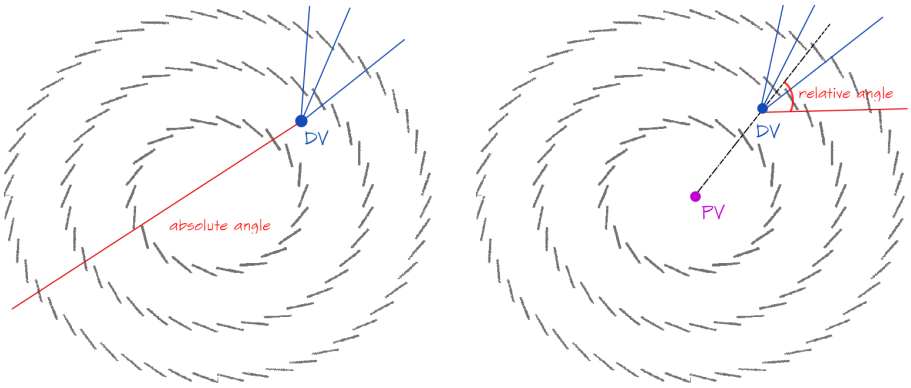

(a) (b)

Figure 10.14.: Simple schematic showing how a track added with absolute angles in the detector frame to a vertex might form vertices that would not be reconstructed by the vertex algorithms (a). While adding the relative angle to the displaced vertex direction from the primary vertex will always yield reconstructable vertices (b).

will form a type of vertex which would not be reconstructed by the vertexing algorithm. An example is shown in Figure 10.14 (a) in the $r\phi$-plane of the ID where the barrel modules are shown in red. A random track (in red) is added to the seed vertex (in blue). The random track with its absolute angle in ϕ points in a total different direction than all the other tracks in the seed vertex. Such a vertex would be removed by the fake removal (Section. 7.2.2) and there will be no such type of vertices in data, they are therefore not wanted. To above creating this type of bad vertices, instead the relative angles between the vertex and the track, $\Delta\phi$ and $\Delta\eta$ are entered into the track templates (as stated above). The relative angles acquired from the template are then added to the angle of the vertex (Fig. 10.14 (b)) yielding a vertex that would be reconstructed.

Figure 10.15 (a) shows the two dimensional projection of one of the track temples in the plane of $\Delta\phi\Delta\eta$. There is a peak present in the middle, near the coordinates 0 and 0, this spike comes from that most of the tracks found in vertices are collimated and have small relative angles to the vertex direction. If

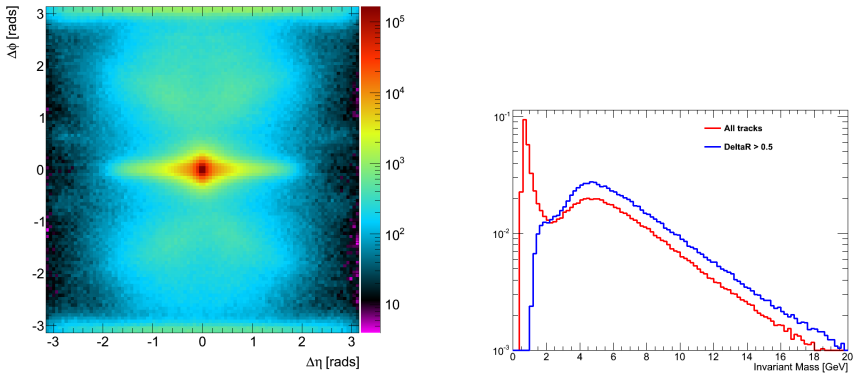

(a) (b)

Figure 10.15.: (a) shows the $\Delta\phi$ versus $\Delta\eta$ distribution of the tracks in the track template for region 8. The tracks with small angles are disregarded. If a random track is picked with a angle, less than 0.5 relative to the seed DV, a new track is randomly chosen from the template. (b) shows how the invariant mass spectrum of the mass template changes, when including (red histogram) and excluding (blue histogram) the low angle tracks from the template. Creating not wanted vertices with low masses is the result of including the small angle tracks.

a random track is picked within this peak, with relative angles in both $\Delta\phi$ and $\Delta\eta$ less than 0.5, the track is discarded and a new random track is taken until the angles are larger than 0.5. The difference in using the small angles (< 0.5) are illustrated in Fig. 10.15 (b), where the red invariant mass distribution is constructed including small angle tracks while the blue distribution shows the resulting spectrum excluding these tracks. The difference is clear, the small angle tracks create a low mass peak which is not wanted in the HMV spectrum.

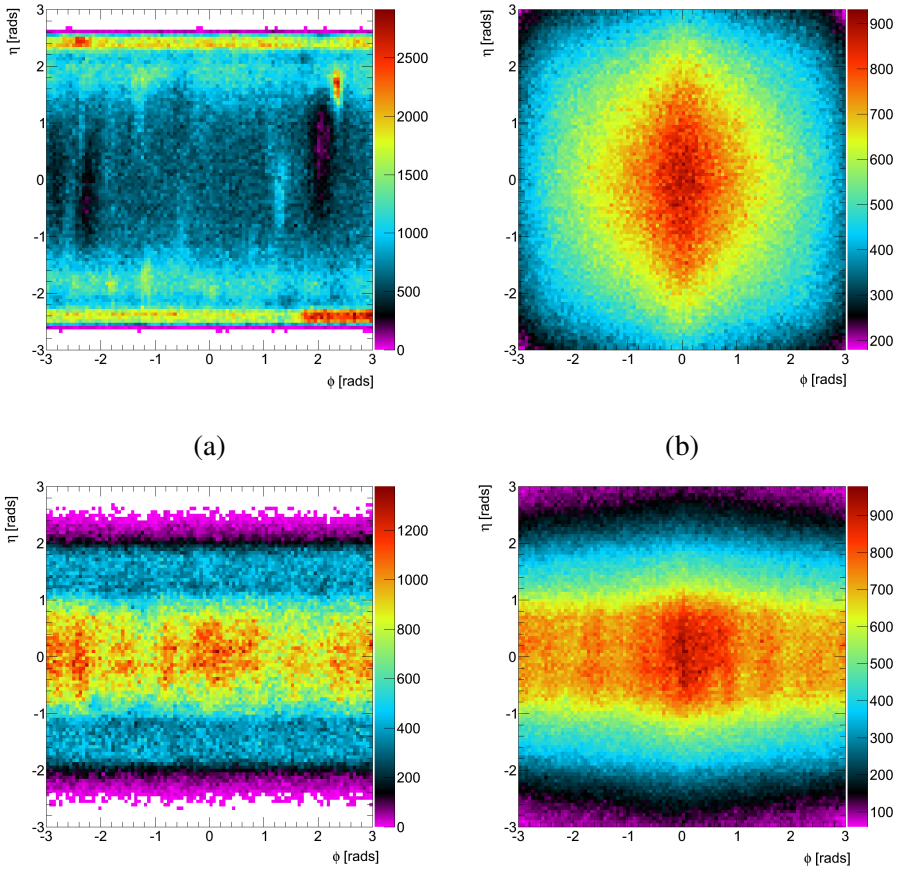

Figure 10.16.: The angular distribution of the tracks found in real vertices in region 0 (a) in the $\eta\phi$ plane while (b) shows the same distribution of created vertices after adding a random track. It is clear that (b) fails to reproduce (a) in region 0. The same is shown for region 9 where (c) is the real spectrum and (d) is the created spectrum, here the created set of vertices with a random track is much more similar to the real spectrum.

A caveat with this method is that the region inside the beam pipe requires special consideration due to the large density of high-η tracks and especially the lack of a fake removal (it is not possible to veto hits in previous layers as the beam pipe is situated before any of the detector layers in r), so this region is treated with a slight modification. While the main principle is the same, the large values of track η seen in region 0 (Fig. 10.13 (b)) mean that the use of $\Delta\eta$ (and $\Delta\phi$) is not the optimal solution. Instead, in this region, using directly η and ϕ shows a better agreement with data in the control and validation regions for DV_3 and DV_4. To confirm this reasoning two sets of track property spectra for region 0 are compared. The first set is all tracks found in real vertices. The second set is created from plotting the track parameters of all tracks in displaced vertices **after** adding a random track. Figure 10.16 illustrates this, the first set is (a) while the "created" spectrum is (b). It is clear that adding a random track with relative angles in this region do not replicate the spectrum of real tracks. Instead, filling the track template for region 0 with the absolute angles works here much better. Because of this the absolute track parameters are filled into the template for region 0 but **only** for region 0. Figure 10.16 (c) and (d) are the same two set of track parameters in region 9 here the two spectra agree within reason so here evidently the relative angles are the best solution.

Crossing factor: The last part is to estimate the crossing probability or crossing factor f. Stated again as a reminder; the high mass distributions h_i are created using a high number of vertices corresponding to the number of DV_{i-1} seed vertices. The templates therefore need to be scaled by the probability to have a random crossings (as it is now, there would be a 100% probability to have a random crossing as a random track is added to each seed vertex and this is not true). The fraction of vertices crossed by a random track is derived from the vertices in the control region. The mass-template h_3 is normalised to the actual invariant mass spectrum $R(DV_3)$ for DV_3 found in data. The fraction f, is defined as following:

$$f = \frac{\int_4^{\inf} R(DV_3)\, \mathrm{d}m_{DV}}{\int_4^{\inf} h_3\, \mathrm{d}m_{DV}}, \tag{10.7}$$

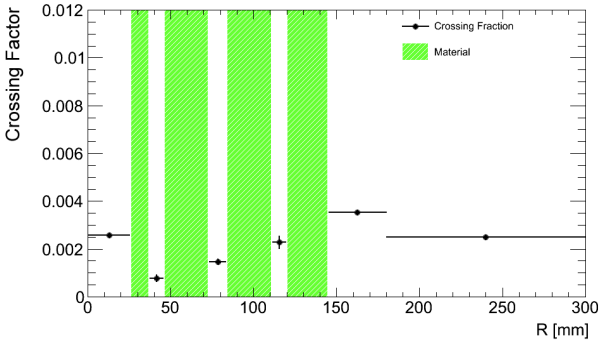

Figure 10.17.: The crossing fractions computed for each radial region are shown by the black dots. The green intervals indicate the regions with vetoed material.

where both the distributions are integrated from 4 GeV to infinity. The low part of the random cross templates is not of interest but only the HMV and a limit at minimum of 4 GeV was set for the integration. The crossing fraction f, is computed for each radial region in the control region on three track displaced vertices (Fig. 10.17). The crossing fractions are validated by applying f to h_4 and see if the estimated number of vertices using the HMV template corresponds well to the magnitude of the real spectrum $R(DV_4)$. Figure 10.18 shows the integrated number of vertices expected by fh_4 for masses above 10 GeV for all regions, compared to the number observed in data. The agreement in the validation region gives solid ground continuing to the use of these crossing fractions also for higher-track-multiplicity estimates i.e. the signal region. Region 1 at radius of 40 to 50 mm has a small volume and the estimated number of vertices is way below 1 which is agreement with the observation of 0 vertices (it is not possible to see less than 1 vertex).

10.5.2. Assembling the templates

The combination of all these parts, the final model $model_i$ (Eq. 10.2) for $i = 3$ and 4, for all regions compared with the real distribution shows very good

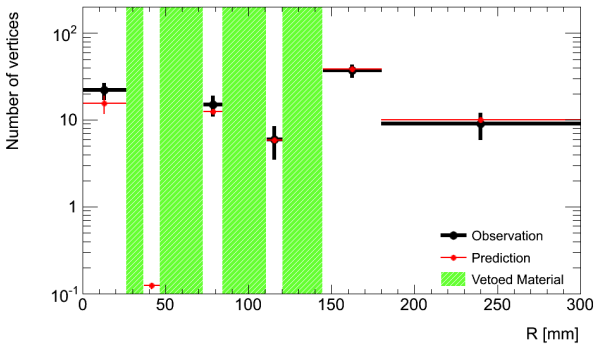

Figure 10.18.: The number of vertices, with mass over 10 GeV in the validation region is plotted. The black dots are for what is observed in data, while the red dots are the values predicted using the random crossing method. Vetoed material regions are indicated by the green areas. Superb agreement between the observation and the prediction can be noted in the validation region and demonstrates that the technique is valid.

agreement over the full range (Fig. 10.19 and Fig. 10.20). There are slight disagreements in the LMV regions at masses around 4 GeV in regions 0 and 2 (Fig. 10.19 (a) and (b) respectively) but as this is below the signal region requirement of 10 GeV it is not considered as crucial and will have no significant impact on the background estimation.

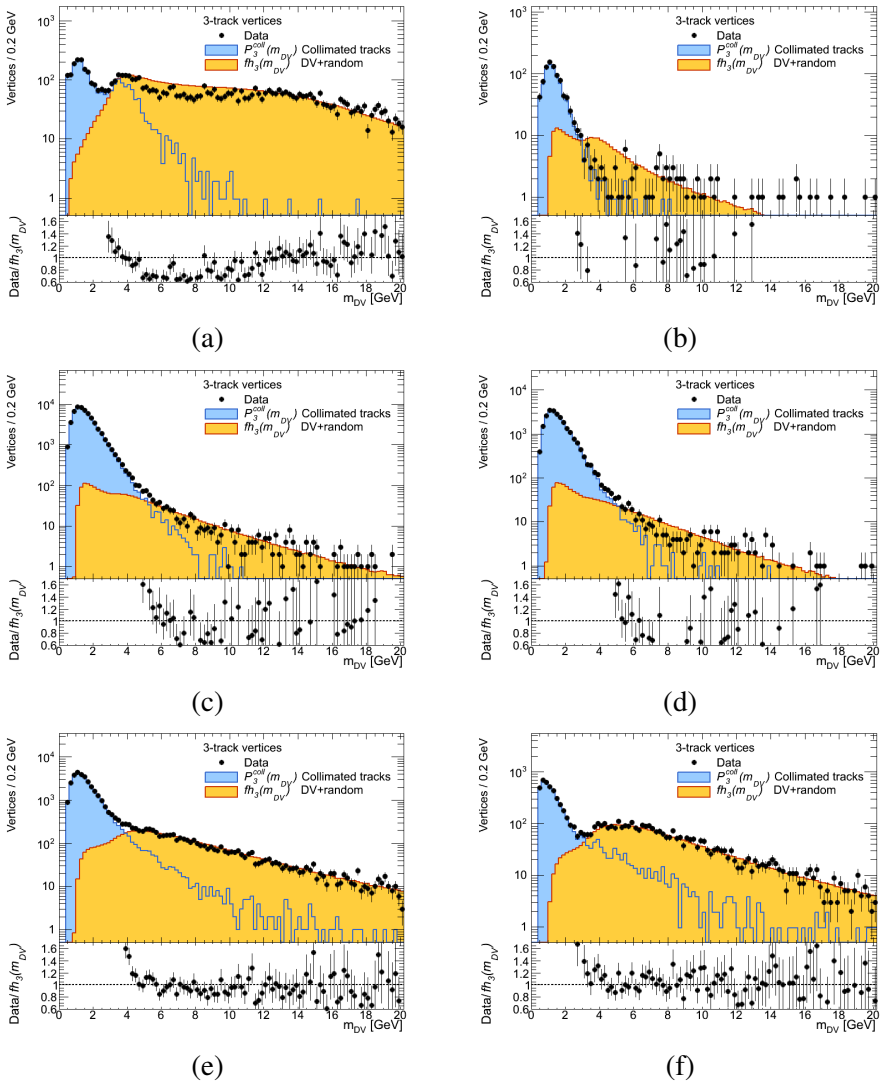

Figure 10.19.: The final templates for the six radial regions that are not vetoed by the material map are shown for three track DVs. The blue histogram shows the low mass template while the orange histogram is the template from the DV+random track method. Data are the black points. Great agreement is seen, here by design as the crossing fraction is derived from the data and templates for three track DVs. There are certain discrepancies at lower invariant masses (a) and (b). The method is designed to replicate the spectrum of high mass vertices so these differences in the shape are assumed to have little or no impact on the background estimation.

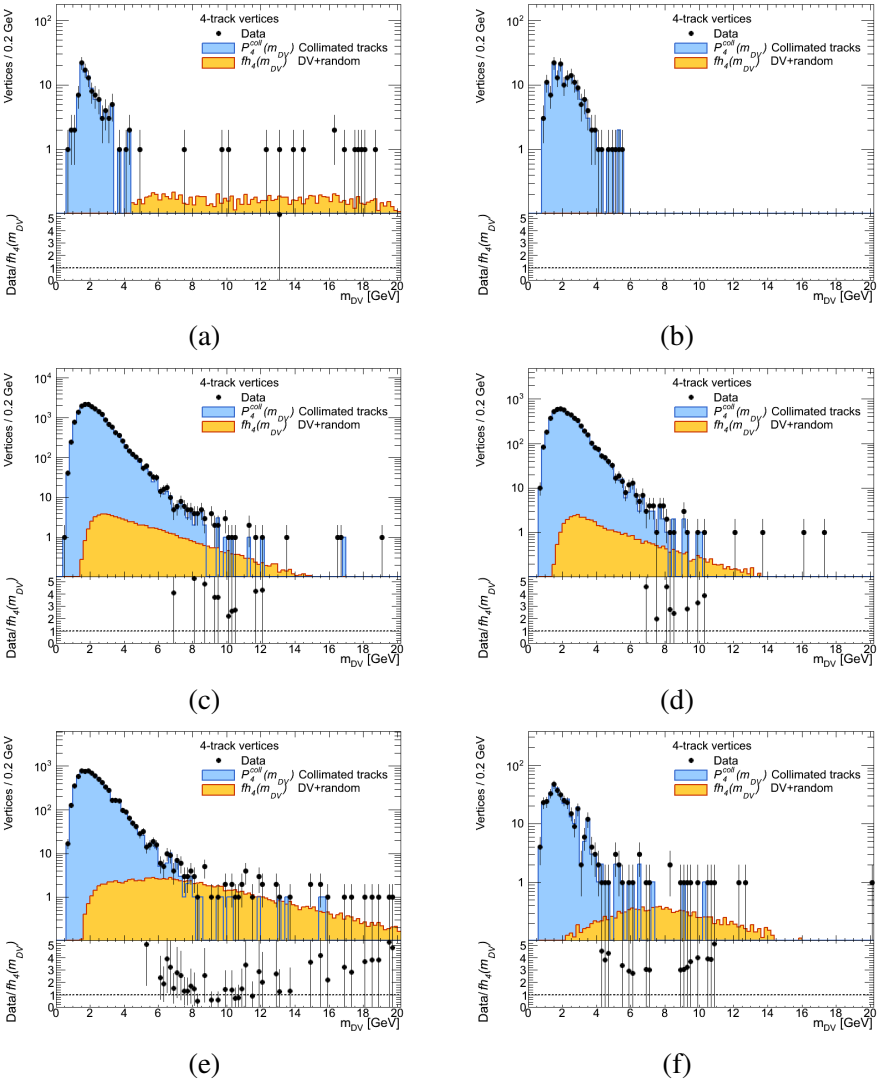

Figure 10.20.: The final templates for the six radial regions that are not vetoed by the material map are shown for four track DVs. The blue histogram shows the low mass template while the orange histogram is the template from the DV+random track method. Data are the black points.

10.6. Estimated Number of Vertices

Each region $model_i$ is integrated from 10 GeV to estimate the number of expected vertices of the given track multiplicity. Table 10.1 contains the total numbers from all regions and for all possible track combinations of interest. The resulting number of vertices from the merged vertices source is added (2+2 and 2+3). The "Rest DV", refers to an assumption made that the sum of all higher track multiplicities than 5+1, will not be larger than the contribution for 5+1. The remaining contribution of higher track combinations is then taken to be 6.2 ± 0.2 at maximum. These numbers are computed using all the displaced vertices without applying any event selection criteria. An event-level scale factor sf_{ev}, applied to the total estimated vertices to produce the real number of vertices expected in the signal region after all cuts. The scale factor sf_{ev} is simply extracted by the fraction of events in data that passes the event selection, this factor is 1.38%.

The final part is to investigate the systematic uncertainties related to the background estimation techniques. A 100% factor is already applied to the estimate of merged vertices. The remaining sources of uncertainties lie with the shape of the random crossing mass templates and the crossing fraction. A method to vary the integration limits for computing the crossing fraction gives an estimation of both these two sources. Varying the lower limit in Eq. 10.7 by ±5 GeV, gives a change in the total number of vertices (in all regions) of 10%. This factor is then taken as the uncertainty in the random crossing technique.

Applying an event-level scaling factor sf_{ev} is based on the assumption that the event cuts are uncorrelated with the number of displaced vertices. However, it is found to not be the case and small fluctuations in the average number of DV as a function of the event selection criteria are observed. This means that for instance, applying a high-p_{T} trigger might make an event more prone to has a DV. A maximum deviation of +5% vertices is noted as the cuts vary. The event-level scale factor is then taken to be 5% larger, $1.38\% \times 1.05$, so including the systematic uncertainties, the new factor is $sf_{\text{ev}} = 1.45\%$. Including all sources of systematic uncertainties and scaling the total number of vertices

Table 10.1.: Total number of estimated background vertices with a mass $m_{DV} >$ 10.0 GeV in the control, validation and finally signal regions, from vertices crossed by random tracks and merged vertices, using the full integrated luminosity of 20.3fb^{-1}. Observations are not stated for the signal region as the number here is part of the results.

Control and Validation Regions			
	3 Track DV	4 Track DV	
	2+1 DV	3+1 DV	2+2 DV
Estimation	5442 ± 8.0 (stat.)	79.1 ± 0.9 (stat.)	3.5 ± 3.5 (stat.)
Observation	5453	89	
Signal Region			
		5 Track DV	
		4+1 DV	2+3 DV
Estimation		15.7 ± 0.4 (stat.)	0.03 ± 0.03 (stat.)
		6 Track DV	$6 > TrackDV$
		5+1 DV	Rest
Estimation		6.2 ± 0.2 (stat.)	6.2 ± 0.2 (stat.)
Total Estimated Vertices in the Signal Region			
28.2±0.5(stat.)			

expected, 28.2 ± 0.5 (Table 10.1), with $sf_{\text{ev}} = 1.45\%$, by which the final number background vertices is computed to be 0.41 ± 0.06. The error includes the statistical uncertainties added in quadrature to the systematic uncertainties.

In previous publication, a much less refined method was used to estimate the random crossing background. This method had a 100% systematic uncertainty assigned to it. The improvement of the technique reviewed in this chapter has yielded a significant reduction of the total uncertainties on the estimate from 100% to 14.6%.

To conclude, the background expected when looking for a high mass displaced vertex with at least five tracks is small and less than one expected vertex. This result, of a minimal background, strongly emphasises the unique experimental opportunity for this type of unique signatures.

11. Results

Particle physics experiments have in the recent years started to adopt the same scheme of reporting results by setting upper limits on the variable of interest e.g. production cross-sections, branching ratios and masses of particles. Uniformity in the practice and methods used allows for direct comparison between experiments within the high energy physics community and potentially with close-lying fields like astroparticle physics. Therefore, the first section in this chapter includes short introduction to the limit-setting procedures. The material in this section is heavily based on the recommendations for limit-setting procedures for the DØ experiment [88]. The method has been utilised by many experiments through the years and is also common practice for the A Toroidal LHC ApparatuS (ATLAS) Experiment. The result of the $DV + jets$ search is presented afterwards, followed by the model-independent and model-dependent limits. A short discussion concludes the chapter, comparing the results with previously set limits.

11.1. The CL_s Method

The well-known statistical limit-methods of the Bayesian credible intervals or Frequentist confidence intervals are sound functioning approaches when the statistics are large enough so that the results are dominated by the signal. However, if this is not the case, and the experimental data is plagued with low statistics or rather overshadowed by large backgrounds - the latter which is mostly true in the front-edge experiments. Both methods possess a weakness to misinterpret the frequentist results as testimony about a theory founded

on the collected data instead of the proper interpretations about the data's compatibility with said theory [89].

In the CL_s method two null hypotheses are evaluated by two likelihood functions $L(b)$ and $L(s + b)$. The background hypothesis b is confirmed, if the observed data can be explained by existing physics, i.e. Standard Model (SM) physics. Rejection of b means that new physics are required to explain the observations. Since typically data are not background free a second statement about the signal+background, the $s + b$ hypothesis is constructed. Both hypotheses are put to the test by a test statistic that is defined by one point σ_{obs} - the combined result of a search using the whole set of experimentally collected data. As an example, the ratio Q of likelihood functions constructed by Poisson probabilities P:

$$Q = \frac{P(q|s+b)}{P(q|b)}, \tag{11.1}$$

with the Poisson probabilities:

$$P(q|H) = \prod_{i=1}^{n_{bins}} \frac{(H_i)^{n_i} e^{-H_i}}{n_i!}, \tag{11.2}$$

where H_i is the hypothesis under testing. The test statistics Eq. 11.1 is commonly rewritten in logarithmic form using Eq. 11.2 with $H_i = s_i + b_i$ and $H_i = b_i$:

$$-2\ln Q = 2\sum_{i=1}^{n_{\text{bins}}} s_i - 2\sum_{i=1}^{n_{\text{bins}}} n_i \ln(1 + \frac{s_i}{b_i}), \tag{11.3}$$

where $\ln(1 + \frac{s_i}{b_i})$ can be seen as an event weight. Vital to the procedure is the background estimation that corresponds to b_i and depends generally on the SM background cross-sections, the integrated luminosity, and selection efficiencies. The signal s_i depends on the signal cross-sections, the branching ratios, the integrated luminosity, and the signal efficiency. Finally, n_i represents the number of events in bin i. In the case of the Displaced Vertex (DV)

analysis, the background is mostly dependent on mis-reconstruction and the crossing fraction as described in Chapter 10, as well as the integrated luminosity and the selection efficiencies. Typically, a number of simple Monte Carlo (MC) simulations are generated to get a satisfying number of events for signal and background. An event-weight as previously defined is assigned to each event depending on the test-variable.

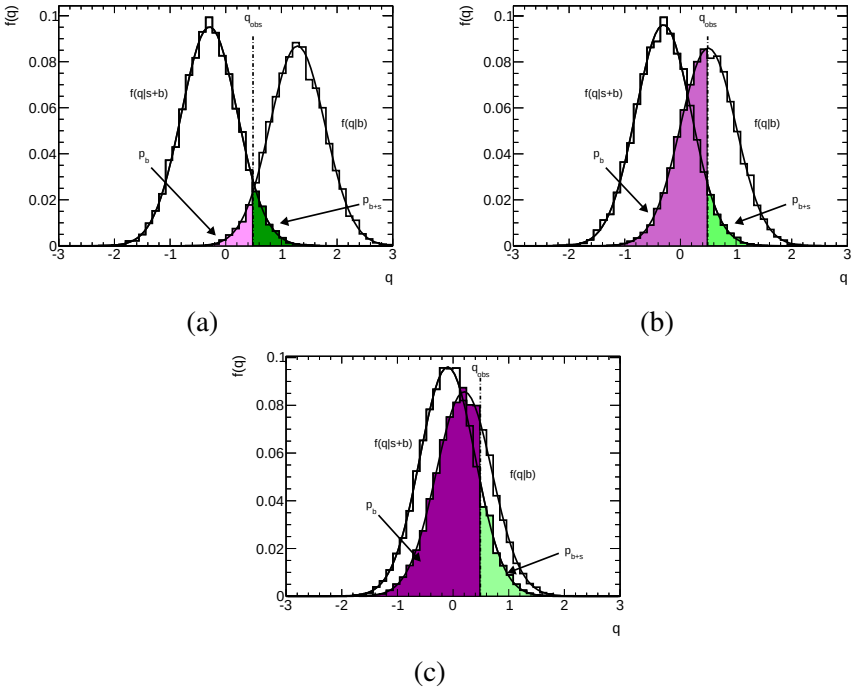

Figure 11.1.: Schematic view of the probability density for the two hypotheses, $f(q|s+b)$ and $f(q|b)$ as Gaussian distributions, and of how the signal distinction, that is p_{s+b}/p_b changes as the probability, i.e. the production cross-section for signal s, decreases from top to bottom plot.

Figure 11.1 shows an example of the probability density functions for $f(q|s+b)$ and $f(q|b)$ as Gaussian distributions. The probability that the background hypothesis is true given the observed value σ_{obs} is represented by the p-value

p_b, indicated by the partially magenta coloured histogram. Likewise, the green histogram shows p_{s+b} as the p-value of the signal+background hypothesis. As the properties change for both distributions, i.e. different production cross-sections for the signal processes or major significant background, the signal distinction p_{s+b}/p_b decreases from (a) to (c).

The individual confidence level of the background and the signal+background hypotheses are tested by Eq. 11.4 and Eq. 11.5 respectively.

$$p_b = 1 - CL_b = P(Q \geq Q_{\text{obs}}|\text{background}), \tag{11.4}$$

$$p_{s+b} = CL_{s+b} = P(Q \leq Q_{\text{obs}}|\text{signal + background}), \tag{11.5}$$

Each equation tests the consistency of the data with the hypothesis to a certain confidence level. The hypothesis is deemed as excluded at a 95% confidence level if $CL_x < 0.05$. The main point here is that the CL_{s+b} hypothesis is sensitive to the statistical behaviour of the background. Even if the signal efficiency is minute when the background is lower than expected due to statistical fluctuations, the signal+background hypothesis can be excluded even if the experiment lack any sensitivity to said signal. Not as stringent as CL_{s+b} and at the loss of some sensitivity with the use of the signal hypothesis, Eq. 11.6 can avoid the foretold problems. The signal is presumed to be excluded if $CL_s < 0.05$

$$CL_s = \frac{CL_{s+b}}{CL_b} \tag{11.6}$$

An example of the CL_s method where a signal hypothesis has been confirmed is the search for the Higgs boson. The ATLAS experiment, in 2012, produced Figure 11.2 [3] using the CL_s method. The solid black line represents the CL_s hypothesis defining the signal strength of the Higgs boson as a function of m_H at a 95% confidence level. The dashed line represents the background-only hypothesis CL_b with green and yellow error bands for $\pm 1\sigma$ and $\pm 2\sigma$. The bump at around 125 GeV shows that the signal strength at this mass is several sigma larger than the expected background.

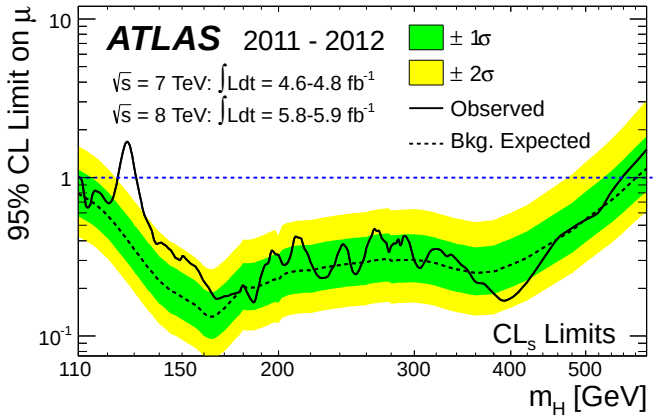

Figure 11.2.: Limits at a 95% confidence level on the signal strength as a function of the mass of the Higgs Boson set by ATLAS using the CL_s method on data collected during 2011 and 2012 [3].

11.2. Search Results

Preceding the completion of this thesis, the displaced vertex search was published, on behalf of the ATLAS Collaboration, and the search results for the $DV + jets$ channel, together with four other DV channels were reported in the article *Search for massive, long-lived particles using multitrack displaced vertices or displaced lepton pairs in pp collisions at* $\sqrt{s} = 8$ TeV *with the ATLAS detector* [5]. This publication reported that no events containing a massive, high track multiplicity displaced vertex have been observed in any channel. Since this thesis is based upon this Supersymmetry (SUSY) search and vice versa, the results in this paper are the same as the ones presented in this thesis. However, additional upper limits on the model-dependent cross-sections on extra signal points for R-Parity Violation (RPV) scenarios are included in this thesis.

All the vertices passing the full set of the selection requirements described in Section 9.1, *except* for the signal region criteria, are plotted in Fig. 11.3 [5].

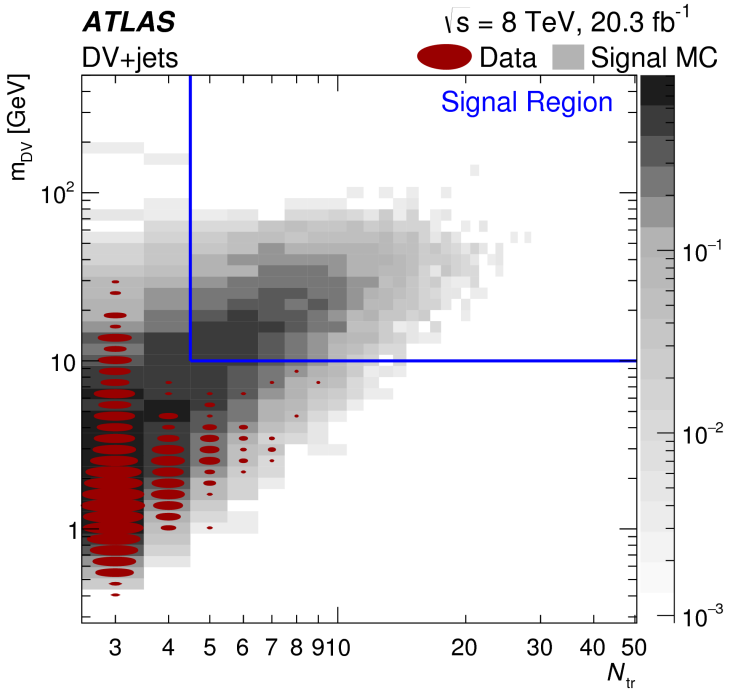

Figure 11.3.: The number of reconstructed displaced vertices, passing all the event and vertex selection criteria with the exception of the signal region requirements, is shown by red ellipses for data. The area of the ellipses is logarithmically proportional to the amount of vertices. A signal MC sample, SIGMC1, is added to provide a comparison of how a signal might look. The signal region is indicated by the blue box. No vertices in data are noted in the signal region [5].

These vertices are plotted in the two dimensional frame of invariant mass versus the track multiplicity of the vertices. The red ellipses are the vertices seen in data and the gray histogram shows one of the signal MC samples SIGMC1. The blue rectangle indicates the signal region with $N_{tr} \geq 5$ of the DV and the mass, $m_{DV} > 10$ GeV. No signal vertex is observed as clearly seen by the lack of any red ellipse (data) in the blue rectangle. Figure 11.4 provides a split view in the form of three projections of the invariant mass for

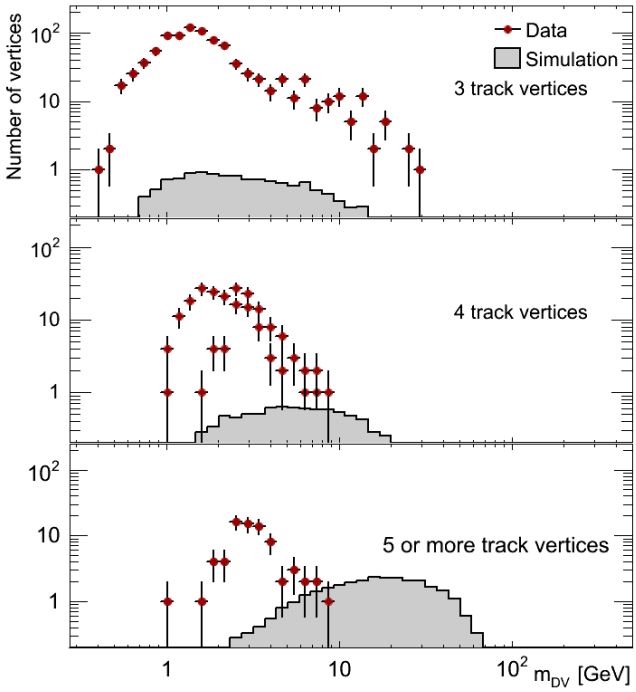

Figure 11.4.: The number of reconstructed displaced vertices, divided into their track multiplicity. The top plot shows three track vertices, the middle plot shows four track vertices while the bottom shows track multiplicities of five or more tracks. Both data and a signal MC sample (SIGMC1) is added to show the comparison. The MC sample is normalised to the luminosity of data.

three, four, and five or more track in the DV starting from the top going down in the plot, simulation normalised to luminosity. The signal significance of the MC (gray) is seen when the track multiplicity increases. It is clear that data (red points) are not present at high mass and high track multiplicities.

Table 11.1 shows the number of events in data remaining after each of the selection cuts, similarly to what was done in Table 9.1 for one of the signal MC samples. The trigger, the pre-selection and the signal region requirements remove the majority of events.

Table 11.1.: The Event Selection includes all the requirements for data. The triggers, pre-selection, primary vertex and displaced vertex cuts are listed in the Table with the corresponding Relative and Overall efficiencies of that specific selection cut. The DV_{nTrk} is the strictest and removes virtually all of the remaining events. No events containing a high track multiplicity, massive vertex are seen after all applied selection criteria.

Event Selection			
	Number of Events	Relative Efficiency (%)	Overall Efficiency (%)
All Events	26563830	100	100
Trigger	5654866	21.3	21.3
Pre-Selection	458891	8.1	1.7
PV Selection	458244	99.9	1.7
Jet Cleaning	143177	31.2	0.5
Displaced Vertex Selection			
DV Selection	74758	52.2	0.3
Material Veto	44302	59.3	0.2
$DV_{\text{nTrk}} \geq 5$	73	0.2	$0.3{\cdot}10^{-3}$
$DV_{\text{mass}} > 10$	0	0	**0**

A powerful feature of the displaced vertex analysis is that it is developed to be near generic, independent of the physics models. Therefore, the search is sensitive to any massive Long Lived Particle (LLP) decaying in the Inner Detector (ID) yielding a sufficient amount of tracks. Owning to this fact, upper limits on the production cross-section of a LLP can be set in a model independent approach. This will be discussed in Section 11.3. Exclusion limits, interpreted for the RPV SUSY, are provided in Section 11.4 for all the RPV couplings in the signal samples.

11.3. Model Independent Limits

A model independent limit is set by considering the probability that a produced vertex with a certain cross-section would have been observed in the collected amount of data with the given background. An upper limit on the

visible cross-section given the observed number of events N can be derived from;

$$N = N_{\text{signal}} + N_{\text{background}} \quad \text{where,} \tag{11.7}$$

$$N_{\text{signal}} = \epsilon \cdot \sigma_{vis} \cdot L. \tag{11.8}$$

The number of background events $N_{\text{background}}$ simply is the number estimated in Section 10. The number of signal events N_{signal} expected is given by the combination of the integrated luminosity L and the efficiency ϵ times the cross-section σ_{vis}. The model independent upper limit on the cross-section can then be derived from rewriting Eq. 11.8 assuming 100% acceptance and efficiency;

$$\sigma_{\text{vis}} \approx \frac{N - N_{\text{background}}}{L} \tag{11.9}$$

Inserting the known values, $N_{\text{upper}} = 3.0$, which is a +95% interval of the observation of zero events, the luminosity $L = 20.3$ fb^{-1} and the estimated number of background vertices 0.41 vertices per event. One then, obtains;

$$\sigma_{\text{vis}} \approx \frac{3 - 0.41}{20.3} \approx 0.13 \text{ [fb]}. \tag{11.10}$$

However, this is only a rough estimate. To obtain the real upper limit on the production cross-section all uncertainties on the background and luminosity must be included in the calculation as well as including the statistical test using the whole likelihood expression (Eq. 11.3). Furthermore, the statistics are scares i.e. there are the zero observed events. Instead to ensure statistical certainty, a set of MC simulations is generated to test the probability of a zero observation as described in the previous section of the CL_s method. The uncertainty on the background estimation is ±0.06 vertices and the uncertainty in the luminosity measurement on 2012 data is ±2.8% [52]. An upper limit on the cross-section at a 95% confidence level is set at 0.14 fb [59].

11.4. Model Dependent Limits

Similarly, using the CL_s method, model dependent upper limits are set. These limits are set considering the specific production and decay processes, including the masses and coupling strengths.

What is needed is to set model dependent limits are the following points.

- The signal efficiencies of the specific process for the analysis. All these are computed for different values of $c\tau$ shown in Section 9.4 for all the different couplings.
- Any uncertainties on the signal efficiency are necessary to be included in the limit setting procedure. Large uncertainties reduce the possibility to set strict limits so it is important to have as small uncertainties as possible.
- As for the visible cross-section limits, the uncertainty on the luminosity is included.
- The background and the uncertainty on the background estimation needs to be input into the calculations.

A set, corresponding to 2000 MC simulations is generated according to a probability distribution function (PDF) constructed as a Poisson distribution given the information listed above (yielding a test statistics like the one given in Eq. 11.3). These test samples are created to test the likelihood hypothesis of the CL_s method. In the case of this analysis there is only one bin ($n_{\mathrm{bins}} = 0$). Each simulation gives a value whether or not the given hypothesis is in agreement with the observation, if it is excluded by 5%. If 95% of the test statistics shows the same results the upper limits on the production cross-section of the specific process can be set using the equation;

$$\sigma_{\mathrm{prod}}(c\tau_i) \approx \frac{N - N_{\mathrm{background}}}{L \cdot \epsilon_i}. \tag{11.11}$$

The limits are set, going from 1 mm to 1 meter.

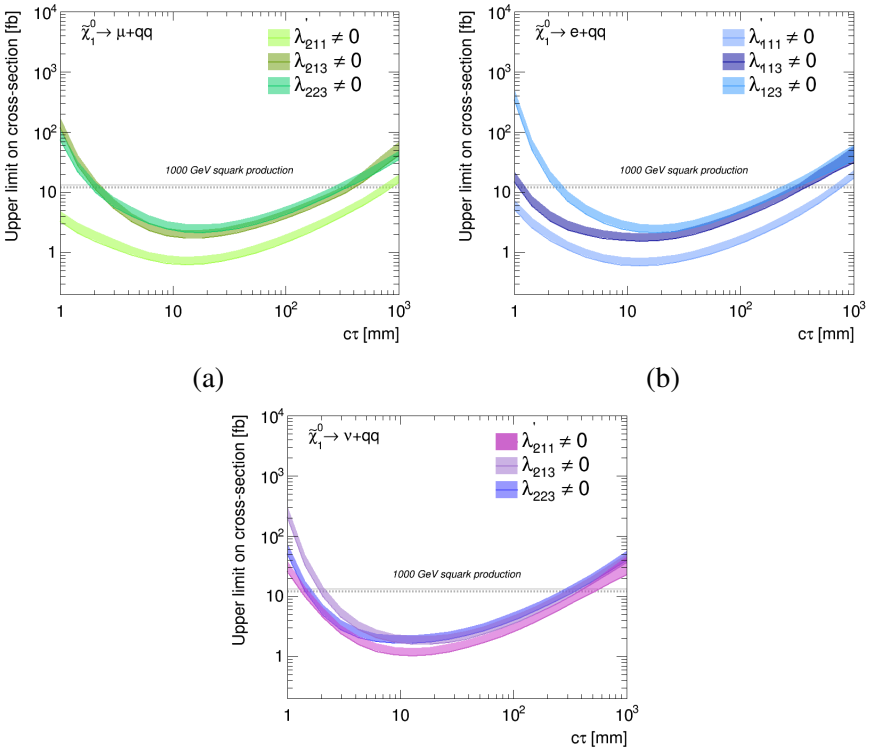

Figure 11.5.: The model dependent limit for production cross-section for the SUSY with RPV is shown for a set of various scenarios where one of the RPV couplings $\lambda'_{ijk} \neq 0$. The limit curves are the upper limit on the production cross-section versus the proper decay length $c\tau$. The Lightest Supersymmetry Particle (LSP) decay into $\mu + qq$ is shown in (a). Similarly, (b) shows the model dependent limits for neutralino decay into final states containing an electron, $e + qq$. Finally, (c) includes the decays to jets and a neutrino, $\nu + qq$.

The model dependent limits, as a function of $c\tau$, for the couplings $\tilde{\chi}_1^0 \to \mu + qq$ are presented in Fig. 11.5 (a) for both light and heavy flavour jets. Similarly, Fig. 11.5 (b) illustrates the limits for the decays, $\tilde{\chi}_1^0 \to e + qq$.

Finally, Fig. 11.5 (c) includes the limits for the decays with a neutrino in the final state, $\tilde{\chi}_1^0 \rightarrow \nu + qq$. The gray line in the plots indicates the cross-section for the squark production, $pp \rightarrow \tilde{q}\tilde{q}$ where the squarks have mass of 1000 GeV. The results are divided into through which lepton flavour the decay occur i.e. index i in λ_{ijk} is set to either 1 or 2 for electron and muon respectively. Stating again to remind the reader, the analysis is only done considering a DV plus jets, no lepton object is actually required in the final state. The results for $\tilde{\chi}_1^0 \rightarrow \nu + qq$ show less stringent exclusions as this mode always "lose" one track due to the invisible neutrino.

At lower lifetimes, the particles are more likely to decay outside the fiducial volume, e.g. at radius less than 4 mm. This is where the analysis lack any sensitivity as vertices at these distances are removed by cuts (Section 9.1.2). The upper limits are weaker in just these intervals of $c\tau \leq 4$ mm and this fact is illustrated the limit curves in all three plots (a) (b) and (c) in Fig. 11.5.

Due to the large statistical uncertainties at very small values of $c\tau$ the limit setting procedure fail to converge and produce fluctuating values depending on the signal sample considered. Again, to stress the point, the analysis is not really sensitive to these short lifetimes as the majority of LLP will decays before the fiducial region. The same goes for larger values of proper decay lengths $c\tau > 100$ mm, where instead the particles are more likely to decay at radius larger than the fiducial volume at $r > 300$ mm. Here again, the upper limit curve turns up again and cannot make a strict exclusions as the analysis is not as sensitive.

When considering heavy flavour quarks in the decay with the couplings λ'_{213}, λ'_{223}, λ'_{113}, and λ'_{123}, the analysis again loses signal efficiency (Table 9.2) and the limits are slightly worse compared to decay only including light flavour jets. This fact is especially obvious in Fig. 11.5 (a) and (b) where the curves belonging to λ'_{211} and λ'_{111} are clearly provide stricter exclusions. The differences seen are down to that when heavy flavour quark decays produce secondary or rather in this case, a tertiary vertex from, for an example a B-meson. The displaced decay will remove energy and with that, tracks from the initial displaced vertex. Less tracks will mean significant loss in vertex reconstruction efficiency, this fact has been mention before and can be plainly

Table 11.2.: Showing the upper limits on the production for the given processes at four different values of proper decay length $c\tau$.

Coupling	Upper limit on cross-section [fb]			
	1 mm	10 mm	100 mm	1000 mm
$\tilde{\chi}_1^0 \rightarrow \mu + qq$				
λ'_{211}	3.1	0.6	1.6	13
λ'_{213}	113.7	1.9	4.0	32.2
λ'_{223}	68.4	2.1	4.3	35.6
$\tilde{\chi}_1^0 \rightarrow e + qq$				
λ'_{111}	5.0	0.4	1.6	18.4
λ'_{113}	1.7	1.7	3.2	21.3
λ'_{123}	305.2	2.1	4.5	20.9
$\tilde{\chi}_1^0 \rightarrow \nu + qq$				
λ'_{211}	27.8	1.0	1.6	21.8
λ'_{213}	203.2	1.8	4.9	39.9
λ'_{223}	41.8	1.8	4.8	37.1

seen in Fig. 9.1 and also in the signal efficiency plots in Fig. 9.4. Table 11.2 includes numerical values of the upper limits on the cross-sections for all the nine signal samples at four points of $c\tau$ = 1, 10, 100 and 1000 mm.

The upper limits on the production cross-sections are difficult to directly translate into limits on the couplings as many factors are involved - the production particle mass, the LLP mass, the lifetime, and the coupling strength. What one can do is to re-interpret the signal efficiencies and significance. Unfortunately, performing such a type of analysis is outside the scope of this thesis. However, in the following discussion section, the results of two re-interpretations, performed by theorists and are based on several experimental searches for long lived particles performed, are included to provide a comparison of the DV analysis and other experimental searches.

11.5. Discussion

Generally, the light flavour decays provide a stricter limit on the cross-section σ_{prod} as can be seen for the limit curves in Fig. 11.5 for the couplings λ'_{i11}. The reason for this is simply the larger signal efficiencies owning to the improved vertex reconstruction efficiencies for the events containing light flavour jets. An explanation for the parabolic behaviour of the limit curves simply translates into the signal efficiency's performance as a function of $c\tau$. For example, take the light blue curve corresponding to λ'_{111} in Fig. 9.8. Here, the efficiency increases from 5% up to 25% as $c\tau \rightarrow 10 - 20$ mm. After passing the efficiency peak, the efficiency once again drops as $c\tau \rightarrow 1000$ mm. Now, observe the same light blue limit curve in Fig. 11.5 (b), then the corresponding behaviour can be seen. The strictest limit is set around $c\tau \sim 20$ mm where the efficiency peaked. Looser limits are set at either side of the peak value as the signal efficiency is lower for values of $c\tau < 4$ mm and $c\tau > 100$ mm. Comparatively, the model independent limit value of ~ 0.14 makes sense assuming a 100% efficiency.

The previous ATLAS search, in 2013, reported limits only for the $DV + \mu$ channel using the same data set collected in 2012 at $\sqrt{s} = 8$ TeV of an integrated luminosity of 20.3 fb^{-1}. Upper limits on the cross-section for 1000 GeV squark production set were at 5.4 fb [62] (The purple curve in Fig. 11.6). Developing the $DV + jets$ final state has open up for the capability to produce stricter exclusion limits. Comparison of the old 5.4 fb to the new upper limit of 0.14 fb indicates the power of the $DV + jets$ channel in this area.

Direct comparisons of results are not straight forward as the majority of searches is in one way or the other dependent on the target models. Often the limits are set on the mass of the LLP or on the branching ratios. ATLAS has a wide range of searches for LLPs. The searches in this range are aimed at SUSY scenarios that might produce a LLP and other exotic Beyond Standard Model (BSM) theories e.g. Hidden Valley. A summary plot for searches of SUSY in ATLAS is shown in Fig. 11.7. Lower limits on the mass of LLP are given as results of several searches, in the part entitled "Long-lived particles". The Displaced Vertex Analysis result from the $DV + \mu$ channel is included in this plot [62], and is yet to be updated with the results from the latest publication.

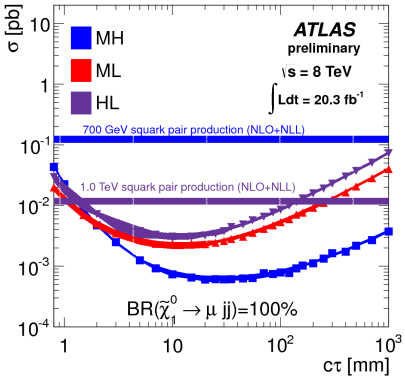

Figure 11.6.: Upper limits on the production cross-section for the $DV + \mu$ channel from the previous publication of the displaced vertex analysis in reference [62]. Setting limits for RPV SUSY on three different mass points. The first letter in the legend, M indicates a squark mass of 700 GeV while an H represent 1000 GeV. The second letter is the neutralino mass, where H is a mass of 494 GeV and L is a lighter version of 108 GeV.

However, the old provided mass limit on $\tilde{q}$ still holds for the RPV scenario. Moreover, the prompt searches for RPV SUSY are listed with similar mass lower limits.

Outside ATLAS Collaboration the most powerful limits set on LLP of similar lifetimes is by the CMS Collaboration in their search *Search for long-lived neutral particles decaying to quark-antiquark pairs in proton-proton collisions at* $\sqrt{s} = 8$ *TeV* [58]. They report, in this publication limits for RPV SUSY of $0.5 - 3$ fb for proper decay length of $2 - 40$ cm.

A review of the LLPs searches at the Large Hadron Collider (LHC) using Run-1 is summarised in reference [91]. Several LHC searches for long-lived particles are recasted on RPV, bRPV, GMSB and split-SUSY scenarios. The previous mentioned CMS search proves to be extremely powerful at setting exclusion limits for lifetimes from $0.1 - 10^6$ mm. Figure 11.8 shows a plot from this study, where the results from several searches are recast on the Dy-

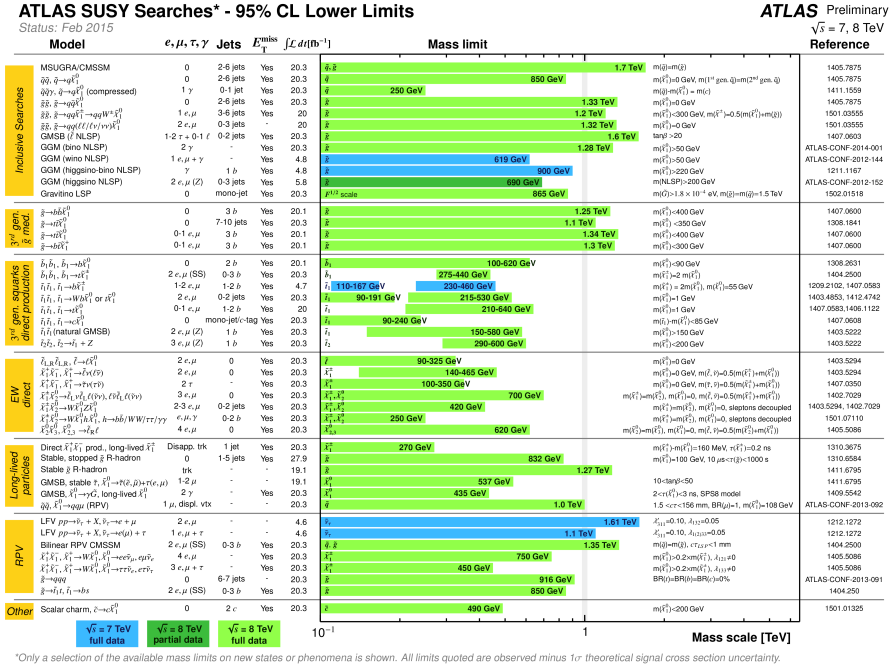

*Only a selection of the available mass limits on new states or phenomena is shown. All limits quoted are observed minus 1σ theoretical signal cross section uncertainty.

Figure 11.7.: The current lower limits on the production sparticles in various SUSY scenarios [90] (Status at 2015 February). Limits on long lived particles are set for a number of models including RPV with the results from the $DV+\mu$ search in 2014 [62] (The summary plot has not been updated to include results published after February 2015). Comparable mass-limits are set for prompt RPV.

namical RPV scenario. The limits are set on the $\tilde{t}$ squark, for the decay $\bar{b}\bar{b}$-pairs. This is a different process than the one studying in this thesis however, it is hard making comparisons without doing this kind of recast as seldom the analyses target the exactly same decays or masses. The CMS Experiments search for LLP decaying to quark-antiquark pairs (labelled in the figure as "CMS dijet") proves to dominate, and provides the strictest limits on the stop mass for a wide range of $c\tau$. This report precedes the publication of the latest ATLAS DV search and only include the old channel of a DV+μ that is significantly less generic. This plot is added as a reference to be compared

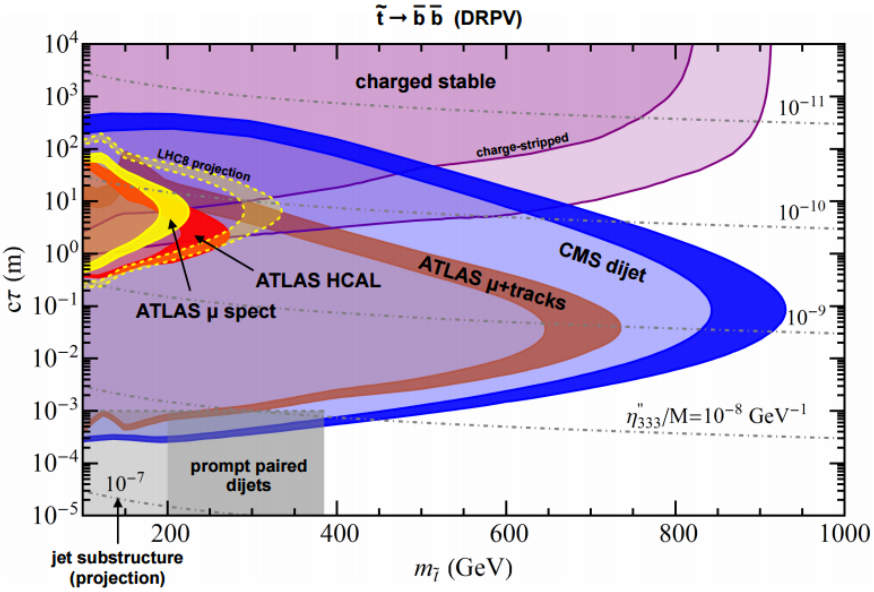

Figure 11.8.: The result of recasting several experimental searches at the ATLAS Experiment and the Compact Muon Solenoid (CMS) Experiment. Showing limits on $m_{\tilde{t}}$ versus proper decay length $c\tau$ on the Dynamical RPV framework for mass limits on decays $\tilde{t} \rightarrow \bar{b}\bar{b}$. The 2013 ATLAS search for $DV + \mu$ is labeled as "ATLAS μ+tracks" while the CMS search for LLP decaying to quark-antiquark pairs is named "CMS dijet". The latter dominates the parameter space for the meta-stable particles, much owning to its acceptance and efficiency [91].

with the newer results. In a later, similar, publication targeting *Phenomenology of Long-Lived LSP with R-Parity Violation* by C. Csáki et al. includes the latest iteration of the ATLAS DV analysis [5]. The results are yet again compared with the "CMS dijet" analysis but also with heavy stable charged particle searches from CMS [93] for longer lifetimes. Figure 11.9 from this newer interpretation, again shows the same scenario as Fig. 11.8. In the target lifetime range the ATLAS $DV + jets$ (marked as ATLAS-jets) provides the most rigorous exclusions. This is true for additional plots in this study shows and indicate the power of the new ATLAS DV analysis.

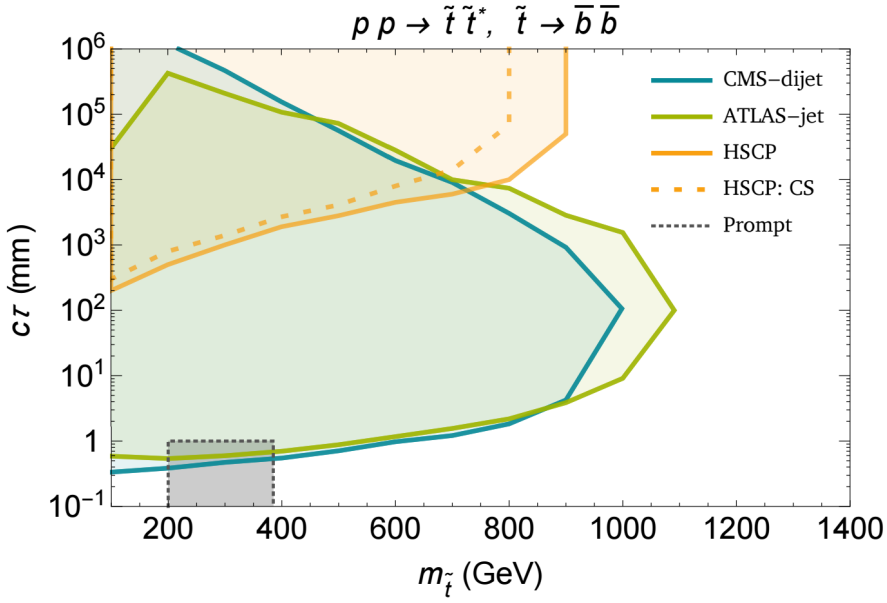

Figure 11.9.: The exclusion on the stop mass versus lifetime of an assumed long-lived LSP in R-parity violating scenarios are shown recasting a number of experimental analysis, set by C. Csáki et. all in their article [92]. The curves shows the respective exclusions at 95% CL for each of the analysis considered, the CMS-dijet, ATLAS-jet (the ATLAS DV+jets search treated in this thesis), HSCP (heavy stable charged particle searches by CMS) and limits on the prompt scenarios. The most powerful exclusion is provided by the ATLAS DV+jets search.

To summarise; The Displaced Vertex Analysis at the ATLAS Experiment has provided, at the date of writing, the most stringent upper limits of massive LLP with proper decay lengths $c\tau$ of $1 - 1000$ mm. Owning to the fact that the analysis is generic and is sensitive to any massive particle decaying few millimetres from the Interaction Point (IP) regardless of the underlying theory. The search is therefore extremely powerful, given the near zero background events expected, if a vertex is found it could directly point towards a discovery. Finding out exactly what particle decayed and which model it belongs to would be a secondary matter.

12. Conclusion

Several shortcomings in the Standard Model (SM) theory of particle physics and the gap between the energy scale of the quantum world and the macro universe indicate that the theory, despite its success, is not a complete theory. There exist numerous theories making extensions upon the SM, attempting to offer explanations to the phenomena yet to be understood. The presence of significantly long-lived particles is common in several of these theories of *new physics*; as a consequence of e.g. mass degenerate particles, weak coupling strengths or suppressed decays due to splitting in the mass spectra. These particles would evade the standard experimental searches for *new physics*. Neglecting to explore the territory of long-lived particles is passing up on a great opportunity to make a new discovery. This is the case, especially, considering the current status, at the time of writing, of the experimental searches as no signs of beyond the SM physics have been observed.

The experimental search for massive Displaced Vertex (DV) originated from the decays of massive Long Lived Particle (LLP) has been presented. Data collected in 2012, by the A Toroidal LHC ApparatuS (ATLAS) Experiment, at the Large Hadron Collider (LHC), are scrutinised to find collision events containing signs of LLP decays. The DV analysis is a universal search technique in the sense that it is not specifically dependent on an underlying theoretical model. The analysis is designed to be sensitive to a unique type of signature lacking counterpart in the SM. Thus, an observation of a DV could point directly to *a discovery* making the search an extremely powerful tool.

This thesis discuss the newly developed channel searching events with a $DV + jets$ final state by the ATLAS Experiment and the interpretation of the search results on the R-Parity Violation (RPV) Supersymmetry (SUSY) scenario.

Removing the previous analysis criterion requirement of an associated muon to the vertex allowed for increased signal efficiency. Furthermore, yielding a higher signal acceptance of LLP decays, now including decays bereft of any leptons. The analysis is track based in that only a number of tracks are needed to reconstruct the LLP decay point. The only exception is that events containing a number of relative high transverse momentum jets are selected, i.e. jet objects are triggered on. The signal efficiency to reconstruct a displaced vertex is approximately 25%, here stating the maximum value but it varies with proper decay lengths ($c\tau$). Decreasing efficiency is seen depending on the decay length from the interaction point of the proton-proton collision, owing to direct consequence of fewer and fewer hits in the silicon tracking volume as the secondaries cross less tracker layers. Comparatively, the $DV + \mu$ channel has for similar signal samples maximum efficiencies at 10%.

The Hadronic Interaction Analysis that studies the material distribution in the ATLAS Inner Detector (ID) has made it possible to create a material map. Nuclear interactions with the material are the largest source of background vertices. However, this contribution is reducible by vetoing any vertex found in the material regions. The material map has been extended, to include a much larger volume yielding that the fiducial radial extent increased from $r < 180$ mm to $r < 300$ mm. The effective volume, the volume left after applying the veto has been increased from 0.02 m^3 to 0.07 m^3.

The Hadronic Interaction Analysis is also a tool to quantify the material budget in the detector and by using Re-Tracking increased the targeted total volume of the material study from 0.09 m^3 to 0.3 m^3, which is an increase by a factor of about 3. This analysis provides precise measurements of the material distribution as well as pointing out deficit in the material description where for instance components are missing. The results have yielded an improved modelling of the tracking efficiency. This technique is on the front line of Run-2 as the material budget needs to be updated due to the insertion of an additional detector layer. The analysis has quickly provided new radiology imagery of the detector and pointed out missing amount of material in the simulations, with greater details than any other study can due to the resolution.

A small dilemma with the increased acceptance for the $DV + jets$ channel

is that it does not only hold for signal events but applies similarly for background events. A new more sophisticated method to estimate the amount of background vertices became more vital for this final state (in the previous analysis, associating a muon with the vertex help reducing the background significantly to a factor 1% of the one of the channel treated in this thesis). Since there are no massive displaced vertices originating from known physics, the background processes to this analysis are fake and mis-reconstructed vertices. Subsequently, an advanced method, to estimate the amount of fake vertices that could imitate a signal vertex, has been developed and exhaustively optimised to take into account all the difficult correlations of track and vertex parameters. The estimated number of background vertices to the $DV + jets$ channel is 0.41 ± 0.06 vertices, which includes a total uncertainty on the method of 14%, both systematic and statistical uncertainties. The number of estimated vertices is less than one. The preceding method used to estimate the fake vertices had an uncertainty of $\sim 100\%$. Applying this exceedingly large uncertainty to 0.41 vertices yield a number close to one, which would handicap the analysis (which makes a point out of being a zero background analysis) where more than one event needs to be observed to point towards a discovery. The significantly improved background estimation technique is therefore, crucial to the $DV+jets$ channel. Moreover, a more precise determined number of expected background events reduce the uncertainty on the exclusion limits.

The results reported that no event containing a massive, high-track multiplicity DV was observed. Upper limits on the production cross-section were set for the case of RPV SUSY. Furthermore, a model independent limit is set to 0.14 fb yielding a significant improvement from the preceding limit of 5.4 fb.

For RPV SUSY of $\tilde{q}\tilde{q}$ where $\tilde{q} \rightarrow \tilde{\chi}_1^0 + qq$ and finally $\tilde{\chi}_1^0 \rightarrow l + qq$ limits on the upper production cross-sections are set from 100 fb for $c\tau < 4$ mm and $c\tau > 100$ mm down to 0.5 fb for the interval 4 mm $< c\tau <$ 100 mm; given decay of the neutralino through the RPV coupling λ'_{211}, λ'_{213}, λ'_{233}, λ'_{111}, λ'_{113}, and λ'_{123} The ATLAS Experiment results are slightly stricter than the ones reported in the Compact Muon Solenoid (CMS) Experiments search for DV at 0.5 fb.

A. Definitions

A.1. Definitions

This section aims to provide the unfamiliarised reader with a summary of common definitions and concepts used in High Energy Physics (HEP) to facilitate the pace with which the reader can proceed.

- **ATLAS Coordinate Frame** is defined at the centre of the detector as $xyz = [0,\ 0,\ 0]$ (Fig. A.1 (a)). The xyz coordinate frame is a right handed system; with all three axis perpendicular with respect to each other. With the z-axis along the beam line in the anti-clockwise direction. The x- and y-axis make up the transverse plane, perpendicular to the beam line. The x-axis points, inward, towards the centre of the LHC. While the y-axis is directed in the upwards. ATLAS is frequently referred to be a cylindrical frame of reference. The xy-plane is represented by circle coordinates, r for the radial coordinate and ϕ for the angle. The angle with respect to beam line or the z-axis is defined by θ. All these coordinates are demonstrated by the schematic sketch in Fig. A.1 (b).
- **Pseudorapidity η** is a second way, next to θ to described the angle relative the beam axis from a particles trajectory. The pseudorapidity is defined as in Eq. A.1 and Fig. A.1 (c) show the correlation between η and θ.

$$\eta = -\ln\left[\tan\left(\frac{\theta}{2}\right)\right] \tag{A.1}$$

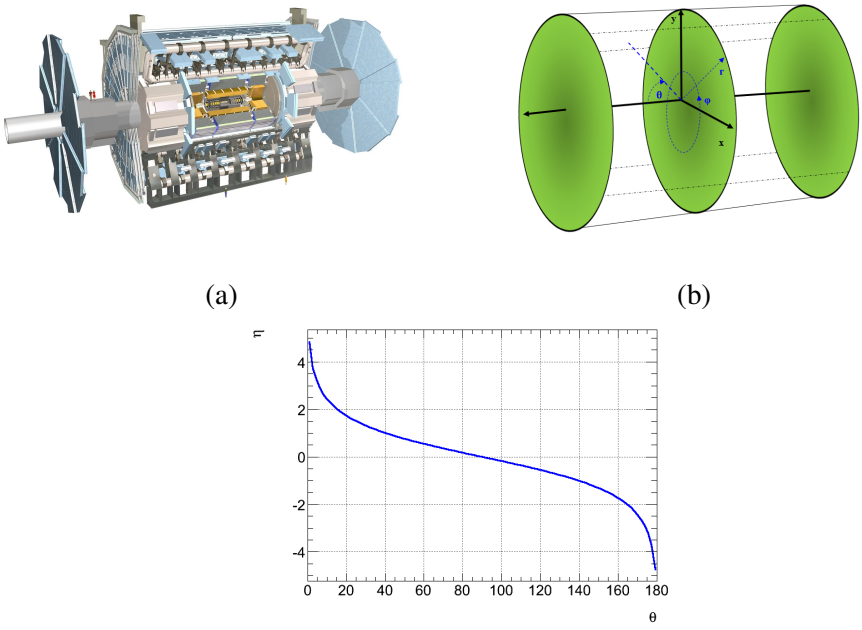

Figure A.1.: The ATLAS detector (a) [94] and (b) the two coordinate representation of the detector. The black coordinates represent the xyz-frame while the blue indicate the $r\phi\theta$-frame. The pseudorapidity as a function of θ is shown in (c).

- **Primary Vertex** is the point at which the partition of the protons' interaction with each other, giving rise to an interaction (interaction point). The primary vertex is reconstructed using the trajectories from the particles created in such an interaction; from the primary tracks. Figure A.2 shows a simple conceptual drawing of the primary vertex close-by the pp-collision. The basic of the vertex reconstruction can be found in Section 7.2.

- **Secondary Vertex** on the other hand is a reconstructed secondary inter-

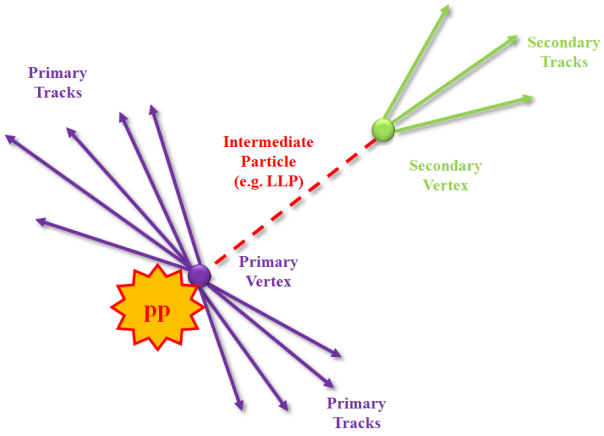

Figure A.2.: The primary vertex is a reconstructed interaction point after the protons collided and interacted.

action. A particle with longer lifetime, created at the primary interaction point, can travel a certain distance in the detector before it decays (Fig. A.2). The displacement of a secondary vertex from the primary vertex depends on the particles' life time. For instance, these particles can be strange mesons or baryons such as, Kaons (K) or Lambdas (λ). Section 7.2.2 aims to explain the techniques used to reconstruct secondary vertices.

- **Particle Track** refers to the trajectory with which a particle traverses the detector. The particles are "tracked" using their interaction with active material in the detector modules; providing with coordinates in space along the trajectory. Section 7.1 explains the methods used to reconstruct particle tracks.

- **Impact Parameters**, in ATLAS, are defined - the standard way - as the distance of the closest approach between object A (e.g. a track) to a reference object B (e.g. the interaction point). **The Transverse** and **the Longitudinal** impact parameters are denoted with $\boldsymbol{d_0}$ and $\boldsymbol{z_0}$ respectively.

- **Perigee** - Closest Distance of Approach - the tracks are in general represented by five parameters (Eg. A.2). These classify all important properties of a given track. The Primary Vertex (PV) or the Interaction Point (IP) is often used as a reference point. Figure A.3 illustrates an example where a track passes close-by the *xy*-plane, the transverse and longitudinal distances are marked as well as the angles.

$$\bar{q} = (d_0, z_0, \phi, \theta, \frac{q}{p}) \tag{A.2}$$

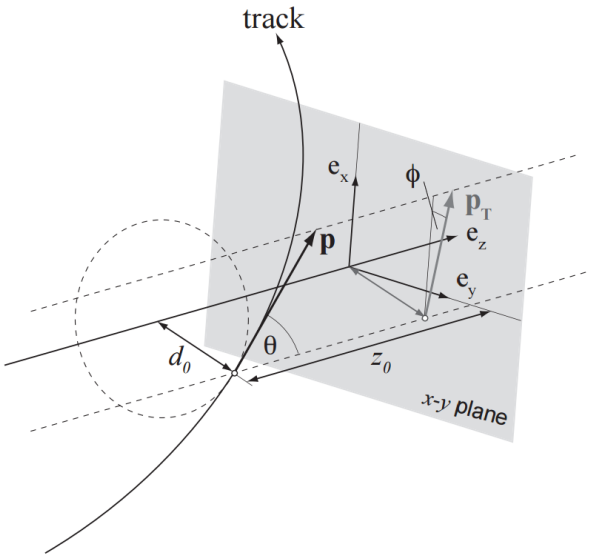

Figure A.3.: The track perigee distance of closet approach, of the track with the respect to a reference point, often the PV [95].

- **Momentum representation**, measuring the momentum of particles is a primary concept of particle physics. It is either done by applying a magnetic field so that charged particles traveling through the detector can measure the momentum given the curvature of the tracks. Or in the case of a neutral particle, the calorimeters provide energy and momentum

measurements by absorption. Commonly an objects momentum is given in the transverse plane p_{T}. By using the angles ϕ, η and θ (where $\theta = 2\tan^{-1}(e^{\eta})$) combined with the p_{T} the whole three-momentum of an object can be defined (Eq. A.3).

$$\bar{p} = \begin{cases} p_x = p_{\mathrm{T}}\cos(\phi) \\ p_y = p_{\mathrm{T}}\sin(\phi) \\ p_z = p_{\mathrm{T}}\tan(\theta) \end{cases} \qquad \text{where, } p_{\mathrm{T}} = \bar{p}\sin(\theta) \tag{A.3}$$

- **Centre of Mass Energy (s)** specifies the energy available in a beam-beam collision experiment; $s = (p_1 + p_2)^2$ where p_i denotes the momentum of beam 1 and 2. The available collision energy is often quoted as $\sqrt{s} = 8$ TeV (here for the value of 8 TeV is which energy the LHC ran during 2012).

- **Luminosity** is defined as the number (N) of events per a time unit (t) given the cross section (σ) of a process [96]; defined as Eq. A.4. **The integrated luminosity** is a way to define the amount of data collected during a defined time period (Eq. A.5). Multiplying the integrated luminosity with the cross section of interest gives the number of observed events for the given process. For example, if you have an integrated luminosity of 1 fb^{-1} one can then expect to observe one event with a cross section of 1 fb. The luminosity is a method to measure the performance and productivity of the detector.

$$L = \frac{1}{\sigma}\frac{dN}{dt} \quad [cm^{-2}s^{-1}] \tag{A.4}$$

$$L_{\mathrm{int}} = \int_0^T L dt \tag{A.5}$$

- **Pile-Up μ** corresponds to the average number of collisions per bunch crossing. The amount of pile-up has a significant impact on the whole event, as additional signals in the sub-detectors make it more difficult to disentangle what happened after collision.

A.2. Extra Signal Efficiency Systematic Uncertainty Plots

Additional plots containing the relative and absolute systematic uncertainties for all signal Monte Carlo (MC) samples can be seen in Fig. A.4 to Fig. A.11 for SIGCM2-SIGMC9 respectively.

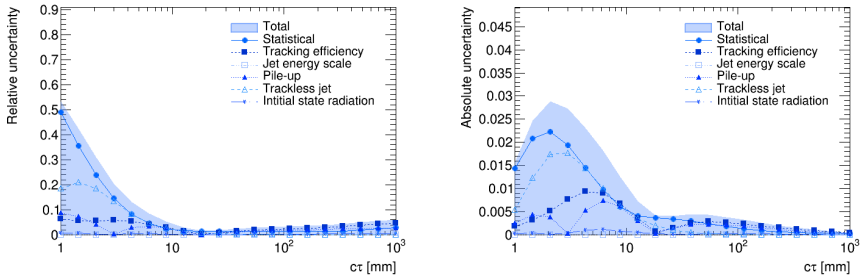

(a) (b)

Figure A.4.: The filled curve is the total systematic uncertainties for SIGMC2 as a function of proper decay length. The different markers show the individual contribution for a single specific source. The relative uncertainty to the signal efficiency is shown in (a) while (b) shows the absolute uncertainty.

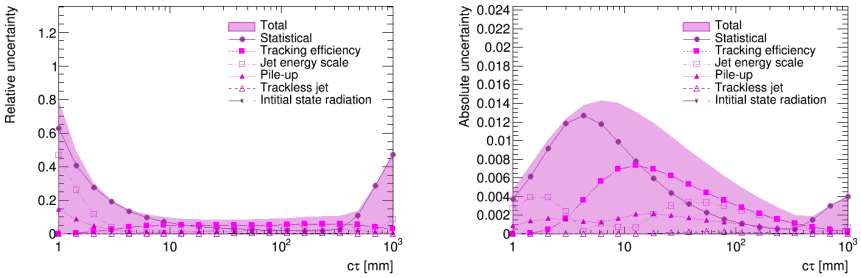

(a) (b)

Figure A.5.: The filled curve is the total systematic uncertainties for SIGMC3 as a function of proper decay length. The different markers show the individual contribution for a single specific source. The relative uncertainty to the signal efficiency is shown in (a) while (b) shows the absolute uncertainty.

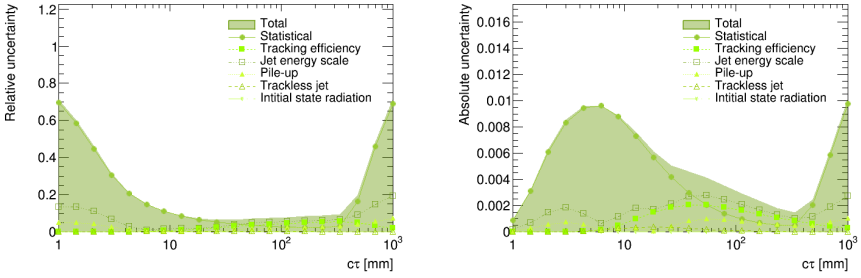

(a) (b)

Figure A.6.: The filled curve is the total systematic uncertainties for SIGMC4 as a function of proper decay length. The different markers show the individual contribution for a single specific source. The relative uncertainty to the signal efficiency is shown in (a) while (b) shows the absolute uncertainty.

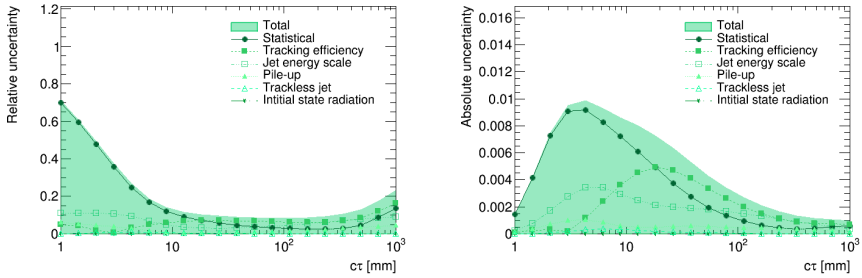

(a) (b)

Figure A.7.: The filled curve is the total systematic uncertainties for SIGMC5 as a function of proper decay length. The different markers show the individual contribution for a single specific source. The relative uncertainty to the signal efficiency is shown in (a) while (b) shows the absolute uncertainty.

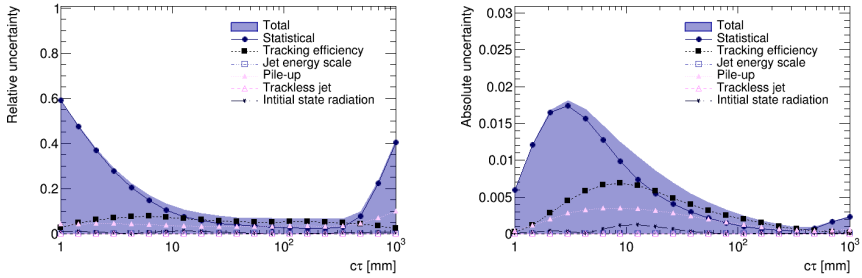

(a) (b)

Figure A.8.: The filled curve is the total systematic uncertainties for SIGMC6 as a function of proper decay length. The different markers show the individual contribution for a single specific source. The relative uncertainty to the signal efficiency is shown in (a) while (b) shows the absolute uncertainty.

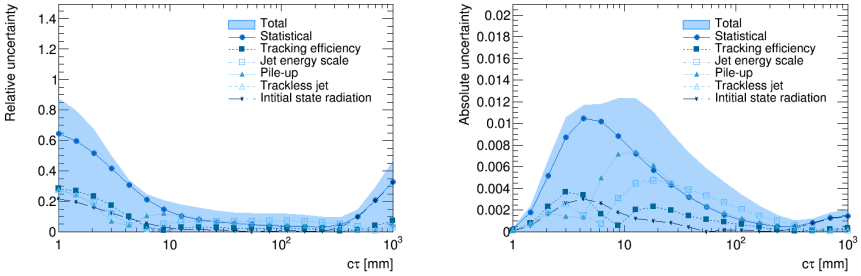

(a) (b)

Figure A.9.: The filled curve is the total systematic uncertainties for SIGMC7 as a function of proper decay length. The different markers show the individual contribution for a single specific source. The relative uncertainty to the signal efficiency is shown in (a) while (b) shows the absolute uncertainty.

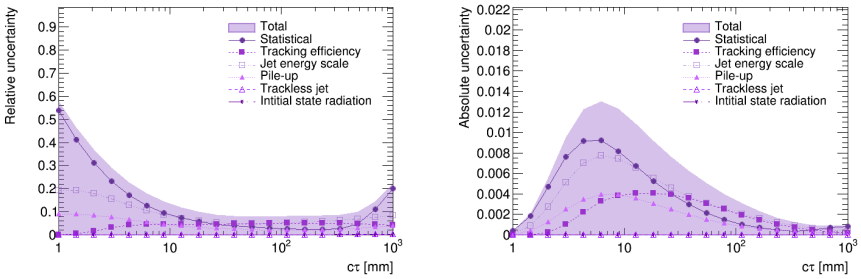

(a) (b)

Figure A.10.: The filled curve is the total systematic uncertainties for SIGMC8 as a function of proper decay length. The different markers show the individual contribution for a single specific source. The relative uncertainty to the signal efficiency is shown in (a) while (b) shows the absolute uncertainty.

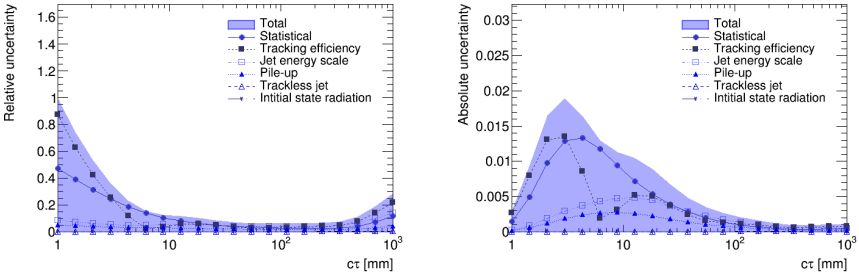

(a) (b)

Figure A.11.: The filled curve is the total systematic uncertainties for SIGMC9 as a function of proper decay length. The different markers show the individual contribution for a single specific source. The relative uncertainty to the signal efficiency is shown in (a) while (b) shows the absolute uncertainty.

Bibliography

[1] J.J Thomson, *Cathode Rays*, The Electrician **39** (1897) 104.

[2] E.Rutherford et al., *The scattering of alpha and beta particles by matter and the structure of the atom*, Philosophical Magazine **21** (1911) 669–688.

[3] ATLAS Collaboration, *Observation of a new particle in the search for the Standard Model Higgs boson with the ATLAS detector at the LHC*, Phys. Lett. **B716** (2012) 1–29, arXiv: 1207.7214 [hep-ex].

[4] CMS Collaboration, *Observation of a new boson at a mass of 125 GeV with the CMS experiment at the LHC*, Phys. Lett. **B716** (2012) 30–61, arXiv: 1207.7235 [hep-ex].

[5] ATLAS Collaboration, *Search for massive, long-lived particles using multitrack displaced vertices or displaced lepton pairs in pp collisions at* $\sqrt{s} = 8$ TeV *with the ATLAS detector*, Phys. Rev. **D92** (7 2015) 072004, arXiv: 1504.05162 [hep-ex].

[6] B. Martin and G. Shaw, *Particle Physics*, Manchester Physics Series, Wiley, 2008, ISBN: 9780470721537.

[7] T. Ferbel, *Experimental techniques in high energy physics*, Addison-Wesley Pub. Co. Inc.,Reading, MA, 1987, ISBN: 9780201114874.

[8] R. N. Cahn and G. Goldhaber, *The Experimental Foundations of Particle Physics*, Second, Cambridge Books Online, Cambridge University Press, 2009, ISBN: 9780511609923.

[9] S. P. Martin, *A Supersymmetry Primer*, arXiv: 9709356 [hep-ph].

[10] W. Pauli, *Über den Zusammenhang des Abschlusses der Elektronengruppen im Atom mit der Komplexstruktur der Spektren*, Zeitschrift für Physik A Hadrons and Nuclei **31**.1 (1925) 765–783.

[11] L. Álvarez Gaumé and J. Ellis, *Eyes on a prize particle*, Nat. Phys. **7**.2-3 (2011) 2–3.

[12] F. Englert and R. Brout, *Broken Symmetry and the Mass of Gauge Vector Mesons*, Phys. Rev. Lett. **13** (1964) 321–323.

[13] P. W. Higgs, *Broken Symmetries and the Masses of Gauge Bosons*, Phys. Rev. Lett. **13** (1964) 508–509.

[14] K. Olive et al., *Review of Particle Physics*, Chin. Phys. **C38** (2014) 090001.

[15] T. Aoyama et al., *Revised value of the eighth-order QED contribution to the anomalous magnetic moment of the electron*, Phys. Rev. **77** (5 2008) 053012.

[16] S. G. Karshenboim, *Progress in the accuracy of the fundamental physical constants: 2010 CODATA recommended values*, Physics-Uspekhi **56**.9 (2013) 883.

[17] ATLAS Collaboration, *SM Total Production Cross Sections Measurements*, https://atlas.web.cern.ch/Atlas/GROUPS/PHYSICS/CombinedSummaryPlots/SM/, 2015 (accessed July, 2015).

[18] J. Beringer et al., *Review of Particle Physics*, Phys. Rev. **86**.1, 010001 (2012) 010001.

[19] H. Miyazawa, *Baryon Number Changing Currents*, Progr. Theor. Exp. Phys. **36** (1966) 1266–1276.

[20] H. Miyazawa, *Spinor Currents and Symmetries of Baryons and Mesons*, Phys. Rev. **170** (1968) 1586–1590.

[21] R. N. Cahn, I. Hinchliffe and L. J. Hall,
The hierarchy problem in supersymmetric grand unified theories,
Phys. Lett. **109**.6 (1982) 426 –430.

[22] S. Dimopoulos and H. Georgi,
Softly broken supersymmetry and SU(5),
Nuclear Physics B **193**.1 (1981) 150 –162, ISSN: 0550-3213.

[23] I. Aitchison,
Supersymmetry in Particle Physics: An Elementary Introduction,
Cambridge University Press, 2007, ISBN: 9781139467056.

[24] W. Beenakker et al.,
Squark and gluino production at hadron colliders,
Nucl. Phys. **B492** (1997) 51–103,
arXiv: hep-ph/9610490 [hep-ph].

[25] M. Kaku, *Introduction to Superstrings and M-Theory*,
Graduate Texts in Contemporary Physics, ISBN: 9780387985893.

[26] Y. F. Chan et al.,
LHC Signatures of a Minimal Supersymmetric Hidden Valley,
JHEP **1205** (2012) 155, arXiv: 1112.2705 [hep-ph].

[27] S. Eidelman et al., *Review of Particle Physics*,
Phys. Lett. **592**.1–4 (2004) 1 –5.

[28] H. Nishino et al., *Search for Proton Decay via $p \to e^+\pi^0$ and $p \to \mu^+\pi^0$ in a Large Water Cherenkov Detector*,
Phys. Rev. Lett. **102**.14, 141801 (2009) 141801,
arXiv: 0903.0676 [hep-ex].

[29] L. Randall and R. Sundrum,
Out of this world supersymmetry breaking,
Nucl. Phys. B **557** (1999) 79–118,
arXiv: hep-th/9810155 [hep-th].

[30] G. F. Giudice et al., *Gaugino mass without singlets*,
JHEP **12**, 027 (1998) 27, arXiv: hep-ph/9810442 [hep-ph].

[31] D. Prieur, 'GMSB SUSY models with non pointing photons signatures in ATLAS at the LHC', *Proceedings, 40th Rencontres de Moriond on QCD and High Energy Hadronic Interactions: La Thuile, Aosta Valley, Italy, March 12-19, 2005*, 2005 335–338, arXiv: hep-ph/0507083 [hep-ph].

[32] J. D. Wells, 'Implications of supersymmetry breaking with a little hierarchy between gauginos and scalars', *11th International Conference on Supersymmetry and the Unification of Fundamental Interactions (SUSY 2003) Tucson, Arizona, June 5-10, 2003*, 2003, arXiv: hep-ph/0306127 [hep-ph].

[33] N. Arkani-Hamed et al., *Aspects of split supersymmetry*, Nucl. Phys. **B709** (2005) 3–46, arXiv: hep-ph/0409232 [hep-ph].

[34] R. Barbier et al., *R-parity violating supersymmetry*, Phys.Rept. **420** (2005) 1–202, arXiv: hep-ph/0406039 [hep-ph].

[35] M. Fairbairn et al., *Stable massive particles at colliders*, Phys.Rept. **438** (2007) 1–63, arXiv: hep-ph/0611040 [hep-ph].

[36] D. Decamp et al., *ALEPH: A detector for electron-positron annnihilations at LEP*, Nucl. Instrum. Meth. **A294** (1990) 121–178.

[37] K. Ahmet et al., *The OPAL detector at LEP*, Nucl. Instrum. Meth. **A305** (1991) 275–319.

[38] *The Construction of the L3 Experiment*, Nucl. Instrum. Meth. **A289** (1990) 35–102.

[39] P. A. Aarnio et al., *The DELPHI detector at LEP*, Nucl. Instrum. Meth. **A303** (1991) 233–276.

[40] R. Barate et al., *Search for pair production of longlived heavy charged particles in e+ e- annihilation*, Phys. Lett. **B405** (1997) 379–388, arXiv: hep-ex/9706013 [hep-ex].

[41] G. Abbiendi et al., *Search for stable and longlived massive charged particles in e+ e- collisions at $s^{(1/2)}$ = 130-GeV to 209-GeV*, Phys. Lett. **B572** (2003) 8–20, arXiv: hep-ex/0305031 [hep-ex].

[42] M. Acciarri et al., *Search for heavy neutral and charged leptons in e^+e^- annihilation at $S^{(1/2)}$ = 183-GeV and 189-GeV*, Phys. Lett. **B462** (1999) 354–364, arXiv: hep-ex/9909007 [hep-ex].

[43] P. Abreu et al., *Search for heavy stable and longlived particles in e+ e- collisions at $s^{(1/2)}$ = 189-GeV*, Phys. Lett. **B478** (2000) 65–72, arXiv: hep-ex/0103038 [hep-ex].

[44] L. Evans and P. Bryant, *LHC Machine*, JINST **3**.08 (2008) S08001.

[45] ATLAS Collaboration, *The ATLAS Experiment at the CERN Large Hadron Collider*, JINST **3**.08 (2008) S08003.

[46] CMS Collaboration, *The CMS experiment at the CERN LHC*, JINST **3**.08 (2008) S08004.

[47] K. Aamodt et al., *The ALICE experiment at the CERN LHC*, JINST **3** (2008) S08002.

[48] J. Alves A. Augusto et al., *The LHCb Detector at the LHC*, JINST **3** (2008) S08005.

[49] ATLAS Collaboration, *The ATLAS TRT barrel detector*, JINST **3** (2008) P02014.

[50] P Strizenec, *Performance of the ATLAS Liquid Argon Calorimeter after three years of LHC operation and plans for a future upgrade*, JINST **9**.09 (2014) C09007, arXiv: 1306.6756 [physics.ins-det].

[51] ATLAS Collaboration, *Commissioning of the ATLAS Muon Spectrometer with Cosmic Rays*, Eur. Phys. J. **C70** (2010) 875–916, arXiv: 1006.4384 [physics.ins-det].

[52] ATLAS Collaboration, *Improved luminosity determination in pp collisions at sqrt(s) = 7 TeV using the ATLAS detector at the LHC*, Eur. Phys. J. **C73**.8 (2013) 2518, arXiv: 1302.4393 [hep-ex].

[53] V. Abazov et al., *Search for neutral, long-lived particles decaying into two muons in $p\bar{p}$ collisions at $\sqrt{s}$ = 1.96-TeV*, Phys. Rev. Lett. **97** (2006) 161802, arXiv: hep-ex/0607028 [hep-ex].

[54] V. Abazov et al., *Search for Resonant Pair Production of long-lived particles decaying to b anti-b in p anti-p collisions at $s^{(1/2)}$ = 1.96 TeV*, Phys. Rev. Lett. **103** (2009) 071801, arXiv: 0906.1787 [hep-ex].

[55] F. Abe et al., *Search for long-lived parents of Z^0 bosons in $p\bar{p}$ collisions at $\sqrt{s}$ = 1.8 TeV*, Phys. Rev. **D58** (1998) 051102, arXiv: hep-ex/9805017 [hep-ex].

[56] CMS Collaboration, *Search in leptonic channels for heavy resonances decaying to long-lived neutral particles*, JHEP **1302** (2013) 085, arXiv: 1211.2472 [hep-ex].

[57] CMS Collaboration, *Search for long-lived particles that decay into final states containing two electrons or two muons in proton-proton collisions at $\sqrt{s}$ = 8 TeV*, Phys. Rev. **D91**.5 (2015) 052012, arXiv: 1411.6977 [hep-ex].

[58] CMS Collaboration, *Search for long-lived neutral particles decaying to quark-antiquark pairs in proton-proton collisions at $\sqrt{s}$ = 8 TeV*, Phys. Rev. **D91**.1 (2015) 012007, arXiv: 1411.6530 [hep-ex].

[59] ATLAS Collaboration, *Search for long-lived, weakly interacting particles that decay to displaced hadronic jets in proton-proton collisions at $\sqrt{s}$ = 8 TeV with the ATLAS detector*, Phys. Rev. **D92**.1 (2015) 012010, arXiv: 1504.03634 [hep-ex].

[60] G. Aad et al., *Search for displaced vertices arising from decays of new heavy particles in 7 TeV pp collisions at ATLAS*, Phys. Lett. **B707** (2012) 478–496, arXiv: 1109.2242 [hep-ex].

[61] ATLAS Collaboration, *Search for long-lived, heavy particles in final states with a muon and multi-track displaced vertex in proton-proton collisions at $\sqrt{s}$ = 7 TeV with the ATLAS detector*, Phys. Lett. **B719** (2013) 280–298, arXiv: 1210.7451 [hep-ex].

[62] ATLAS Collaboration, *Search for long-lived, heavy particles in final states with a muon and a multi-track displaced vertex in proton-proton collisions at sqrt(s) = 8 TeV with the ATLAS detector.* (2013), URL: https://inspirehep.net/record/1260972.

[63] ATLAS Collaboration, *A study of the material in the ATLAS inner detector using secondary hadronic interactions*, JINST **7**.01 (2012) P01013.

[64] S. Weinzierl, *Introduction to Monte Carlo methods* (2000), arXiv: hep-ph/0006269 [hep-ph].

[65] ATLAS Collaboration, *Measurement of jet shapes in top-quark pair events at $\sqrt{s}$ = 7 TeV using the ATLAS detector*, Eur. Phys. J. **C73**.12 (2013) 2676, arXiv: 1307.5749 [hep-ex].

[66] T. Sjostrand, S. Mrenna and P. Z. Skands, *PYTHIA 6.4 Physics and Manual*, JHEP **0605** (2006) 026, arXiv: hep-ph/0603175 [hep-ph].

[67] T. Sjöstrand et al., *An introduction to {PYTHIA} 8.2*, Comput. Phys. Commun. **191**.0 (2015) 159 –177.

[68] G. Corcella et al., *HERWIG 6: An Event generator for hadron emission reactions with interfering gluons (including supersymmetric processes)*, JHEP **0101** (2001) 010, arXiv: hep-ph/0011363 [hep-ph].

[69] J. Alwall et al., *MadGraph 5 : Going Beyond*, JHEP **1106** (2011) 128, arXiv: 1106.0522 [hep-ph].

[70] S. Agostinelli et al., *GEANT4: A Simulation toolkit*, Nucl.Instrum.Meth. **A506** (2003) 250–303.

[71] D. Costanzo et al., *ATLAS detector simulation* (2005), URL: http://inspirehep.net/record/1194793.

[72] ATLAS Collaboration, *The ATLAS Simulation Infrastructure*, English, Eur. Phys. J. C **70**.3 (2010) 823–874.

[73] ATLAS Collaboration, *Display of a collision event showing tracks in the Inner Detector system.* http://atlas.web.cern.ch/Atlas/public/EVTDISPLAY/events2009.html, 2009 (accessed July, 2015).

[74] R. O. Duda and P. E. Hart, *Use of the Hough Transformation to Detect Lines and Curves in Pictures*, Commun. ACM **15**.1 (1972) 11–15.

[75] R. E. Kalman, *A New Approach to Linear Filtering and Prediction Problems*, ASME. J. Basic Eng. **D82** (1960) 35–45.

[76] R Mankel, *Pattern recognition and event reconstruction in particle physics experiments*, Rep. Prog. Phys. **67**.4 (2004) 553.

[77] T Cornelissen et al., *The new ATLAS track reconstruction (NEWT)*, JPCS **119**.3 (2008) 032014.

[78] ATLAS Collaboration, *Performance of the ATLAS Inner Detector Track and Vertex Reconstruction in the High Pile-Up LHC Environment* (2012), URL: https://inspirehep.net/record/1204277.

[79] ATLAS Collaboration, *Performance of primary vertex reconstruction in proton-proton collisions at $\sqrt{s}$ =7 TeV in the ATLAS experiment* (2010), URL: https://inspirehep.net/record/1204019.

[80] S. Das, *On a New Approach for Finding All the Modified Cut-Sets in an Incompatibility Graph*, IEEE Trans. Comput. **22**.2 (1973) 187–193.

[81] ATLAS Collaboration, *Vertex reconstruction performance.* http://atlas.web.cern.ch/Atlas/GROUPS/PHYSICS/IDTRACKING/PublicPlots/ATL-COM-PHYS-2012-474/, 2012 (accessed July, 2015).

[82] W. Lampl et al., *Calorimeter clustering algorithms: Description and performance* (2008), URL: http://inspirehep.net/record/807147.

[83] M. Cacciari, G. P. Salam and G. Soyez, *The Anti-k(t) jet clustering algorithm*, JHEP **0804** (2008) 063, arXiv: 0802.1189 [hep-ph].

[84] T. Barillari et al., *Local hadronic calibration* (2009), URL: http://inspirehep.net/record/811642.

[85] ATLAS Collaboration, *Jet energy measurement with the ATLAS detector in proton-proton collisions at $\sqrt{s}$ = 7 TeV*, Eur. Phys. J. **C73**.3 (2013) 2304, arXiv: 1112.6426 [hep-ex].

[86] ATLAS Collaboration, *Charged-particle multiplicities in pp interactions measured with the ATLAS detector at the LHC*, New J.Phys. **13** (2011) 053033, arXiv: 1012.5104 [hep-ex].

[87] J. Alwall, S. de Visscher and F. Maltoni, *QCD radiation in the production of heavy colored particles at the LHC*, JHEP **2009**.02 (2009) 017.

[88] V. B. et al., *Recommendation of the ad-hoc committee on limit-setting procedures to be used by DØ in Run II*, DØ Note 4629 (2004), URL: http://www-d0.fnal.gov/Run2Physics/WWW/documents/Reports/Limit_Landsberg.pdf.

[89] A. L. Read, *Presentation of search results: the CL s technique*, J. Phys. G.: Nuclear and Particle Physics **28**.10 (2002) 2693.

[90] ATLAS Collaboration, *ATLAS SUSY Searches - 95% CL Lower Limits*, https://atlas.web.cern.ch/Atlas/GROUPS/PHYSICS/CombinedSummaryPlots/SUSY/ATLAS_SUSY_Summary/, 2015 (accessed July, 2015).

[91] Z. Liu and B. Tweedie, *The Fate of Long-Lived Superparticles with Hadronic Decays after LHC Run 1*, JHEP **06** (2015) 042, arXiv: 1503.05923 [hep-ph].

[92] C. Csaki et al., *Phenomenology of a Long-Lived LSP with R-Parity Violation*, JHEP **08** (2015) 016, arXiv: 1505.00784 [hep-ph].

[93] CMS Collaboration, *Searches for long-lived charged particles in pp collisions at $\sqrt{s}$=7 and 8 TeV*, JHEP **07** (2013) 122, arXiv: 1305.0491 [hep-ex].

[94] J. Pequenao,
'Computer generated image of the whole ATLAS detector', 2008,
URL: https://cds.cern.ch/record/1095924.

[95] A. Salzburger, *The ATLAS Track Extrapolation Package* (2007),
URL: http://inspirehep.net/record/1196562.

[96] D. Brandt, *Intermediate accelerator physics. Proceedings, CERN Accelerator School, Zeuthen, Germany, September 15-26, 2003* (2006), ed. by D. Brandt.

Acronyms

pp	proton-proton.
vev	Vacuum Expectation Value.
ALICE	A Large Ion Collider Experiment.
AMSB	Anomaly Mediated Supersymmetry Breaking.
ATLAS	A Toroidal LHC ApparatuS.
BCM	Beam Condition Monitor.
BEH	Brout-Englert-Higgs.
BSM	Beyond Standard Model.
CERN	Conseil Européen pour la Recherche Nucléaire.
CMS	Compact Muon Solenoid.
DV	Displaced Vertex.
EM	Electromagnetic.
FSR	Final State Radiation.
GMSB	Gauge Mediated Supersymmetry Breaking.
GUT	Grand Unification Theory.
HEP	High Energy Physics.
HMV	High Mass Vertex.

ID	Inner Detector.
IP	Interaction Point.
ISR	Initial State Radiation.
LEP	Large Electron-Positron Collider.
LHC	Large Hadron Collider.
LHCb	Large Hadron Collider beauty.
LLP	Long Lived Particle.
LMV	Low Mass Vertex.
LSP	Lightest Supersymmetry Particle.
LUCID	LUminosity measurement using Cerenkov Integrating Detector.
MB	Minimum Bias.
MC	Monte Carlo.
MS	Muon Spectrometer.
MSSM	Minimal Supersymmetry Standard Model.
NN	Neural Network.
Pixel	Pixel Tracker.
PV	Primary Vertex.
QCD	Quantum Chromo Dynamics.
QED	Quantum Electro Dynamics.
RPC	R-Parity Conservation.
RPV	R-Parity Violation.
SCT	Silicon Tracker.
SM	Standard Model.
SUSY	Supersymmetry.
TRT	Transition Radiation Tracker.